U.PORTO
FEUP FACULDADE DE ENGENHARIA
UNIVERSIDADE DO PORTO

DEPARTAMENTO DE ENGENHARIA MECÂNICA

Power Loss in Planetary Gearboxes Including the Influence of Gear Elastic and Dynamic Effects

Pedro Miguel Teixeira Marques

2017

Pedro Miguel Teixeira Marques

Power Loss in Planetary Gearboxes Including the Influence of Gear Elastic and Dynamic Effects

A Thesis submitted to Faculdade de Engenharia da Universidade do Porto

PROGRAMA DOUTORAL EM ENGENHARIA MECÂNICA

Supervisor: Doctor Ramiro C. Martins
Co-Supervisor: Professor Jorge H. O. Seabra

Departamento de Engenharia Mecânica
Faculdade de Engenharia da Universidade do Porto

Porto, 2017

Ó rodas, ó engrenagens, *r-r-r-r-r-r-r* eterno!
Forte espasmo retido dos mecanismos em fúria!

...pode parecer descabido, mas...

Acknowledgements

I have started my Integrated Masters in Mechanical Engineering at Faculdade de Engenharia da Universidade do Porto (FEUP) in September 2007 and finished it in 2012. Right after finishing the Integrated Masters I had the opportunity to start the Mechanical engineering PhD program (ProDEM - Programa Doutoral em Engenharia Mecânica) and I took it. I started my PhD in September of 2012.

Since the beginning I had to face many challenges, I had to push myself into unknown territory I had to stand up, I had to grow, I had to evolve, but hey, It is by pushing or being pushed that we become better and stronger! I have learned so much in these four years! I also have some good memories of great and sometimes epic moments from the time spent in this "adventure". With this said I would like to give a heart felt thank you to some people who have been around through this journey.

First of all I would like to say a big thank you to my family. My mother, my father and my little sister (not so little anymore) who were always there to fully supported me.

I would also like to greatly acknowledge to my supervisors Dr. Ramiro C. Martins and Prof. Jorge H. O. Seabra whom without this work wouldn't have been possible. They have always fully supported me, their guidance was precious a precious thing!

I have very much appreciated the company, all the unforgettable and priceless moments that I spent in the company of my fellow colleagues at CETRIB: André Gama, Anvar Maxkamov, Armando Campos, Beatriz Graça, Carlos Fernandes, David Gonçalves, Jorge Castro, Dipak Wagre, José Brandão, Luís Magalhães, Maroua Hammami and Tiago Cousseau.

I would also like to acknowledge to Eng. Jorge Reis who greatly contributed to the development and assembly of the control board of the no-load gearbox test rig.

I could not forget to give a special thank you to the students that have worked with me during their Masters Dissertation. David Costa, Diogo Pereira, João Filipe and Raquel Camacho, your work, conclusions, thoughts and different perspectives played a very important role in what was achieved in my PhD. We surely had our moments!

Thank you all!

Institutional and Financial Support

I am grateful to FEUP (Faculdade de Engenharia da Universidade do Porto) and all the people from the Mechanical Engineering Department.

I am also thankful to INEGI (Instituto de Ciência e Inovação em Engenharia Mecânica e Engenharia Industrial) who has supported me as the host institution by providing all the necessary test rigs and lab equipment to perform my work.

I gratefully acknowledge the funding through several projects and grants whom without this work would not have been possible:

- National Funds through Fundação para a Ciência e Tecnologia (FCT),under the PhD grant SFRH/BD/104791/2014 and under the projects EXCL/SEM-PRO/0103/2012 and EXCL-II/SEM-PRO/0103/2012;
- COMPETE and National Funds through Fundação para a Ciência e a Tecnologia (FCT), under the project Incentivo/EME/LA0022/2014;
- Quadro de Referência Estratégico Nacional (QREN), through Fundo Europeu de Desenvolvimento Regional (FEDER), under the project NORTE-07-0124-FEDER-000009 - Applied Mechanics and Product Development;
- NORTE-01-0145-FEDER-000022 - SciTech - Science and Technology for Competitive and Sustainable Industries, cofinanced by Programa Operacional Regional do Norte (NORTE2020), through Fundo Europeu de Desenvolvimento Regional (FEDER);
- LAETA under the project UID/EMS/50022/2013.

Abstract

In recent years, environmental and sustainability issues have acquired major importance, propelling the investments in renewable energy sources. Worldwide efforts have been made to increase the energetic and operational efficiency of equipments. Many machines have a motor or some other kind of propelling mechanism that have an input that rotates at fixed speed or in a range of speeds that is not the desired one. In many situations in order to overcome these issues gearboxes are used. Designing a transmission with the care of maximizing efficiency while keeping proper operating safety factors has become a necessity. The main purpose of this work was to study the influence of operating conditions and gear oil formulation in the efficiency of meshing gears (applied to a planetary gearbox) including elastic and dynamic effects.

Four wind turbine gear oils were selected, characterized and gearbox efficiency tests were performed in a gearbox test rig with recirculating power. A no-load power loss gearbox test rig was also developed, so that both load and no-load power loss measurements were performed. A numerical classical gearbox power loss model was developed aiming to understand the influence of each component in the gearbox power loss.

At nominal load the most important power loss sources are the gears. An accurate gear load loss prediction is quite dependent of the gear tooth load sharing model that is considered. Three quasi-static gear load sharing models were developed for both internal or external spur and helical gears.

Aiming to understand the influence of gear dynamics in gear power loss, a four degree of freedom lumped mass gear dynamics model accounting, for time varying mesh stiffness, friction and damping, was also developed.

The findings and the models developed for a simple gear pair were applied to study the power loss behaviour of a planetary gearbox.

The experimental tests in the planetary gearbox showed that different lubricants promote very different power loss behaviours. The more refined solutions for the load distribution model proved to be fundamental in obtaining accurate power loss predictions.

The dynamic power loss model results have showed that average power loss can be affected by gear dynamics.

Resumo

Nos últimos anos as preocupações relacionadas com questões ambientais e de sustentabilidade tem aumentado, potenciando assim os investimentos em energias renováveis. Têm sido feitos esforços internacionais para aumentar a eficiência energética e operacional dos equipamentos de modo a que se poupem recursos. Muitos das máquinas e equipamentos têm um motor ou algo equivalente com fim de potenciar uma dada acção e muitas vezes esse elemento motor funciona numa gama de velocidades que não é a adequada para o fim ao qual este se destina. Nestes casos muitas das vezes são usadas caixas de engrenagens (multiplicadoras ou redutoras). Projectar caixas de engrenagens maximizando a eficiência enquanto se mantém os factores de segurança tornou-se uma necessidade. O principal objectivo deste trabalho é o de estudar a influência das condições de funcionamento e do lubrificante na eficiência do engrenamento (aplicado a uma caixa de engrenagens planetária) tendo em conta efeitos elásticos e dinâmicos.

Quatro óleos de engrenagens para aerogeradores foram selecionados e caracterizados. A influência do lubrificante na eficiência de uma caixa de engrenagens planetária foi depois estudada num banco de ensaios com recirculação de potência. Foi ainda desenvolvido um banco de ensaios para estudar as perdas de potência independentes da carga. Foi também desenvolvido um modelo numérico de eficiência para caixas planetárias com o objectivo de perceber a influência de cada um dos componentes na eficiência.

Em condições nominais de funcionamento a maior fonte de perdas são as engrenagens. Se o objectivo é melhorar a previsão, torna-se então necessário aprofundar o estudo do modo como as perdas de potência nas engrenagens se desenvolvem. A previsão desta componente está fortemente dependente da formulação para a repartição de carga entre os dentes das engrenagens. Foram então desenvolvidos três modelos quase-estáticos de repartição de carga formulados de modo a que a sua aplicação possa ser feita a engrenagens de dentado recto e helicoidal externas ou internas.

De modo a perceber a influência da dinâmica do engrenamento na eficiência de um par de engrenagens foi desenvolvido um modelo dinâmico torsional com quatro graus de liberdade que tinha em conta a variação da rigídez do dentado, o atrito e o amortecimento.

Os modelos desenvolvidos para um par simples de engrenagens foram também aplicados a uma caixa de engrenagens planetárias de modo a perceber a influência de tais fenómenos na perda de potência.

Os resultados experimentais mostraram que diferentes formulações de lubrificante para a mesma aplicação promovem desempenhos muito diferentes no que à eficiência

diz respeito. Os desenvolvimentos conseguidos com os modelos de distribuição de carga foram fundamentais para a melhoria da previsão da perda de potência da caixa planetária.

Foi ainda demonstrado que os efeitos dinâmicos têm influência na perda de potência.

Résumé

Depuis les années 90 les questions environnementales et de développement durable ont gagné une importance majeure qui ont catalysé les investissements dans les énergies renouvelables. Partout au monde des efforts ont été menez pour augmenter le rendement énergétique et opérationnelle des équipements. Fréquemment les machines ont un moteur ou un autre mécanisme de propulsion qui tourne dans une gamme de vitesses qui ne correspond pas à la vitesse de service, demandant l'utilisation d'une transmission par engrenages pour adapter ces vitesses. La conception de transmissions mécaniques avec rendement maximisé est devenue un impérative, tout en gardant les facteurs de sécurité nécessaires. Donc, l'objectif principale de ce travail est l'étude de l'influence des conditions de fonctionnement et de la formulation de d'huile sur le rendement des engrenages (appliquées à une engrenage planétaire), tenant compte de la déformation élastique et du comportement dynamique des dents.

Quatre huiles d'engrenages pour des éoliennes ont été sélectionnés et caractérisés, et des essais de rendement de d'engrenages planétaires ont été réalisés sur un banc d'essais pour transmissions, avec circulation de puissance, aussi bien que sur un banc essais à vide, spécifiquement développé pour cet effet. Un modèle analytique classique de pertes de puissance dans les boîtes d'engrenages a été développé avec le but de comprendre et quantifier l'influence de tous les paramètres et composants sur les pertes.

A la charge nominale, les engrenages sont responsables par la grande majorité des pertes. De toute façon la prévision précise des pertes de puissance sous charge est fortement dépendant du modèle de répartition de la charge sur les dents de l'engrenage. Trois modèles quasi statique ont été développés pour les engrenages hélicoïdales à denture extérieure et intérieure.

De façon à comprendre l'influence de la dynamique des engrenages sur les pertes de puissance, un modèle dynamique à masses discrètes avec quatre degrés de liberté a été développée, tenant compte de la variation de rigidité, d'amortissement et de frottement entre les dents pendant l'engrènement.

Les modèles et les conclusions et ces études ont été appliquées à une engrenage planétaire de façon à comprendre ses pertes de puissance pendant son fonctionnement à vide et sous charge.

Les essais de validation menés sur l'engrenage planétaire ont montré que les huiles lubrifiantes génèrent des pertes de puissance très différentes. Les solutions plus détaillées de la distribution de charge sur les dentures ont prouvé être fondamentales pour l'obtention de prévisions d'haute précision des pertes de puissance.

Les résultats des simulations ont clairement mis en évidence l'influence du comportement dynamique des engrenages sur les pertes des pertes de puissance de l'engrenage planétaire.

Keywords

Efficiency
Power loss
Load distribution
Gear dynamics
Planetary gears
Churning loss

Palavras chave

Eficiência
Perda de potência
Repartição de carga
Dinâmica do engrenamento
Caixas de engrenagens planetárias
Perdas por chapinagem

Mots-clés

Rendement
Puissance dissipée
Répartition de la charge
Dynamique des engrenages
Train épicycloïdal
Perte de puissance par barbotage

Contents

List of Figures

List of Tables

List of Equations

Nomenclature

Symbol	Units	Description
a	m	Centre distance
$a_{0,1,2,3,4}$	-	Coefficients dependent on tip contact ratio
A_{Air}	m^2	Ventilated area of the gearbox
A_{ca}	m^2	Total housing area of the gearbox
A_{Heat}	m^2	Global heat transfer area of the gearbox
A_{rad}	m^2	Radiation reference area
b	m	Gear width
b_i	m	Coefficients for the EHL based formula (Xu Hai)
B	mm	Rolling bearing width
C_{ch}	Nm	churning torque
CFD	-	Acronym for computational fluids dynamics
C_m	-	Non-dimensional churning torque
$c_{A,B}$	N/m	Rolling bearing spring constant
c_{1c}	Ns/m	Damping coefficient
c_{1p}	Ns/m	Damping coefficient
c_c	Ns/m	Damping coefficient
c_{pw}	Ns/m	Damping coefficient
c_{s2}	Ns/m	Damping coefficient
c_{sp}	Ns/m	Damping coefficient
c_{w2}	Ns/m	Damping coefficient
c_{wp}	Ns/m	Damping coefficient
CoF	-	Acronym for coefficient of friction
d	mm	Rolling bearing bore diameter
D	mm	Rolling bearing outside diameter
DGBB	-	Acronym for deep groove ball bearing
D^{Mto}	-	Parameter for μ^{Mto}
d_m	m	Bearing mean diameter
DoF	-	Acronym for degree of freedom
d_{sh}	mm	Shaft diameter
d_{ai}	m	Addendum diameter of gear i
d_{bi}	m	Base diameter of gear i
d_{pi}	m	Pitch diameter of gear i
F	N	Force
f_A	-	Variable used for the calculation of the frictional moment of drag losses

F_a	N	Axial Force
F_{bn}	N	Total tooth normal force
F_{bt}	N	Tooth normal force (transverse section)
FCNRB	-	Acronym for Full-complement needle roller bearing
FEM	-	Acronym for finite element method
$f_N(\xi)$	N/mm	Normal force per length
$F_N(\xi)$	N	Surface normal force
Fr	-	Froude number
F_r	N	Radial Force
F_{rij}	N	Radial force at ij
f_t	-	Variable used for the calculation of the frictional moment of drag losses
F_{tij}	N	Tangential force at ij
f_0	-	Coefficient dependent on bearing design and lubrication method
F_0^{axi}	N	Pre-load force
f_0	-	no-load loss coefficient
$f_{1,2}$	-	Coefficient that takes into account the direction of load application
G_{rr}	Nm	Variable for the calculation of the rolling frictional moment
G_{sl}	Nm	Variable for the calculation of the sliding frictional
g	m/s^2	Gravity acceleration
$H(t)$	-	Heaviside function
H_{tooth}	-	tooth height
h	m	Oil immersion depth, figure 1.5
h_0	m	Minimum oil film thickness
H_V	-	Gear loss factor
H_V^{Buc}	-	Gear loss factor (Buckingham)
H_V^{Nie}	-	Gear loss factor (Niemann and Winter)
H_V^{num}	-	Gear loss factor (numerical)
H_V^{Ohl}	-	Gear loss factor (Ohlendorf)
H_V^{OhlM}	-	Gear loss factor (Modified Ohlendorf)
I_x	m	Flow length (path of flow filament along housing wall)
J_1	kgm^2	Mass moment of inertia of body 1
J_2	kgm^2	Mass moment of inertia of body 2
J_c	kgm^2	Mass moment of inertia of body c
J_p	kgm^2	Mass moment of inertia of body p
J_s	kgm^2	Mass moment of inertia of body s
J_w	kgm^2	Mass moment of inertia of body w
k^{cai}	-	Cai's single mesh stiffness
K_{1c}	Nm/rad	Torsional stiffness constant

K_{1p}	Nm/rad	Torsional stiffness constant
K_{w2}	Nm/rad	Torsional stiffness constant
K_{pr}^{t}	N/m	Time dependent mesh stiffness
K_{pw}^{t}	N/m	Time dependent mesh stiffness
K_{s2}	Nm/rad	Torsional stiffness constant
K_{sp}^{t}	N/m	Time dependent mesh stiffness
K_a	N	Axial load on the tapered roller bearings, necessary for the pre-load calculation
K_{max}^{ISO}	N/m	Maximum single stiffness (ISO)
$K_{ball,roll}$	-	Rolling element related constant
K_{rs}	-	Replenishment/starvation coefficient
K_Z	-	Bearing type related geometric constant
$l_i^{s,h}(\xi)$	-	Length of a single line of contact
$L^{s,h}(\xi)$	-	Sum of the lengths of the lines of contact
l	m	Average sum of contacting lines length
l_g	-	Parameter for the calculation of $a_{0,1,2,3,4}$
m	m	Gear module
m_g	-	Parameter for the calculation of $a_{0,1,2,3,4}$
M^{rol}	Nm	Total frictional moment of a bearing
M_0^{rol}	Nm	No-load friction moment of a needle bearing
M_1	Nm	Moment in DoF 1
M_1^{rol}	Nm	Load friction moment of a needle bearing
M_2	N	Moment in DoF 2
M_2^{rol}	Nm	Axial Load friction moment of a needle bearing
$M_{A,D,ext,mot,i}$	Nm	Moment or torque (index related to the application point)
$M_{drag}^{ball,roll}$	Nm	Frictional moment of drag losses (SKF)
M_{rr}	Nm	Rolling frictional moment (SKF)
M_{seal}	Nm	Frictional moment of the bearing seal (SKF)
M_w	Nm	Torque applied in the driven gear (w)
M_{sl}	Nm	Sliding frictional moment (SKF)
n	rpm	Rotational speed
N	-	Number of planets (planetary gearbox)
n_g	-	Parameter for the calculation of $a_{0,1,2,3,4}$
p	Pa	Pressure
P_h	GPa	Maximum Hertzian perssure
PoA	-	Acronym for plane of action
PoC	-	Acronym for path of contact
PR	-	Acronym for planet-ring
p_{VZP}	W/mm	Evolution of gears load losses per unit of contact length
P_{VZP}^{single}	W	Evolution of the gears load losses for a single tooth pair
P_{VZP}^{total}	W	Evolution of the total gear load losses
P_{VZP}^{G}	W	Average gear load losses (integral method)

P_{IN}	W	Transmitted power (gear mesh)
P_V	W	Total power loss
P_{VD}	W	Seals power loss
P_{VL}	W	Rolling bearings losses
P_{VZ0}	W	Gears no-load power losses
P_{VZP}	W	Gears load losses
P_{VX}	W	Auxiliary losses
$\dot{Q}_{cd}$	W	Heat flow rate due to conduction
$\dot{Q}_{cv}$	W	Heat flow rate due to convection
$\dot{Q}_{rad}$	W	Heat flow rate due to radiation
$\dot{Q}_{total}$	W	Total heat flow rate
r_{ai}	m	Addendum radius of gear i
r_{pi}	m	Pitch radius of gear i
R_a	m	Arithmetic mean roughness
R_{zi}	μm	maximum height of roughness
Re_c	-	Critical Reynolds number
r_{bi}	m	Base radius of gear i
R_S	-	Variable used for the calculation of the frictional moment of drag losses (rolling bearings)
R	J	Rayleigh dissipation function
R_X	m	Equivalent radius
R_{zi}	μm	Maximum height of average roughness
$R_{1,2}$	-	Geometric constants for rolling frictional moment (SKF)
S	μm	Surface roughness
S_m	m^2	Gear immersion surface area
S_g	-	Gear geometry parameter
SR	-	Slide-to-roll ratio
SP	-	Acronym for sun-planet
S_p	-	Modified Stribeck parameter
T	J	Total kinetic energy
T^{mesh}	s	Mesh period
T_{Oil}	$^\circ$ C	Oil sump temperature
T_{Room}	$^\circ$ C	Room temperature
TRB	-	Acronym for taper roller bearing
u	-	Gear ratio
$U_{1,2}$	m/s	Surface tangential velocity
V	J	Total elastic potential energy
V.I.	-	Viscosity index
v_b	m/s	Base cylinder tangential speed
v_g	m/s	Sliding velocity
v_{tb}	m/s	Base cylinder transverse tangential speed
V_M	-	Drag loss factor

V_{air}	m/s	Air velocity
V_e	m/s	Entrainment velocity
X_L	-	Lubricant parameter
X_R	-	Parameter for μ_{mz}^M
Y	-	Axial load factor for single-row bearings
z_i	-	Number of teeth of gear i
α	Pa^{-1}	Coefficient of piezoviscosity
α_{SKF}	-	Variable used to calculate G_{rr}
$\alpha_{cnv,forced}$	W/mK	Forced convective heat transfer coefficient
$\alpha_{cnv,free}$	W/mK	Free convective heat transfer coefficient
$\alpha_{cnv,combined}$	W/mK	Combined convective heat transfer coefficient
α_{Heat}	W/mK	Global heat transfer coefficient
α_{rad}	W/mK	Radiation heat transfer coefficient
α_t	rad	Transverse pressure angle
β_b	rad	Base helix angle
δW_{nc}	J	Work of non-conservative forces
Δ	%	Relative error
ΔT	°C	Stabilized operating temperature
ω	rad/s	rotational speed
ϵ	–	Emission ratio of housing surface
ϵ_α	-	Transverse contact ratio
ϵ_β	-	Overlap ratio
$\epsilon_{1,2}$	-	Tip contact ratio
η_0	Pas	Dynamic viscosity at the oil bath temperature
γ	s^{-2}	Centrifugal acceleration
Λ	-	Specific film thickness
Λ^v	-	Parameter for gear efficiency (Velex)
μ_{bl}^D	-	Boundary reference COF (Doleschel)
μ_{bl}^{Mto}	-	Boundary reference COF (Matsumoto)
μ_{bl}^{SKF}	-	Boundary reference COF (SKF)
μ_{EHD}^D	-	Fluid film reference COF (Doleschel)
μ_{EHD}^{Mto}	-	Fluid film reference COF (Matsumoto)
μ_{EHD}^{SKF}	-	Fluid film reference COF (SKF)
μ_{mz}^D	-	Coefficient of friction (Doleschel)
μ^{Fer}	-	Coefficient of friction (Fernandes)
μ^{Mto}	-	Coefficient of friction (Matsumoto)
μ^{seal}	-	Seal coefficient of friction (Croes)
μ^{Xu}	-	Coefficient of friction (Xu)
μ_{mz}^{fer}	-	Average coefficient of friction (Fernandes)
μ_{mz}^{ISO}	-	Average coefficient of friction (ISO 6336-4)
μ_{mz}^{KL}	-	Average coefficient of friction (kelley-Lemanski)
μ_{mz}^M	-	Average coefficient of friction (Michaelis)

μ^S_{mz}	-	Average coefficient of friction (Schlenk)
μ_{sl}	-	Sliding friction coefficient (SKF)
ν_0	cSt	Kinematic viscosity
ϕ^D	-	Friction sharing function (Doleschel)
ϕ^{Fer}	-	Friction sharing function (Fernandes)
ϕ^{Mto}	-	Friction sharing function (Matsumoto)
ϕ_{bl}	-	Sliding friction sharing function (SKF)
ϕ_{ish}	-	Inlet shear heating reduction factor
ϕ_{rs}	-	Kinematic replenishment/starvation reduction factor
ψ_i	-	Non-dimensional coefficient
ρ_{oil}	-	Oil bulk density
ρ^v	-	Gear efficiency (Velex)
θ	rad	Angle, figure 1.5
ξ	-	Non-dimensional coordinate along the path of contact
ω	rad/s	Angular speed
ω^i_n	rad/s	Natural frequency
ω^i_{self}	rad/s	Self-excitation speed

Introductory notes

In recent years, environmental and sustainability issues have acquired major importance propelling the investments in renewable energy sources. Worldwide efforts have been made to increase the energetic and operational efficiency of equipments aiming to save resources [1–13].

One of the most relevant renewable energy is wind power which is obtained through wind turbines, converting the kinetic energy of the wind into mechanical energy. The blades in the wind turbines are designed to spin as the air flows through them, converting the kinetic energy of the wind into mechanical energy - torque - which is transmitted along the main shaft to the generator. The rotor rotational speed and torque are transformed by the main gearbox in order to match the necessary operating conditions of the generator. The gearbox might have different configurations, although one of the most used designs has two planetary stages plus a helical gear stage at the end. The efficiency of these multiplying gearboxes, with this arrangement or similar is already quite good. Nevertheless, any efficiency increase will have a significant impact, reducing the power loss and the operating temperature. In a three stage gearbox used in 1 MW wind turbines, an improvement of 0.33% per gear stage leads to an overall efficiency improvement of 1% which represents an energy gain of 10 kW. The average household energy consumption world wide for 2011 was 3338 kWh, [14], representing 0.38 kW per household. This means that such a slight improvement as 0.33% would allow each wind turbine to supply at least 20 extra households. As little as it may seem, taking into account all the already existent wind farms with wind turbines usually with a capacity ranging 1.5-3 MW, the slight improvements on the efficiency of a gearbox should not be neglected.

Many machines and mechanisms, like the aforementioned wind turbines, have a motor or some other kind of propelling mechanism that have an input that rotates at fixed speed or in a range of speeds that is not the desired one [15, 16]. In many situations in order to overcome these issues gear transmissions are used. Designing a gearbox with the care of maximizing efficiency while keeping proper safety factors has become a necessity. Optimizing the gearbox efficiency, also leads to lower operating temperatures which benefits the working life of all components. Lower operating temperatures can also potentially lead to a lower failure probability, therefore lowering the maintenance costs [17].

Efficiency driven gear designs are already possible through an improved gear tooth design or selecting the most suitable gear oil formulation [18–21], or even, combining these two possibilities.

Höhn *et al.* [22] presented a study that showed that it is possible to improve gearbox power loss acting on both gear geometry design and rolling bearing selection.

Recently Petry-Johnson *et al.* [23] presented a test methodology to measure spur gear efficiency under high speed and variable torque conditions, the influence of some of the gear design variables were evaluated in the power loss. Later on Chang *et al.* [24] used these results to validate the power loss model he had developed.

More recently Fernandes *et al.* [1–3] performed extensive experimental testing and modelling of the power losses generated by three different gear geometries. The rolling bearings model as well as the gear loss models were properly calibrated from simple experimental tests. The same lubricants were later used in another experimental campaign [9] and power loss predictions using the calibrated model were in good agreement with the measurements.

Detailed gearbox efficiency estimations will lead to the design of more reliable and efficient gearboxes, which can save resources not only during development, but also through the gearbox's expected life.

Purpose and Research work

The main purpose of the work presented in this thesis was to study the influence of operating conditions and gear oil formulation including gear elastic and dynamic effects in the efficiency of a gearbox, in particular planetary gearboxes. In order to achieve such feat a lot of experimental work was done. Several analytical models were also developed as well as their numerical implementation through the form of computer programs.

A series of efficiency tests in a recirculating power back-to-back gearbox test rig were conducted aiming to understand the influence of operating conditions and gear oil formulation in the power loss of a gearbox. Before these tests took place the chemical and physical characterization of four selected wind turbine gear oils was done. This characterization included the density and viscosity (dynamic and kinematic) variations with temperature, ICP and FTIR analysis. Film thickness and traction measurements were also performed in a ball-on-disc device.

The back-to-back gearbox test rig was also modified to support planetary gearboxes. New gearbox mounts, some couplings and test rig shafts were designed. The commercially available planetary speed reducers that were selected were also modified to be compatible with a series of temperature measuring probes. The test rig software was revised and an extensive calibration procedure was also conducted.

A no-load gearbox power loss test rig was also developed and designed from the ground up. The no-load power loss of the planetary gearbox tested in the back-to-back gearbox test rig was measured in this newly developed no-load loss test rig.

This work had a very strong experimental component. The author did not only perform the experimental tests, but was also responsible for the maintenance procedures including the oil changes, assembling and disassembling of the gearboxes and gearbox test rigs. The total time spent on these tasks alone was above fifteen hundred hours.

As referenced at the beginning of this section, this work also had a strong analytical and numerical component.

A classical numerical power loss model for planetary gearboxes was developed and implemented. The main goal of this model was to study the influence of each power loss component in the total power loss of the gearbox. It was concluded that the gears were one of the major power loss contributors in the case of wind turbine planetary gearboxes (low speed and high torque).

Being the gears one of the main power loss components, the focus was on refining the prediction of the power loss between meshing tooth pairs which depends on the gear tooth load distribution problem. The load distribution was assumed to be dependant not only on tooth and shaft stiffness, but also on the masses of the rotating bodies (shafts and gears).

The load distribution and gear dynamics problems were first studied for a simple gear pair. Three quasi-static gear tooth load sharing models for spur and helical external or internal gears were developed:

- The simplest of the three (rigid model) is based on Heaviside step functions to describe the load distribution along the path of contact.
- The second model (elastic model) takes an analytical approach to gear tooth load distribution based on the single tooth mesh stiffness.
- The third model (local elastic model) is based in the minimization of the constrained total potential energy. It considers tooth compliance as well as frictional effects allowing to obtain both friction dependent load distribution and mesh stiffness functions. In some cases the mesh stiffness function had very steep variations due to the transitions between meshing tooth pairs, but also the frictional effects. These kind of stiffness variations are to a great degree responsible for dynamic excitations. This raised the question: "What would be the effects of gear dynamics in the power loss?"

Many authors have already studied gear dynamics. In previous works the innovations in gear dynamics were mainly in the detail of the dynamic models (more degrees of freedom, varying mesh stiffness and friction, gyroscopic, rocking effects...) and the main focus usually were in the dynamic overloads, critical speeds, transmission errors and gear noise [25].

A torsional four degree of freedom lumped mass gear dynamics model for a single gear pair accounting for time varying mesh stiffness, friction (constant and local COF), damping as well as external inertias connected to elastic shafts was developed. The differential equations of motion were deduced from the Principle of Least Action.

After the load distribution and gear dynamic problems were studied for a single gear pair the same concepts were applied to a planetary gear. The quasi-static load distribution models were developed in such a way that they could be directly applied to the planetary gear. Resting on the same principles of the single gear pair dynamic model a torsional n-DoF planetary gear dynamic model was also developed.

The load distribution and gear dynamics models were implemented through the form of a computer program. When possible, the author took advantage of open source software, more specifically the FEM solver and 3D tetrahedral mesh generator. The final revision of the software that was developed consists of more than 16000 lines of code (excluding the open source libraries).

Thesis outline

This document is the result of more than four years of work. The thesis is divided in 5 chapters. The order in which this document is organized does not necessarily reflect the real order of events.

Chapter **1 - Classical Gearbox Powerloss Model** is dedicated to the presentation of the classical gearbox power loss model. It starts with the more commonly used and accepted power loss models for rolling bearings, seals and gears which are presented and discussed.

In Chapter **2 - Developments for a Gear Pair: Load Sharing and Power Loss in Meshing Gears** the load sharing problem between meshing gears is discussed. Three models developed are introduced and some results for the tree types of spur gears are presented.

Chapter **3 - Developments for a Gear Pair: Gear Dynamics and Power Loss** is dedicated to the gear dynamics problem. The model that was developed is presented and the influence of gear dynamics in power loss discussed.

Chapter **4 - Power Loss in a Multiplier Planetary Gearbox Lubricated with Wind Turbine Gear Oils** is dedicated to an experimental and numerical study in a multiplier planetary gearbox lubricated with wind turbine gear oils. The influence of operating conditions and gear oil formulation in the power loss and its components is studied. The lubricants that were selected are presented. The gearbox test rigs and all of the experimental procedures are explained. The numerical power loss model for the full planetary gearbox is also introduced and its estimations compared with the experimental results.

In Chapter **5 - Planetary Gears: Load Sharing and Local Power loss (quasi-static vs dynamic)** a planetary gear dynamics model is introduced and the effects of gear dynamics in power loss at selected operating conditions is evaluated.

Chapter **6 - Conclusions and Future Work** is dedicated to the main conclusions as well as ideas for future works.

1. Classical Gearbox Powerloss Model

The study of gearbox efficiency, mainly the prediction of it, has always been considered a quite difficult task. The combinations of different types of gears, shaft arrangements, rolling bearings, other elements and housing designs is almost infinite. Combined with the almost infinite design possibilities, the operating conditions, namely speed and torque, as well as other factors and environmental variables like humidity and ambient temperature complicate the problem even further.The efficiency of gears has been a topic of study for many years. Power loss models for gears and rolling bearings have been developed in the past [26–29]. The problem of the prediction of gearbox efficiency is still an active topic of research specially considering the ever increasing demands for operating efficiency of machines and mechanisms.

According to Höhn *et al.* [28], the total power loss in a gearbox is the sum of gears, bearings, seals and auxiliary losses, figure 1.1.

Gear and bearing losses can be separated in no-load and load losses. No-load losses occur with the rotation of mechanical components, even without torque transmission. No-load losses are mainly related to lubricant viscosity and density as well as immersion depth of the components in a sump lubricated gearbox, but it also depends on operating conditions and internal design of components and the gearbox casing.

Load dependent losses occur in the contact of the power transmitting components. Load losses depended on the transmitted torque, coefficient of friction and sliding velocity in the contact areas of the components.

The auxiliary losses (P_{VX}) are there to account for other dissipative sources that are not generated by gears, bearings or the sealing elements.

Usually, for nominal operating conditions, the dominant power losses of a gearbox are the load losses. When working at high speeds and with low or moderate loads, no-load losses can overcome the load losses.

In behalf of improving gearbox efficiency, it is fundamental to understand how each component contributes to the total power loss and how the operating conditions and the lubricant formulation can influence each energy dissipation source.

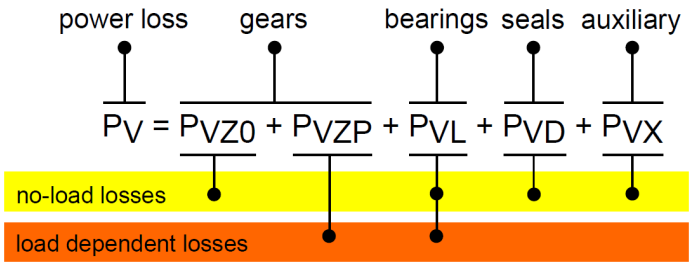

Figure 1.1.: Different power loss mechanisms in a gearbox [28].

1.1. Power loss in gears

Gear friction power loss stands as one of the most influential power loss components, if not the most, when high power is transmitted at low speeds or at nominal operating conditions.

The classical model for gear power loss is presented in equation (1.1.1). This model was first proposed by Ohlendorf [30]. In this model a constant and average coefficient of friction μ_{mz} is assumed. The gear loss factor H_V was initially developed for spur gears (elastic effects were disregarded).

$$P_{VZP} = P_{IN} \cdot \mu_{mz} \cdot H_V \tag{1.1.1}$$

In equation (1.1.1) P_{IN} is the effective power that is transmitted, ($P_{IN} = F_{bti} \cdot \omega_i \cdot r_{bi}$), μ_{mz} is the average coefficient of friction and H_V is a gear loss factor which takes into account the load distribution and sliding velocity along the path of contact.F_{bti} represented the tooth normal force projected in the transverse plane and it is defined according to equation (1.1.2).

$$F_{bti} = \frac{M_i}{r_{bi}} \tag{1.1.2}$$

The main discussion in this chapter will be around the sliding losses. It should be noted that rolling power losses also occur in meshing gears. In most of the scenarios the rolling losses can be disregarded [28].

1.1.1. Gear loss factor

According to Wimmer [31], the general formula for the gear loss factor can be expressed according to equation (1.1.3) (this equation was obtained from equation (2.5.2) assuming a constant coefficient of friction and defining a reference load (F_{bt}) and speed ($\omega \cdot r_b$).) In fact this equation should not be taken separately from equation (1.1.1).

$$H_V^{num} = \frac{1}{p_{bt}} \int_0^b \int_A^E \left[\frac{F_N(x,y)}{F_{bt}} \cdot \frac{v_g(x,y)}{v_b} \right] dxdy \tag{1.1.3}$$

Ohlendorf

Ohlendorf [30] first introduced equation (1.1.4) to calculate the gear loss factor for spur gears. This equation is not proven for helical gears and/or gears with profile shifts. It is valid for $1 \leq \epsilon_\alpha \leq 2$ and $\epsilon_{1/2} \leq p_{et}$, also it does not take into account meshing tooth elasticity in the load distribution.

$$H_V^{Ohl} = \frac{\pi \cdot (u+1)}{z_1 \cdot u \cdot \cos(\beta_b)} \left(1 - \epsilon_\alpha + \epsilon_1^2 + \epsilon_2^2\right) \tag{1.1.4}$$

Niemann and Winter

Niemann and Winter [32] proposed a gear loss factor that is shown in equation (1.1.5).

$$H_V^{Nie} = (1+u)\frac{\pi}{z_1 \cos\beta_b}\frac{1}{\epsilon_\alpha}\left(\frac{1}{\epsilon_\alpha} - 1 + (2k_0^2 + 2k_0 + 1)\epsilon_\alpha\right) \tag{1.1.5}$$

k_0 is defined according to equation (1.1.10).

Buckingham

Buckingham [26] developed an expression for the efficiency of a meshing gear pair. A gear loss factor (equation (1.1.6)) can also be derived from this approach.

$$H_V^{Buc} = (1+u)\frac{\pi}{z_1 \cos\beta_b}\frac{1}{\epsilon_\alpha}\left(2k_0^2 - 2k_0 + 1\right) \tag{1.1.6}$$

k_0 is also defined according to equation (1.1.10).

Ohlendorf (improved)

According to Wimmer [31] in order to account for a broader range of gears equation (1.1.7) can be considered instead of (1.1.4).

$$H_V^{OhlM} = \frac{\pi(u+1)}{z_1 \cdot u\cos(\beta_b)}\left(a_0 + a_1|\epsilon_1| + a_2|\epsilon_2| + a_3|\epsilon_1|\epsilon_1 + a_4|\epsilon_2|\epsilon_2\right) \tag{1.1.7}$$

Based on ϵ_1, ϵ_2 and ϵ_α three parameters are defined (ceil is rounding up to the nearest more positive integer):

- l_g - ceil(ϵ_1);
- m_g - ceil(ϵ_2);
- n_g - ceil(ϵ_α);

Based on these parameters, (l_g, m_g and n_g) the a_0 to a_4 coefficients of equation (1.1.7) are calculated according Table 1.1.

Table 1.1.: Values for the a_i, $(i = 1:4)$, coefficients of equation (1.1.7).

	$\boldsymbol{\epsilon_\alpha < 1}$	$\boldsymbol{\epsilon_\alpha > 1}$ $\boldsymbol{\epsilon_1 < 0 \vee \epsilon_2 < 0}$	$\boldsymbol{\epsilon_\alpha > 1}$ $\boldsymbol{\epsilon_1, \epsilon_2 > 0}$ $\boldsymbol{l_g + m_g = n_g}$	$\boldsymbol{\epsilon_\alpha > 1}$ $\boldsymbol{\epsilon_1, \epsilon_2 > 0}$ $\boldsymbol{l_g + m_g = n_g + 1}$
$\boldsymbol{a_0}$	0	0	$\frac{2l_g m_g}{n_g}$	$\frac{2(l_g m_g - n_g)}{n_g - 1}$
$\boldsymbol{a_1}$	0	1	$\frac{l(l-1) - m_g(m_g-1) - 2l_g m_g}{n_g(n_g-1)}$	$\frac{l(l-1) + m_g(m_g-1) - 2(m_g-1)n_g}{n_g(n_g-1)}$
$\boldsymbol{a_2}$	0	1	$\frac{-l(l-1) + m_g(m_g-1) - 2l_g m_g}{n_g(n_g-1)}$	$\frac{l_g(l_g-1) + m_g(m_g-1) - 2(m_g-1)n_g}{n_g(n_g-1)}$
$\boldsymbol{a_3}$	$\frac{1}{\epsilon_\alpha}$	0	$\frac{2m_g}{n_g(n_g-1)}$	$\frac{2(m_g-1)}{n_g(n_g-1)}$
$\boldsymbol{a_4}$	$\frac{1}{\epsilon_\alpha}$	0	$\frac{2l_g}{n_g(n_g-1)}$	$\frac{2(l_g-1)}{n_g(n_g-1)}$

Velex

Velex *et al.* [33] which did no *a priori* assumption on tooth load distribution by using generalized displacements, in order to calculate the efficiency of a meshing gear pair, obtained a closed form solution for the efficiency of a meshing gear pair,equation (1.1.8), (constant coefficient of friction was assumed). It turns out that the equation suggested by Buckingham (1.1.6) is an approximation of the one suggested by Velex *et al.* [33] when $\mu << 1$.

$$\rho^v = 1 - \mu \cdot (1+u) \cdot \frac{\pi}{z_1} \cdot \frac{1}{\cos\beta_b} \cdot \epsilon_\alpha \cdot \Lambda^v(\mu) \tag{1.1.8}$$

with

$$\Lambda^v(\mu) = \frac{2k_0^2 - 2k_0 + 1}{1 - \mu \cdot \left(\frac{\tan\alpha_t \cdot (2k_0 - 1) - \frac{\pi}{z_1}\epsilon_\alpha \cdot (2k_0^2 - 2k_0 + 1)}{\cos\beta_b} \right)} \tag{1.1.9}$$

where

$$k_0 = \frac{z_1}{2\pi \cdot \epsilon_\alpha \cdot u} \left(\sqrt{\left(\frac{r_{a2}}{r_{p2}}\right)^2 \frac{1}{\cos^2\alpha_t} - 1} - \tan\alpha_t \right) \tag{1.1.10}$$

1.1.2. Coefficient of friction in meshing gears

In the early stages of the 20th century Stribeck published several works [34–37] on the influence of the lubrication regime on the coefficient of friction of contacting bodies. Figure 1.2 shows a Stribeck curve. Stribeck curves, as they are known today, are still considered a powerful method to compare lubricants in what regards traction coefficient under the different lubrication regimes. Recently Brandão *et al.* [38–40] introduced an innovation under the form of a modified Hersey parameter (including piezoviscous effects as in equation (4.2.1)) that allows to more accurately compare the lubricants regarding lubrication regime in a Stribeck curve.

The coefficient of friction, CoF $\mu(x, y)$, is one of the most difficult parameters to accurately estimate (in equation (2.5.2)) because it is dependent of not only physical and chemical properties of the lubricants, but also on macro and micro geometric features of the surfaces in contact and the load distribution.

Gears very often operate under mixed film lubrication and a large number of empirical equations for the average coefficient of friction along the path of contact (mainly mixed film lubrication) have been published [22, 41–52].

Most of the aforementioned formulas were obtained from curve fitting of measured data collected in twin-disk tests.

Two groups of formulations can be found in the literature. The formulas that take into account the sliding speed, making it suitable for local coefficient of friction prediction. Buckingham [26] was the first to introduce a local CoF formula based on experimental results. This formula took into account the oil, speed, load, material and surface finishing, but it only considered the sliding speed. In the same group of formulations Misharin's [41], O'Donoghue and Cameron's [43], Drozdov and Gravikov's [44],

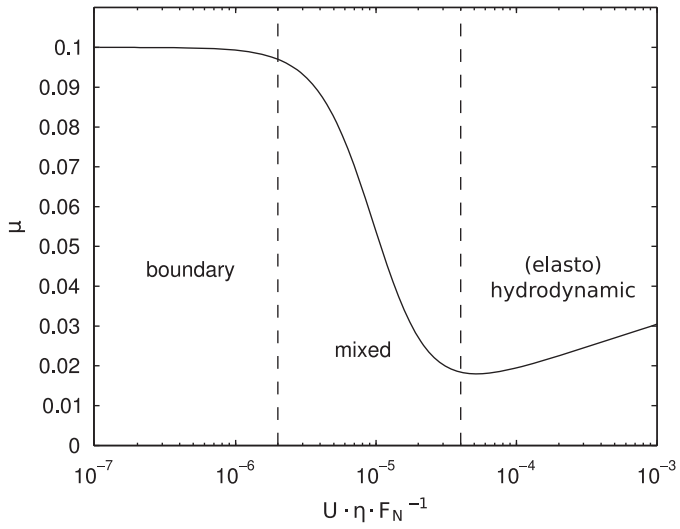

Figure 1.2.: Example of an "ideal" Stribeck curve: the curve progresses from full-film (elasto)hydrodynamic, to mixed, to boundary film lubrication as the rolling speed decreases [39].

Kelley and Lemanski's [46], Naruse's [45], Hai Xu [53] and Fernandes' [52] can be included.

Figure 1.3 shows the typical evolution of the coefficient of friction along the path of contact for a spur gear.

In 1958 Ohlendorf [30] presented an equation for the average CoF along the path of contact. In this category of developments Eiselt [42], Matsumoto [51, 54], Michaelis [47] ISO 6336-4 [49], Schlenk [48], Doleshchel [22] and Fernandes' [52] can be included.

The coefficient of friction between the teeth of a gear pair has a crucial influence on the gear mesh analysis since it directly influences the contact temperature, power loss and failure probability. Its definition is extremely complex in the case of gears since all of the lubrication regimes can coexist along the meshing line.

The next paragraphs present some of the CoF formulations that are found in the literature.

Kelley-Lemanski

Kelley and Lemanski [46] derived equation (1.1.11) for the coefficient of friction from experiments in twin disk machines. The authors also validated their results for meshing gears. This equation can't be applied to calculate the evolution of the coefficient of friction along the path of contact because the sliding speed is in denominator and the coefficient of friction approaches infinity as the meshing process gets closer to the pitch point, where the sliding velocity is zero.

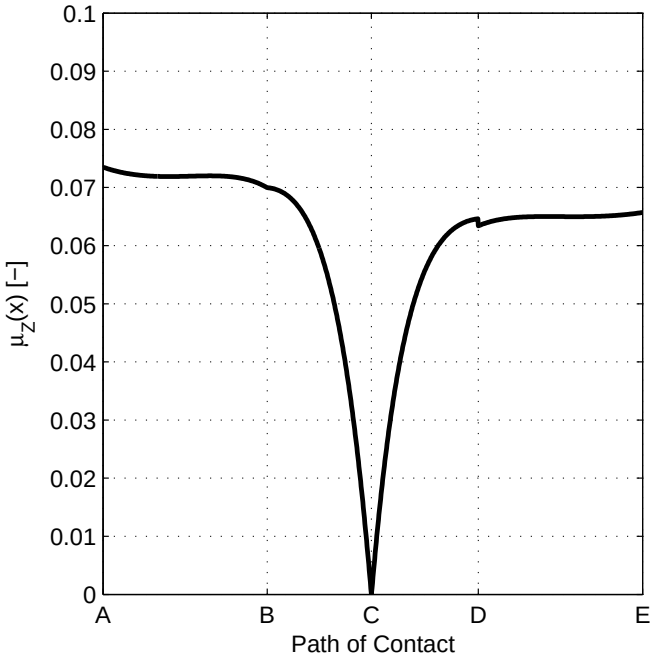

Figure 1.3.: Typical evolution of the CoF along the path of contact for a spur gear.

$$\mu_{mz}^{KL} = 0.0127 \cdot \log_{10}\left(\frac{F_N}{b} \cdot \frac{29652}{\eta_0 \cdot v_g \cdot (U_1 + U_2)^2}\right) \tag{1.1.11}$$

Michaelis

Michaelis *et al.* [47] proposed equation (1.1.12) to predict the average coefficient of friction between gear teeth. This equation was also based on experimental results from twin disk machines. Compared to equation (1.1.11) this approach introduces the influence of the average roughness, R_a, but the sliding speed is omitted.

$$\mu_{mz}^{M} = 0.045 \cdot \left(\frac{F_N/b}{(U_1 + U_2) \cdot R_X}\right)^{0.2} \eta_0^{-0.05} \cdot X_R \tag{1.1.12}$$

$$X_R = 8.8 \cdot \sqrt[4]{\frac{R_a}{d_{p1}}} \tag{1.1.13}$$

Schlenk

One of the most well known average coefficient of friction models for gears was proposed by Schlenk *et al.* [48]. This model is simple and relies on key parameters such as operating conditions, gear geometry, surface finish and lubricant characteristics.

One of the main advantages of this model is that given a proper lubricant factor X_L it can be used to predict the average coefficient of friction between meshing tooth pairs for different base oils and addictive packages. Fernandes *et al.* [2,21] have done extensive experimental work in a FZG test rig to find the lubricant parameters for different wind turbine gear oils.

The Schlenk *et al.* [48] formulation for the average coefficient of friction is presented in equation (1.1.14).

$$\mu_{mz}^{S} = 0.048 \cdot \left(\frac{F_{bn}}{l \cdot R_X \cdot (U_1 + U_2)} \right)^{0.20} \cdot \eta_0^{-0.05} \cdot R_a^{0.25} \cdot X_L \tag{1.1.14}$$

In Schlenk's equation (1.1.14) R_a is the arithmetic mean roughness and X_L is the lubricant correction factor ($X_L = 1$ for non-additised mineral oils in mixed film lubrication).

$$l = \epsilon_\alpha \cdot \frac{b}{\cos(\beta_b)} \tag{1.1.15}$$

ISO 6336

The expression proposed by ISO [49], equation (1.1.16), usually yields higher than expected values for the coefficient of friction. This formula has the same structure, yet different exponents, from the one proposed by Michaelis [47] and later by Schlenk [48].

$$\mu_{mz}^{ISO} = 0.143 \cdot \left[\frac{F_N/b \cdot R_a}{R_X \cdot \eta_0 \cdot (U_1 + U_2)} \right]^{\frac{1}{4}} \tag{1.1.16}$$

Hai Xu

Hai Xu, [53] proposed a coefficient of friction based on results obtained with an EHD model (numerical results) that was validated with experimental traction curves. After validation, the model was ran ≈ 10000 times varying different operating conditions. These results were then fitted using a custom function based on key parameters as represented in equation (1.1.17). Table 1.2 shows the range of operating conditions used in the EHD model simulations in order to derive the coefficients in Table 1.3.

$$\mu^{Xu} = e^{f(SR,P_h,\nu_0,S)} P_h^{b2} \left|SR\right|^{b3} V_e^{b6} \mu_0^{b7} R^{b8} \tag{1.1.17}$$

$$f(SR,P_h,\nu_0,S) = b_1 + b_4 \left|SR\right| P_h \log_{10}(\nu_0) + b_5 e^{-\left|SR\right| P_h \log_{10}(\nu_0)} + b_9 e^{S} \tag{1.1.18}$$

Table 1.2.: Range of the parameters used in the parametric study [53].

Lubricants	75W90 gear oil
Inlet temperature, ° C	50 - 110
Radius of curvature ($\boldsymbol{R_X}$), m	0.005 - 0.08
Entraining velocity ($\boldsymbol{V_e}$), m/s	1 - 20
Slide-to-roll ratio ($\boldsymbol{SR}$)	0.005 - 1.0
Surface roughness ($\boldsymbol{S}$), μm	0 - 0.4
Maximum Hertzian pressure ($\boldsymbol{P_h}$), GPa	0.5-2.5

Table 1.3 shows the coefficients b_1 to b_9 that go in equations (1.1.17) and (1.1.18).

Table 1.3.: Coefficients for the EHL based formula, [53].

$\boldsymbol{b_1}$	-8.916465	$\boldsymbol{b_2}$	1.03303	$\boldsymbol{b_3}$	1.036077
$\boldsymbol{b_4}$	-0.354068	$\boldsymbol{b_5}$	2.812084	$\boldsymbol{b_6}$	-0.100601
$\boldsymbol{b_7}$	0.752755	$\boldsymbol{b_8}$	-0.390958	$\boldsymbol{b_9}$	0.620305

Doleschel

Doleschel [22,50] defined the coefficient of friction in a gear mesh as a combination of boundary film friction μ_{bl}^D and a portion of fluid film friction μ_{EHD}^D.

μ_{mz}^D is then defined as a weighted linear combination of the boundary and fluid film lubrication based on the analysis of the relative film thickness, Λ. The weight factor, ϕ^D, is defined as the portion of fluid friction.

The friction coefficient in a gear mesh μ_{mz}^D is then defined according to equation(1.1.19). In this equation μ_{mz}^D is the mixed friction coefficient, μ_{bl}^D is the boundary friction coefficient, μ_{EHD}^D is the fluid friction coefficient and ϕ^D is the portion of fluid film friction.

$$\mu^D = (1 - \phi^D) \cdot \mu_{bl}^D + \phi^D \cdot \mu_{EHD}^D \tag{1.1.19}$$

The portion ϕ^D of fluid and solid friction depends on the relative film thickness Λ in the contact as expressed by equation (1.1.20). Figure 1.4 shows a representation of ϕ^D equation (1.1.20).

$$\phi^D = \begin{cases} \Lambda - 0.25 \cdot \Lambda^2, \ for\ \Lambda < 2 \\ \\ 1, \ for\ \Lambda \geq 2 \end{cases} \tag{1.1.20}$$

The boundary friction coefficient and the fluid friction coefficient can be derived from experimental results in FZG-VA tests, [22, 50].

Matsumoto

Recently S. Matsumoto *et al.* [51] suggested a new experimentally validated formula for the coefficient of friction under mixed lubrication conditions which was an advancement of a previous work by the same author [54].

Matsumoto's formulation is based on boundary (μ_{bl}^{Mto}) and full film (μ_{EHD}^{Mto}) coefficients of friction which are combined using a sharing function that depends on the specific film thickness. Equations (1.1.21), (1.1.22) and (1.1.23) are the model proposed by Matsumoto *et al.* [51]. In these equations μ^{Mto} is the coefficient of friction, ϕ^{Mto} is the sharing parameter, R_{zi} is the maximum height of the surface roughness of body i and h_0 is the EHD minimum film thickness.

$$\mu^{Mto} = \mu_{EHD}^{Mto} \cdot (1 - \phi^{Mto}) + \mu_{bl}^{Mto} \cdot \phi^{Mto} \tag{1.1.21}$$

$$\phi^{Mto} = \frac{1}{2} \cdot \log\left(D^{Mto}\right) \tag{1.1.22}$$

$$D^{Mto} = \frac{R_{z1} + R_{z2}}{h_0} \tag{1.1.23}$$

The main innovation in this formulation was the consideration of the maximum height of the surface roughness (R_z) instead of the average roughness. Figure 1.4 shows a representation of ϕ^{Mto} equation (1.1.22).

Fernandes

Recently Fernandes *et al.* [52] proposed a new set of equations for the estimation of the CoF in gears. The model is based on a load sharing function approach which was based on a modified Hersey parameter. This new formulation includes the influence of the pressure-viscosity oil parameter. The results that were obtained with this approach correlate very well with previous existing experimental results.

According to Fernandes *et al.* [52] two different formulations are proposed, a global average CoF (1.1.24) and a local (1.1.27) CoF.

$$\mu_{mz}^{Fer} = 0.014 \left(\frac{S_g}{S_p} \right)^{1/4} \cdot X_L \tag{1.1.24}$$

$$S_g = \frac{R_a}{(R_X \cdot \epsilon_\alpha \cdot \frac{b}{\cos \beta_b})^{1/2}} \tag{1.1.25}$$

$$S_p = \frac{(U_1 + U_2) \cdot \eta_0 \cdot \alpha^{1/2}}{F_N^{1/2}} \tag{1.1.26}$$

$$\mu^{Fer} = \mu_{bl}^{Fer} \cdot (1 - \phi^{Fer}) + \mu_{EHD}^{Fer} \cdot \phi^{Fer} \tag{1.1.27}$$

$$\phi^{Fer} = \frac{1}{2} \cdot \log \left(S_p \cdot S_g \times 10^9 \right) \tag{1.1.28}$$

Both formulations take into account the key parameters in what regards semi-empirical CoF formulations. These parameters rely on two non-dimensional quantities S_g (1.1.25) and S_p (1.1.26) which can be correlated with the CoF and the specific film thickness, Λ. μ_{EHD}^{Fer} and μ_{bl}^{Fer} are properly obtained from experimental results. The equation that was proposed for the constant and average CoF has an interesting advantage compared to other equations found in the literature, it uses the same X_L as the one found in Schlenk's equation (1.1.14). Schlenk's work was recently adopted in the ISO standard 14179-2 [52]. In the majority of the cases the equation proposed by Fernandes *et al.* (1.1.24) yields results which are very close to the ones obtained with Schlenk's equation 1.1.14, generally closer to the experimental results [52].

Figure 1.4 shows a comparison of the partition functions for the portion of fluid and solid friction in an EHD contact. [52]. The range of parameters that was considered is presented in table 1.4.

Table 1.4.: Geometrical properties and operating conditions range [52].

Property	Lower value	Upper value
$\boldsymbol{R_a}$ $[\mu m]$	0.181	0.906
$\boldsymbol{R_z}$ $[\mu m]$	1.845	9.225
$\boldsymbol{b}$ [mm]	10	50
$\boldsymbol{R_X}$ [mm]	4.2	12.57
$\boldsymbol{\eta}$ [mPas]	3.9	97.5
$\boldsymbol{\alpha}$ $[Pa^{-1}]$	0.839×10^{-8}	2.096×10^{-8}
$\boldsymbol{U_S}$ [m/s]	0.432	8.63
$\boldsymbol{F_{bn}}$ [N]	2000	8000
$\boldsymbol{S_p}^*$ [-]	1.7×10^{-9}	2.7×10^{-6}
$\boldsymbol{S_g}^*$ [-]	7.2×10^{-6}	1.4×10^{-4}

* Resulting from combination of values above.

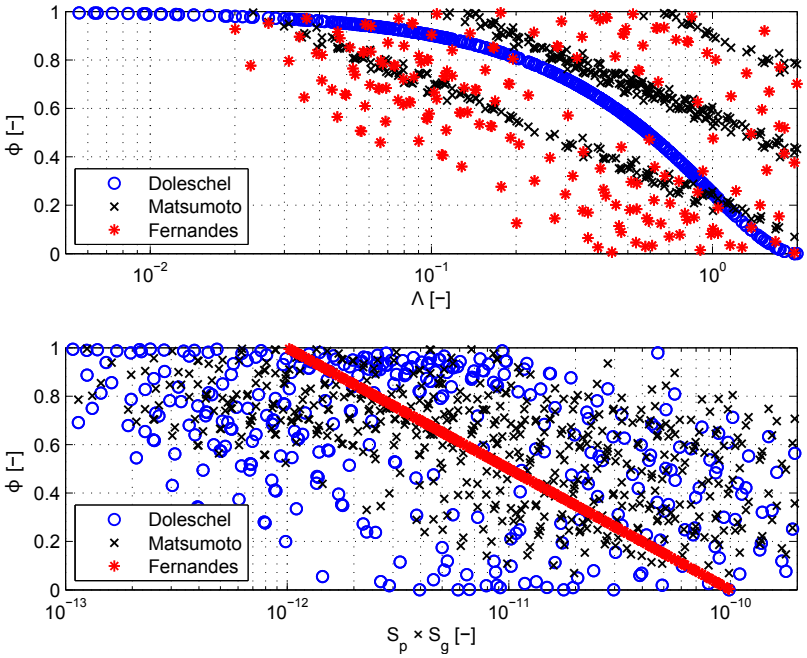

Figure 1.4.: Comparison of the partition functions for the portion of fluid and solid friction in an EHD contact. [52].

1.2. Power loss due to fluid-body interactions

For dip lubricated gears, oil churning is a major source of power loss which is related to the fluid circulation generated by rotating gears partly immersed in the air-lubricant mixture [22, 28, 55, 56]. The power loss due to dip lubricated gears can be subdivided in multiple components: windage, churning and squeezing.

The windage power losses arise due to the interaction of a mechanical component and a single phase fluid that can be either air or lubricant. These losses evolve with rotational speed and become significant only for high tangential speeds or for fluids with high viscosity grades and densities.

The churning losses are similar to the windage losses, but involve at least two phases. These losses are the most important load independent power losses in geared transmissions: the majority of the gearboxes, in fact, are dip lubricated and, therefore, subjected to churning losses.

The squeezing power losses are losses of a lower order of magnitude and arise due to the fact that the cavity between two teeth is reducing its volume during the engagement causing pressure gradients and therefore, additional fluxes.

Terekhov [57] studied the gear churning losses caused by high viscosity lubricants (200 to 2000 cSt) at low speeds and tested gears with modules ranging from 2 to 8 mm. Later, in 1983, Lauster and Boos [58] presented the results on their studies about gear churning losses in truck transmissions. Boness [59] studied the churning loss caused by discs rotating in water or oil. Höhn *et al.* [28] presented a viscosity independent single flow regime model for the gear churning losses caused by a pinion/wheel pair. Seetharaman *et al.* [60] proposed a physic-based fluids mechanics model to predict the no-load power losses due to churning and windage.

More recently Changenet *et al.* [55, 56] deducted from dimensional analysis a set of equations to calculate a dimensionless gear drag torque. These equations are selected according to different flow regimes dependent on a critical Reynolds number (related to the flow nature) and a centrifugal acceleration parameter (related to fluid projection by the rotating gears). These authors have also reported that there is a relation between lubricant aeration and gear churning loss [61]. In another work, Changenet *et al.* [62] verified that the internal housing geometry of a gearbox significantly influences the churning loss behaviour.

In Changenet's gear churning loss model [55] the torque loss is given by equation (1.2.1).

$$C_{ch} = \frac{1}{2} \cdot \rho_{oil} \cdot \omega^2 \cdot r_p^3 \cdot S_m \cdot C_m \tag{1.2.1}$$

C_m (equation (1.2.1)) is the drag dimensionless group, S_m the immersed surface of the pinion/wheel, (flank and teeth), r_p the pinion reference radius, ω the angular frequency and ρ_{oil} the bulk density of the lubricant at the working temperature.

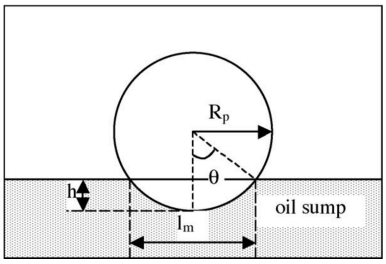

Figure 1.5.: Geometrical data of the gear immersed surface [55].

The dimensionless drag group was derived by dimensional analysis using the Vashy-Buckingham theorem [55, 56]. Then the dimensionless drag group is expressed according to equation (1.2.2).

$$C_m = \psi_1 \cdot \left(\frac{h}{d_p}\right)^{\psi_2} \cdot \left(\frac{V_0}{d_p^3}\right)^{\psi_3} Fr^{\psi_4} \cdot Re_c^{\psi_5} \cdot \left(\frac{b}{r_p}\right)^{\psi_6} \tag{1.2.2}$$

The ψ_i (equation (1.2.2)) coefficients are derived from experimental results. The ψ_i numerical values depend on the working conditions, and four sets of coefficients (depending on the nature of the flow regimes), are used depending on the value of the centrifugal acceleration parameter (1.2.3).

$$\gamma = \omega^2 \cdot (r_p \cdot b \cdot m)^{\frac{1}{3}} \tag{1.2.3}$$

The Froude (Fr) and critical Reynolds (Re_c) numbers are defined according to equations (1.2.4) and (1.2.5).

$$Fr = \frac{r_p \cdot \omega^2}{g} \tag{1.2.4}$$

$$Re_c = \frac{r_p \cdot b \cdot \omega}{\nu_0} \tag{1.2.5}$$

The C_m parameter used for each flow conditions depends not only on the centrifugal acceleration (γ, equation (1.2.3)), but also on the critical Reynolds number (Re_c, equation (1.2.5)), as it follows:

a) if $\gamma < 750$ m/s^2 and $Re_c < 4000$

$$C_m = 1.366 \cdot \left(\frac{h}{d_p}\right)^{0.45} \cdot \left(\frac{V_0}{d_p^3}\right)^{0.1} \cdot Fr^{-0.6} \cdot Re_c^{-0.21} \cdot \left(\frac{b}{r_p}\right)^{0.21} \tag{1.2.6}$$

b) if $\gamma < 750$ m/s^2 and $Re_c > 4000$

$$C_m = 0.239 \cdot \left(\frac{h}{d_p}\right)^{0.45} \cdot \left(\frac{V_0}{d_p^3}\right)^{0.1} \cdot Fr^{-0.6} \cdot \left(\frac{b}{r_p}\right)^{0.21} \tag{1.2.7}$$

c) if $\gamma > 1250$ m/s^2 and $Re_c < 4000$

$$C_m = 20.797 \cdot \left(\frac{h}{d_p}\right)^{0.1} \cdot \left(\frac{V_0}{d_p^3}\right)^{-0.35} \cdot Fr^{-0.88} \cdot Re_c^{-0.21} \cdot \left(\frac{b}{d_p}\right)^{0.85} \tag{1.2.8}$$

d) if $\gamma > 1250$ m/s^2 and $Re_c > 4000$

$$C_m = 3.644 \cdot \left(\frac{h}{d_p}\right)^{0.85} \cdot \left(\frac{V_0}{d_p^3}\right)^{-0.35} \cdot Fr^{-0.88} \cdot \left(\frac{b}{d_p}\right)^{0.85} \tag{1.2.9}$$

It should be noted that an interpolation between the equations should be performed when 750 m/s^2 $< \gamma <$ 1250 m/s^2.

This model is usually applied to spur gears, but it can be extended to helical gears. In this way the geometrical parameter that accounts for the immersed surface of the pinion (S_m) [55] is defined according to equation (1.2.10).

$$S_m = r_p^2 \cdot (2\theta - \sin 2\theta) + d_b \cdot \theta + 2 \cdot \frac{z \cdot \theta \cdot H_{tooth} \cdot b}{\pi \cdot \cos\alpha \cdot \cos\beta} \tag{1.2.10}$$

The θ angle in equation (1.2.10) is calculated according to Figure 1.5. Finally to obtain the churning power loss on a single pinion the churning torque loss, (C_{ch}) is multiplied by the angular speed, (ω), resulting on equation (1.2.11).

$$P_{VZ0} = C_{ch} \cdot \omega \tag{1.2.11}$$

According to Changenet *et al.* [55, 56] the total churning power losses on the gearbox are calculated as the sum of the individual losses on each pinion/wheel. This method was demonstrated to give good results for pinion/wheel pairs rotating clockwise, figure 1.6. When working at a counter-clockwise rotation additional loss mechanisms appear making inappropriate to estimate the churning power loss as the sum of the individual losses on each gear pair [55, 56].

From a physical point of view, Changenet *et al.* [55, 56], pointed out that this difference is probably due to the trapping of lubricant by meshing teeth and by a swell effect, see figure 1.7, which dissipates energy and increases the immersion depth of the pinion.

Figure 1.6.: Definition of the senses of rotation of a gear pair [55, 56].

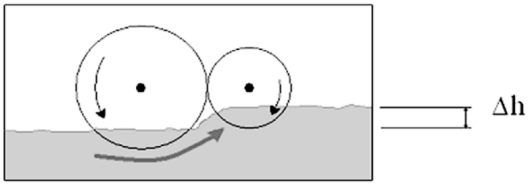

Figure 1.7.: Schematic representation of the swell effect [55, 56].

This variation in the churning loss due to swell effect is expressed in terms of a dimensionless variation of the churning torque ΔC_m and ΔP_{VZ0} is sought under the form of equation (1.2.12) in which all the geometrical data are those of the gear.

$$\Delta P_{VZ0} = \frac{1}{2} \cdot \rho \cdot \omega^3 \cdot r_p^3 \cdot S_m \cdot \Delta C_m \tag{1.2.12}$$

From the experimental results, Changenet *et al.* [55, 56] drawn the following conclusions:

- For isothermal conditions the viscosity of the lubricant has a weak influence on ΔP_{VZ0} and the Reynolds number is discarded in the formulation.
- ΔP_{VZ0} is sensitive to angular frequency thus making it proportional to $Fr^{\psi 7}$
- For identical pinions and gears, no swell effect can be generated due to symmetry. In these conditions ΔP_{VZ0} is found to be close to zero, thus demonstrating that the air-lubricant trapping by the teeth is negligible and consequently proving that the swell effect is prominent.

After these conclusions ΔC_m was derived according to equation (1.2.13).

$$\Delta C_m = 17.7 \cdot Fr^{-0.68} \cdot \frac{u-1}{u^8} \cdot \left[1 - \left(\frac{h}{r_p} \right)_{gear} \right] \tag{1.2.13}$$

Changenet *et al.* [55] obtained good correlations between numerical and experimental results using this model. Since these equations do not take into account the aeration of the lubricant (presence of air in the lubricant manifested by the production of a significant number of very fine spherical air bubbles increasing the churning loss) on the oil sump during operation, some deviations between the experimental and

numerical results at higher speeds and/or temperatures above 55 °C are expected for certain lubricants [61].

In recent years, with the increasing computing power of desktop computers, CFD is becoming a more and more attractive approach to solve this kind of problems.

Recently Concli *et al.* [63] proposed a solution for the problem of the churning power loss in a planetary speed reducer which was based in a CFD approach, with promising results, but even with the current CFD models it is not possible to simulate all the relevant effects at once.

The majority of the works presented on this topics are results of experimental tests [55, 56, 58–61, 64]. Sometimes from the experimental results a semi-analytical formulation is also derived. The problem of all of these calculation methods is that they are accurate as long as the real operating conditions are similar to the conditions of the experiments. Furthermore, these models usually neglect some important influencing parameters.

Despite being demonstrated in several works [7,55,58] that most of the gear churning loss models usually yield quite different results when applied to the same gearbox and that they are valid for a very small set of conditions at the same operating conditions, it is still worthy to study previous attempts of gear no-load loss formulations, since this exercise can prove to be quite useful in what regards gaining more insight about the main influencing effects in this type of gear losses.

According to the several works that were referenced in this section there are three main groups of factors that influence gear no-load losses:

- Lubricant oil properties and lubrication method;
- Operating conditions;
- Gearbox design.

Lubricant properties like kinematic and dynamic viscosity as well as density at the operating conditions play a vital role in these types of losses. Other properties like surface tension which are often disregarded can also be quite important. It has been shown [61] that surface tension is related to bubble formation (aeration) in dip lubrication which is associated with increased no-load power losses. Oil immersion depth is also an important variable in dip lubrication.

The lubricant temperature, defining factor for the operating lubricant properties is in one way or another defined by the operating conditions. Furthermore, the motion of the rotating components in the gearbox, between other things, is a very important factor in defining the flow regime which is tied to the no-load power loss due to lubricant circulation.

One other factor that plays a fundamental role in the way that the lubricant flows is the gearbox design, i.e. internal design of the gearbox and surface roughness, shafts and gear arrangements.

More recently [65] it was shown that there are some other variables that greatly influence the no-load torque loss. The experiments performed by S. Chen *et. al.* [65] and Changenet *et. al* [62] showed that adding deflectors and plates to the gearbox internal design can be a tool to manipulate the oil flow within a gearbox thus modifying the no-load loss. In the same series of experiments Chen [65] also demonstrated that the Steady-State Oil Surface Profile (SOSP) is a very important factor for the gear churning problem since it is the steady-state "shape" of the oil flow thus determining the immersion depth of the components which was previously pointed out as a very important factor.

Oil trapping and squeezing no-load losses are disregarded in some works which can be quite important in some situations [60].

1.3. Power loss in rolling bearings

Rolling bearings which support the loadings transmitted by the gears through the shafts. Depending on the type, transmitted loads and design constraints different types of rolling bearings can be found in a gearbox, such as:

- Deep Groove ball bearings (DGBB);
- Cylindrical roller bearings (CRB);
- Tapered roller bearings (TRB);
- (Full complement) Needle roller bearings (FC - NRB).

The important role of rolling bearing power loss in machines have attracted many researchers to try to identify and model the power loss mechanisms in rolling bearings.

Tapered roller bearings can promote much higher power loss than other types of bearings, and those losses vary substantially with the pre-load.

Bearing manufacturers usually provide straight methods to calculate the power loss generated by the rolling bearings. The models employed to do such predictions are usually derived from large amounts of experimental data.

1.3.1. Coulomb model

In experimental tests the total frictional torque of a rolling bearings is measured. A global coefficient of friction formula can be devised based on the Coulomb approach. Equation (1.3.1) is the statement of this approach.

$$\mu_{Cou}^{rol} = \frac{M^{rol}}{F \cdot d_{bore}/2} \tag{1.3.1}$$

where

$$F = \sqrt{F_r^2 + F_a^2} \tag{1.3.2}$$

Hundreds of experimental tests with different lubricants at different conditions and rolling bearing dimensions can be performed in order to find an average μ_{Cou}^{rol} for a given rolling bearing type. Such values for μ_{Cou}^{rol} are usually given in tables by the rolling bearing manufacturers like SKF [66]. Eschmann also proposes such tables in one of his works [29].

1.3.2. Old SKF model (Modified Arvrid Palmgren)

The torque loss in a rolling bearing [28] is assumed to be the sum of the load ($M_1^{rol}+M_2^{rol}$) and no-load (M_0^{rol}) torque loss sources, equation (1.3.3). Such approach was first proposed by Arvrid Palmgren [29].

$$M^{rol} = M_0^{rol} + M_1^{rol} + M_2^{rol} \tag{1.3.3}$$

The frictional torque M_0^{rol} results mainly from the lubricant friction, but also from the rolling element friction in the cage pockets and the cage friction at its guide surfaces. M_0^{rol} depends predominantly on the operational viscosity of the lubricant (ν_0), the speed (n), the design (f_0) and size of the bearings (d_m). Equations (1.3.4), (1.3.5) were found to be in agreement with experimental findings [28]

for $\nu_0 \cdot n < 2000$ mm^2/s·min:

$$M_0^{rol} = 1.6 \times 10^{-8} \cdot f_0 \cdot d_m^3 \tag{1.3.4}$$

for $\nu_0 \cdot n \geq 2000$ mm^2/s·min:

$$M_0^{rol} = 10^{-10} \cdot f_0 \cdot (\nu_0 \cdot n)^{2/3} \cdot d_m^3 \tag{1.3.5}$$

The frictional torque M_1^{rol} results mainly from the rolling and sliding friction. It hardly changes with the speed, but changes considerably with the rolling element pressure and therefore load. It is additionally influenced by the design (f_1) and size (d_m) of the rolling bearing. M_1^{rol} can be calculated according to equation (1.3.6) [28].

$$M_1^{rol} = 10^{-3} \cdot f_1 \cdot F \cdot d_m \tag{1.3.6}$$

The frictional torque M_2^{rol} results mainly from the contact between the faces of the rolling elements and the edges of the inner and outer rings due to axial loads.

$$M_2^{rol} = 10^{-3} \cdot f_2 \cdot F_a \cdot d_m \tag{1.3.7}$$

The f_0, f_1 and f_2 coefficients in equations (1.3.4), (1.3.5),(1.3.6) and (1.3.7) were obtained experimentally and reference values can be consulted in ref. [28].

1.3.3. New SKF friction torque model (2004)

For several years the approach presented in the previous subsection was considered the standard (used by various rolling bearing manufacturers) regarding rolling bearing power loss prediction. Recently SKF [66] introduced a more advanced model to predict the power loss in rolling bearings. Fernandes *et al.* [1,5,67–69] have presented several works were the model is applied to experimental results in rolling bearings lubricated with wind turbine gear oils.

According to SKF [66] the frictional torque M^{rol} in a rolling bearing is composed of four different torque loss sources, M_{rr} is the rolling frictional torque, M_{sl} is the sliding frictional torque, M_{seal} is the frictional torque of the seal(s) and M_{drag} is the frictional torque of drag losses, churning, splashing etc. Equation (1.3.8) is the mathematical statement of the total torque loss in a rolling bearing [66].

$$M^{rol} = M_{rr} + M_{sl} + M_{seal} + M_{drag} \tag{1.3.8}$$

The total bearing power loss is then defined according to equation (1.3.9).

$$P_{VL} = M^{rol} \cdot n \cdot \frac{\pi}{30} \times 10^{-3} \tag{1.3.9}$$

On each one of the following subsections each one of the individual components stated above will be more closely defined.

Rolling frictional torque

The rolling frictional torque is calculated according to equation (1.3.10). G_{rr} depends on the loading conditions, bearing type and mean diameter. The kinematic viscosity of the lubricant (ν_0) and the angular speed (n) are also important parameters.

$$M_{rr} = \phi_{ish} \cdot \phi_{rs} \cdot G_{rr} \cdot (\nu_0 \cdot n)^{0.6} \tag{1.3.10}$$

Furthermore, in order to more closely follow the real behaviour of the rolling bearing, additional effects should be considered. Between these effects the considered ones are:

- Inlet shear heating reduction;
- Replenishment/starvation speed effects for oil-spot, oil jet, grease and low level oil bath lubrication;
- Mixed lubrication for low speeds and/or low viscosities.

In order to account for the aforementioned effects the rolling frictional torque should be multiplied by two correction factors, the inlet shear heating reduction factor ϕ_{ish}, and the kinematic replenishment/starvation reduction factor ϕ_{rs}.

When sufficient lubricant is available in the rolling bearing, not all of it can go through the contacts since only a tiny amount of lubricant is used to build up the film thickness. The excess lubricant will form a separated reverse flow bubble that by shearing effects will produce heat and by consequence will lower the viscosity of the lubricant entering the contact. For the effect described above, the inlet shear heating reduction factor can be obtained approximately from equation (1.3.11).

$$\phi_{ish} = \frac{1}{1 + 1.84 \times 10^{-9}(n \cdot d_m)^{1.28} \cdot \nu_0^{0.64}} \tag{1.3.11}$$

Due to the rolling bearing speed or high viscosity, the lubricant at the edges of the contacts might not have enough time to replenish the raceways, this effect is called "kinetic starvation" and causes a drop in the film thickness and in the rolling frictional torque. For the conditions described above the kinematic replenishment/starvation reduction factor can be obtained approximately from equation (1.3.12). It depends on the kinematic replenishment/starvation constant (K_{rs}) and the on rolling bearing and geometry (K_Z, D, d).

$$\phi_{rs} = \frac{1}{e^{k_{rs} \cdot \nu_0 \cdot n \cdot (d+D) \cdot \sqrt{\frac{k_z}{2 \cdot (D-d)}}}} \tag{1.3.12}$$

Sliding frictional torque

The sliding frictional torque is calculated according to equation (1.3.13). G_{sl} depends on the loading conditions, rolling bearing type and mean diameter. The sliding coefficient of friction (μ_{sl}) is also a very important factor.

$$M_{sl} = G_{sl} \cdot \mu_{sl}^{SKF} \tag{1.3.13}$$

The sliding friction coefficient μ_{sl} can be calculated according to equation (1.3.14). μ_{EHD}^{SKF} is the full film coefficient of friction and μ_{bl} is the boundary coefficient of friction. ϕ_{bl} is the weighting factor for the sliding coefficient of friction and can be calculated according to equation (1.3.15). μ_{EHD}^{SKF} and μ_{bl}^{SKF} have reference values that are recommended by SKF [66]. In a series of recent works Fernandes *et al.* [1, 4–6] showed that the reference μ_{bl}^{SKF} and μ_{EHD}^{SKF} are often overestimated by SKF [66]. The process of obtaining more accurate μ_{bl}^{SKF} and $\mu_{EHD}^{SKF}$for a specific lubricant was also described in the same set of works.

$$\mu_{sl}^{SKF} = \phi_{bl} \cdot \mu_{bl}^{SKF} + (1 - \phi_{bl}) \cdot \mu_{EHD}^{SKF} \tag{1.3.14}$$

$$\phi_{bl} = \frac{1}{e^{2.6\times10^{-8}\cdot(n\cdot\nu_0)^{1.4}\cdot d_m}} \tag{1.3.15}$$

Drag losses in oil bath lubrication

In oil bath lubrication, the rolling bearing is partially, or in special situations, completely submerged. Under these conditions the size and geometry of the oil reservoir together with the oil level used can have a substantial impact on the bearing friction torque. Depending on the rolling bearing type, SKF [66] suggests equations (1.3.16) and (1.3.17) for the drag losses in ball and roller bearings respectively.

$$M_{drag}^{ball} = 0.4 \cdot V_M \cdot K_{ball} \cdot d_m^5 \cdot n^2 + 1.093 \cdot 10^{-7} \cdot n^2 \cdot d_m^3 \cdot \left(\frac{n \cdot d_m^2 \cdot f_t}{\upsilon}\right)^{-1.379} \cdot R_s \tag{1.3.16}$$

$$M_{drag}^{roll} = 4 \cdot V_M \cdot K_{roll} \cdot C_W \cdot B \cdot d_m^4 \cdot n^2 + 1.093 \cdot 10^{-7} \cdot n^2 \cdot d_m^3 \cdot \left(\frac{n \cdot d_m^2 \cdot f_t}{\upsilon}\right)^{-1.379} \cdot R_s \tag{1.3.17}$$

In equations (1.3.16) and (1.3.17) V_M is a variable that is a function of the oil level and K_{ball} and K_{roll} depend on the rolling bearing type (ball or roller).

Rolling bearing seal losses

The rolling bearing seals losses are defined according to equation (1.3.18). The constants $K_{S1,2}$ and β_R depend on the geometry and rolling bearing seal type.

$$M_{seal} = K_{S1} \cdot d_s^{\beta_r} + K_{S2} \tag{1.3.18}$$

1.4. Power loss in seals

In most applications, seal power losses represent a minor fraction of the total power loss of a gearbox, and are almost negligible when compared to the losses of other components.

Croes *et al.* [70] suggested that the frictional losses in sealing elements is a problem that is yet to be fully understood. The contact zone is quite small and the microscopic phenomena is not easy to parametrize. Equation (1.4.1) is one of the simplest approaches.

$$P_{VD}^{C} = \frac{1}{2} \cdot \mu^{seal} \cdot F_R \cdot d_{sh} \cdot \omega \tag{1.4.1}$$

In equation (1.4.1) the main problem is in obtaining the correct radial force F_R and the coefficient of friction μ^{seal} (which are interconnected). The frictional torque resulting from this radial load is only a part of the total friction loss at the seals. Type of atmosphere being sealed, pressure differential across the seal, tangential speed, ambient temperature and the lubricant and method of lubrication are just some of the parameters that influence the seals losses.

Another very well known approximation suggested by Simrit (a seal manufacturer) is given in equation (1.4.2) [28, 71].

$$P_{VD}^{S} = 7.69 \times 10^{-6} \cdot d_{sh}^{2} \cdot n \tag{1.4.2}$$

In equation (1.4.2) d_{sh} is the shaft diameter and n is the shaft rotational speed.

The seals power loss is independent of the transmitted torque, being the major influences the seal design, operating speed and the shaft diameter. It is very likely that equation (1.4.2) needs to be adjusted to account for different seal materials as well as different lubricants [28].

Linke [72, 73] developed a variation of the Simrit formula (equation (1.4.2))to take into account different oil viscosities (equation (1.4.3)).

$$P_{VD}^{L} = [145 - 1.6 \cdot T_{Oil} + 350 \cdot \log\log(\nu_{40} + 0.8)] \times 10^{-7} \cdot d_{sh}^{2} \cdot n \tag{1.4.3}$$

Kettler [73, 74] also developed a formula (equation (1.4.4)) that takes into account the influence of oil viscosity in the seals losses.

$$P_{VD}^{K} = 7.9163 \times 10^{-6} \cdot F_D \cdot d_{sh}^{2} \cdot n \tag{1.4.4}$$

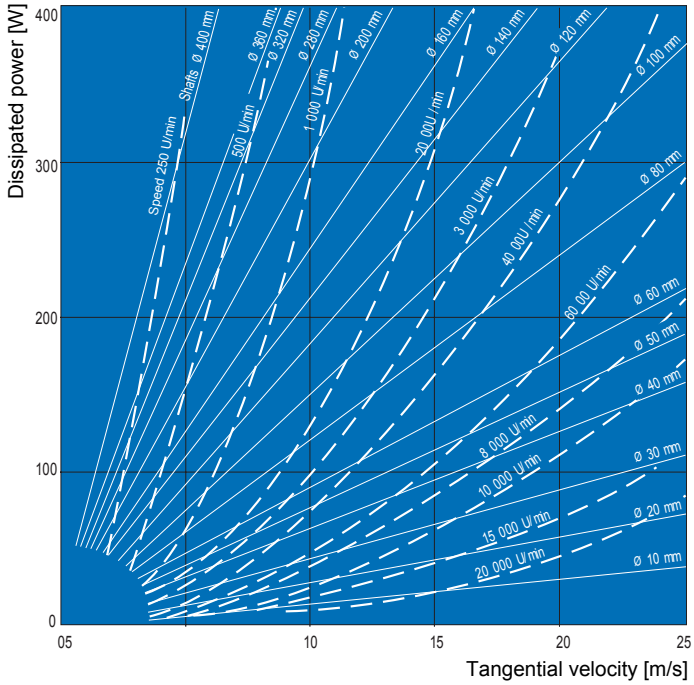

Figure 1.8.: Friction loss on a seal for a SAE 20 engine oil at $T = 100$ °C [71].

In equation (1.4.4) F_D represents the effect of the temperature dependent viscosity change.

More recently Bauer *et al.* [75] performed experimental studies on the power loss of lip seals and its influencing parameters. Bauer has concluded that in addition to the aforementioned influencing parameters shaft wear at the sealing contact also plays an important role in seal friction. According to Bauer *et al.* [75] it is almost impossible to accurately predict lip seal frictional losses, not only due to the very complex nature of the problem but also because the losses can even be greatly influenced by the assembling.

1.5. Power loss and thermal equilibrium

During operation a gearbox dissipates heat, which will be dissipated to the surrounding environment. According to thermodynamics and as suggested by Höhn [28], who developed an isothermal model, the mechanical energy that is dissipated by the gearbox must be equal to the thermal energy that the surrounding environment receives at stabilized conditions, equation (1.5.1). This means that under thermal equilibrium the power loss of the gearbox will be the same as the heat that is being received by the surrounding environment of the gearbox (equation (1.5.1)).

$$P_V = \dot{Q}_{total} \tag{1.5.1}$$

The main heat transfer mechanisms are conduction, convection and radiation, equation (1.5.2).

$$\dot{Q}_{total} = \dot{Q}_{cd} + \dot{Q}_{cv} + \dot{Q}_{rad} \tag{1.5.2}$$

The heat flow by radiation from the surface of the gearbox housing can be calculated from equation (1.5.3).

$$\dot{Q}_{rad} = \alpha_{rad} \cdot A_{rad} \cdot (T_{oil} - T_{room}) \tag{1.5.3}$$

The radiation heat transfer coefficient α_{rad} can be calculated according to equation (1.5.4).

$$\alpha_{rad} = 0.23 \times 10^{-6} \cdot \epsilon \cdot \left(\frac{T_{oil} - T_{room}}{2} \right)^3 \tag{1.5.4}$$

In previous investigations Höhn *et al.* [28] showed that due to the movement of the shafts, cooling air from the driving motor etc, real free convection is never verified on practical applications.

The free convection coefficient suggested on [28] is the empirical formula of equation (1.5.5).

$$\alpha_{cnv,free} = 18 \cdot h_{ca}^{-0.1} \cdot \left(\frac{T_{oil} - T_{room}}{T_{room}} \right)^{0.3} \tag{1.5.5}$$

Even for low air speeds there is a substantial increase on the convection heat transfer coefficient.

The heat transfer coefficient for forced convection is then given by equation (1.5.6).

$$\alpha_{cnv,forced} = 8.6 \cdot I_x^{-0.34} \cdot V_{air}^{0.64} \tag{1.5.6}$$

When only part of the housing is subjected to an air flow, the combined convective transfer coefficient can be determined from equation (1.5.7).

$$\alpha_{cnv,combined} = \alpha_{cnv,free} \cdot \left(1 - \frac{A_{air}}{A_{ca}} \right) + \alpha_{cnv,forced} \cdot \frac{A_{air}}{A_{ca}} \tag{1.5.7}$$

The total heat transfer coefficient is then the sum of various heat transfer coefficients (equation (1.5.8)).

$$\alpha_{Heat} = \alpha_{cnv,combined} + \alpha_{rad} \tag{1.5.8}$$

In order to take into account the heat dissipation due to conduction an increase on convective and radiant areas might be considered. Some authors [28] suggest $1.5-2.5$ times the respective areas.

The total heat dissipation from the housing surface is described by equation (1.5.9).

$$\dot{Q}_{total} = \dot{Q}_{cnv} + \dot{Q}_{rad} \tag{1.5.9}$$

Thermal conduction reflects the small amount of heat that is transferred to the shafts, couplings and foundations of the gearbox. Convection and radiation comprise the heat transfer that occurs through the external surface of the gearbox.

Höhn *et al.* [28] suggested then that the total heat flow rate could be calculated according to the equation (1.5.10).

$$\dot{Q}_{total} = \alpha_{Heat} \cdot A_{Heat} \cdot (T_{Oil} - T_{Room}) \tag{1.5.10}$$

In equation (1.5.10) α_{Heat} is the heat transfer coefficient (which takes into account the heat transfer due to conduction, convection and radiation), A_{Heat} is the external area of the gearbox and T_{Room} is the room temperature.

To be noticed, is the fact that equation (1.5.10) does not take into account other relevant characteristics of the surrounding air, such as relative humidity. Bearing in mind that the specific heat of dry air and water vapour are, at atmospheric pressure:

- $c_{p_{dry\ air}} = 1.01$ kJ/kg°C
- $c_{p_{water\ vapour}} = 1.84$ kJ/kg°C

It is not difficult to understand that the relative humidity might be a relevant factor in the relation between the stabilization temperature $(T_{Oil} - T_{Room})$ and the total heat flow rate, therefore and despite its simplicity equation 1.5.10 can only be applied in very controlled environments.

Martins *et al.* [76–81] performed an extensive campaign of experimental tests in an FZG test rig at different load stages and temperatures. A mechanical power loss model was coupled to a thermal model with the aim of finding the coefficients of friction between the meshing tooth pairs.

More recently Changenet *et al.* [82, 83] presented a model based upon the first principle of thermodynamics for transient conditions where the gearbox is divided

into lumped elements with a uniform temperature connected by thermal resistances which account for the different heat transfer mechanisms. This model uses a thermal network approach coupled with the mechanical power loss model to obtain the temperature distribution the gearbox. The power dissipated by each one of the components in a gearbox is quite dependent of the average local temperature of the oil that lubricates that same component, therefore this approach should yield better results than the classical isothermal approach which considers just the oil sump temperature. Figure 1.9 shows the thermal network of an FZG test rig [83].

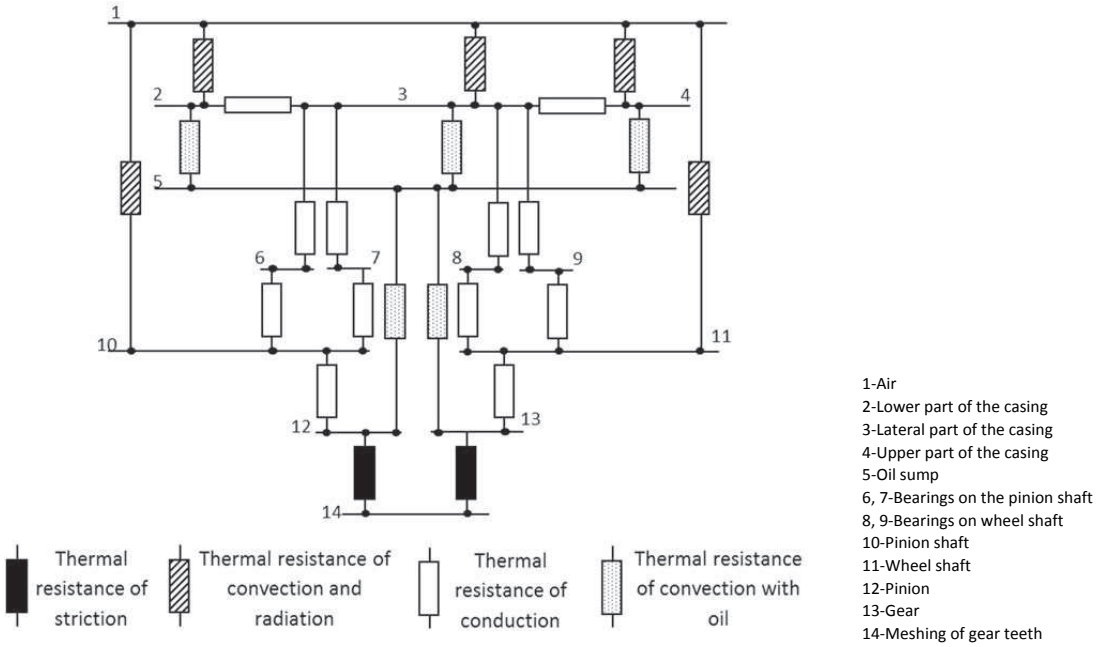

Figure 1.9.: Thermal network of an FZG test rig [83].

1.6. Closure

Through the course of this chapter it has become apparent that there are many solutions for the same power loss problems (gears, rolling bearings and seals). The problem with many of these solutions is that the majority of the models have parameters that are lubricant dependent and the only known way to find such parameters is through experimental investigation so the results will then depend on the experimental procedure. Some recent works [1, 2] presented a comprehensive way to calibrate the power loss models for gears and rolling bearings with application to a parallel axis and a planetary gearbox [3, 9].

Several authors [22, 28, 46, 47, 49] already presented formulas based on empirical studies that aim to provide an average and constant (sometimes adapted to find the local CoF) coefficient of friction along the path of contact. As referred in chapter 1, Xu [53] proposed an experimentally validated formula derived from a very large amount of numerical simulations that can be used to calculate the coefficient of friction along the path of contact in a meshing teeth pair. Recently the validity of

the coefficient friction models based on sharing functions (boundary film friction and full film friction) has been questioned [52].

One of the main deficiencies of any state of the art power loss models is in the prediction of the no-load losses, where different models applied to the same conditions yield very different results, differences of orders of magnitude between the models are sometimes calculated. Experimental measurement of the gearbox no-load losses are at this stage still the way to go.

Despite most of the time having a small role in the overall power loss, the prediction of the seals losses is still a very difficult task.

There are no definite answers to the question to which model is "better", nor it was sought here, some models work better in conditions were others fail and vice versa.

2. Developments for a Gear Pair: Load Sharing and Power Loss in Meshing Gears

At nominal operating conditions the gear load dependent losses are usually the main gearbox power loss component [2, 9, 22]. In its most general form the gear load dependent losses depend on the local tooth load, local coefficient of friction and local sliding velocity, however the most common approach to gear efficiency usually considers a constant and average coefficient of friction, an input power and a gear loss factor that mainly depends on load distribution and sliding velocity (section 1.1). The gear loss factor is by definition obtained from the assumption of a constant and average CoF along the path of contact (subsection 1.1.1). Multiple gear loss factor formulations can be found in the literature [84]. These formulations were developed considering different assumptions and simplifications which limit the applicability of such formulas [84].

In order to obtain more general and accurate methods of estimating gear load losses some of the simplifying assumptions of some classical model gear power loss model (equation (1.1.1)) must be disregarded. This implies that a local load distribution model as well as local coefficient of friction formulations (such as the one that Xu [53] proposed) must be used.

Several works [85–90] just to name a few, considering different approaches already dealt with the load sharing problem in meshing gears. Considering a load distribution taking into account mesh stiffness will lead to a better understanding of not only the power loss along the path of contact, but also allowing more refined calculations of the gear frictional losses. It can also contribute to explain the occurrence of certain tooth flank distress phenomena.

AGMA has suggested a solution for the load distribution in spur gears with unmodified profiles (there is no tip or root relief), AGMA 925-A03 [85]. The formulation presented in AGMA 925-A03 [85] (also known as the rule of "$1/3 - 2/3$") is very well known and it goes as it follows:

for $0 \leq \xi < \epsilon_\alpha - 1$

$$F_N^{A925-03}(\xi) = F_{bn} \cdot \left[\frac{1}{3} + \frac{1}{3} \cdot \frac{1}{\epsilon_\alpha - 1} \cdot \xi \right] \tag{2.0.1}$$

for $\epsilon_\alpha - 1 \leq \xi \leq 1$

$$F_N^{A925-03}(\xi) = F_{bn} \tag{2.0.2}$$

for $1 < \xi \leq \epsilon_\alpha$

$$F_N^{A925-03}(\xi) = F_{bn} \cdot \left[\frac{2}{3} + \frac{1}{3} \cdot \frac{1}{\epsilon_\alpha - 1} \cdot (1 - \xi) \right] \tag{2.0.3}$$

The previous formulation (equations (2.0.1) to (2.0.3)) is not adequate for addendum modified spur gears. Equations (2.0.1) to (2.0.3) are written as a function of ξ which is defined according to figure 2.5. Figure 2.1 shows the application of this formulation to the FZG C40 gear (table 2.1).

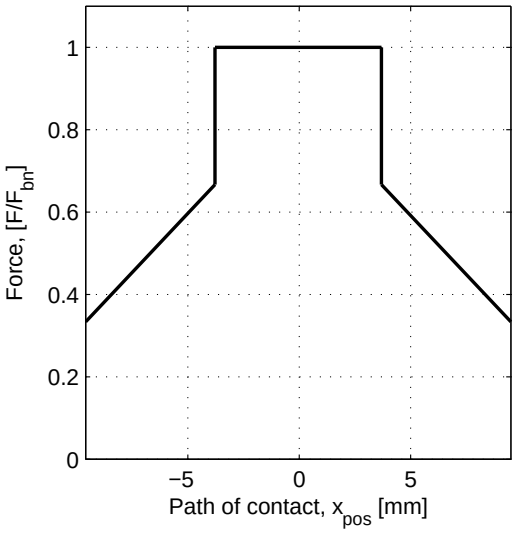

Figure 2.1.: AGMA 925-A03 load distribution for the FZG C40 gear (table 2.1).

In this chapter the load distribution problem is studied considering rigid and elastic teeth while disregarding dynamic and Hertzian effects. The load dependent Hertzian non-linear effects play a more important role in the mesh stiffness than in the load distribution where the non-linear effect is diminished [86]. The results of each model are analysed and compared. A generalized approach on gear power loss is also developed and some results presented.

Three load sharing models were developed:

1. Quasi-static rigid model (analytical);
2. Quasi-static elastic model (analytical);
3. Quasi-static local elastic model (numerical-analytical).

The quasi-static rigid analytical model assumes that at a given position in the path of contact the load per unit of length along a line of contact over a tooth is constant. It is also assumed that the load per unit of length is the same between all

meshing tooth pairs at a given position, therefore inversely proportional to the sum of the lengths of the lines of contact. This first formulation takes advantage of the properties of an approximation of the Heaviside step function to obtain a continuous description of the load distribution [16] based on the lengths of the lines of contact.

The quasi-static elastic model assumes that at a given position in the path of contact the load per unit of length along a line of contact over a tooth is constant, however the load per unit of length is not the same between all meshing tooth pairs at a given position.This model takes the literature definition of stiffness and from there based on the assumption of a rigid gear up to the base cylinder Heaviside functions are combined with the single tooth pair mesh stiffness to obtain a description of the load distribution. The single tooth mesh stiffness per unit of $b/\cos(\beta_b)$ was approximated by a quadratic function.

In fact some authors [86,89] have already shown that the single tooth mesh stiffness has an approximately parabolic/half-sine-wave shape for spur gears. Cai [86] suggests equation (2.0.4) (here modified for the ξ coordinates, figure 2.5) for the single tooth mesh stiffness along the path of contact normalized for the all teeth pair average mesh stiffness along the path of contact. In one of his previous works, Rincon [86] took $k^{Cai}(\xi)$ (2.0.4) and combined it with the ISO 6336-1 average mesh stiffness (K_m^{ISO}) to describe the single teeth pair mesh stiffness for spur gears.

$$k^{Cai}(\xi) = \frac{1}{0.85 \cdot \epsilon_\alpha} \cdot \left[\frac{-1.8}{\epsilon_\alpha^2} \cdot \xi^2 + \frac{1.8}{\epsilon_\alpha} \cdot \xi + 0.55 \right] \tag{2.0.4}$$

Figure 2.2 shows the application of Cai's formulation (2.0.4) to the FZG C40 gear.

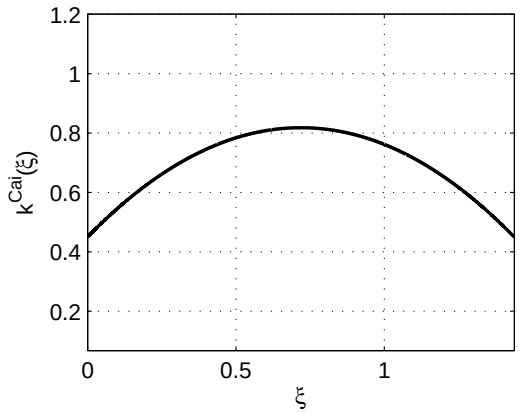

Figure 2.2.: Cai's single tooth pair stiffness, $k^{Cai}(\xi)$ (2.0.4), C40 gear (table 2.1).

The quasi-static local elastic model is based on the minimization of the total potential energy of the gear system. This model can be viewed almost as an extension

of the quasi-static elastic analytical model to the gear face width. Here the compliance coefficients were extracted using an open source FEM solver wrapped in a custom code. The load balance including frictional forces was also introduced using a Lagrange multiplier [15, 16].

The proposed load distribution models will be tested with the different gear geometries presented in table 2.1. Figure 2.3 shows the plane of action tangent to the base circles and then a local projection view that shows the contact lines in the plane of action for three gear geometries (spur and helical gears). The C40 and H501 are "conventional" spur and helical gear geometries, while the H951 is a "low loss" gear [2]. It should be noted that the C40 gear is like an FZG type C gear but with a face width of 40 mm.

Table 2.1.: Geometrical parameters of the C40, H501 and H951 gears.

Gear type:	**C40***		**H501**		**H951**	
	Driven	Driving	Driven	Driving	Driven	Driving
Number of teeth (z_i), [-]	16	24	20	30	38	57
Module (m), [mm]	4.5		3.5		1.75	
Centre distance (a), [mm]	91.5		91.5			
Pressure angle (α), [°]	20		20			
Helix angle (β), [°]	-		15			
Face width (b), [mm]	40		23		23	
Profile shift (x_z), [/]	+0.1817	+0.1715	+0.1809	+0.0891	+1.6915	+2.0003
Addendum diameter (d_{ai}), [mm]	82.64	118.54	80.67	116.27	76.23	111.73
Transverse contact ratio (ϵ_α), [/]	1.44		1.46		0.93	
Overlap contact ratio (ϵ_β), [/]	-		0.54		1.08	
Average roughness (Ra), [μm]	≈0.7		≈0.35		≈0.35	
Material	16MnCr5		16MnCr5			

* - FZG type C gear with a face width of 40 mm;

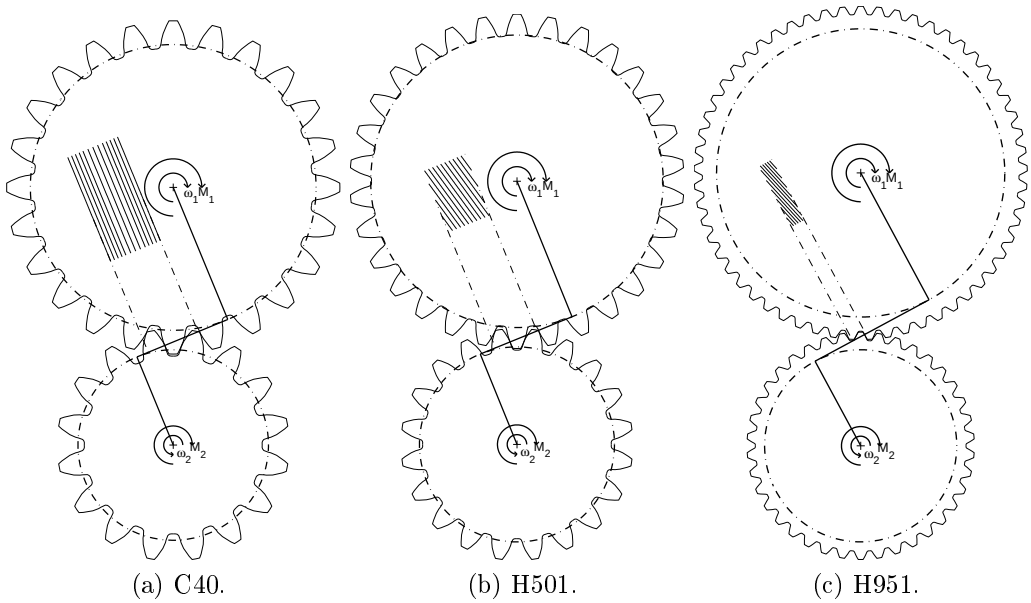

(a) C40. (b) H501. (c) H951.

Figure 2.3.: Gear geometry, plane of action and contact lines (geometric approach) for the C40, H501 and H951 gear geometries in a multiplier configuration.

2.1. Quasi-Static Rigid Model

As previously introduced this model assumes that at a given position in the path of contact the load per unit of length along a line of contact over a tooth is constant. It also assumes that the load per unit of length is the same between all meshing tooth pairs at a given position, therefore inversely proportional to the sum of the lengths of the lines of contact. Therefore, before studying the load distribution one must first analyse the behaviour of the length of the lines of contact along the plane of action.

2.1.1. Considerations about the lines of contact and different gear "species"

In the meshing process the gear teeth are in contact along parallel lines that form a plane which is at every instant normal to the surface of all meshing teeth. This plane, the plane of action (PoA), is also tangent to both base cylinders [91].

In a spur gear, the contact lines are parallel to the lines that are tangent to the plane of action and the base cylinder as represented in Figure 2.4a. In helical gears, the contact lines are at an angle (base helix angle, β_b) with the base cylinder tangency lines as represented in Figures 2.4b and 2.4c.

Considering now that spur gears are the particular case of helical gears when the helix angle is zero, then there can be three different scenarios regarding the overlap ratio, (ϵ_β):

1. $\epsilon_\beta = 0$
2. $\epsilon_\beta \leq \epsilon_\alpha$
3. $\epsilon_\beta > \epsilon_\alpha$

Figures 2.4 show these three different scenarios, i.e., Figure 2.4a shows the lines of contact for a spur gear, Figure 2.4b shows the lines of contact for an helical gear with $\epsilon_\beta \leq \epsilon_\alpha$ (lines of contact cover the entire tooth flank width) and Figure 2.4c also shows the lines of contact for an helical gear, but $\epsilon_\beta > \epsilon_\alpha$ (lines of contact never cover all the tooth flank length).

During the meshing process, there may be more than one teeth pair simultaneously engaged. The lines of contact corresponding to more than one teeth pair simultaneously engaged are separated by a distance equal to the transverse base pitch (p_{bt}) from each other.

In the case of spur gears ($\epsilon_\beta = 0$) a meshing teeth pair enters the "active" section of the plane of action and the line of contact has a length that is equal to the face width of the gears (b).

In helical gears the meshing teeth pair gradually enters the path of contact and the length of the contact lines show a linear increase from 0 up to a maximum and then decrease back to 0 as it leaves the active section of the plane of action. This

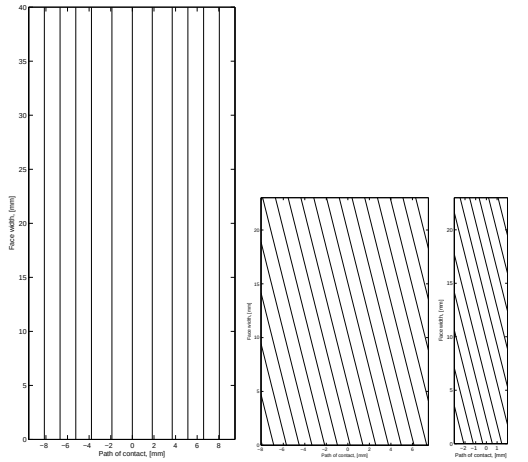

(a) C40. (b) H501. (c) H951.

Figure 2.4.: Lines of contact for three different gear geometries: (a) $\epsilon_\beta = 0$; (b) $\epsilon_\beta \leq \epsilon_\alpha$; (c) $\epsilon_\beta > \epsilon_\alpha$.

maximum can be either a plateau or a peak depending on the relationship between ϵ_β and ϵ_α.

From these considerations, it is possible to define the length and the sum of the lengths of the lines of contact along the active section of the plane of action.

2.1.2. Analytical description of the length of the lines of contact

Let us consider a coordinate ξ that is the non-dimensional coordinate along the path of contact (distance divided by the transverse base pitch, p_{bt}), which is zero at the starting line of the meshing action (figure 2.5).

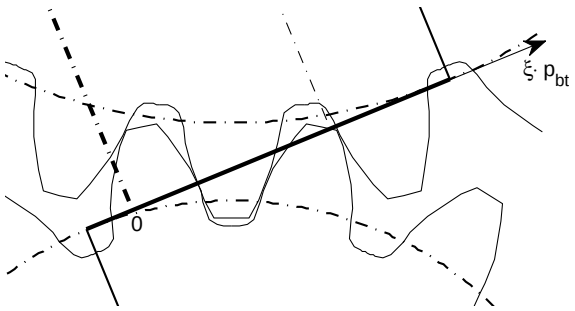

Figure 2.5.: Definition of the ξ coordinates.

For spur gears the length of a contact line over a teeth is a constant, therefore a teeth entering the plane of action can be viewed as a step like increment of constant value in the function describing the sum of the length of contacting lines. The Heaviside function also known as the unit step function is then suited to describe such phenomena.

The Heaviside function can be approximated using equation (2.1.1). For a value of $k = 1000$ the analytic approximation is in good agreement with the theoretical Heaviside function. The interesting thing about using this approach is that there is no need to define independent domains for each time a tooth pair enters or leaves the contact. Equation (2.1.1) is the approximated Heaviside function (figure 2.6).

$$H(\xi) = \lim_{k \to +\infty} \left(\frac{1}{1 + e^{-2 \cdot k \cdot \xi}} \right) \tag{2.1.1}$$

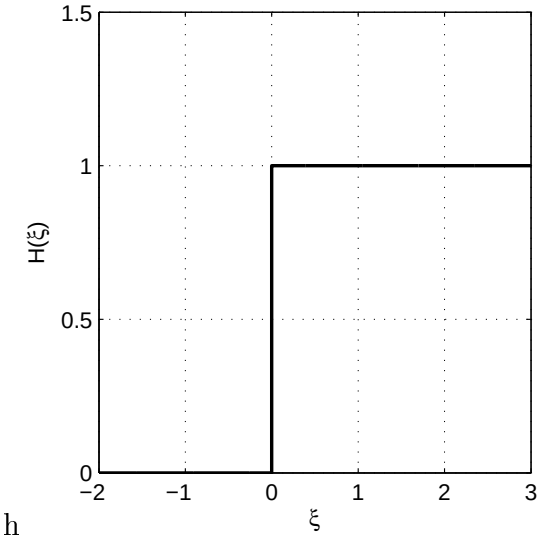

h

Figure 2.6.: Approximation to the Heaviside function, equation (2.1.1).

The ratio of length of the contact line over a tooth to the face width for spur gear geometries ($\beta = 0$) is always constant and equal to 1 in the active section of the plane of action and 0 outside of it. This defines a function that has a shape of square of unitary heigh and ϵ_α length, which can be obtained by subtracting two Heaviside functions shifted by ϵ_α. $Tl^s(\xi)$ (2.1.2) is the statement of such function (figure 2.7a).

$$Tl^s(\xi) = H(\xi) - H(\xi - \epsilon_\alpha) \tag{2.1.2}$$

As previously referred it is known that there can be more than one pair of teeth simultaneously meshing.The meshing pairs are shifted by a distance of p_{bt} from each other, which corresponds to a unit in the coordinate system ξ that was previously defined. So in order to obtain the line lengths of the other meshing pair simultaneously in action one just needs to shift $Tl^s(\xi)$ (2.1.2) back and forth by integer values i, which yields $Ul_i^s(\xi)$ equation (2.1.3) (figure 2.7b). From the definition of ϵ_α and the coordinate ξ it follows that these i integers must be:

$i = -$ floor $(\epsilon_\alpha) : 1 :$ floor(ϵ_α) (floor is rounding down).

$$Ul_i^s(\xi) = \Big[H(\xi - i) - H(\xi - \epsilon_\alpha - i)\Big] \tag{2.1.3}$$

The length of the line of contact for a given tooth pair should only be defined in $0 \leq \xi \leq \epsilon_\alpha$. Since $Tl^s(\xi)$ (2.1.2) is a unit square function it can be used to trim and bound $Ul_i^s(\xi)$ (2.1.3) to the desired domain ($0 \leq \xi \leq \epsilon_\alpha$). This results in equation $l_i^s(\xi)$ (2.1.4) which represents the bounded contact line length to gear face width ratio in a spur gear for the meshing tooth pair i (figure 2.7c).

$$l_i^s(\xi) = Ul_i^s(\xi) \cdot Tl^s(\xi) \tag{2.1.4}$$

It then follows that the trimmed sum of the length of the lines of contact for all active meshing teeth pairs, along the path of contact in a spur gear, is given by equation $L^s(\xi)$ (2.1.5)(figure 2.7d).

$$L^s(\xi) = \left[\sum_{i=-floor(\epsilon_\alpha)}^{floor(\epsilon_\alpha)} Ul_i^s\left(\xi\right)\right] \cdot Tl^s(\xi) \tag{2.1.5}$$

The previous equations (equations (2.1.2) to (2.1.5)) are only valid for spur gears, however for helical gears the thought process is the same. The main difference is in $l_i(\xi)$ (2.1.4). It should be noted here that instead of normalizing the line lengths to the gear face width b, here the line lengths are divided by $b/\cos(\beta_b)$.

For helical gears a Heaviside function can be combined with linear functions to yield the characteristic linear increment, decrement and the constant features of the ratio of the length of a contact line over a single helical tooth per maximum line length ($b/\cos(\beta_b)$). Therefore it follows equation Ul_i^h (2.1.8) for helical gears. Figure 2.8 shows the application of $Ul_i^h(\xi)$ (2.1.7) to a sample helical gear.

$Tl^h(\xi)$ (equation (2.1.6)) is a function whose purpose is to trim the solution to the desired domain $0 \leq \xi \leq \epsilon_\alpha + \epsilon_\beta$.

$$Tl^h(\xi) = H(\xi) - H(\xi - (\epsilon_\alpha + \epsilon_\beta)) \tag{2.1.6}$$

$$\begin{aligned} Ul_i^h(\xi) = \frac{1}{\epsilon_\beta} \cdot \Big[&H(\xi - i) - H(\xi - \epsilon_\beta - i) \cdot (\xi - \epsilon_\beta - i) \\ &- H(\xi - \epsilon_\alpha - i) \cdot (\xi - \epsilon_\alpha - i) \\ &+ H(\xi - (\epsilon_\alpha + \epsilon_\beta) - i) \cdot (\xi - (\epsilon_\alpha + \epsilon_\beta) - i)\Big] \end{aligned} \tag{2.1.7}$$

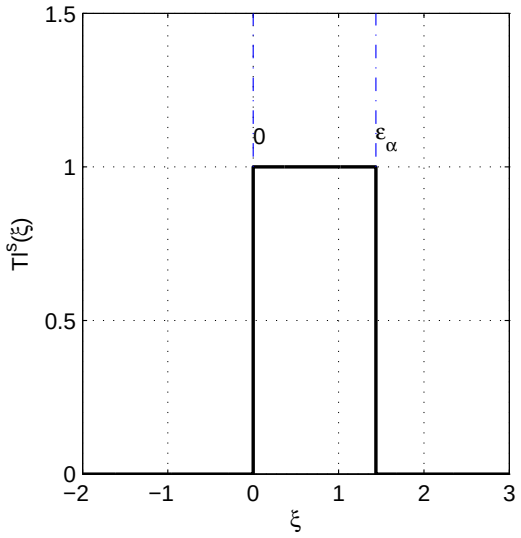

(a) Square trim function, $Tl^s(\xi)$. (2.1.2).

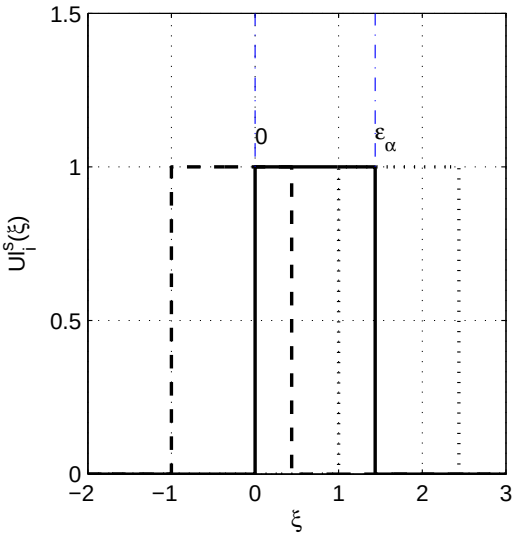

(b) Unbounded contact line length ratio (single spur gear), $Ul_i^s(\xi)$, (2.1.3).

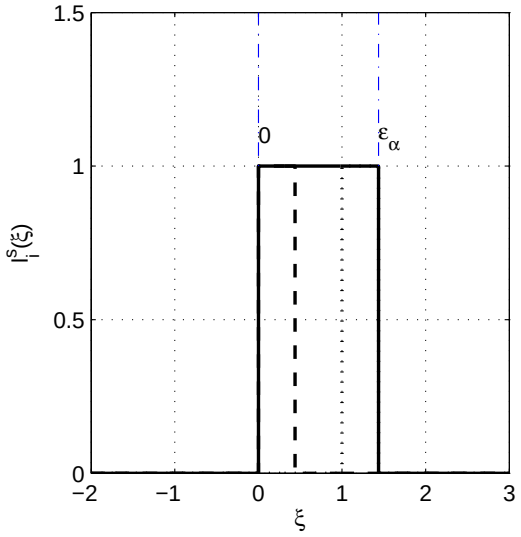

(c) Bounded contact line length ratio (single spur gear), $l_i^s(\xi)$, (2.1.4).

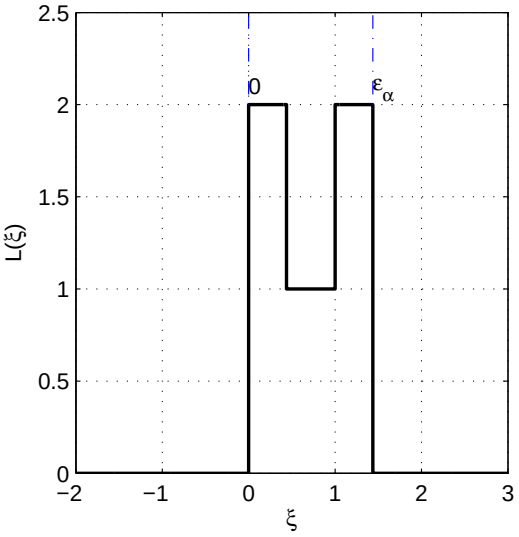

(d) Sum of the lengths of the contact lines (spur gear), $L^s(\xi)$ (2.1.5).

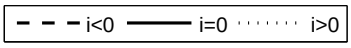

Figure 2.7.: Steps behind the Heaviside approach to the length of the lines of contacts for spur gears.

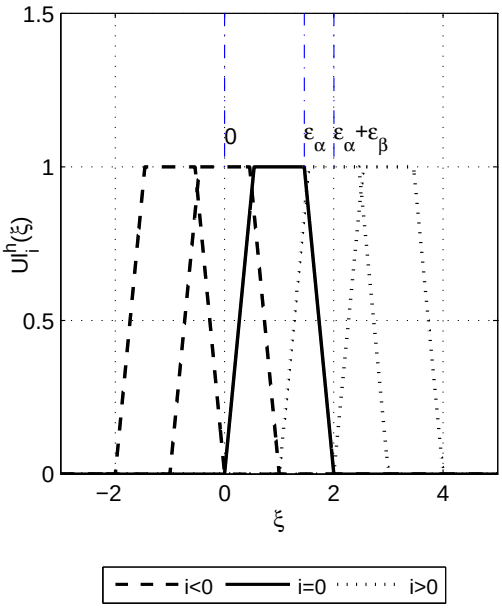

Figure 2.8.: Unbounded contact line length ratio (helical gear), $Ul_i^h(\xi)$, (2.1.7).

$$l_i^h(\xi) = Ul_i^h(\xi) \cdot Tl^h(\xi) \tag{2.1.8}$$

where $i = -\text{floor}(\epsilon_\alpha + \epsilon_\beta) : 1 : \text{floor}(\epsilon_\alpha + \epsilon_\beta)$ (floor is rounding down).

Equation (2.1.9) is the sum of the lengths of the contact lines for all active meshing teeth pairs along the path of contact.

$$L^h(\xi) = \left[\sum_{i=-floor\left(\epsilon_\alpha+\epsilon_\beta\right)}^{floor\left(\epsilon_\alpha+\epsilon_\beta\right)} Ul_i^h(\xi) \right] \cdot Tl^h(\xi) \tag{2.1.9}$$

2.1.3. Results

Figures 2.9 show the application of equations (2.1.4), (2.1.5) (2.1.8) and (2.1.9) to the geometries presented in table 2.1.

In previous works Maatar and Velex *et al.* [92,93] presented an analytical formulation to describe the time-varying contact length between perfect involute spur and helical gears. It was shown that the contact lengths could be expressed as Fourier series.

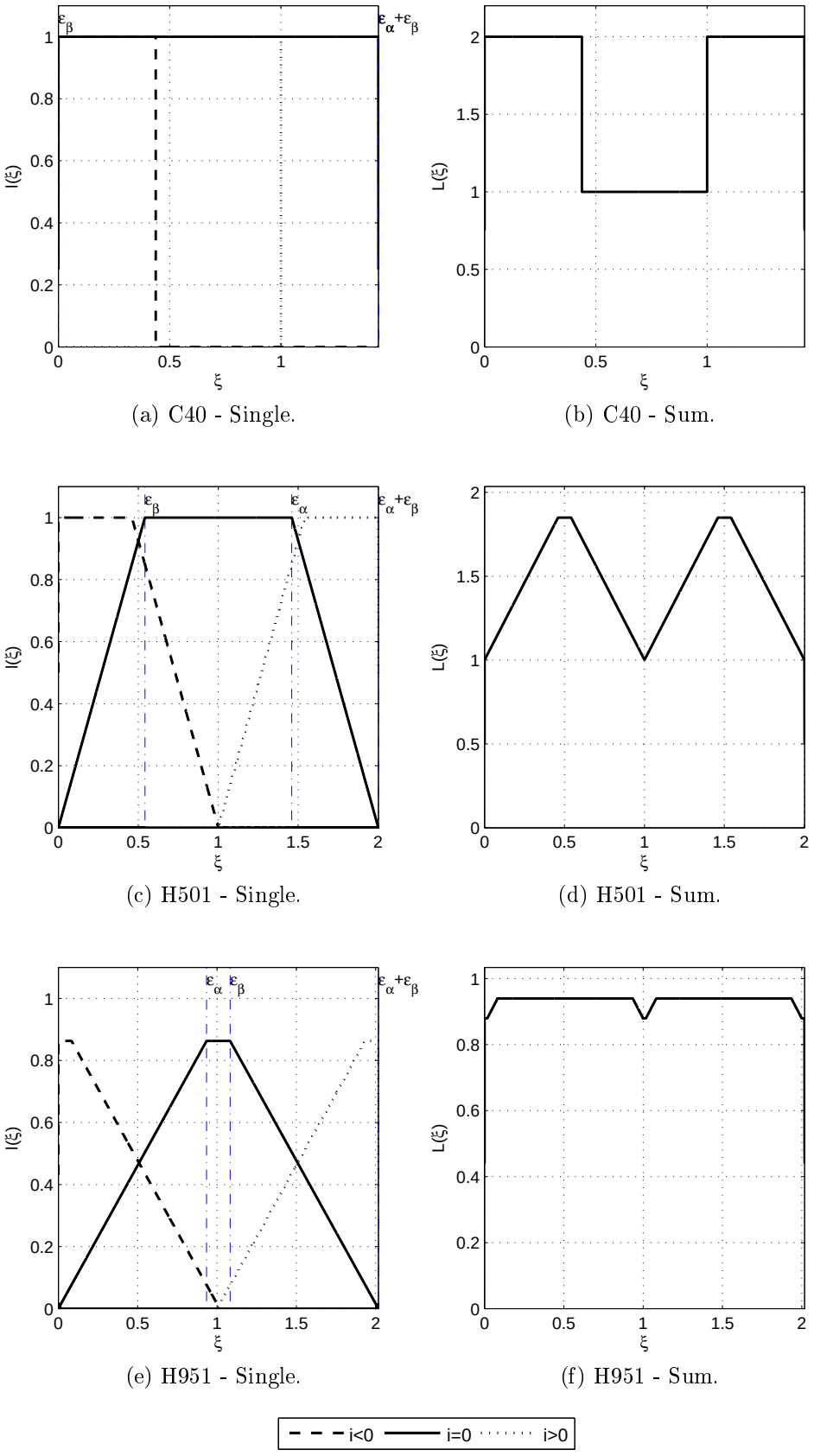

(a) C40 - Single.

(b) C40 - Sum.

(c) H501 - Single.

(d) H501 - Sum.

(e) H951 - Single.

(f) H951 - Sum.

Figure 2.9.: Length of single lines of contact and the combined result for gears C40, H501 and H951.

Figures 2.10 compare the results for the different gear geometries considering the suggested continuous Heaviside approach with the formulation previously introduced by Maatar *et al.* [92]. The k value in equation (2.1.1)) was kept at $k = 1000$ and 50 harmonics were considered for the Fourier based formulation. The Heaviside based formulation produces well defined and continuous transitions even for the case of spur gears in the transition from one to two meshing teeth pairs (figure 2.10b). It should be noted that even for spur gears the proposed formulation yields functions that are continuous and analytically derivable. On the Maatar and Velex approach [92], even for an high number of harmonics the transition is not as smooth as the proposed Heaviside function approach, specially at the transition between different meshing tooth pairs, as observed in figure 2.10b.

In what regards helical gears, both methods yield very good and similar results. The Fourier based approach proposed by Velex *et al.* has the advantage of producing a continuous analytical curve for the sums of the lengths of the lines of contact for n meshing periods, while the Heaviside approach is limited to a single meshing period, $0 \leq \xi \leq \epsilon_\alpha + \epsilon_\beta$.

2.1.4. Load Sharing

Following the definition of $L^{h,s}(\xi)$ the load per unit of length over a tooth along the active section of the plane of action is given by equation (2.1.10). Introducing the notion of $l_i^{h,s}(\xi)$ the resulting normal load acting in a single tooth along the path of contact is defined according to equation (2.1.11).

$$f_N(\xi) = \frac{M_w}{r_{bw}} \cdot \frac{1}{b \cdot L^{h,s}(\xi)} \tag{2.1.10}$$

$$F_{Ni}(\xi) = \frac{M_w}{r_{bw} \cdot \cos(\beta_b)} \cdot \frac{l_i^{h,s}(\xi)}{L^{h,s}(\xi)} \tag{2.1.11}$$

Equation (2.1.11) states that the load supported by a pair of contacting teeth is a force, $\frac{M_w}{r_{bw} \cdot \cos(\beta_b)}$, multiplied by a sharing function. The load sharing function, is the fraction between the length of the contact line over a tooth divided by the sum of the lengths of the contacting lines of all contact pairs in a certain position along the path of contact.

2.1.5. Results

Figures 2.11 show $\frac{l_i(\xi)}{L(\xi)}$ and $\frac{1}{L(\xi)}$ for the different gear geometries.

The differences in the load distribution functions are quite clear. The C40 geometry (figures 2.11a and 2.11b) shows step like increases or decreases in the load sharing functions whether a tooth enter or leaves the plane of action. The helical

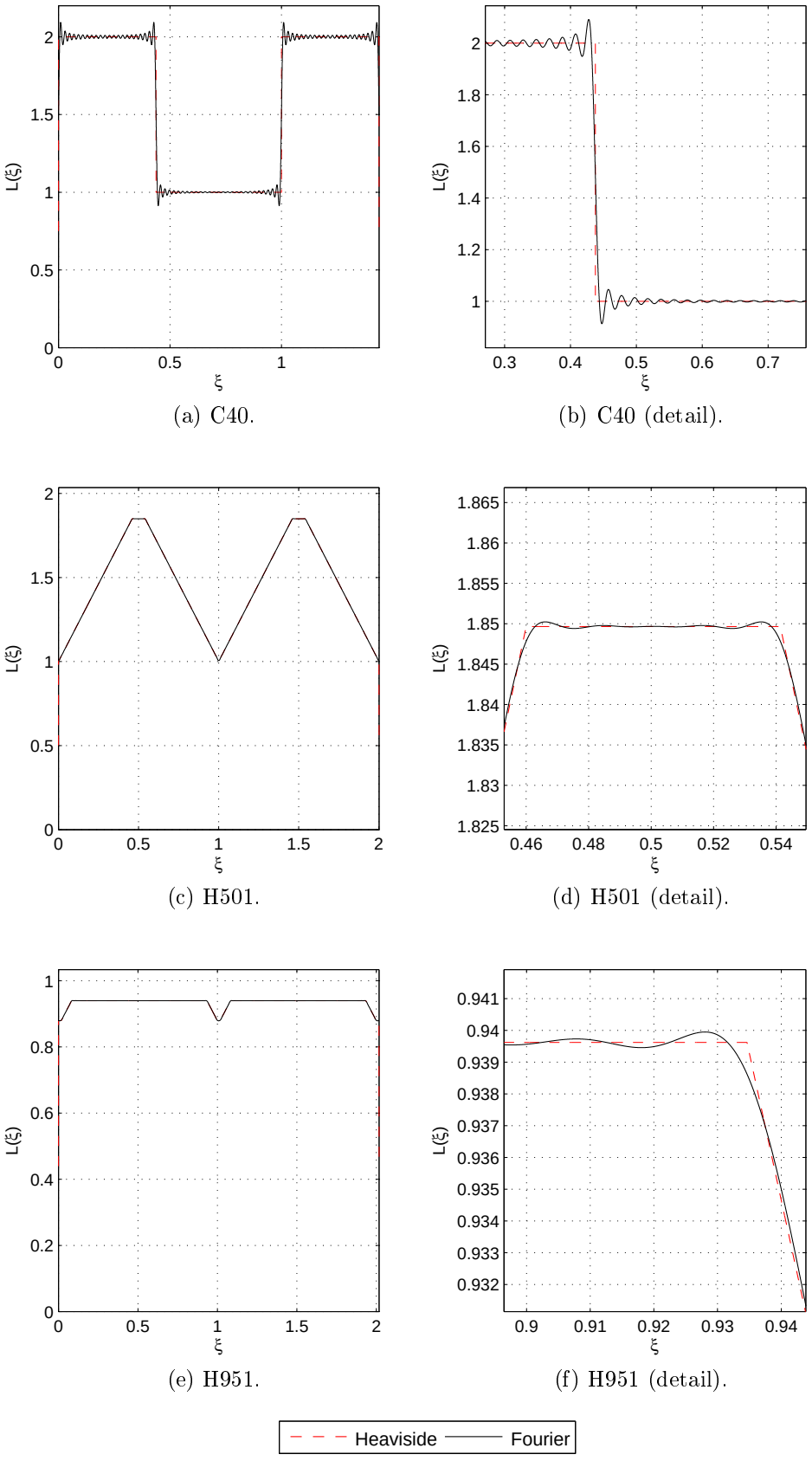

(a) C40. (b) C40 (detail).

(c) H501. (d) H501 (detail).

(e) H951. (f) H951 (detail).

Figure 2.10.: Heaviside vs Fourier [92] formulation for sums of the lengths of the contact lines for gears C40, H501 and H951.

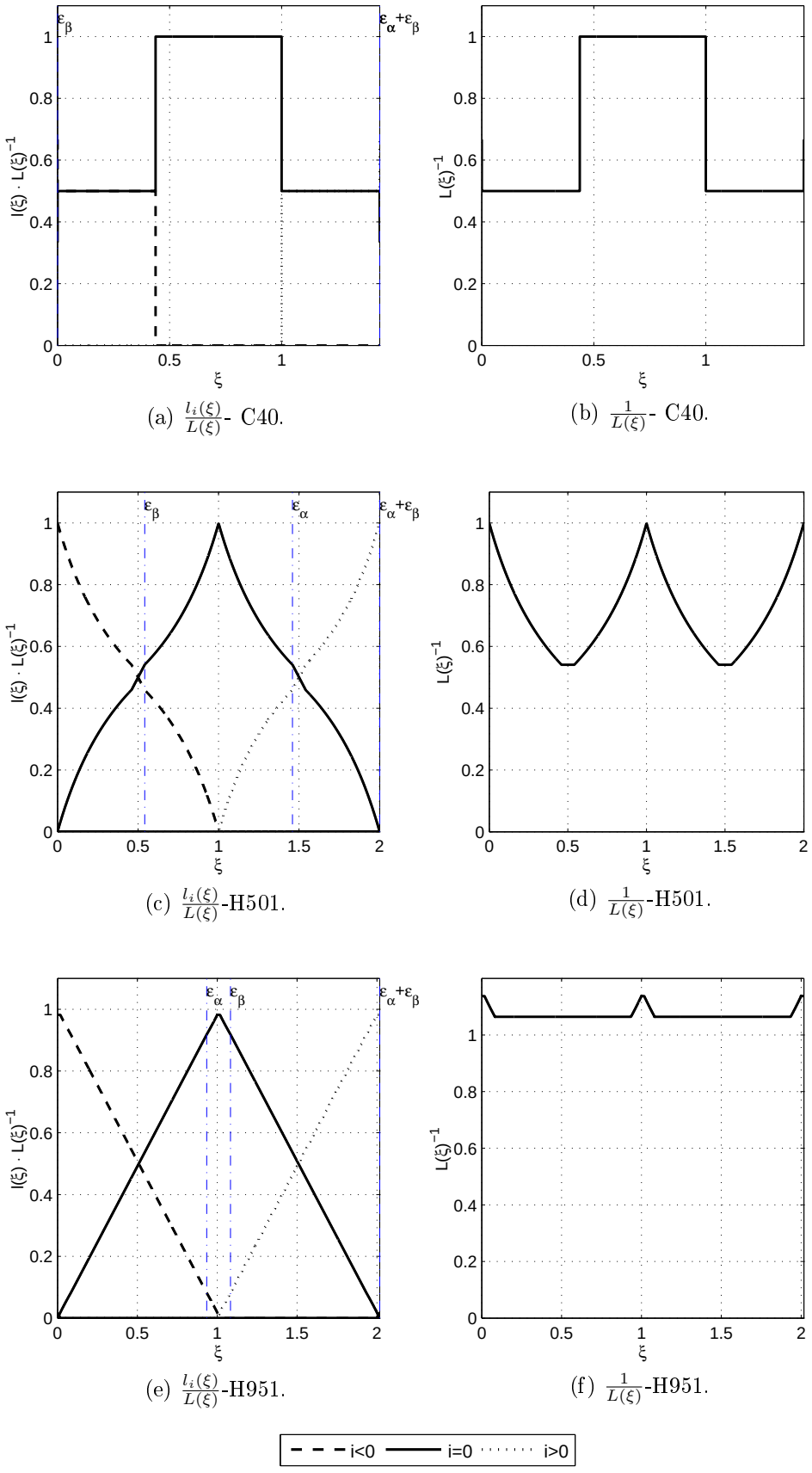

(a) $\frac{l_i(\xi)}{L(\xi)}$- C40.

(b) $\frac{1}{L(\xi)}$- C40.

(c) $\frac{l_i(\xi)}{L(\xi)}$-H501.

(d) $\frac{1}{L(\xi)}$-H501.

(e) $\frac{l_i(\xi)}{L(\xi)}$-H951.

(f) $\frac{1}{L(\xi)}$-H951.

Figure 2.11.: Load sharing functions (rigid) for gears C40, H501 and H951 (quasi-static rigid model).

gears show progressively increasing or decreasing loads when teeth are leaving or entering the plane of action which is a consequence of the "progressive" meshing due to the helical angle. Even between the two helical gears (H501 and H951) some significant differences can be observed. Despite the meshing process being progressive on both of these geometries the relations between ϵ_α and ϵ_β for these gear geometries are quite different which is reflected on the load distribution functions (Figures 2.11c, 2.11d and 2.11e, 2.11f). In the case of H951 $\epsilon_\beta > \epsilon_\alpha$ which means that the maximum value that $\frac{1}{L(\xi)}$ will take is above one because it is not possible to have a full line of contact ($b/\cos(\beta_b)$) over a tooth.

2.2. Quasi-Static Elastic Model

As previously stated this model assumes that at a given position in the path of contact the load per unit of length along a line of contact over a tooth is constant, however the load per unit of length is not the same between all meshing tooth pairs at a given position due to elastic deformation.

Let's assume that the gear body is perfectly rigid up to the base cylinder. Lets also assume that in a loaded gear the angular displacement of the base cylinder is very small ($d\theta$). Since the angular displacement of the base cylinder is very small the length of the arc can be approximated by the displacement δ_b in the direction of the plane of action.

From the literature definition of stiffness (here represented as $K^T(\xi)$) and knowing that the total normal force in the transverse plane is F_{bt} the linear displacement δ_b is given by equation (2.2.1).

$$\delta_b = \frac{F_{bt}}{K^T(\xi)} \tag{2.2.1}$$

For a given tooth pair the load that is supported by that individual pair, i, is the δ_b displacement multiplied by the stiffness of that pair $K_i(\xi)$, (equation (2.2.2)).

$$F_{Ni}^K(\xi) = \delta_b \cdot K_i(\xi) \tag{2.2.2}$$

Therefore combining equations (2.2.1) and (2.2.2) ($F_{bt} = F_{bn}/\cos\beta_b$)the load distribution for a spur gear in the normal plane can be found, equation (2.2.3).

$$F_{Ni}^K(\xi) = \frac{K_i(\xi)}{K^T(\xi)} \cdot F_{bn} \tag{2.2.3}$$

The ISO 6336-1 Standard [94] provides a formulation to calculate the maximum single tooth mesh stiffness (K_{max}^{ISO}) for spur and helical gears with errors that deviate from experimental tests between $+5\%$ and -8% for $100 \leq F_{bt}/b \leq 1600$ N/mm.

One can then define a function for the single tooth pair mesh stiffness per unit of gear width ($b/\cos(\beta_b)$), $K_i^u(\xi)$ (2.2.4).

$$K_i^u(\xi) = k_i^u(\xi) \cdot \frac{K_{max} \cdot \cos(\beta_b)}{b} \tag{2.2.4}$$

As previously stated the single tooth mesh stiffness $K_i^u(\xi)$ can be approximated by a quadratic function. Defining the minimum mesh stiffness according to (2.2.5), a fraction α_k of the maximum stiffness, considering $K_i^u(\xi)$ and the definition of ξ it can be deduced that the unitary single tooth mesh stiffness can be written according to equation (2.2.6).

$$K_{min} = \alpha_k \cdot \frac{K_{max} \cdot \cos(\beta_b)}{b} \tag{2.2.5}$$

$$k_i^u(\xi) = \frac{4 \cdot (\alpha_k - 1)}{(\epsilon_\alpha + \epsilon_\beta)^2} \cdot (\xi - i)^2 - \frac{4 \cdot (\alpha_k - 1)}{\epsilon_\alpha + \epsilon_\beta} \cdot (\xi - i) + \alpha_k \tag{2.2.6}$$

where $i = -\text{ floor}(\epsilon_\alpha + \epsilon_\beta) : 1 : \text{floor}(\epsilon_\alpha + \epsilon_\beta)$ (floor is rounding down).

Figure 2.12 shows the application of $k_i^u(\xi)$ (2.2.6) to the C40 gear, ($\alpha_k = 4/5$, $i = 0$).

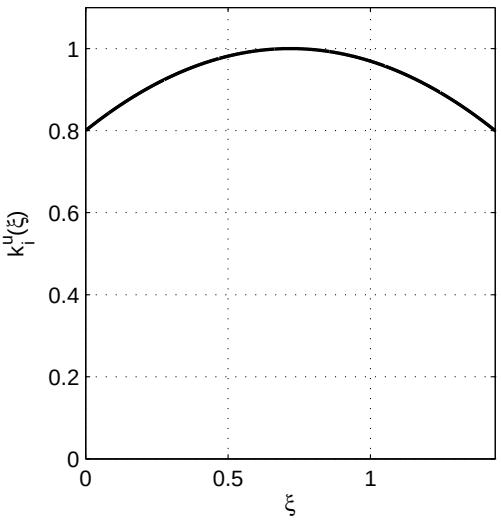

Figure 2.12.: $k_i^u(\xi)$ (2.2.6) ($\alpha_k = \frac{4}{5}$, $i = 0$) for the C40 gear (table 2.1).

An helical gear can be viewed as the sum of spur gear discs of infinitesimal width. Following the hypothesis of constant load along a line of contact, the previous definitions of $K_i^u(\xi)$ (single tooth pair mesh stiffness per unit of $b/\cos(\beta_b)$) and $Ul_i^{h,s}$ (single pair line length per $b/\cos(\beta_b)$) the stiffness for the meshing pair i is described by equation (2.2.7).

$$Kl_i^{h,s}(\xi) = Ul_i^{h,s}(\xi) \cdot \frac{b}{\cos(\beta_b)} \cdot K_i^u(\xi) \cdot Tl^{h,s}(\xi) \tag{2.2.7}$$

Since that multiple meshing teeth pairs are in parallel the total mesh stiffness is given by the sum of the stiffness of those pairs according to equation (2.2.8).

$$KL^{h,s}(\xi) = \left[\sum_{i=-floor\left(\epsilon_\alpha+\epsilon_\beta\right)}^{floor\left(\epsilon_\alpha+\epsilon_\beta\right)} Ul_i^{h,s}(\xi) \cdot \frac{b}{\cos(\beta_b)} \cdot K_i^u(\xi) \right] \cdot Tl^{h,s}(\xi) \tag{2.2.8}$$

The load distribution (total load) is then given by equation (2.2.9).

$$F_{Ni}^{K^u}(\xi) = \frac{Kl_i^{h,s}(\xi)}{KL^{h,s}(\xi)} \cdot F_{bn} \tag{2.2.9}$$

If the load per unit of line length for a single tooth pair is assumed to be constant along a single line of contact, the load per unit length for a single tooth pair along the path of contact is given by equation (2.2.10).

$$f_{Ni}^{Ku}(\xi) = \frac{F_{Ni}^{K^u}(\xi) \cdot \cos(\beta_b)}{Ul_i^{h,s}(\xi) \cdot b} \cdot Tl^{h,s}(\xi) \tag{2.2.10}$$

Figure 2.13 shows the implementation of the quasi-static rigid and elastic gear load distribution models (sections 2.1 and 2.2)

2.2.1. Results

Figures 2.14 show the single tooth and total mesh stiffness and figures 2.15 show the load distribution and load per unit of length for the selected tooth geometries. The results show that the different gears have very different mesh stiffness and load distributions.

The mesh stiffness of the C40 gear has quite abrupt variations. In the transition from two to one single pair of meshing tooth the mesh stiffness falls to about half of what was verified for two meshing tooth pairs. The H501 shows a difference between the maximum and the minimum stiffness of the same order of magnitude as the C40, however this variation is gradual and smooth. The gear with the most constant and smooth mesh stiffness is the H951, which shows an almost constant mesh stiffness along the path of contact.

The mesh stiffness evolution along the path of contact greatly influences not only the load distribution, but also the dynamic behaviour of the gear.

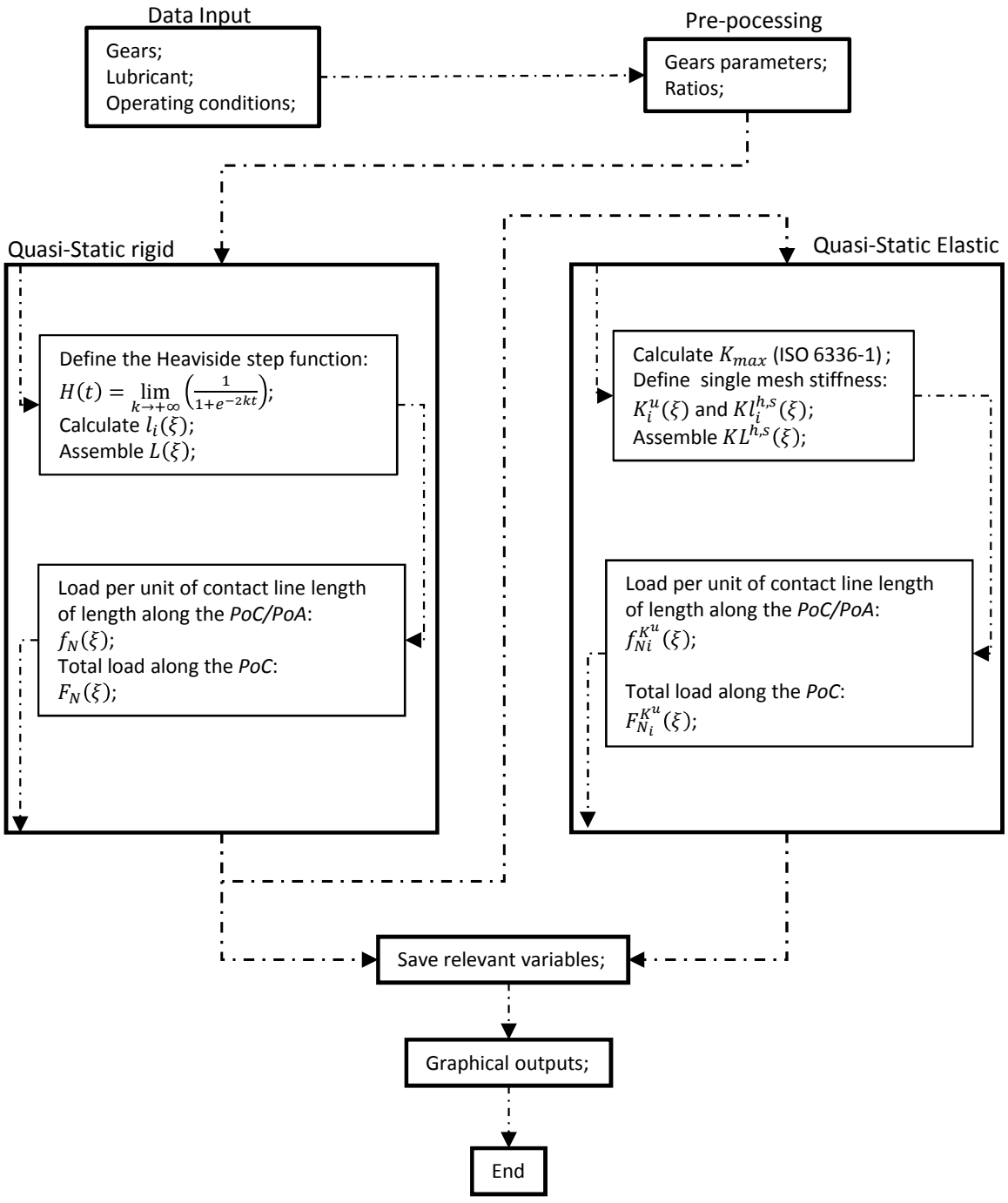

Figure 2.13.: Software implementation of the gear load distribution models presented in sections 2.1 and 2.2.

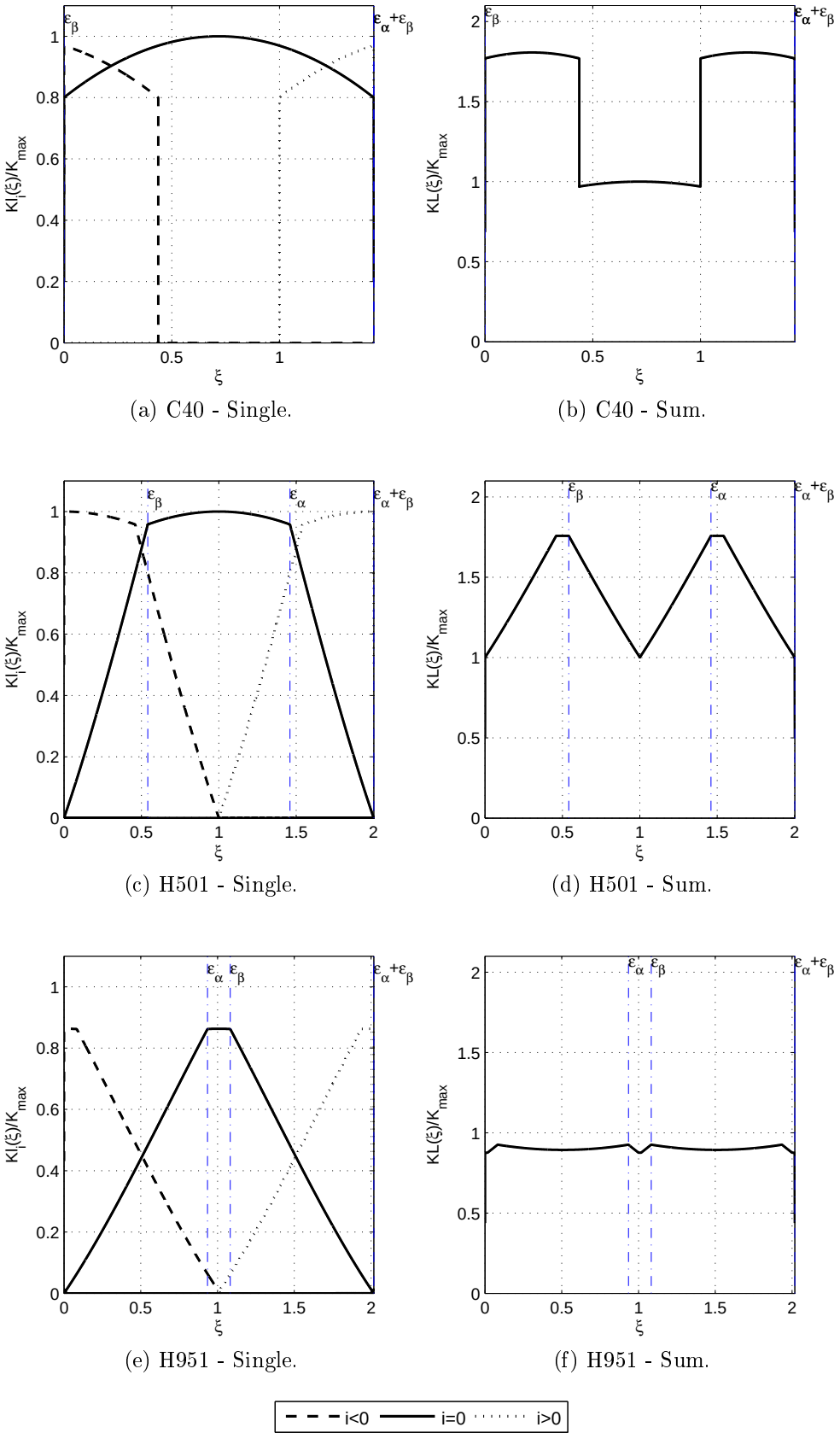

(a) C40 - Single.

(b) C40 - Sum.

(c) H501 - Single.

(d) H501 - Sum.

(e) H951 - Single.

(f) H951 - Sum.

Figure 2.14.: Single and total mesh stiffness for gears C40, H501 and H951 (quasi-elastic rigid model).

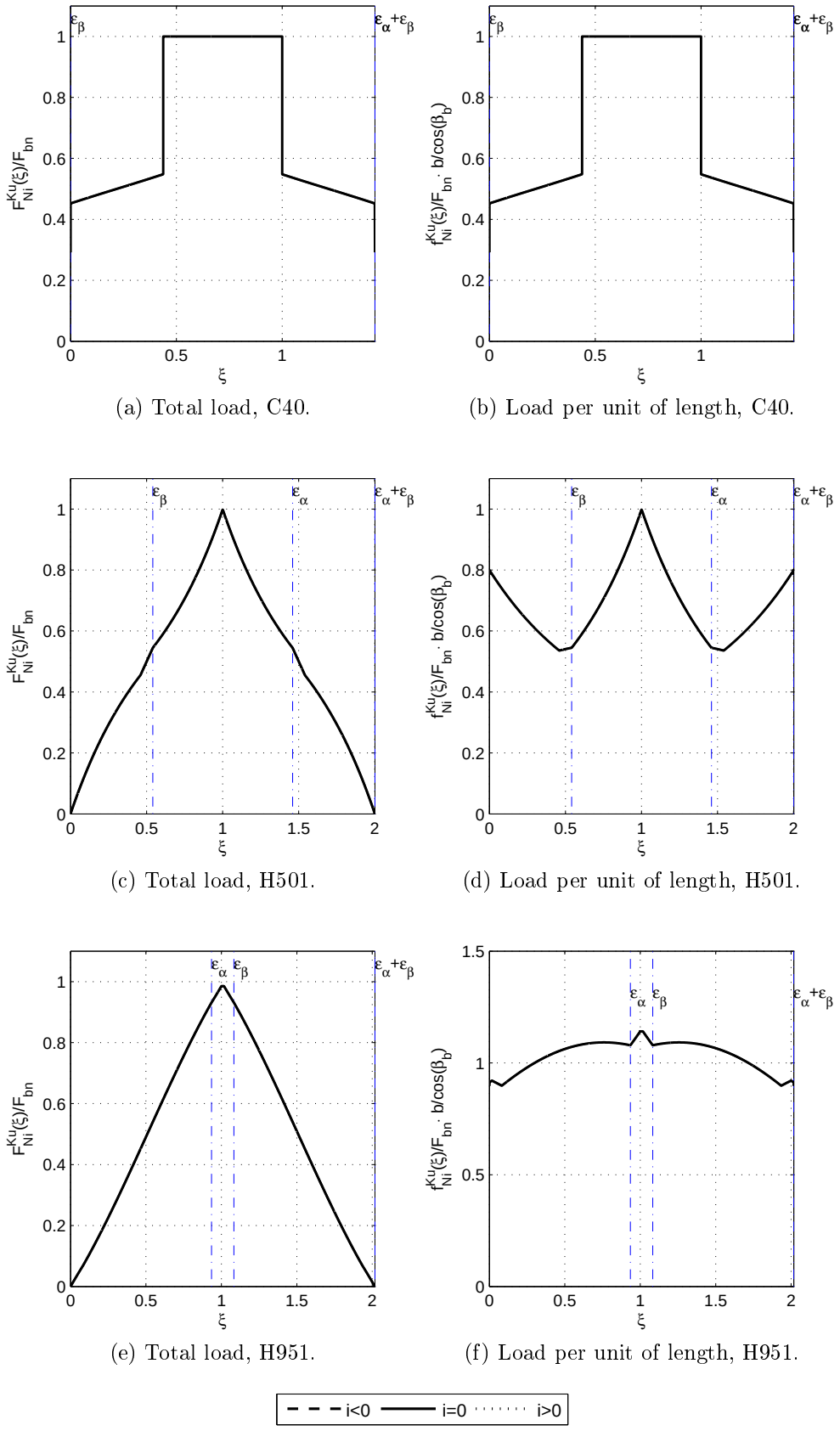

(a) Total load, C40.

(b) Load per unit of length, C40.

(c) Total load, H501.

(d) Load per unit of length, H501.

(e) Total load, H951.

(f) Load per unit of length, H951.

Figure 2.15.: Load sharing for gears C40, H501 and H951 (quasi-elastic rigid model).

2.3. Quasi-Static Local Elastic Model

The geometry of gear teeth is quite complex, therefore, the usage of numerical methods to study the load distribution along the path of contact is viewed as a possibility. In this third approach the dynamic effects will be disregarded, it will also be assumed that the deformation of the teeth is so small that the geometry of the teeth is the same in spite of the elastic deformation.

The torque (M_w) that is transmitted by the driven gear is assumed constant. Several unit forces are distributed over the tooth flank in such a way that at the contact lines these unit forces are in the plane of action and perpendicular to the tooth surface, (Figure 2.16). Taking advantage of finite element codes it is possible to obtain the displacements in the points of interest when the unit loads are applied. This process should be repeated for the driven and driving gears in order to obtain the displacement fields.

In order to obtain the displacement matrix in the direction of interest the vector formed by the components of the displacement that are given by the FEM code must be projected in a direction perpendicular to the tooth surface, which is the dot product between the displacement vector and the correspondent unit force vector.

Let the flexibility coefficient represented by a_{ij} be defined as the displacement in i due to a unit force applied in j. Due to the linear nature of this kind of problems, the displacement δ in i due to any force F_j is given by equation (2.3.1).

$$\delta_{ij} = a_{ij} F_j \tag{2.3.1}$$

The displacement in i due to a combination of normal loads in other points j can be calculated by superposition of effects, equation (2.3.2).

$$\delta_i = \sum_{j=1}^{n} \delta_{ij} = \sum_{j=1}^{n} a_{ij} F_j \tag{2.3.2}$$

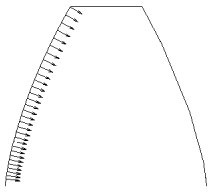

Figure 2.16.: Unit loads perpendicular to the tooth surface for a spur gear for multiple lines of contact (2D view).

The contribution of the normal load F_i to the potential energy of the system can be computed using equation (2.3.3).

$$V_i = \frac{1}{2} F_i \delta_i \tag{2.3.3}$$

The elastic potential energy stored in the teeth of the driving gear, p, or driven gear, w, in the meshing gear pair, k, in a certain position along the path of contact for the n discrete loads at the transverse profile of the teeth is given by equation (2.3.4).

$$V_k^{p,w} = \frac{1}{2} \sum_{i=1}^{n} F_{ik} \left(\sum_{j=1}^{n} a_{ijk}^{p,w} F_{jk} \right) \tag{2.3.4}$$

The elastic potential energy stored in the meshing teeth of the gear for m tooth pairs in contact is then given by equation (2.3.5).

$$V = \sum_{k=1}^{m} \left[\frac{1}{2} \sum_{i=1}^{n} F_{ik} \left(\sum_{j=1}^{n} a_{ijk}^{p} F_{jk} \right) + \frac{1}{2} \sum_{i=1}^{n} F_{ik} \left(\sum_{j=1}^{n} a_{ijk}^{w} F_{jk} \right) \right] \tag{2.3.5}$$

The sum of the forces acting in the flanks of the driving gear must balance the torque that is imposed to the driving gear (if the frictional torque is disregarded). Equation (2.3.6) is the mathematical expression of this balance (torque equilibrium equation of the driven gear divided r_{bw}).

$$\sum_{k=1}^{m} \sum_{j=1}^{n} F_{jk} - \frac{M_w}{r_{bw} \cdot \cos(\beta_b)} = 0 \tag{2.3.6}$$

In equation (2.3.6) the dissipative forces were disregarded. This equation (2.3.6) can be modified to take into account the frictional forces through the coefficient of friction (μ) as represented in equation (2.3.8), where r_{bw} is the base radius of the driven gear and r^{cw} is the distance measured perpendicularly to the contact line up to the intersection with the line of the plane of action that touches the base cylinder of the driven gear multiplied by the cosine of the base helix angle. In this case the combined result of the tooth normal forces and frictional forces should balance the imposed torque, M_w. The sliding velocity is defined according to equation (2.3.7). Figure 2.17 shows load balance for a spur gear pair including friction at two different instants.

$$v_{jk}^{g} = r_{jk}^{cw} \cdot \dot{\theta}_{jk}^{w} - r_{jk}^{cp} \cdot \dot{\theta}_{jk}^{p} \tag{2.3.7}$$

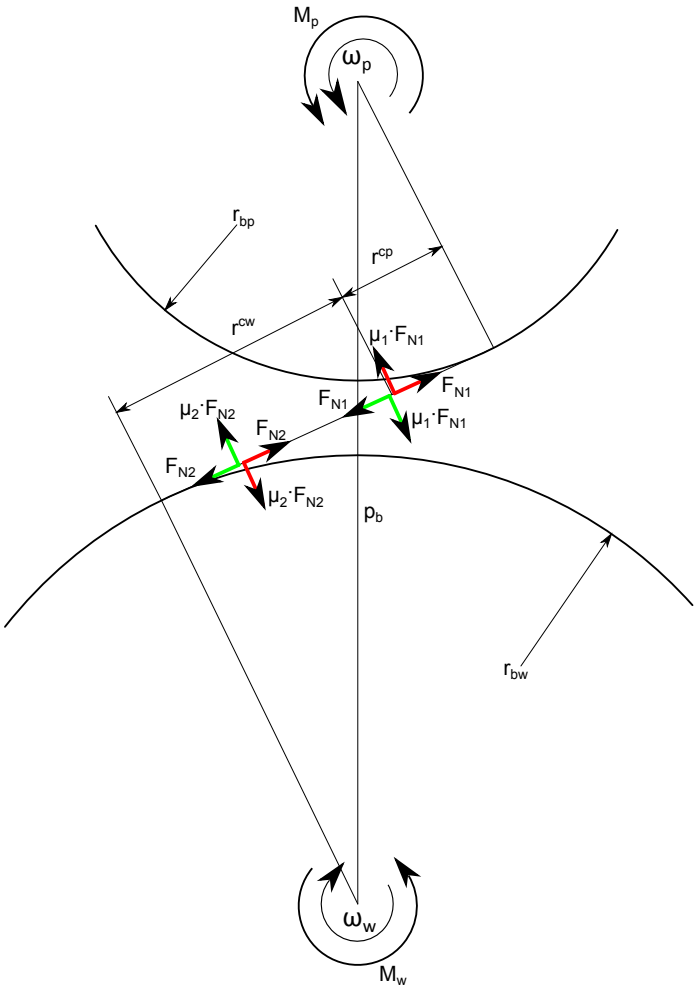

Figure 2.17.: Load balance for a spur gear pair including friction at two different instants.

$$\sum_{k=1}^{m}\sum_{j=1}^{n} F_{jk} - \left[\frac{M_w}{r_{bw}\cdot\cos(\beta_b)} - \sum_{k=1}^{m}\left(\sum_{j=1}^{n} F_{jk}\cdot\mu_{jk}\cdot\frac{v^g_{jk}}{|v^g_{jk}|}\cdot\frac{r^{cw}_{jk}}{r_{bw}} \right) \right] = 0 \tag{2.3.8}$$

Simplifying:

$$\sum_{k=1}^{m}\sum_{j=1}^{n} \left(F_{jk}\cdot\left(1+\mu_{jk}\cdot\frac{v^g_{jk}}{|v^g_{jk}|}\cdot\frac{r^{cw}_{jk}}{r_{bw}} \right) \right) - \frac{M_w}{r_{bw}\cdot\cos(\beta_b)} = 0 \tag{2.3.9}$$

Combining equations (2.3.5) and (2.3.9) the constrained expression for the elastic potential energy acting in the system is obtained as in equation (2.3.10). Note the Lagrange multiplier, λ, imposing the balance conditions through equation (2.3.9).

$$I(F_{11},...,F_{nm},\lambda) = \sum_{k=1}^{m}\left[\frac{1}{2}\sum_{i=1}^{n}F_{ik}\left(\sum_{j=1}^{n}\left(a_{ijk}^{p}+a_{ijk}^{w}\right)F_{jk}\right)\right]+ \\ \lambda\cdot\left[\sum_{k=1}^{m}\sum_{j=1}^{n}\left(F_{jk}\cdot\left(1+\mu_{jk}\cdot\frac{v_{jk}^{g}}{|v_{jk}^{g}|}\cdot\frac{r_{jk}^{cw}}{r_{bw}}\right)\right)-\frac{M_w}{r_{bw}\cdot\cos(\beta_b)}\right] \tag{2.3.10}$$

Considering,

$$[a] = [a^p + a^w] \tag{2.3.11}$$

and simplifying:

$$I(F_{11},...,F_{nm},\lambda) = \sum_{k=1}^{m}\left[\frac{1}{2}\sum_{i=1}^{n}F_{ik}\left(\sum_{j=1}^{n}a_{ijk}F_{jk}\right)\right]+ \\ \lambda\cdot\left[\sum_{k=1}^{m}\sum_{j=1}^{n}\left(F_{jk}\cdot\left(1+\mu_{jk}\cdot\frac{v_{jk}^{g}}{|v_{jk}^{g}|}\cdot\frac{r_{jk}^{cw}}{r_{bw}}\right)\right)-\frac{M_w}{r_{bw}\cdot\cos(\beta_b)}\right] \tag{2.3.12}$$

The distribution of the load over the teeth in a certain mesh instant is the one that minimizes the total energy of the system, equation (2.3.12). The simultaneous system of equations. (2.3.13) allows the calculation of the minimum.

$$\begin{cases} \frac{\partial I(F_{11},...,F_{nm},\lambda)}{\partial F_{11}} = 0 \\ \vdots \\ \frac{\partial I(F_{11},...,F_{nm},\lambda)}{\partial F_{nm}} = 0 \\ \frac{\partial I(F_{11},...,F_{nm},\lambda)}{\partial \lambda} = 0 \end{cases} \tag{2.3.13}$$

Expanding equation (2.3.13) the simultaneous system of equations (2.3.14) is obtained.

$$\begin{cases} \frac{1}{2}\left[\sum_{i=1}^{n} F_{i1}\left(a_{i11}+a_{1i1}\right)\right]+ \\ \lambda\cdot\left[\left(1+\mu_{j11}\cdot\frac{v_{g11}}{|v_{g11}|}\cdot\frac{r_{jk}^{cw}}{r_{bw}}\right)\right]=0 \\ \vdots \\ \frac{1}{2}\left[\sum_{i=1}^{n} F_{im}\left(a_{inm}+a_{nim}\right)\right]+ \\ \lambda\cdot\left[\left(1+\mu_{mn}\cdot\frac{v_{gnm}}{|v_{gnm}|}\cdot\frac{r_{jk}^{cw}}{r_{bw}}\right)\right]=0 \\ \\ \sum_{k=1}^{m}\sum_{j=1}^{n}\left(F_{jk}\cdot\left(1+\mu_{jk}\cdot\frac{v_{jk}^{g}}{|v_{jk}^{g}|}\cdot\frac{r_{jk}^{cw}}{r_{bw}}\right)\right)-\frac{M_w}{r_{bw}\cdot\cos(\beta_b)}=0 \end{cases} \tag{2.3.14}$$

Substituting $C = r_{bw}\cdot\cos(\beta_b)$ and $L_{jk} = 1+\mu_{jk}\cdot\frac{v_{jk}^{g}}{|v_{jk}^{g}|}\cdot\frac{r_{jk}^{cw}}{r_{bw}}$, equation (2.3.14) can be written in matrix form according to (2.3.15).

$$[K]\{F\}-\{\lambda\}=\{0\} \tag{2.3.15}$$

The detailed forms of K (compliance matrix), F (contact line forces) and λ (restrictions) are shown in equations (2.3.16) to (2.3.18).

$$\{F\}=\begin{bmatrix} F_{11} \\ \vdots \\ F_{n1} \\ F_{1k} \\ \vdots \\ F_{nk} \\ F_{1m} \\ \vdots \\ F_{nm} \\ \lambda \end{bmatrix} \tag{2.3.16}$$

$$\{\lambda\}=\begin{bmatrix} 0 \\ \vdots \\ 0 \\ 0 \\ \vdots \\ 0 \\ 0 \\ \vdots \\ 0 \\ \frac{M_w}{C} \end{bmatrix} \tag{2.3.17}$$

$$[K] = \frac{1}{2}\begin{bmatrix}
2a_{11} & \cdots & a_{1n1}+a_{n11} & 0 & \cdots \\
\vdots & a_{ij1}+a_{ji1} & \vdots & \vdots & 0 \\
a_{1n1}+a_{n11} & \cdots & 2a_{nn1} & 0 & \cdots \\
0 & \cdots & 0 & 2a_{11k} & \cdots \\
\vdots & 0 & \vdots & \vdots & a_{ijk}+a_{jik} \\
0 & \cdots & 0 & a_{1nk}+a_{n1k} & \cdots \\
0 & \cdots & 0 & 0 & \cdots \\
\vdots & 0 & \vdots & \vdots & 0 \\
0 & \cdots & 0 & 0 & \cdots \\
2L_{11} & \cdots & 2L_{n1} & 2L_{1k} & \cdots
\end{bmatrix}
\begin{bmatrix}
0 & 0 & \cdots & 0 & 2L_{11} \\
\vdots & \vdots & 0 & \vdots & \vdots \\
0 & 0 & \cdots & 0 & 2L_{n1} \\
a_{1nk}+a_{n1k} & 0 & \cdots & 0 & 2L_{1k} \\
\vdots & \vdots & 0 & \vdots & \vdots \\
2a_{nnk} & 0 & \cdots & 0 & 2L_{nk} \\
0 & 2a_{11m} & \cdots & a_{1nm}+a_{n1m} & 2L_{1m} \\
\vdots & \vdots & a_{ijm}+a_{jim} & \vdots & \vdots \\
0 & a_{1nm}+a_{n1m} & \cdots & 2a_{nnm} & 2L_{nm} \\
2L_{1k} & 2L_{1m} & \cdots & 2L_{nm} & 0
\end{bmatrix} \tag{2.3.18}$$

This linear simultaneous system of equations will lead to the determination of loads which are not only in the plane of action but also perpendicular to the lines of contact. These can be viewed as the result of the integral of a line load over a length. Since, the dynamic effects were disregarded, solving the simultaneous (2.3.15) for a fixed number of points along the path of contact (scanning type simulation) leads to the load distribution. The Lagrange multiplier is an indication of the displacement due to the load and if a unit load ($M_w/C = 1$) is applied the mesh stiffness function can be obtained.

The flexibility coefficients a_i were obtained using the opensource FEM code Elmer-Fem [95]. More details about the FEM implementation can be found in subsection 2.3.1.

Local coefficient of friction (calculation procedure)

The quasi-static load distribution model that was presented in this section can be used in conjunction with a proper coefficient of friction formulation (COF) to calculate the load distribution affected by a locally defined COF. Since the COF is dependent on the load distribution and vice versa, this problem must be solved using a scheme based on iterations. A constant COF (eg. $\mu = 0.05$) is first imposed and the load distribution is calculated based on that COF, then the local COF is

calculated using the previously calculated load distribution and this process goes on until convergence in both COF and load distribution is achieved (figure 2.18).

2.3.1. Some notes on the implementation of the model

A code was developed aiming to implement the formulations presented in this chapter. Figure 2.18 is a schematic of the implementation. Two external open source software routines used:

- *TetGen, A Quality Tetrahedral Mesh Generator and a 3D Delaunay Triangulator* [96]:

  TetGen is a program to generate tetrahedral meshes of any 3D polyhedral domains. TetGen generates exact constrained Delaunay tetrahedralizations, boundary conforming Delaunay meshes, and Voronoi partitions. [96]

- *ElmerFem* [95]:

  Elmer is an open source multiphysical simulation software mainly developed by CSC - IT Center for Science (CSC). Elmer development started 1995 in collaboration with Finnish Universities, research institutes and industry. After its open source publication in 2005, the use and development of Elmer has become international.

  Elmer includes physical models of fluid dynamics, structural mechanics, electromagnetics, heat transfer and acoustics, for example. These are described by partial differential equations which Elmer solves by the Finite Element Method (FEM). [95].

Elmer [95] was used (a custom *Matlab* code generates the *Elmer* solver input files) to obtain the compliance coefficients for the points that are in action during the meshing process. These compliance coefficients are then introduced in the Quasi-Static elastic model (section 2.3) and the load distribution as well was the mesh stiffness are obtained.

The program that was developed allows the modelling of helical and spur gears with wide design parameters, as it automatically generates the gear tooth geometry mesh (tetrahedral geometry).

One of the main challenges in this implementation was in fact the generation of the mesh for spur and helical tooth geometries, mainly the problem of triangulation in 3D space. If some thought is given to this problem it is not possible to directly triangulate in a cloud of points that belong to a concave solid and obtain a boundary surface that has concavities. The boundary of the solution will always be a convex surface in 3D space, and a gear tooth has concavities. The problem is then in defining the boundary surface of tooth mesh in 3D space. In 2D space a similar effect occurs for concave polygons.

By converting the 3D surface mesh in a 2D convex problem this issue could be solved. So the 3D triangulation problem was converted in a 2D problem. The solution

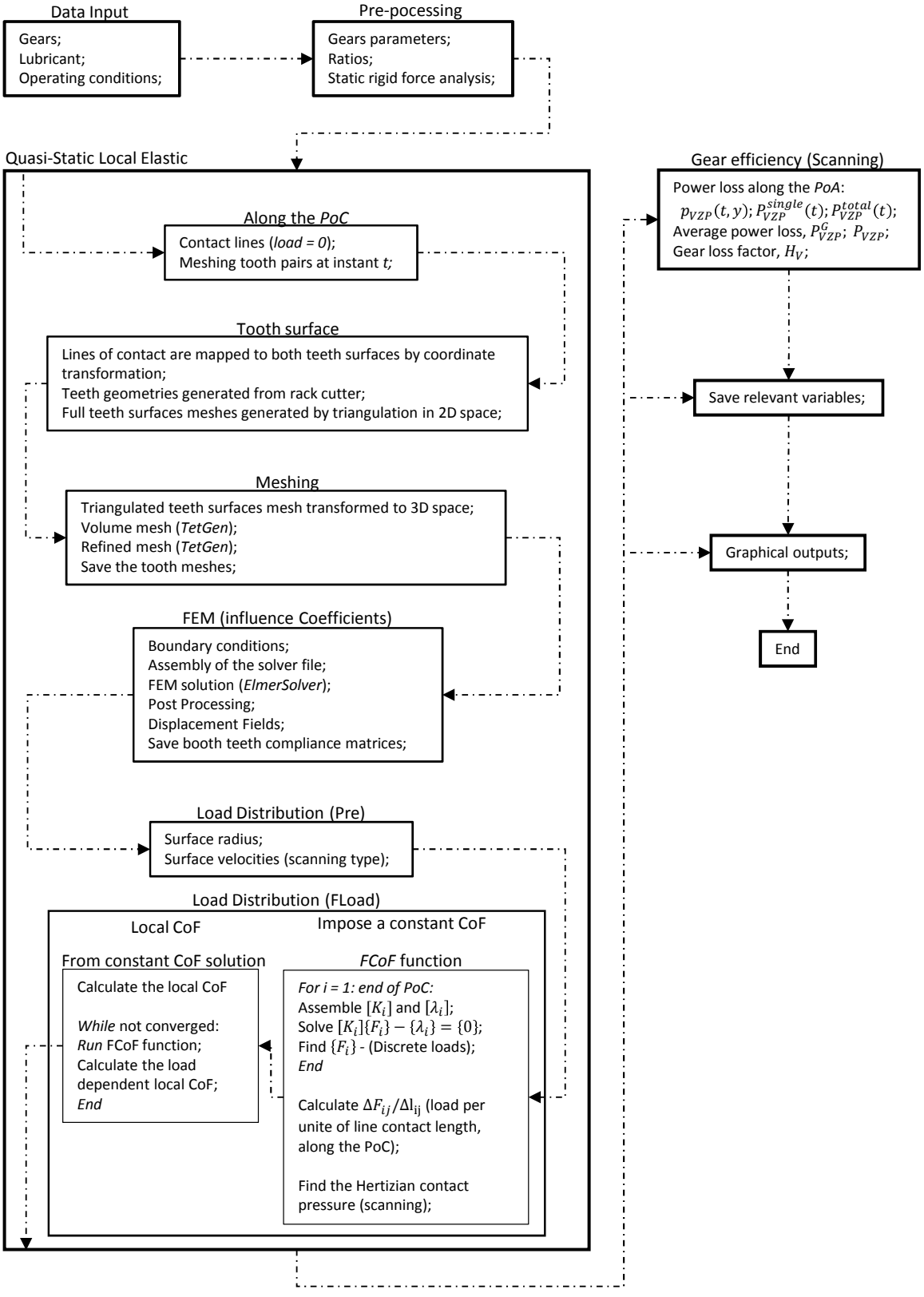

Figure 2.18.: Software implementation of the quasi-static power loss model.

that was found to the problem of gear tooth surface generation and meshing in 3D space is presented in Figure 2.19 and described below:

1. The gear teeth surface geometry is generated by a rack cutter according to the formulation proposed by Litvin *et al.* [97]. The lines of contact along the plane of action are defined at regular intervals.
2. The contact lines are mapped to the surface of the teeth. The points of the initial tooth geometry that are in the active area of the tooth are also replaced by the points that make up the lines of contact.
3. The combined points in 3D space define the 3D surface to triangulate. The 3D surface is unfolded and straightened to 2D space. Once defined in 2D space and the boundaries are convex the surface is easily triangulated with any 2D Delaunay triangulator.
4. The geometry is rebuilt in 3D space substituting the 2D coordinates by its original ones in 3D space while keeping the knowledge about the connections that make up the triangles.
5. The 3D tooth surface mesh is feed to *TetGen* [96] and the tooth mesh is obtained. The mesh is refined considering a set of rules which take into account (between others): element distortion, average element volume, rate at which the average element size increases away from the refined surface. It should be noted that the points of the original surface mesh are always kept in their original locations, so that the theoretical lines of contact are kept immaculate.
6. The points that participate in the boundary conditions are defined.(Fixed surface and unit loads along the points that make up the lines of contact).

2.3.2. Results

The model that was presented in this section has the capability of considering the frictional effects in the load distribution and mesh stiffness. The results here presented were obtained considering $\mu = 0$, $\mu = 0.1$ and the Xu [53] local CoF μ^{Xu}. As for the operating conditions the results were obtained considering an operating speed of 1200 rpm and torque of 477.78 Nm on the driving gear.

As previously stated the local CoF model that was implemented, $\mu^{Xu}(x, y)$ is the one that was suggested by Xu *et al.* [53]. A ISO VG 320 PAO oil at 80°C was considered. More details about this CoF formulation can be found in subsection 1.1.2.

The results presented in figure 2.20 show that the frictional effects have an impact in the load distribution which is quite noticeable at the point of reversal of the sliding velocity, the pitch point ($x_{pos} = 0$) specially for the C40 gears where a step or a slope can be observed. This step or slope is more pronounced in the case of $\mu = 0.1$. In the cases where $\mu = \mu^{Xu}(x, y)$ the pitch point transition is smoother mainly because $\mu = \mu^{Xu}(x, y) = 0$ when the sliding velocity is also zero. Due to the local nature of

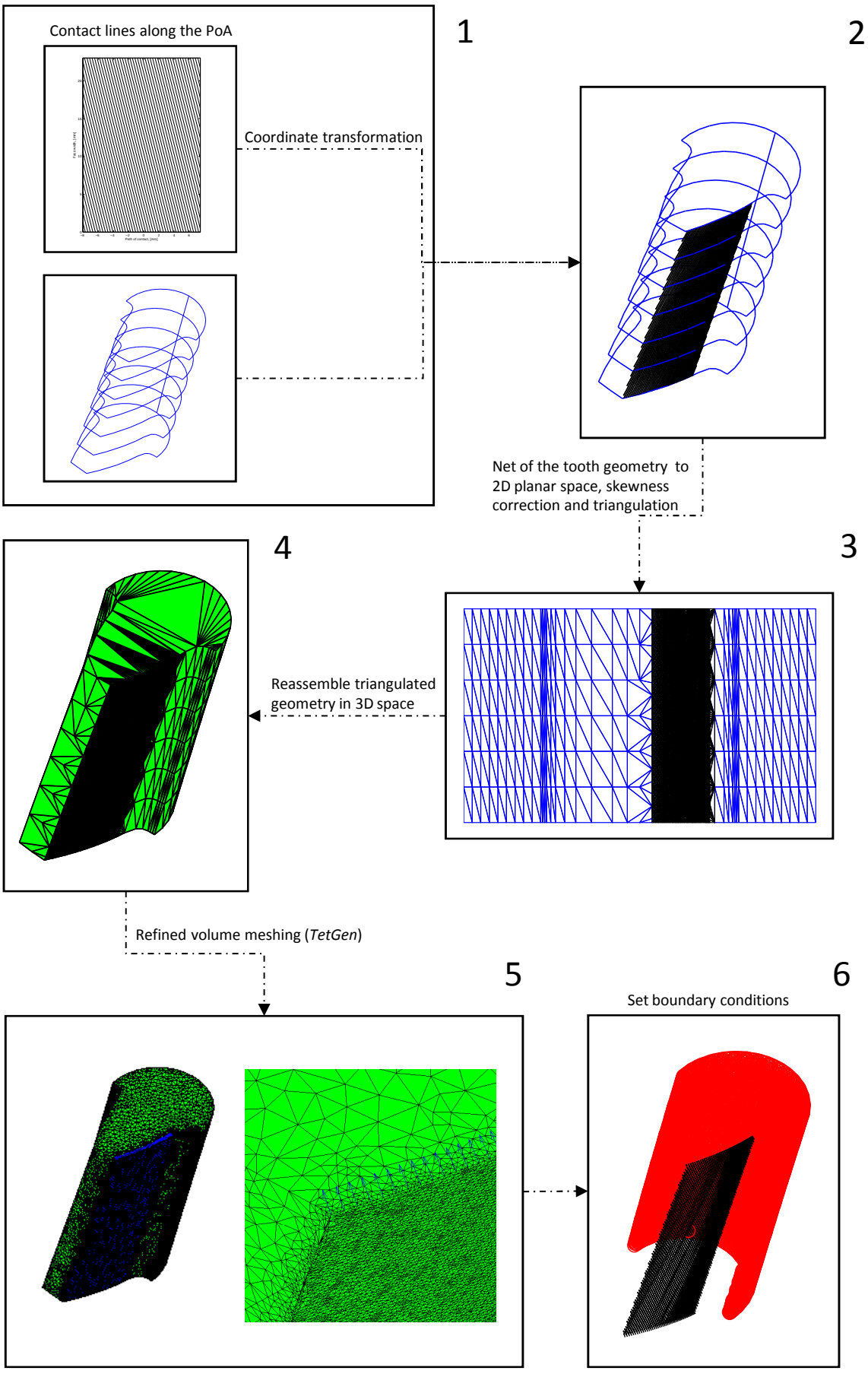

Figure 2.19.: Tooth mesh generation taking into account the lines of contact.

$\mu = \mu^{Xu}(x, y)$ it is believed that the "smoother slope evolution" at the vicinity of the pitch point is closer to reality (at least qualitatively) than the constant CoF approach ($\mu = 0.1$).The free edge effect in the load distribution can also be observed.

Comparing figure 2.20d with 2.20g it could be noted that the maximum load peaks occur at very different locations. These differences have to do with the nature the gears. In the H501 $\epsilon_\alpha > \epsilon_\beta$ and in the H951 $\epsilon_\alpha < \epsilon_\beta$. In the case of the H501 the maximum load peaks appear at the beginning of the meshing process while in the case of the H951 the peaks appear at the points where a contact line starts at the the edge of the tip of a tooth and finish at the line of active meshing near the tooth base.

In figures 2.21 the influence of the CoF in the total load distribution and mesh stiffness becomes more apparent. Once again the frictional effects are more important in the spur gear geometry in both load distribution and mesh stiffness (step like features appear at the pitch point).The modifications in both load distribution and mesh stiffness are more subtle in the helical gears (H501 and H951), nevertheless it should be noticed that the total load increases before the pitch point and decreases after it (also noticed in the C40 gear). The mesh stiffness is also slightly modified by frictional effects, specially in the case of the C40 gear in the vicinity of the pitch point (figure 2.21b).

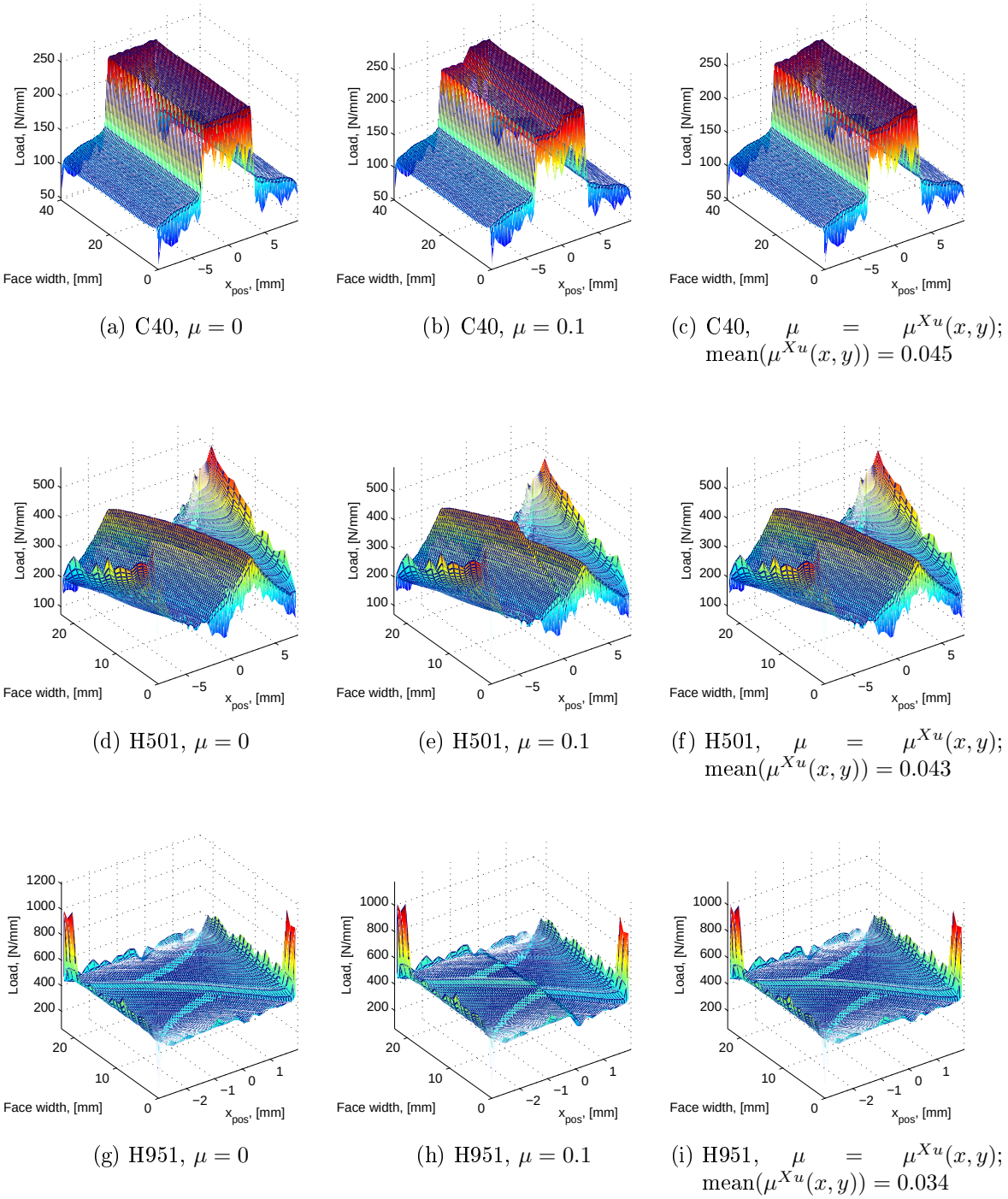

(a) C40, $\mu = 0$

(b) C40, $\mu = 0.1$

(c) C40, $\mu = \mu^{Xu}(x, y)$; $\text{mean}(\mu^{Xu}(x, y)) = 0.045$

(d) H501, $\mu = 0$

(e) H501, $\mu = 0.1$

(f) H501, $\mu = \mu^{Xu}(x, y)$; $\text{mean}(\mu^{Xu}(x, y)) = 0.043$

(g) H951, $\mu = 0$

(h) H951, $\mu = 0.1$

(i) H951, $\mu = \mu^{Xu}(x, y)$; $\text{mean}(\mu^{Xu}(x, y)) = 0.034$

Figure 2.20.: Load distribution (per unit of contact line length) considering different coefficients of friction for gears C40, H501 and H951.

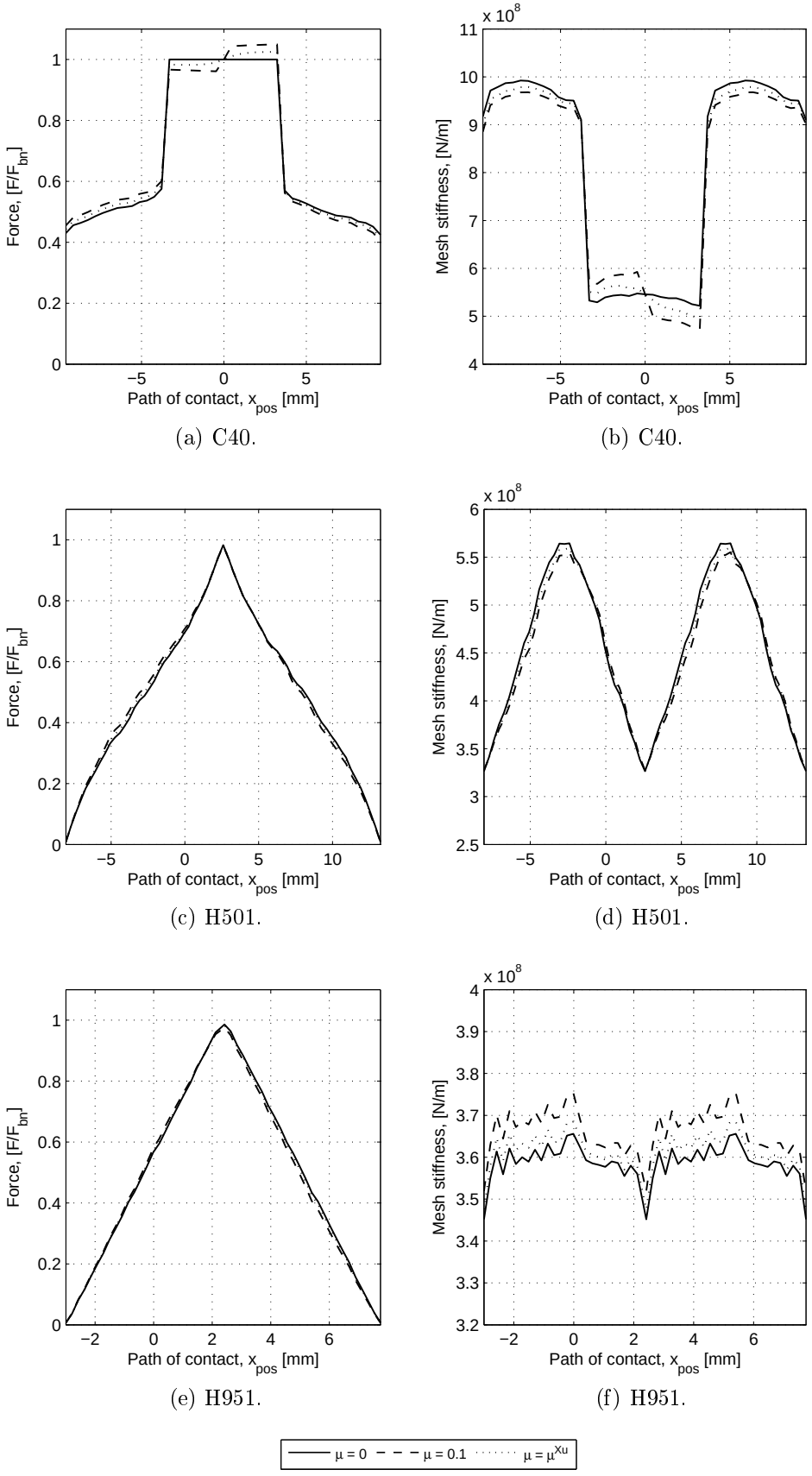

(a) C40. (b) C40.

(c) H501. (d) H501.

(e) H951. (f) H951.

Figure 2.21.: Load distribution and mesh stiffness obtained considering different coefficients of friction for gears C40, H501 and H951.

2.4. Load distribution models: comparison

In the beginning of this chapter a solution for the load distribution taking advantage of the properties of the Heaviside function was presented (quasi-static rigid model). This approach was purely geometrical and elastic effects were disregarded. Due to the disregarded effects the validity of this approach is debatable. Two elastic load distribution models were also presented. One of these models is an extension of the rigid model which takes advantage of the Heaviside functions and the single tooth stiffness (quasi-static elastic model). The other elastic model was based on the minimization of the constrained potential energy, frictional effects were also considered in the load distribution (quasi-static local elastic model).

The models suggested in sections 2.1 and 2.2 do not take into account frictional effects so in order to do a proper comparison, the CoF was imposed as $\mu \approx 0$ for the model that was proposed in section 2.3 (quasi-static local elastic model). The quasi-static rigid and elastic models both assume a constant load per unit of length in a single tooth pair while the quasi-static local elastic model does not make this assumption. Therefore in order to compare these three models the total load supported by a single tooth pair along the path of contact is considered.

The model that was presented in section 2.2 needs external inputs, namely the maximum single stiffness and α_k. Table 2.2 shows the values of K_{max} that were taken. These values were calculated according to ISO 6336-1 [94]. It was found that $\alpha_k = 4/5$ gave a good correlation between the model presented in section 2.2 and the quasi-static local elastic model (section 2.3).

The load distributions F_N/F_{bn} for the three models that were proposed were compared (figures 2.22). For the helical gears (H501 and H951) there is a very good agreement between all three models, however for the C40 spur gear the rigid model performs quite poorly while both elastic models are in agreement with each other.

In terms of mesh stiffness it can be observed that calculating the maximum single tooth stiffness suggested by ISO (Table 2.2) and imposing $\alpha_k = 4/5$ the analytical method $KL(\xi)$ to calculate the total mesh stiffness that was proposed works quite well giving results close to those obtained with the quasi-static local elastic model that was also developed.

Despite the limited number of cases that were studied the analytical elastic model $KL(\xi)$ (section 2.2) seems to be a good alternative to the quasi-static local elastic model if one is not interested in the load distribution along the gear face width (free edge effects and local properties) and frictional effects are to be disregarded.

Table 2.2.: Single pair stiffness according to ISO 6336-1 [94].

Gear	$\boldsymbol{K_{max}^{ISO}}$ [N/m]
C40	5.0483×10^8
H501	3.0923×10^8
H951	3.6293×10^8

The $KL(\xi)$ model also runs several orders of magnitude faster that the quasi-static local elastic model and it is also much easier to implement. The computational and implementation costs of the rigid model over the $KL(\xi)$ model are almost the same therefore $KL(\xi)$ presents by far the best benefit/cost ratio of the three models that were presented.

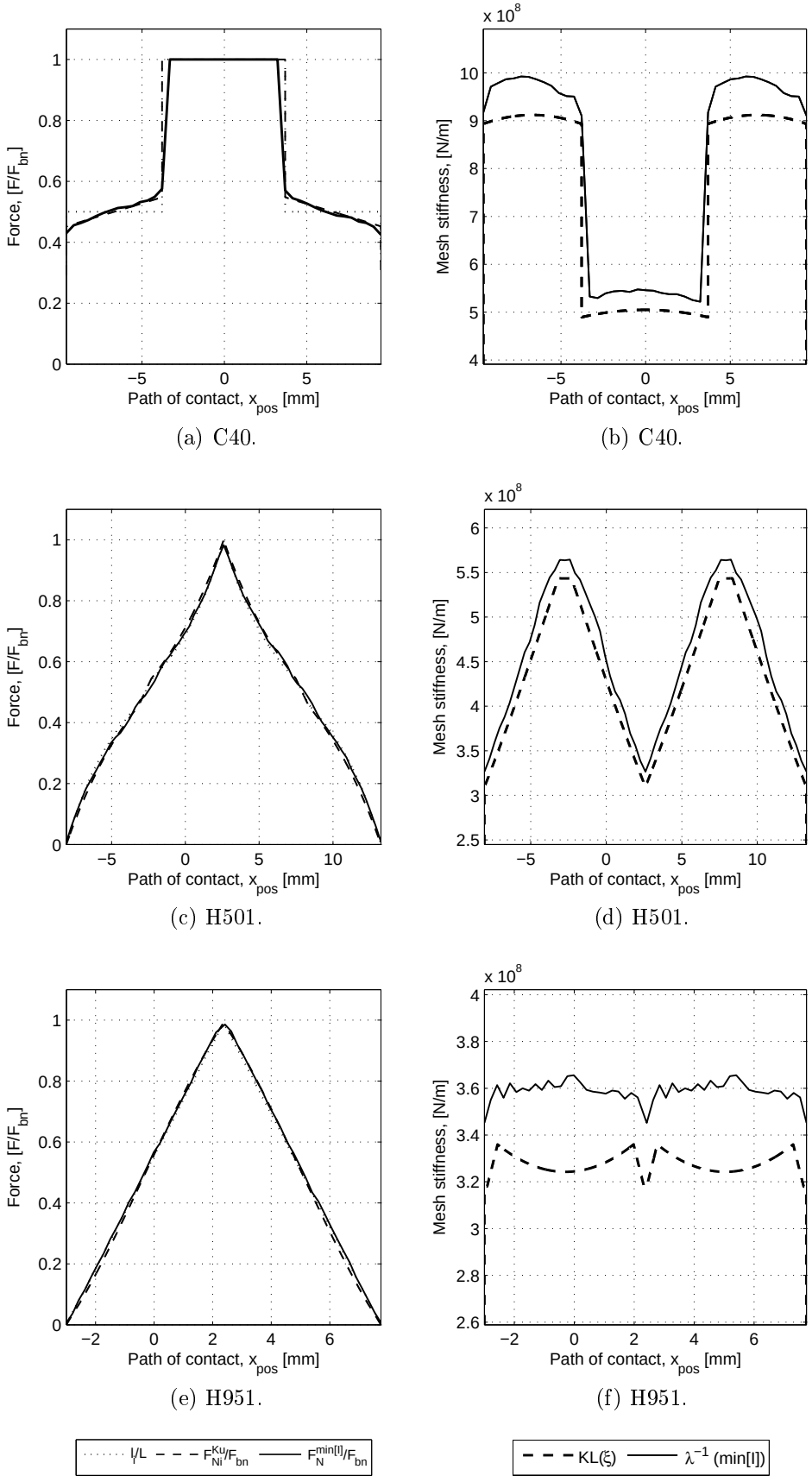

(a) C40. (b) C40.

(c) H501. (d) H501.

(e) H951. (f) H951.

Figure 2.22.: Load sharing and mesh stiffness according to the different models, ($i = 0$, $\mu = 0$, $\alpha_k = 4/5$, $K_{max} = K_{max}^{ISO}$) for gears C40, H501 and H951.

2.5. Power loss in cylindrical gears

In this section a general approach to gear power loss and its application to different cases are presented for the purpose of demonstration. The gear loss factor H_V calculated with the load distribution obtained from the quasi-static local elastic model is compared with some gear loss factors presented in the literature (subsection 1.1.1).

2.5.1. General power loss formulation

The sliding power loss per unit of gear face width between meshing gear tooth can be calculated according to equation (2.5.1). This equation considers a Coulomb friction model (the friction force is the normal force, $F_N(t,y)$, multiplied by a coefficient, $\mu(t,y)$ and the result is then integrated over the tooth face width, b, to obtain the power loss along the path of contact for a single tooth mesh which is described here by equation (2.5.2).

$$p_{VZP}(t,y) = F_N(t,y) \cdot \mu(t,y) \cdot v_g(t,y) \tag{2.5.1}$$

$$P_{VZP}^{single}(t) = \int_0^b \left[F_N(t,y) \cdot \mu(t,y) \cdot v_g(t,y)\right] dy \tag{2.5.2}$$

Since there can be multiple pairs of teeth in contact along the meshing line the total power loss is calculated according to (2.5.4) by superposition of the functions described by equation (2.5.2). These functions are at a distance of p_{bt} or a mesh period (T^{mesh}) from each other. If the function that describes the total power loss along the path of contact (equation (2.5.4)) is integrated for a mesh period T^{mesh} over this same path, the total energy that is dissipated is obtained. Divide this energy by the mesh period and the average power loss is obtained (equation (2.5.5)). The mesh period is given by (2.5.3), where z is the number of teeth and ω is the rotational frequency of gear i in rads/s.

$$T^{mesh} = \frac{2\pi}{\omega_i \cdot z_i} \tag{2.5.3}$$

$$P_{VZP}^{total}(t) = \sum_{i=-floor(\epsilon_\alpha+\epsilon_\beta)}^{floor(\epsilon_\alpha+\epsilon_\beta)} P_{VZP}^{single}(t - i \cdot T^{mesh}) \tag{2.5.4}$$

$$P_{VZP}^{G} = \frac{\int_{0}^{T^{mesh}} P_{VZP}^{total}(t)}{T^{mesh}} \tag{2.5.5}$$

The formulation above presented is general to spur and helical gears can be used to calculate the average power loss considering a time and space varying load distribution, CoF and sliding velocity.

Considering the classical P_{VZP} formulation (1.1.1) a gear loss factor can be defined as shown in equation (2.5.6). It should be noted that equation (2.5.6) should only be applied to situations when the CoF is assumed to be constant along the plane of action.

$$H_{V}^{G} = \frac{P_{VZP}^{G}}{P_{IN} \cdot \mu_{mz}} \tag{2.5.6}$$

2.5.2. A remark on different coordinate systems and mesh time

In this section the power loss is specified as a function of the meshing time t. However in section 2.1.2 a coordinate system ξ was defined according to figure 2.5. The relation between t and ξ is straight forward. In fact, from the definition of ξ, p_{bt} and the involute property of the gears the relation between t and ξ is direct as shown by equation (2.5.7).

$$t(\xi) = \xi \cdot T^{mesh} \tag{2.5.7}$$

The results from the quasi-static full compliance elastic model (section 2.3) are given in distance along the path of contact centred at the pitch point, (x_{pos} coordinates). The relation between ξ and the just described coordinate system is given by equation (2.5.8).

$$x_{pos}(\xi) = (\xi - \epsilon_1) \cdot p_{bt} \tag{2.5.8}$$

Given the relation expressed in equation (2.5.7) and solving (2.5.8) to find ξ, $t(x_{pos})$ is given by equation (2.5.9).

$$t(x_{pos}) = \left[\frac{x_{pos}}{p_{bt}} + \epsilon_1 \right] \cdot T^{mesh} \tag{2.5.9}$$

2.5.3. Results

The goal with this section was not to study the quasi static power loss or the average power loss itself, but rather to present the results of application of a general approach to study of the power loss along the path of contact and the average power loss. This methodology is here referred as a general approach because all the quantities in equation (2.5.1) can be taken locally as shown in figures 2.23 to 2.26.

Figures 2.23 to 2.25 show the load distribution, Hertzian pressure, sliding velocity, coefficient of friction and power loss per unit of length for the gear geometries presented in table 2.1. These results were obtained considering a speed of 1200 rpm and a torque of 477.78 Nm at the driving gear. The lubricant that was selected was a wind turbine gear oil, ISO VG 320 PAO based lubricant (PAOR, table 4.3) at 80 °C.

Figures 2.26 show the power loss along the path of contact considering the results presented in figures 2.23 to 2.25.

The average power loss P^G_{VZP} (2.5.5) was calculated for the selected operating conditions and CoF formulation and the average power loss results are presented in table 2.3.

Table 2.3.: Average power loss P^G_{VZP} calculated according to equation (2.5.5).

Gear:	**C40**	**H501**	**H951**
$\boldsymbol{P^G_{VZP}}$ [W]	552.8	481.7	172.5

These results come in line with what was already known for the C40, $H501$ and H951 gear geometries. The C40 and H501 gears promote much higher power loss than the H951 gear. The reason for this is that the H951 has a much shorter path of contact which promotes lower sliding velocities at the same input speed as observed in figures 2.23c, 2.24c and 2.25c.

2.5.4. Gear loss factor

The gear loss factor H_V, is dependent of the gear geometry and load conditions and it's an indicator of the efficiency associated to a certain gear despite the working conditions, the transmitted power and the lubricant used.

The gear loss factor concept presented in equation (2.5.6) should only be applied in situations where the CoF is assumed to be constant along the plane of action. The load distribution model that was presented in section 2.3 considers frictional and elastic effects in the load distribution. This indicates that for different CoF values different load distributions will be obtained. The gear loss factor H^G_V (2.5.6) was then calculated considering different values for μ_{mz}. Table 2.4 shows the results that were obtained considering three different CoF values. The load distribution will be dependent of the CoF, therefore the gear loss factor will be modified.

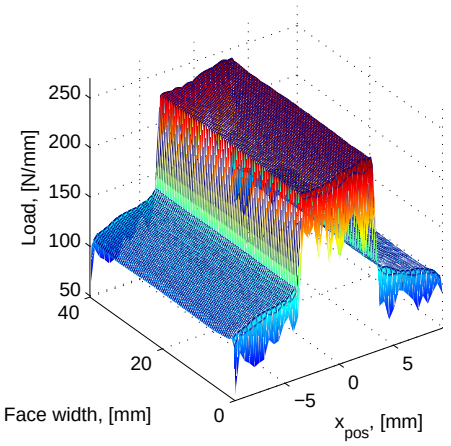

(a) Load per unit of line length, $f_N(x, y)$.

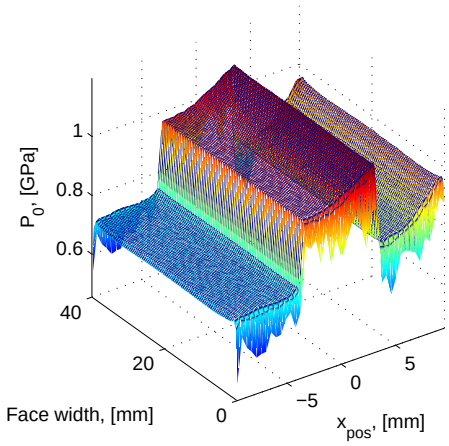

(b) Hertzian pressure, P_0.

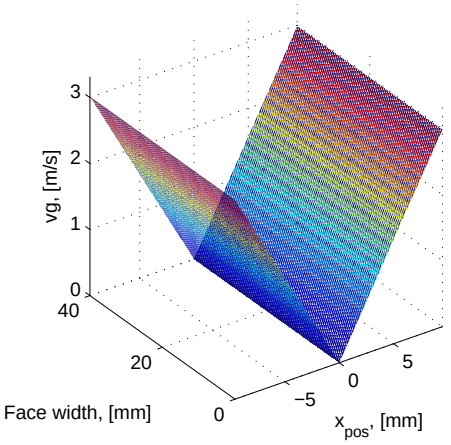

(c) Sliding velocity, V_g.

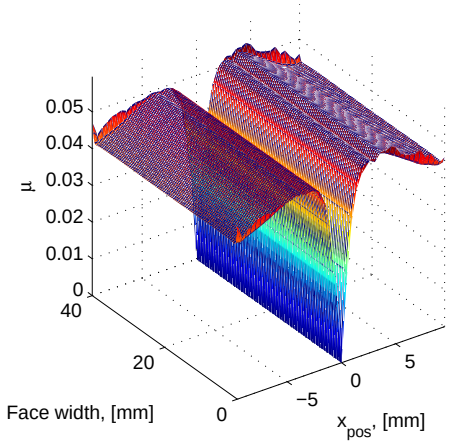

(d) Coefficient of friction, $\mu^{Xu}(x, y)$.

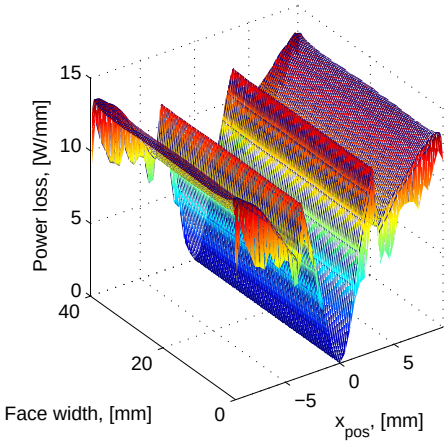

(e) Power loss per unit of line length, $p_{VZP}(x, y)$.

Figure 2.23.: Local power loss $p_{VZP}(x, y)$ and local quantities involved (1200rpm, 477.78Nm at driving gear) - C40.

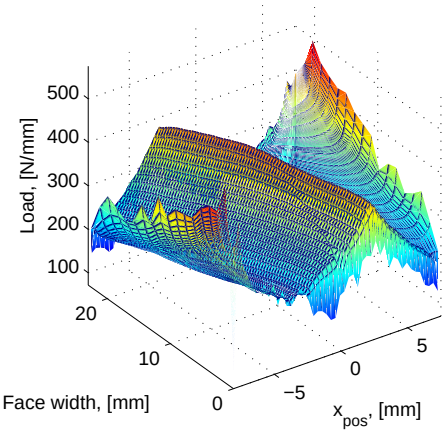

(a) Load per unit of line length, $f_N(x, y)$.

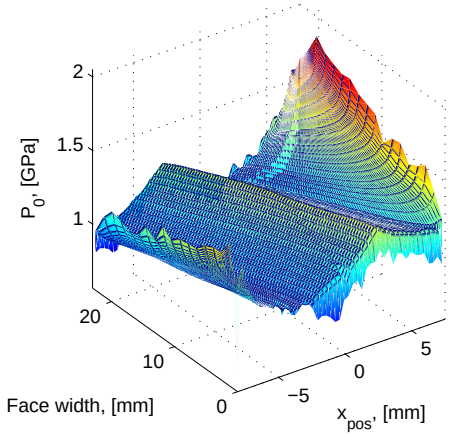

(b) Hertzian pressure, P_0.

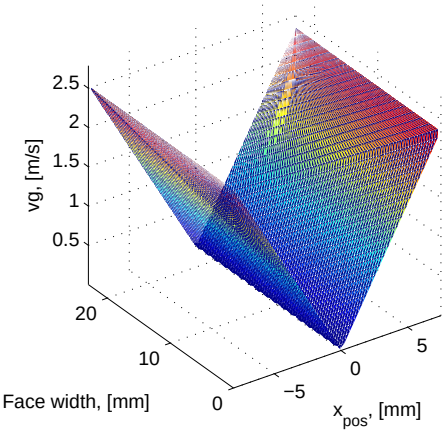

(c) Sliding velocity, V_g.

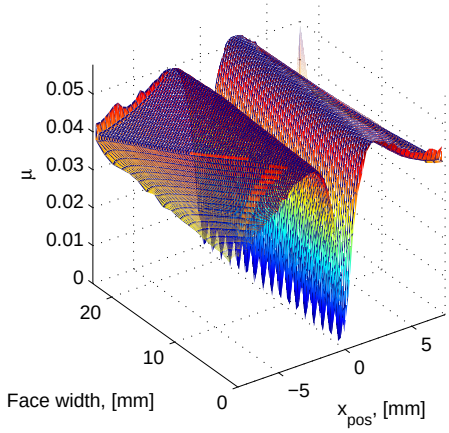

(d) Coefficient of friction, $\mu^{Xu}(x, y)$,

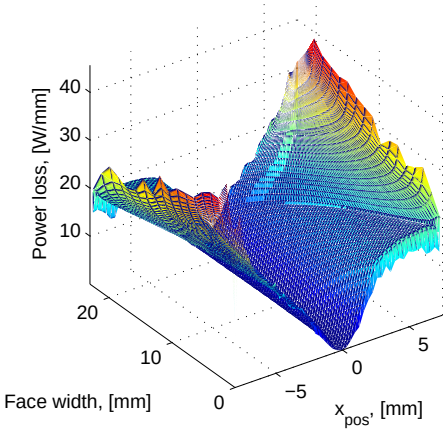

(e) Power loss per unit of line length, $p_{VZP}(x, y)$.

Figure 2.24.: Local power loss $p_{VZP}(x, y)$ and local quantities involved (1200rpm, 477.78Nm at driving gear) - H501.

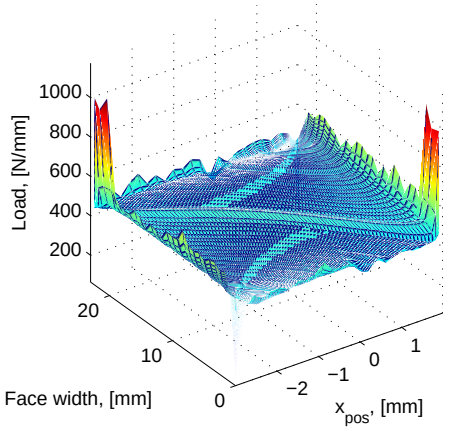

(a) Load per unit of line length, $f_N(x, y)$.

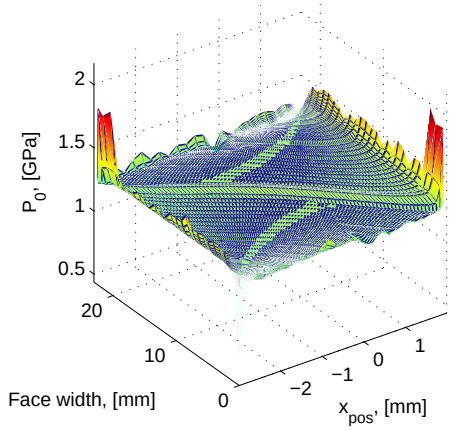

(b) Hertzian pressure, P_0.

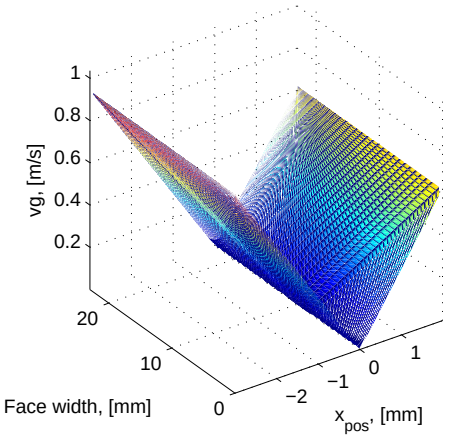

(c) Sliding velocity, V_g.

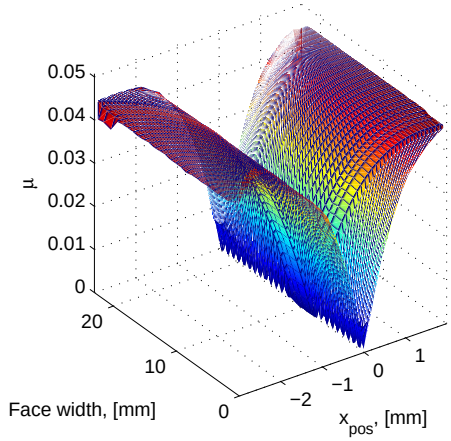

(d) Coefficient of friction, $\mu^{Xu}(x, y)$.

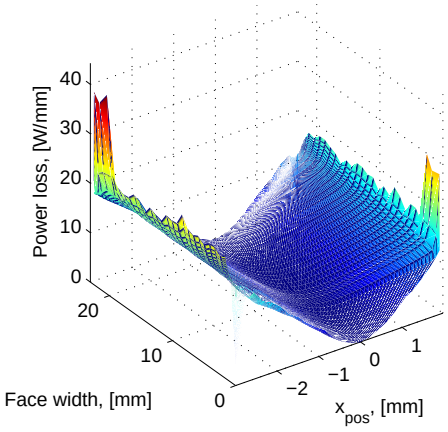

(e) Power loss per unit of line length, $p_{VZP}(x, y)$.

Figure 2.25.: Local power loss $p_{VZP}(x, y)$ and local quantities involved (1200rpm, 477.78Nm at driving gear) - H951.

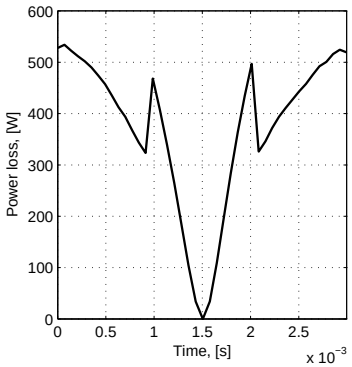

(a) $P_{VZP}^{single}(t)$ - C40.

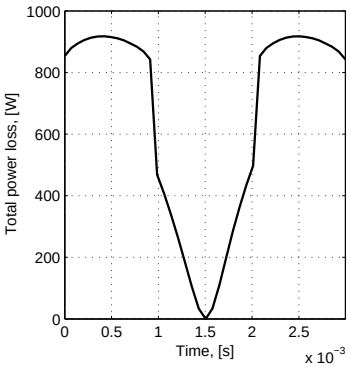

(b) $P_{VZP}^{total}(t)$ - C40.

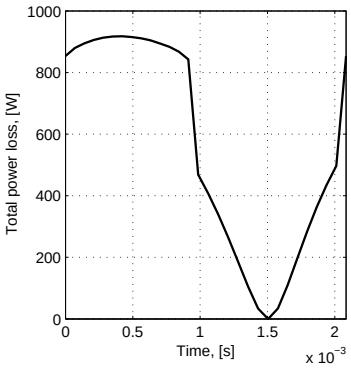

(c) $P_{VZP}^{total}(0:t:T^{mesh})$ - C40.

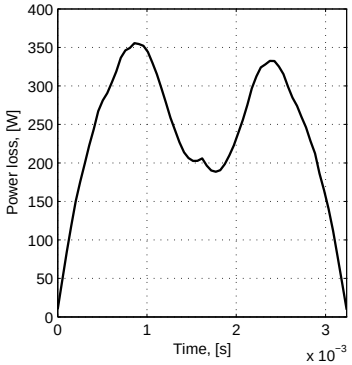

(d) $P_{VZP}^{single}(t)$ - H501.

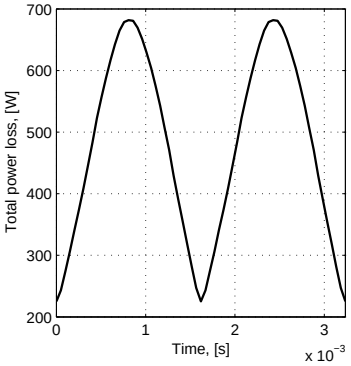

(e) $P_{VZP}^{total}(t)$ - H501.

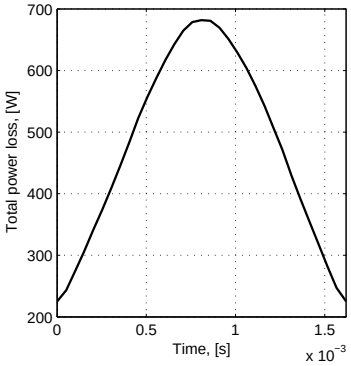

(f) $P_{VZP}^{total}(0:t:T^{mesh})$ - H501.

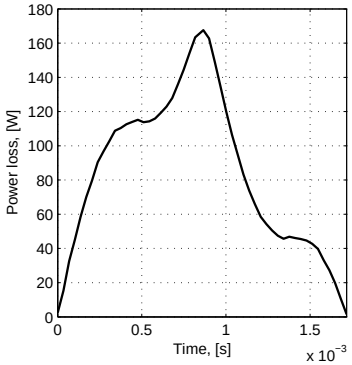

(g) $P_{VZP}^{single}(t)$ - H951.

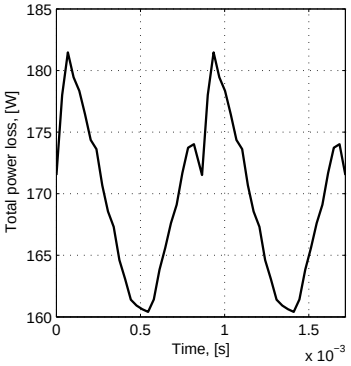

(h) $P_{VZP}^{total}(t)$ - H951.

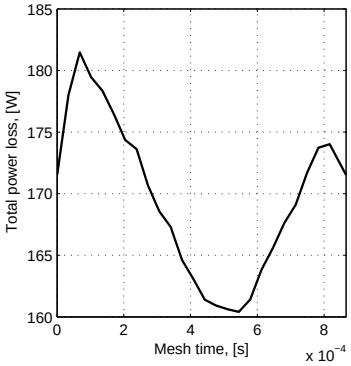

(i) $P_{VZP}^{total}(0:t:T^{mesh})$ - H951.

Figure 2.26.: Power loss for gears C40, H501 and H951.

Table 2.4.: Gear loss factor considering rigid and elastic load sharing and constant friction.

H_V	C40	Δ [%]	H501	Δ [%]	H951	Δ [%]
Rigid [84]	0.1949	-	0.1873	-	0.0684	-
Ohlendorf [30]	0.1949	0	0.1639	−12.5	0.0739	8.0
H_V^G, **QSLEM** ($\mu = 0$)	0.1969	1.0	0.1853	−1.1	0.0705	2.9
H_V^G, **QSLEM** ($\mu = 0.05$)	0.1978	1.5	0.1858	−0.8	0.0705	3.0
H_V^G, **QSLEM**($\mu = 0.1$)	0.1987	1.9	0.1862	−0.6	0.0706	3.2

QSLEM: quasi-static local elastic model.

In a series of very recent papers *Fernandes et al.* [1–3, 21] presented a complete methodology for the estimation of gear box power loss. Schlenk's [48] CoF formulation was used to estimate the gear friction losses. In fact the lubricant factor X_L (1.1.14) was estimated from power loss tests in the FZG test rig for different oils at varying operating conditions [2, 21] (loads and speeds). The gear frictional losses were calculated by subtracting the measured no-load loss and estimated rolling bearing losses to the total measured power loss [2]. The gear friction losses were then known and the gear loss factor was numerically calculated [84], so equation (1.1.1) can be used to estimate the average CoF, μ_{mz}, in that particular operating condition. This was done for different operating conditions so that a lubricant parameter X_L (1.1.14) could be optimized for each lubricant.

In the aforementioned works it was evident that in order to have a good gear power loss estimation a good gear loss factor formulation is needed because it will not only influence the values of the calibrated lubricant parameter X_L (1.1.14), but also directly the estimation of the gear losses for other gear geometries through the gear loss factor itself and also X_L. In fact in other work Fernandes *et al.* [84] showed different gear loss factor formulations give very different results.

The results presented in table 2.4 indicate that frictional and elastic effects have an impact in the load distribution which will yield a variation in the estimated average CoF μ_{mz} and by consequence in the lubricant factor X_L. This by no means indicates that the approach introduced by Fernandes *et al.* [2] is wrong or that it should not be used, it means that despite the excellent results obtained in [2, 3, 21] there is still room for improvement.

2.6. Closure

This chapter dealt with the load distribution problem including frictional effects in spur and helical gears, as well as a generalized approach to power loss estimation. Three different, yet simple load distribution models, were proposed from the rigid tooth approach to the elastic solution including friction. A generalized power loss formulation was also presented.

The results obtained with the elastic models (load distribution and mesh stiffness) were in agreement with each other when $\mu = 0$.

The most advanced of the models considered the frictional effects in the load balance, so that modifications in the load distribution and mesh stiffness were observed due to friction (in the load distribution per unit of length the free edge effects were also observed). The frictional and elastic effects were clearly visible in results obtained for the spur gears, where a step could be observed at the pitch point in the case of constant CoF formulation. When the local CoF was considered the transition was done smoothly without sudden steps, but a slope was still observed. In the case of helical gears the frictional effects seem to play a lesser role in the load distribution even when the constant CoF is considered.

From the generalized gear power loss approach an average power loss and gear loss factors could be calculated. The differences that were observed in the gear loss factors (rigid vs elastic+friciton) can be relevant depending on the accuracy and refinement of the desired power loss prediction. The calibration of the lubricant factor X_L that is used in Schlenk's *et al.* [48] average COF formulation can be done according to the methodology proposed by Fernandes *et al.* [2]. In this methodology an accurate gear loss factor is a fundamental piece in finding accurate X_L values and power loss estimations.

In subsection 2.3.2 and section 2.4 some figures (2.21 and 2.22) with the mesh stiffness along the path of contact considering different methods and CoF formulations were presented. Regardless of the similarity of the results yielded by the proposed models something else should be noted: The mesh stiffness evolution along the path of contact appears to vary with gear geometry and frictional effects. Mesh stiffness variations are known to be one of the main sources for gear dynamic excitations. The main variations in the mesh stiffness occur due to the transitions between meshing cycles. It was also demonstrated that frictional effects have the potential to modify the mesh stiffness, specially in the case of spur gears.

In this chapter the studies were done considering a quasi-static approach. The consideration of inertia effects and mesh stiffness induced excitations in the behaviour of a gear system will lead to a time varying total normal load along the path of contact, even at stationary conditions. The local CoF formulation proposed by Xu [53] (equations (1.1.17) to (1.1.18)) μ^{Xu}, which was demonstrated to replicate experimental results quite well, depends of the local load in a non-linear fashion. Since the local CoF is dependent of the local load and the local load varies with the dynamic total normal force it follows that the combination of both of the effects may introduce variations in the estimated average power loss comparing with the quasi-static power loss model assumption.

3. Developments for a Gear Pair: Gear Dynamics and Power Loss

Chapter 2 was dedicated to the study of the influence of the load distribution and elastic effects on gear power loss [15, 16]. Three load distribution models were presented, a quasi-static rigid, a quasi-static elastic model and a quasi-static local elastic model. The quasi-static elastic load distribution model [15, 16] also allowed to obtain the mesh stiffness function including frictional effects. It was verified that both tooth pair transition and frictional effects introduced important variations in the aforementioned mesh stiffness. In fact it is well known [25] that mesh stiffness variations are one of the main causes of gear noise and vibration.

Many machines have a motor that rotates at fixed speed or in a range of speeds that is not the desired one. In many situations in order to overcome these issues gear transmissions are used. Optimizing gearbox efficiency in statically loaded conditions is a step in the right direction, but it is also important to understand what happens when the gears are rotating since dynamic effects can often be a determining factor in the gearbox load carrying capacity. Detailed gearbox efficiency estimations in quasi-static and dynamic conditions can lead to the design of more reliable and efficient gearboxes, which can save resources not only during development, but also through the gearbox's expected life [98].

In previous works [25] several authors have dealt with the problem of gear dynamics. The main innovations in gear dynamics were mainly in the detail of the dynamic models (more degrees of freedom, varying mesh stiffness and frictional, gyroscopic, rocking effects...). In those works the main focus was usually in the dynamic overloads, critical speeds, transmission errors and gear noise [99–102]. Özgüven *et al.* [25] made a very comprehensive analysis and categorization of the existing gear dynamic models.

According to Özgüven *et al.* [25] it is possible to group the mathematical models developed in gear dynamics in the following way:

1. Simple dynamic factor models: This group includes most of the early studies in which a dynamic factor that can be used in gear root stress formulae is determined. These studies include empirical and semi-empirical approaches as well as recent dynamic models constructed just for the determination of a dynamic factor.

2. Models with tooth compliance: There is a very large number of studies which include only the tooth stiffness as the potential energy storing element in the system. That is, the flexibility (torsional and/or transverse) of shafts, bearings,

etc, are all neglected. In such studies the system is usually modelled as a single degree of freedom spring-mass system. There is an overlap between the first group and this group since such simple models are sometimes developed for the sole purpose of determining the dynamic factor.

3. Models for Gear Dynamics: Such models include the flexibility of the other elements as well as the tooth compliance. Of particular interest have been the torsional flexibility of shafts and the lateral flexibility of the bearings and shafts along the line of action.

4. Models of Geared Rotor Dynamics: In some studies, the transverse vibrations of a gear-carrying shaft are considered in two mutually perpendicular directions, thus allowing the shaft whirl. In such models, the torsional vibration of the system is usually considered.

5. Models for Torsional Vibrations: The models in the third and fourth groups consider the flexibility of the gear teeth by including a constant or time varying mesh stiffness in the model. However, there is also a group of studies in which the flexibility of gear teeth is neglected and a torsional model of a geared system is constructed by using torsionally flexible shafts connected with rigid gears. The studies in this group may be viewed as pure torsional vibration problems, rather than gear dynamics problems.

As previously referenced, there not seem to be many studies around gear efficiency including dynamic effects. In this chapter a four degree of freedom (DoF) lumped mass torsional model that takes into account damping and frictional effects was deduced from the Principle of Least Action. The main focus here was not the dynamic analysis, but rather the influence of gear tooth geometry and dynamics in gear power loss. Three different geometries, a spur and two helical gears that were studied in previous works [1, 2, 21], were analysed under different operating conditions and two coefficient of friction approaches. The average power loss in dynamic stabilized conditions is compared to the one predicted using the classical methods presented in references [2, 22, 28] as well as in chapters 1 and 2.

3.1. Model formulation

In this section the proposed lumped mass model for gear dynamics is presented. This model includes gear tooth friction, damping in shafts and between meshing teeth as well as shaft stiffness.

The damping coefficients are considered constant and frictional effects are taken into account in the time varying mesh stiffness. The mesh stiffness including friction effects was calculated from the elastic load distribution model previously introduced [15, 16].

According to L. Landau [103] if one let any system occupy, at instants t_1 and t_2, positions defined by two sets of values of the co-ordinates θ_1 and θ_2 then the condition is that the system moves between these positions in such a way that the

integral (3.1.1) takes the least possible value, (L is the action). This is the Principle of Least Action.

$$S = \int_{t_1}^{t_2} L(\theta, \dot{\theta}, t)dt \tag{3.1.1}$$

Taking the variation of θ it is possible to show that equation (3.1.1) is minimized for a system of multiple particles if the differential equation (3.1.2) is satisfied.

$$\frac{d}{dt}\left(\frac{\partial L}{\partial \dot{\theta}}\right) - \frac{\partial L}{\partial \theta} = 0 \tag{3.1.2}$$

The previous approach does not directly consider the work of non-conservative forces. Hamilton's principle (equation (3.1.3)) is more general and it is usually used in the establishment of the equations of motion of any system.

$$\int_{t1}^{t2} \delta(T - V)dt + \int_{t1}^{t2} \delta W_{nc}dt = 0 \tag{3.1.3}$$

In equation (3.1.3) T is the kinetic energy, V is the potential energy of deformation and position and W_{nc} is the work done by non-conservative forces, (external and dissipation forces). δ is the variation taken between t_1 and t_2.

Admitting that the kinetic energy is a function of the generalized coordinates θ_i and its derivatives $\dot{\theta}_i$ it becomes that $T = T(\theta_{1:n}, \dot{\theta}_{1:n})$. Assuming that the potential energy is a function of the generalized coordinates, it becomes $V = V(\theta_{1:n})$. The variation of the work of the non-conservative forces is simply $\delta W_{nc} = \sum_{i=1}^{n} Q_i \delta\theta_i$ where Q_i are the generalized forces. Plugging T and V as well as δW_{nc} in equation (3.1.3), doing the variation and integrating by parts the Euler-Lagrange equations (equations of motion) are obtained (equations (3.1.4)).

$$\frac{d}{dt}\left(\frac{\partial T}{\partial \dot{\theta}_i}\right) - \frac{\partial T}{\partial \theta_i} + \frac{\partial V}{\partial \theta_i} = Q_i \tag{3.1.4}$$

For a system where the damping forces are proportional to the generalized velocities a viscous dissipation function can be defined according to equation (3.1.5), the Rayleigh dissipation function.

$$R = \frac{1}{2}\sum_{r=1}^{n}\sum_{s=1}^{n} c_{rs}\dot{\theta}_r\dot{\theta}_s \tag{3.1.5}$$

Which results in the generalized force described in equation (3.1.6).

$$Q_i^R = -\frac{\partial R}{\partial \dot{\theta}_i} \tag{3.1.6}$$

Introducing equation (3.1.6) in (3.1.4) the Euler-Lagrange equations including Rayleigh damping take the form of equations (3.1.7).

$$\frac{d}{dt}\left(\frac{\partial T}{\partial \dot{\theta}_i}\right) - \frac{\partial T}{\partial \theta_i} + \frac{\partial V}{\partial \theta_i} + \frac{\partial R}{\partial \dot{\theta}_i} = Q_i \tag{3.1.7}$$

The generalized forces, Q_i, are obtained from δW_{nc} according to equation (3.1.8).

$$Q_i = \frac{\partial \delta W_{nc}}{\partial \delta \theta_i} \tag{3.1.8}$$

The kinetic energy of a single body can be calculated according to equation (3.1.9). The total kinetic energy of a system is the sum of the kinetic energy of all bodies.

$$T = \frac{1}{2} m \vec{v_G} \cdot \vec{v_G} + \frac{1}{2} \vec{\Omega}^T [I_G] \vec{\Omega} \tag{3.1.9}$$

The potential energy of a single elastic element V_k can be calculated according to equation (3.1.10). The total elastic potential energy of a system is the $\sum$ of the potential energy of all elastic bodies. It should be noted that in some situations the gravitational potential $V_G = m \cdot g \cdot \Delta\theta$ energy should also be taken into account.

$$V_k = \frac{1}{2} K_i (\Delta\theta_i)^2 \tag{3.1.10}$$

Consider now a lumped mass system (Figure 3.1) which consists of a meshing gear pair (a moment of inertia for each gear, J_p and J_w) connected with a spring which varies its stiffness in time (K_{pw}^t), two springs connect to each one of the gears to simulate the shafts torsional stiffness (K_{1p} and K_{w2}) and in the other end of each one of these springs a mass to account for each shaft (J_1 and J_2). A damper (c_{pw}) is connected in parallel with the mesh stiffness element. At the end of each shaft there are two moments applied M_1 and M_2. A degree of freedom $\theta_i(t)$ is considered for each mass [98].

The mesh stiffness was considered a function of time and the frictional effects were also included in the aforementioned time dependent mesh stiffness according to [15,16]. This has the advantage to lead, in the end, to a simpler system of equations because no special frictional terms are included [98].

The kinetic energy of the system described in figure 3.1 can be written according to equation (3.1.11).

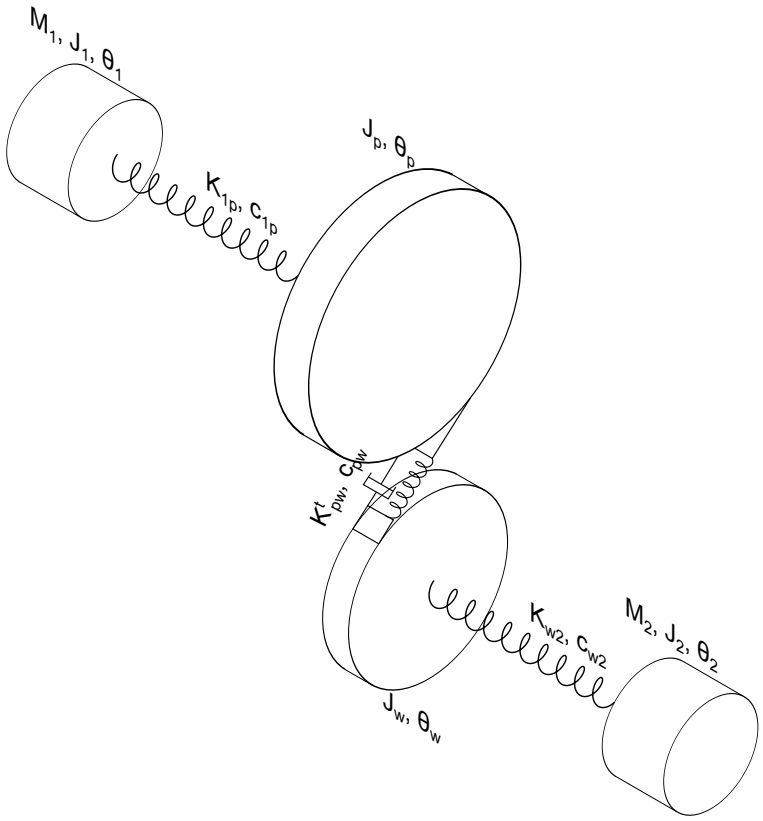

Figure 3.1.: Lumped mass dynamic gear model [98].

$$T = \frac{1}{2} \cdot \left[J_1 \cdot \dot{\theta_1}^2 + J_p \cdot \dot{\theta_p}^2 + J_w \cdot \dot{\theta_w}^2 + J_2 \cdot \dot{\theta_2}^2 \right] \tag{3.1.11}$$

The elastic potential energy can be written according to equation (3.1.12). Gear mesh (K^t_{pw}) and shaft stiffness (K_{1p} and K_{w2}) are considered.

$$V = \frac{1}{2} \cdot \left[K_{1p} \cdot (\theta_p - \theta_1)^2 + K_{w2} \cdot (\theta_2 - \theta_w)^2 + K^t_{pw} \cdot (\theta_w \cdot r_{bw} - \theta_p \cdot r_{bp})^2 \right] \tag{3.1.12}$$

Quantity δW_{nc}, equation (3.1.13), accounts for the work of external forces.

$$\delta W_{nc} = M_1 \cdot \delta\theta_1 - M_2 \cdot \delta\theta_2 \tag{3.1.13}$$

R, equation (3.1.14), adds the damping effects. Gear mesh (c_{pw}) and shaft damping effects (c_{1p} and c_{w2}) are considered.

$$R = \frac{1}{2} \cdot \left[c_{pw} \cdot (r_{bw} \cdot \dot{\theta_w} - r_{bp} \cdot \dot{\theta_p})^2 + c_{1p} \cdot (\dot{\theta_p} - \dot{\theta_1})^2 + c_{w2} \cdot (\dot{\theta_2} - \dot{\theta_w})^2 \right] \tag{3.1.14}$$

Considering equations (3.1.11) to (3.1.14) and applying equations (3.1.7) a system of four diferential equations that describe the motion of the system is obtained, equations (3.1.15) to (3.1.18).

$$J_1 \cdot \ddot{\theta_1} - c_{1p} \cdot (\dot{\theta_p} - \dot{\theta_1}) - [K_{1p} \cdot (\theta_p - \theta_1) + M_1] = 0 \tag{3.1.15}$$

$$\begin{aligned} &J_p \cdot \ddot{\theta_p} + c_{1p} \cdot (\dot{\theta_p} - \dot{\theta_1}) - r_{bp} \cdot c_{pw} \cdot (r_{bw} \cdot \dot{\theta_w} - r_{bp} \cdot \dot{\theta_p}) \\ &- \Big[- K_{1p} \cdot (\theta_p - \theta_1) + K_{pw}^t \cdot r_{bp} \cdot (\theta_w \cdot r_{bw} - \theta_p \cdot r_{bp}) \Big] = 0 \end{aligned} \tag{3.1.16}$$

$$\begin{aligned} &J_w \cdot \ddot{\theta_w} - c_{w2} \cdot (\dot{\theta_2} - \dot{\theta_w}) + r_{bw} \cdot c_{pw} \cdot (r_{bw} \cdot \dot{\theta_w} - r_{bp} \cdot \dot{\theta_p}) \\ &- \Big[K_{w2} \cdot (\theta_2 - \theta_w) - K_{pw}^t \cdot r_{bw} \cdot (\theta_w \cdot r_{bw} - \theta_p \cdot r_{bp}) \Big] = 0 \end{aligned} \tag{3.1.17}$$

$$J_2 \cdot \ddot{\theta_2} + c_{w2} \cdot (\dot{\theta_2} - \dot{\theta_w}) - [-K_{w2} \cdot (\theta_2 - \theta_w) - M_2] = 0 \tag{3.1.18}$$

The equations of motion, equations (3.1.15) to (3.1.18) were numerically solved imposing constant speed at the input ($\dot{\theta_1} = \Omega$) and constant torque at the output (M_2 =const.).

This problem can then be rewritten in matrix form according to equation (3.1.19).

$$[M] \{\ddot{\theta}\} + [C] \{\dot{\theta}\} + [K] \{\theta\} - \{F\} = \{0\} \tag{3.1.19}$$

Equations (3.1.20) to (3.1.24) are the matrices that compose equations (3.1.19).

$$\{\theta\} = \begin{bmatrix} \theta_1 \\ \theta_p \\ \theta_w \\ \theta_2 \end{bmatrix} \tag{3.1.20}$$

$$[M] = \begin{bmatrix} J_1 & 0 & 0 & 0 \\ 0 & J_p & 0 & 0 \\ 0 & 0 & J_w & 0 \\ 0 & 0 & 0 & J_2 \end{bmatrix} \tag{3.1.21}$$

$$[K] = \begin{bmatrix} K_{1p} & -K_{1p} & 0 & 0 \\ -K_{1p} & K_{1p} + r_{bp}^2 \cdot K_{pw}^t & -r_{bw} \cdot r_{bp} \cdot K_{pw}^t & 0 \\ 0 & -r_{bw} \cdot r_{bp} \cdot K_{pw}^t & K_{w2} + r_{bw}^2 \cdot K_{pw}^t & -K_{w2} \\ 0 & 0 & -K_{w2} & K_{w2} \end{bmatrix} \tag{3.1.22}$$

$$[C] = \begin{bmatrix} c_{1p} & -c_{1p} & 0 & 0 \\ -c_{1p} & c_{1p} + r_{bp}^2 \cdot c_{pw} & -r_{bw} \cdot r_{bp} \cdot c_{pw} & 0 \\ 0 & -r_{bw} \cdot r_{bp} \cdot c_{pw} & c_{w2} + r_{bw}^2 \cdot c_{pw} & -c_{w2} \\ 0 & 0 & -c_{w2} & c_{w2} \end{bmatrix} \tag{3.1.23}$$

$$\{F\} = \begin{bmatrix} -M_1 \\ 0 \\ 0 \\ M_2 \end{bmatrix} \tag{3.1.24}$$

3.2. Natural modes and self-excitation

In a dynamic system the amplitude of vibration is highest for excitations near the modal frequencies. The characteristic problem was then studied for the system presented in figure 3.1 aiming to understand the range of operating speeds at which maximum amplitude of vibration occurs.

The natural modes of vibration (modal shapes and frequencies) were calculated for the gears presented earlier considering the mass and stiffness properties presented in table 3.1. The damping parameters, c_{pw}, c_{1p} and c_{w2}, (figure 3.1) were forced 0 in order to solve de characteristic problem.

The mass properties of the gears, J_P and J_W, were calculated from the dimensions of the gears' pitch diameter and face width. The average mesh stiffness was obtained averaging the mesh stiffness obtained with the quasi-static local elastic model (section 2.3) for a single meshing period ($\mu = 0$), shown in table 3.2.

Figures 3.2 show the modal shapes normalized to unitary modal masses for the three gear geometries. As it was expected the modal shapes for each gear pair are quite similar (similar inertias). The natural frequencies are displayed in table 3.3.

The system is positive semi-definite, so the first mode is a rigid body mode with a natural frequency of 0 rpm, the modal shape follows the gear ratio. The second mode appears at around ≈ 4250 rpm for all gears, the modal shape indicates that the gears are in opposition of phase.

Table 3.1.: Mass and stiffness properties (gear dynamics model, figure 3.1).

Property	**Value**	**Units**
$\boldsymbol{J_1}$	4.0×10^{-2}	kgm^2
$\boldsymbol{J_2}$	4.0×10^{-2}	kgm^2
$\boldsymbol{K_{1p}}$	8.0×10^{3}	Nm/rad
$\boldsymbol{K_{w2}}$	8.0×10^{3}	Nm/rad

Table 3.2.: Gears mass parameters and average mesh stiffness ($\mu = 0$).

Gear	$\boldsymbol{J_P}$ [kgm^2]	$\boldsymbol{J_W}$ [kgm^2]	$\boldsymbol{K_{pw}}$ [N/m]
C40	4.2×10^{-3}	8.2×10^{-4}	7.27×10^{8}
H501	2.5×10^{-3}	4.9×10^{-4}	4.55×10^{8}
H951	2.0×10^{-3}	4.0×10^{-4}	3.58×10^{8}

Table 3.3.: Modal frequencies considering the average mesh stiffness ($\mu = 0$).

$\boldsymbol{\omega_n^i}$ [rpm]	**C40**	**H501**	**H951**
$\boldsymbol{\omega_n^0}$	0	0	0
$\boldsymbol{\omega_n^1}$	4264.3	4260.6	4256.5
$\boldsymbol{\omega_n^2}$	20279.9	26142.8	28876.4
$\boldsymbol{\omega_n^3}$	365721.4	378503.4	353830.9

C40 H501 H951

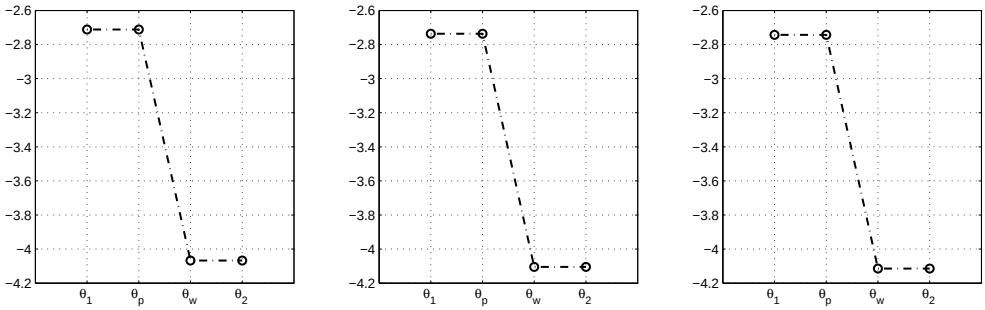

(a) Mode 0, 0rpm. (b) Mode 0, 0 rpm. (c) Mode 0, 0 rpm.

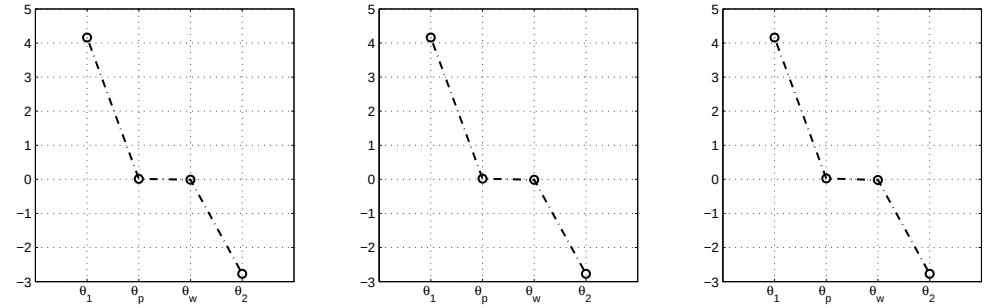

(d) Mode 1, 4264.3 rpm. (e) Mode 1, 4260.6 rpm. (f) Mode 1, 4256.5 rpm.

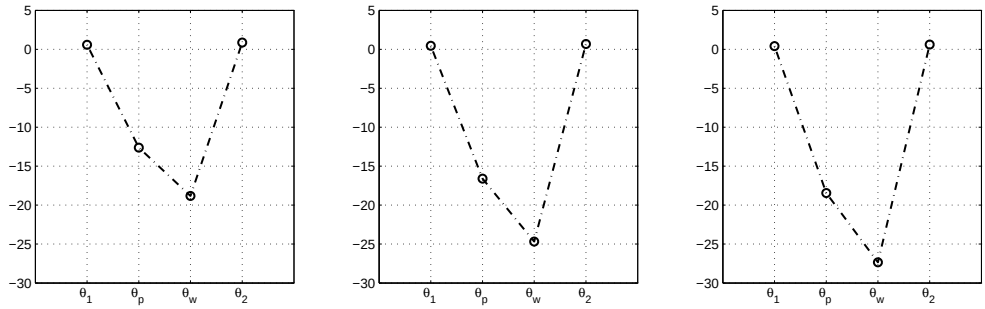

(g) Mode 2, 20279.9 rpm. (h) Mode 2, 26142.8 rpm. (i) Mode 2, 28876.4 rpm.

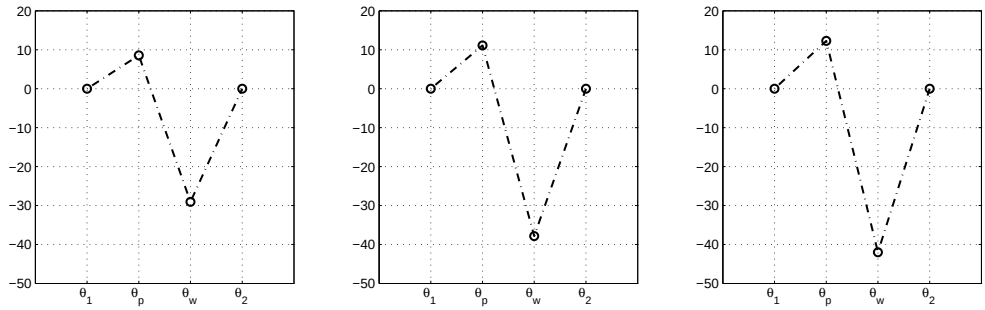

(j) Mode 3, 365721.4 rpm. (k) Mode 3, 378503.4 rpm. (l) Mode 3, 353830.9 rpm.

Figure 3.2.: Modal shapes normalized to unitary modal masses.

3.2.1. Self-excitation (parametric excitation)

The characteristic problem was studied considering the average mesh stiffness however the mesh stiffness varies periodically in time, being the period of this variation coincident with the meshing period T^{mesh}. The time varying mesh stiffness introduces a periodic excitation which has a frequency $(2\pi/T^{mesh})$ that is $z_{1,2}$ times higher that the frequency of rotation of the shaft. This means that it is possible to excite the natural modes at rotational speeds that are much lower (self-excitation speeds) than the actual natural frequency corresponding to that particular mode. The self-excitation speeds can be calculated equalling the mesh period to the natural period of a certain mode, as represented in equation (3.2.1).

$$T^{mesh} = \frac{2\pi}{\omega_n^i} \tag{3.2.1}$$

Considering the definition of T^{mesh} (2.5.3) that was previously introduced, equation 3.2.2 is obtained for the self-excitation speeds.

$$\omega_{self}^i = \frac{\omega_n^i}{z_{1,2}} \tag{3.2.2}$$

The self-excitation speeds for the gear model presented in figure 3.1 were calculated from the natural modes presented in section 3.2.

In figures 3.3 the points at which ω^{self} intersects $\omega_n^i/z_{1,2}$ are the self excitation speeds. The self excitation speeds for the different modes were calculated according to equation (3.2.2), the results are presented in table 3.4.

Table 3.4.: Self excitation speeds.

	C40		**H501**		**H951**	
ω_{self}^i [rpm]	$\omega_n^{1:3}/z_1$	$\omega_n^{1:3}/z_2$	$\omega_n^{1:3}/z_1$	$\omega_n^{1:3}/z_2$	$\omega_n^{1:3}/z_1$	$\omega_n^{1:3}/z_2$
ω_{self}^1	177.7	266.5	142.0	213.0	74.7	112.0
ω_{self}^2	845.0	1267.5	871.4	1307.1	506.6	759.9
ω_{self}^3	15238.4	22857.6	12616.8	18925.2	6207.6	9311.3

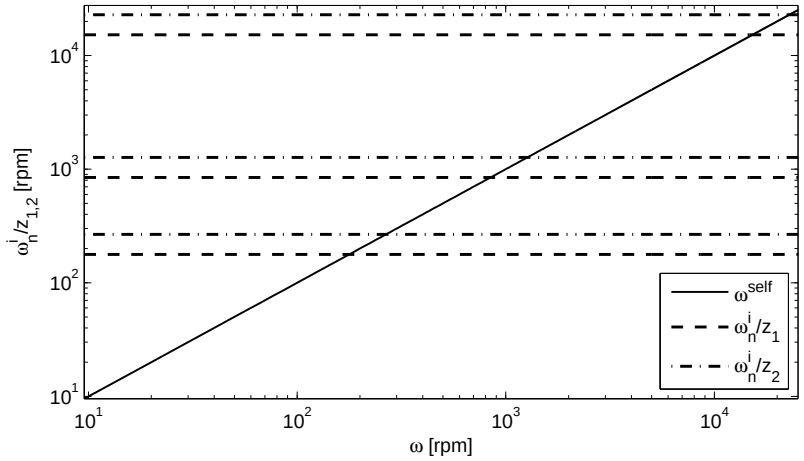

(a) C40.

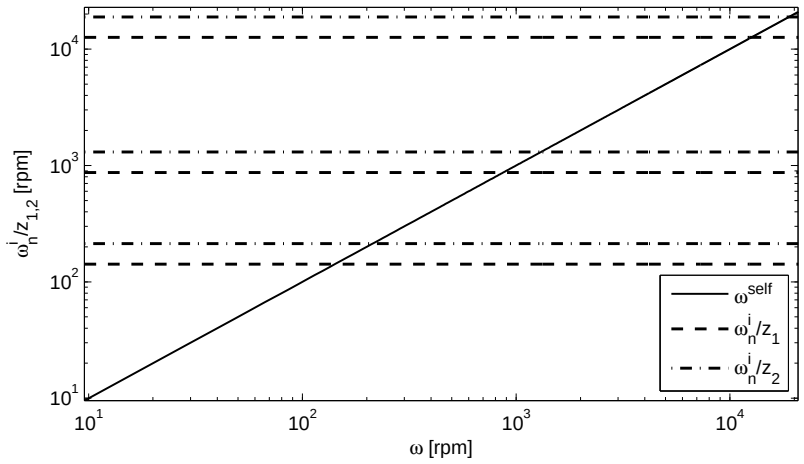

(b) H501.

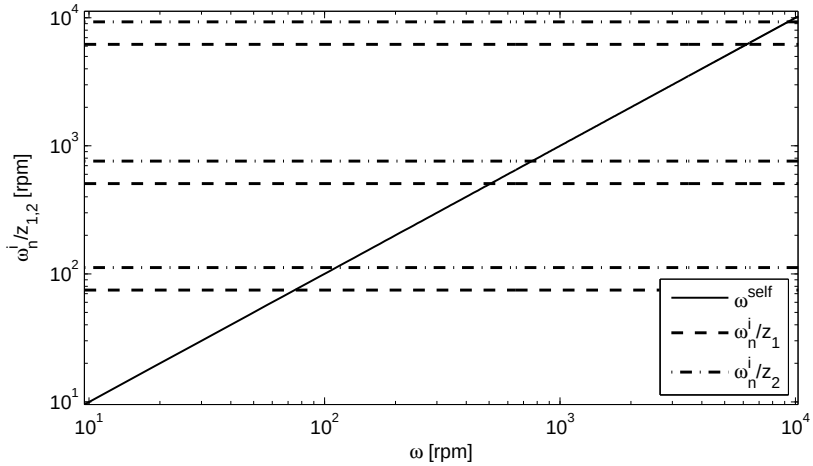

(c) H951.

Figure 3.3.: Self excitation speeds due to the time varying mesh stiffness.

3.3. Power loss simulations

As it was noted in the closure section of chapter 2 the consideration of inertial effects and mesh stiffness induced excitations in the behaviour of a gear system will lead to a time varying total normal load along the path of contact, even at stationary conditions. The local CoF formulation proposed by Xu [53] (equations (1.1.17) to (1.1.18)) μ^{Xu}, which was demonstrated to replicate experimental results quite well [53], depends of the local load in a non-linear fashion. Since the local CoF is dependent of the local load and the local load varies with the dynamic total normal force it follows that the combination of both of the effects may introduce variations in the estimated average power loss comparing with the quasi-static power loss model assumption. The aim of this section is then to evaluate the potential effect of dynamic loads in the estimation of the average power loss.

Speeds near the ones presented in tables 3.3 and 3.4 are prone to induce high vibration amplitudes which may result in substantial dynamic overloads. These high amplitude modes near de critical speeds have the potential to result in dynamic normal tooth loads below zero, which means that the meshing teeth loose contact, therefore rendering the proposed gear dynamics model invalid in such situations. Simulation conditions that make the meshing teeth loose contact will be disregarded.

Previously, the natural modes were studied forcing the damping parameters c_{pw}, c_{1p} and c_{w2}, (figure 3.1) to 0, however some reference values for the mesh damping c_{pw} can be found in the literature [25]. For the current simulations the values of $c_{pw} = 700$ Ns/m and $c_{1p} = c_{w2} = 0.04$ Nm·s were selected according to Vedmar's *et al.* work [101], shown in table 3.5.

Table 3.5.: Damping coefficients for the single gear pair simulations [101].

Property	Value	Units
$\boldsymbol{c_{pw}}$	700	Ns/m
$\boldsymbol{c_{1p}}$	0.04	Nm·s
$\boldsymbol{c_{w2}}$	0.04	Nm·s

The time varying mesh stiffness, K_{pw}^t, was obtained according to the method suggested in section 2.3 where the load distribution was calculated minimizing the total potential energy of the system and the boundary conditions introduced using a Lagrange multiplier. The frictional effects in gear dynamics were taken into account in the time varying mesh stiffness. The local CoF formulation proposed by Xu [53] was considered (detailed in 1.1.2).

A centred finite differences scheme was used to numerically solve equations (3.1.15) to (3.1.18). A proper integration time Δt (between 5×10^{-7} and 5×10^{-5} depending on the input speed) was selected for each simulation. As for the boundary conditions, the input speed ($\dot{\theta}_1$) and output torque (M_2) were fixed.

For each simulation four different speeds and one load were considered (table 3.6). The lubricant that was selected was an ISO VG 320 PAO based lubricant (PAOR, table 4.3) at 80 °C.

Table 3.6.: Operating conditions at driving gear (dynamic simulations; PAOR, table 4.3) at 80 °C).

Load	**Speed**	**Gear**		
M_2 [Nm]	$\dot{\theta}_1$ [rpm]	**C40**	**H501**	**H951**
477.78	ω^1_{self}	177.7	142.0	74.7
	ω^2_{self}	845.0	871.4	506.6
	ω^1_n	4264.3	4260.6	4256.5
	ω	1200	1200	1200

The amplitude of vibration is the highest in the vicinity of the natural modes, therefore the first two self excitation speeds as well as the first natural frequency were selected. An additional simulation at 1200 rpm (between ω^2_{self} and ω^1_n) was also performed. Simulations at ω^3_{self} speeds (high speeds) were avoided due to meshing tooth loosing contact in such conditions (the dynamic power loss model is not valid in such scenarios).

3.4. Results

As it was previously suggested a periodic mesh stiffness variation is equivalent to a periodic load and the larger the total stiffness variation and its variation rate are potentially more aggressive are the dynamic effects. Figures 3.4 show the mesh stiffness for a single mesh period for the different gear geometries at the simulated operating conditions. Some minor variations due to dynamic frictional effects can be observed in some of the figures, namely figure 3.4a. The most important thing to note here is the mesh stiffness for the C40 gear which varies in a step like fashion at the transition from two to a single meshing tooth pair, so naturally the dynamic effects due to mesh stiffness excitation will be more relevant in the case of the C40 gear.

Figures 3.5 show the normalized load distribution ($F_N(t)/F_{bn}$) taking into account frictional effects at stabilized dynamic conditions. The results clearly show that for the selected simulation conditions the dynamic load amplitude is the highest for the C40 spur gear. This comes as no surprise because the C40 spur gear mesh stiffness varies in a step like fashion, as observed in figures 3.4. The H501 and H951 helical gears show much lower dynamic load amplitudes than the spur gear mainly due to the much smoother mesh stiffness variations. It should be noted that the H951 mesh stiffness is almost constant which translated in the very low dynamic load amplitudes at the selected simulation conditions.

Figures 3.6 to 3.17 show the power loss simulations for the conditions presented in table 3.6. The stabilized dynamic average power loss results are presented in table 3.7. The results show that there are some differences between the local quasi-static and local dynamic average power loss. The differences are at their highest 3.6% (60 W) for the C40 simulation at ω^1_n. The C40 gear shows also the highest load variations (dynamic overload up to 2 according to figure 3.7a) along the path of contact for the

simulated operating conditions. In the case of the H501 and H951 gears the dynamic overloads due to mesh stiffness and self-excitation do not seem as relevant as in the spur gear, mainly due to the smoother mesh stiffness transitions as shown in figures 3.4.

The average power loss is calculated according to equation (2.5.5) which depends on the local properties of the CoF, sliding velocity and load distribution. This indicates that the differences between the quasi-static and dynamic average power loss depend on the local variation of such properties. Tables 3.8, 3.9 and 3.10 show the differences between the averages of the quasi-static and dynamic CoF, sliding velocity and load distribution along the plane of action. The spur gear shows the highest variations of average load, speed and CoF along the path of contact, which was somewhat expected due to the nature of the mesh stiffness of this spur gear. There is no clear and apparent relation between the average CoF, load and speed variations (quasi-static vs dynamic) and the quasi-static and dynamic average power loss.

Initially it was suggested that including dynamic effects in the average power loss could potentially change the average power loss, namely due to the non-linear load dependence of the local CoF, it turns out that differences exist not only due to local CoF variations with the dynamic load and sliding velocities, but also directly due to dynamic load and sliding velocities.

Figures 3.6e, 3.7e, 3.8e and 3.9e and 3.12e clearly show the influence of dynamic effects (dynamic load and sliding velocity) in the CoF evolution along the plane of action.

It should be noted that the H951 results appear to be influenced by mesh stiffness variations due to numerical approximations, as it can be observed in figures 3.4, nevertheless this gear has the curious property of having an almost constant mesh stiffness, which results in a smoother operation and less mesh stiffness induced dynamic effects which should result in a better match between the quasi-static and dynamic average power loss results.

The differences in the average load for the quasi static simulations (total normal load is kept constant and at 477.78Nm) for a given gear are due to the fact that the frictional effects are included therefore affecting the local quasi-static load distribution and its average value.

Table 3.7.: Average power loss at stable dynamic conditions considering the μ^{Xu} local CoF.

Load [Nm]	**Speed** [rpm]	Power loss [W]								
		C40			**H501**			**H951**		
		S	**D**	**Δ** [%]	**S**	**D**	**Δ** [%]	**S**	**D**	**Δ** [%]
477.78	$\boldsymbol{\omega^1_{self}}$	99.3	97.2	2.2	70.7	70.5	0.3	14.2	14.2	0
	$\boldsymbol{\omega^2_{self}}$	403.3	389.9	3.4	361.3	357.3	1.1	79.4	78.1	1.7
	$\boldsymbol{\omega^1_n}$	1728.3	1668.1	3.6	1505.4	1483.6	1.5	538.8	525.3	2.6
	1200	552.82	539.2	2.5	481.7	477.7	0.8	172.5	168.1	2.6

S - Quasi-static load; **D** - Dynamic load

Table 3.8.: Average CoF at stable dynamic conditions considering the μ^{Xu} local CoF formulation.

Load [Nm]	**Speed** [rpm]	**CoF** [–]								
		C40			**H501**			**H951**		
		S	**D**	**Δ** [%]	**S**	**D**	**Δ** [%]	**S**	**D**	**Δ** [%]
477.78	ω^1_{self}	0.0543	0.0544	-0.2	0.0531	0.0530	0.2	0.0452	0.0452	0.0
	ω^2_{self}	0.0464	0.0464	0.0	0.0443	0.0442	0.22	0.0373	0.0373	0.0
	ω^1_n	0.0395	0.0400	-1.25	0.0377	0.0378	-0.3	0.0301	0.0301	0.0
	1200	0.0448	0.0451	-0.7	0.0429	0.0428	0.2	0.0342	0.0342	0.0

S - Quasi-static load; **D** - Dynamic load

Table 3.9.: Average sliding velocity (m/s) at stable dynamic conditions considering the μ^{Xu} local CoF formulation.

Load [Nm]	**Speed** [rpm]	**Sliding Velocity** [m/s]								
		C40			**H501**			**H951**		
		S	**D**	**Δ** [%]	S	D	**Δ** [%]	S	D	**Δ** [%]
477.78	ω^1_{self}	0.230	0.224	2.7	0.146	0.146	0.0	0.0256	0.0256	0.0
	ω^2_{self}	1.09	1.04	4.8	0.893	0.876	1.9	0.173	0.174	-0.6
	ω^1_n	5.51	5.33	3.4	4.37	4.37	0.0	1.46	1.46	0.0
	1200	1.55	1.50	3.3	1.23	1.23	0.0	0.410	0.410	0.0

S - Quasi-static load; **D** - Dynamic load

Table 3.10.: Average load (N/mm) at stable dynamic conditions considering the μ^{Xu} local CoF formulation.

Load [Nm]	**Speed** [rpm]	**Load** [N/mm]								
		C40			**H501**			**H951**		
		S	**D**	**Δ** [%]	**S**	**D**	**Δ** [%]	**S**	**D**	**Δ** [%]
477.78	ω^1_{self}	160.0	163.8	-2.3	280.1	281.1	-0.4	467.2	469.2	-0.4
	ω^2_{self}	158.8	164.6	-3.5	280.0	280.5	-0.2	467.7	469.9	-0.5
	ω^1_n	158.7	164.4	-3.4	279.9	279.7	0.1	468.1	465.8	0.0
	1200	158.8	163.5	-2.9	280	279.8	0.1	467.9	467.0	0.2

S - Quasi-static load;**D** - Dynamic load

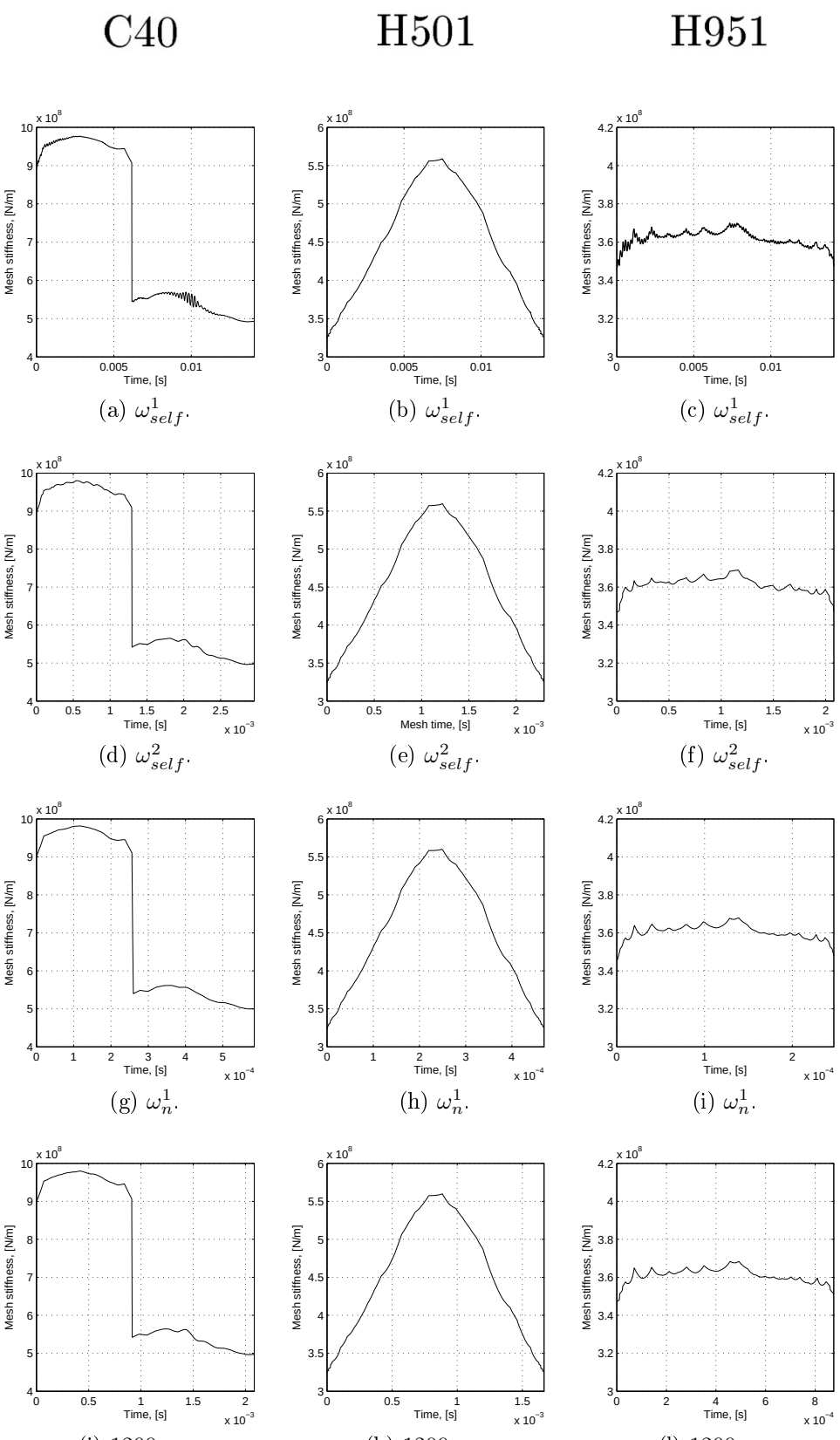

(a) ω^1_{self}. (b) ω^1_{self}. (c) ω^1_{self}.

(d) ω^2_{self}. (e) ω^2_{self}. (f) ω^2_{self}.

(g) ω^1_n. (h) ω^1_n. (i) ω^1_n.

(j) 1200 rpm. (k) 1200 rpm. (l) 1200 rpm.

Figure 3.4.: Mesh stiffness taking into account frictional effects at stabilized dynamic conditions.

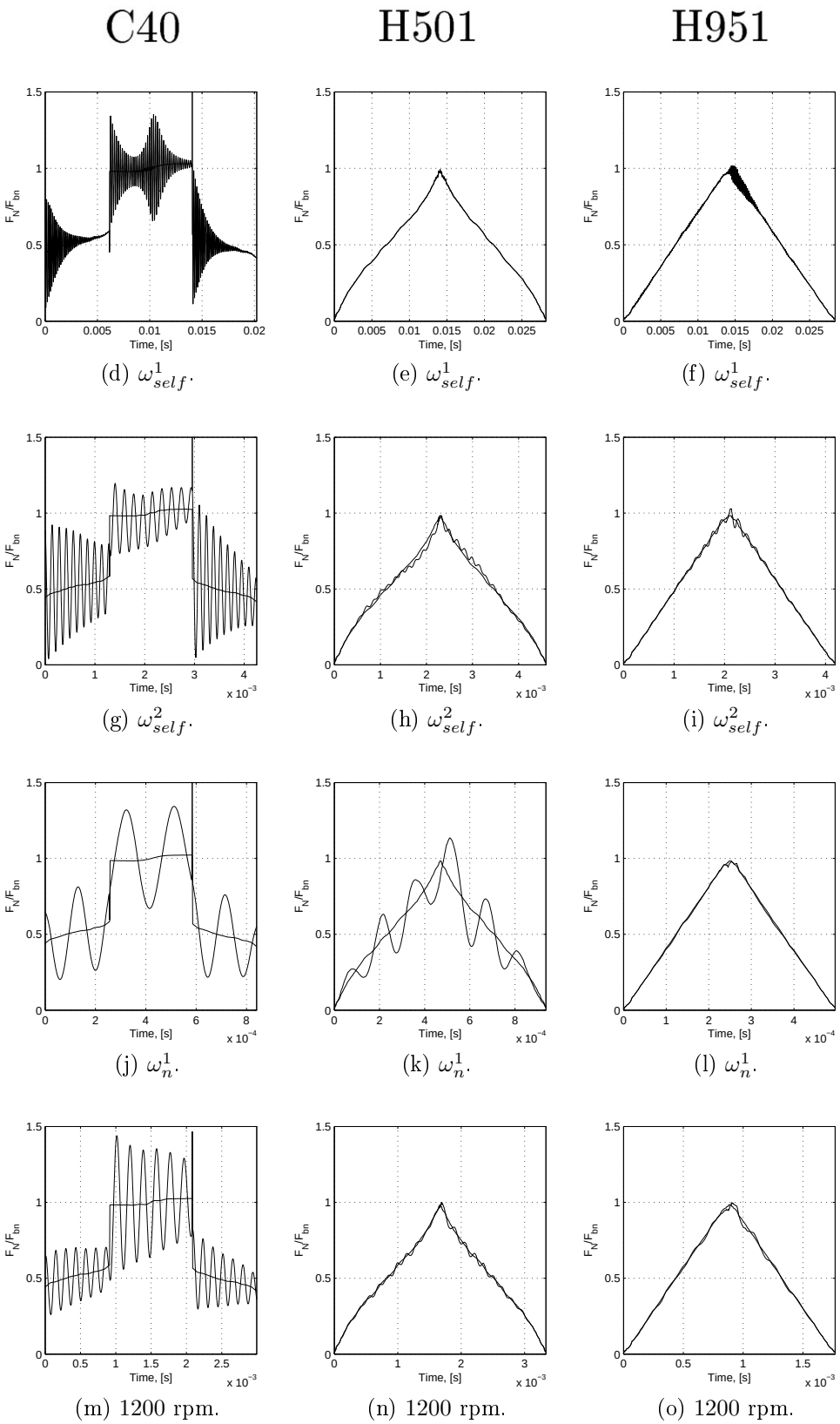

(d) ω^1_{self}. (e) ω^1_{self}. (f) ω^1_{self}.

(g) ω^2_{self}. (h) ω^2_{self}. (i) ω^2_{self}.

(j) ω^1_n. (k) ω^1_n. (l) ω^1_n.

(m) 1200 rpm. (n) 1200 rpm. (o) 1200 rpm.

Figure 3.5.: Normalized load distribution ($F_N(t)/F_{bn}$) taking into account frictional effects at stabilized dynamic conditions.

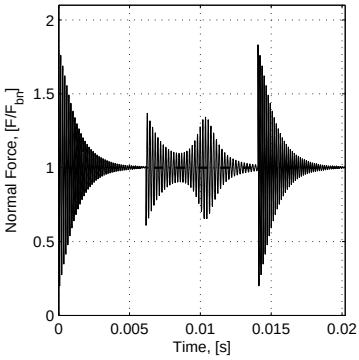

(a) Total normal force, $F_{bn}(t)$.

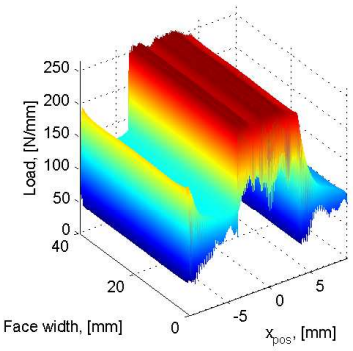

(b) Load per unit of line length, $f_N(x, y)$.

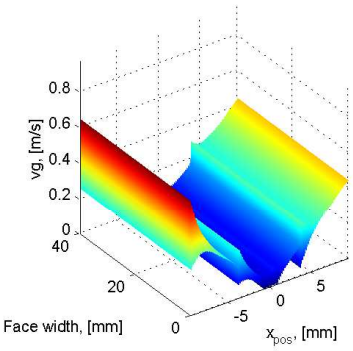

(c) Sliding velocity, $V_g(x, y)$.

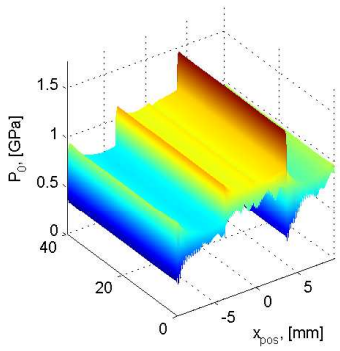

(d) Hertzian pressure, $P_0(x, y)$.

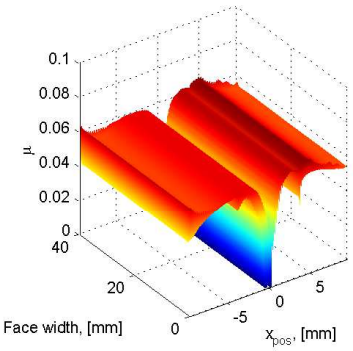

(e) CoF, $\mu^{Xu}(x, y)$.

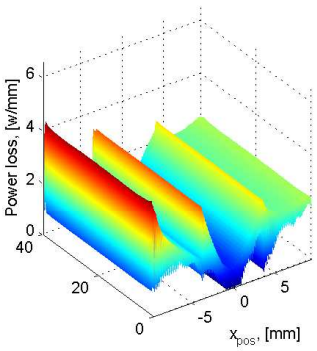

(f) Power loss per unit of line length, $p_{VZP}(x, y)$.

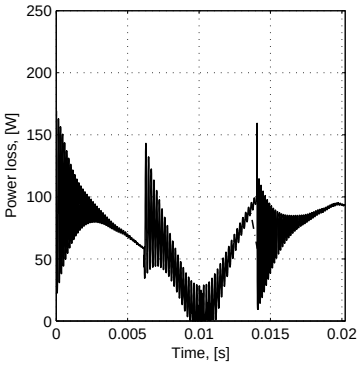

(g) $P_{VZP}^{single}(t)$.

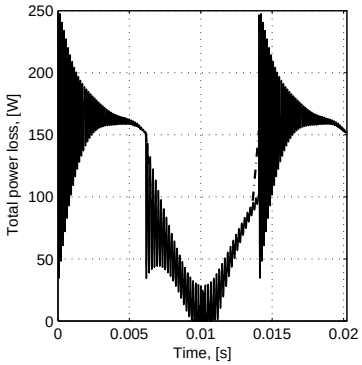

(h) $P_{VZP}^{total}(t)$.

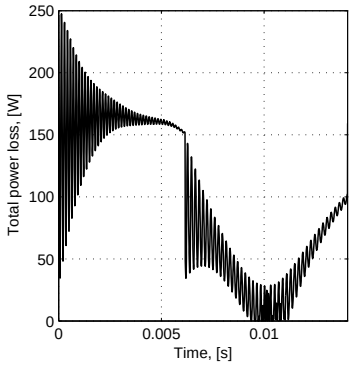

(i) $P_{VZP}^{total}(0 : t : T^{mesh})$.

Figure 3.6.: Local quantities and power loss at stabilized dynamic conditions (ω_{self}^{1} = 177.7 rpm) - C40.

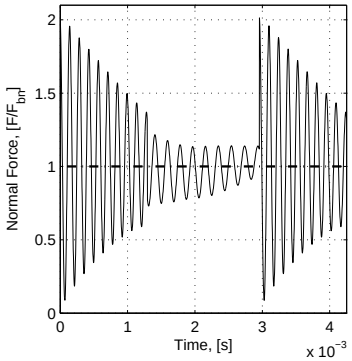

(a) Total normal force, $F_{bn}(t)$.

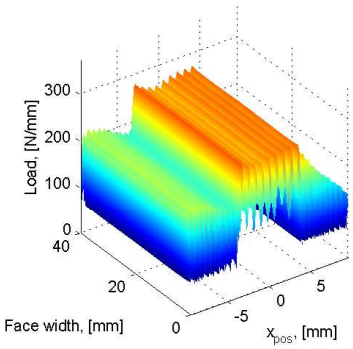

(b) Load per unit of line length, $f_N(x, y)$.

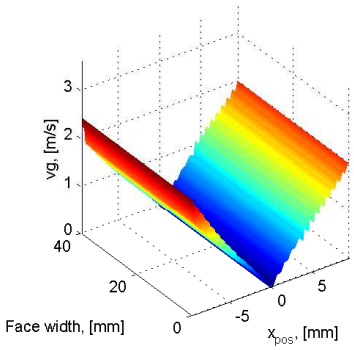

(c) Sliding velocity, $V_g(x, y)$.

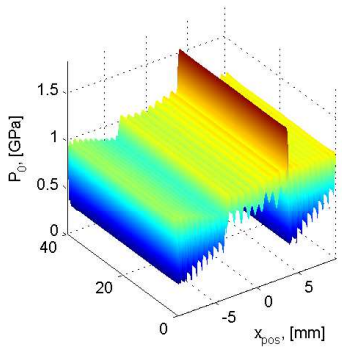

(d) Hertzian pressure, $P_0(x, y)$.

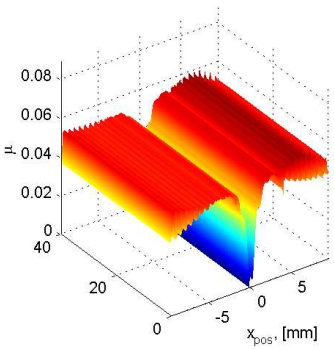

(e) CoF, $\mu^{Xu}(x, y)$.

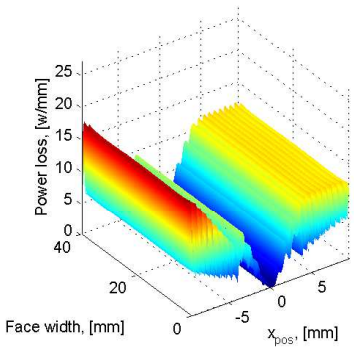

(f) Power loss per unit of line length, $p_{VZP}(x, y)$.

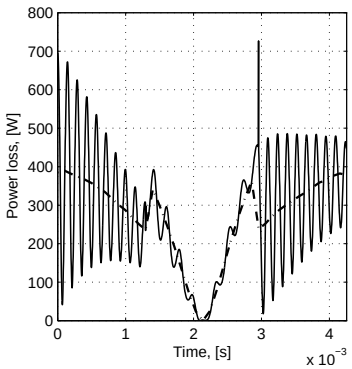

(g) $P_{VZP}^{single}(t)$.

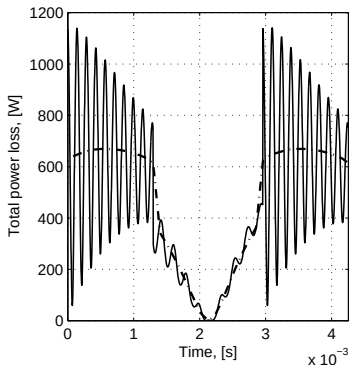

(h) Total power loss.

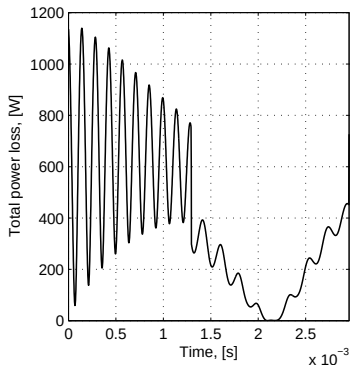

(i) $P_{VZP}^{total}(0 : t : T^{mesh})$.

Figure 3.7.: Local quantities and power loss at stabilized dynamic conditions ($\omega_{self}^2 =$ 845.0 rpm) - C40.

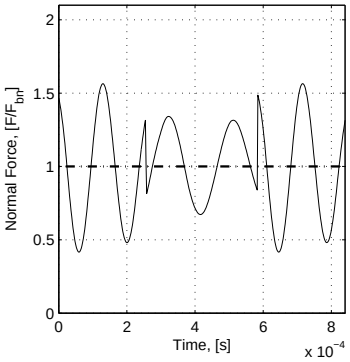

(a) Total normal force, $F_{bn}(t)$.

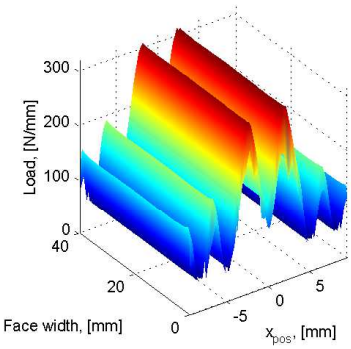

(b) Load per unit of line length, $f_N(x, y)$.

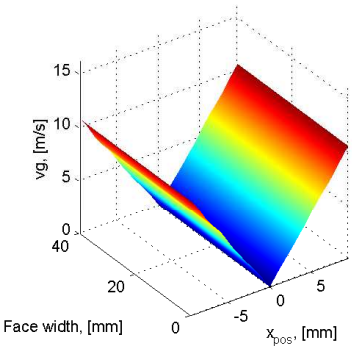

(c) Sliding velocity, $V_g(x, y)$.

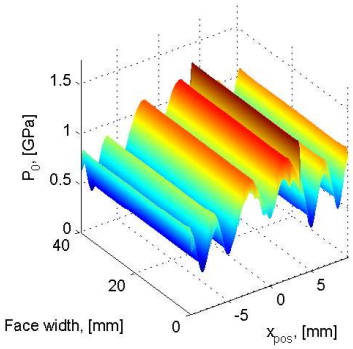

(d) Hertzian pressure, $P_0(x, y)$.

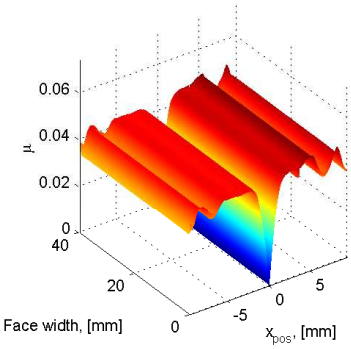

(e) CoF, $\mu^{Xu}(x, y)$.

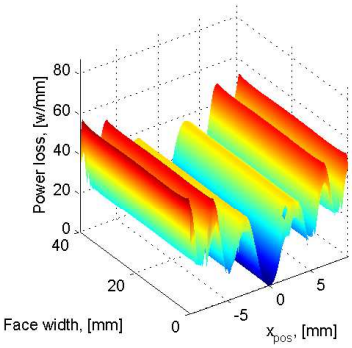

(f) Power loss per unit of line length, $p_{VZP}(x, y)$.

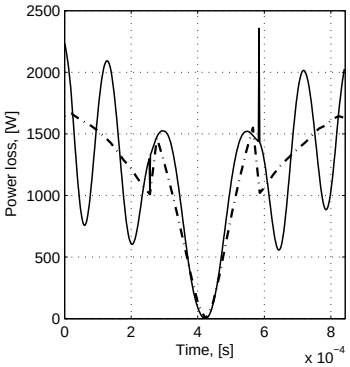

(g) $P_{VZP}^{single}(t)$.

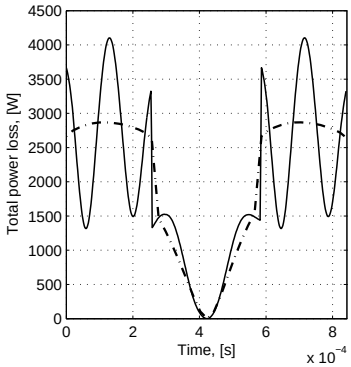

(h) $P_{VZP}^{total}(t)$.

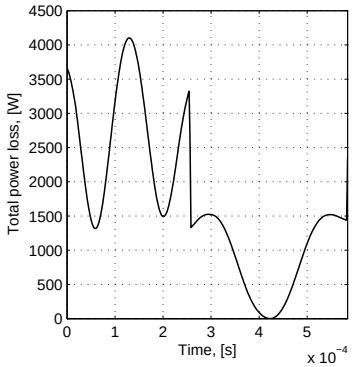

(i) $P_{VZP}^{total}(0 : t : T^{mesh})$.

Figure 3.8.: Local quantities and power loss at stabilized dynamic conditions ($\omega_n^1 = 4264.3$ rpm) - C40.

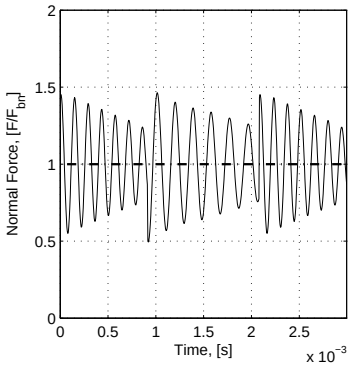

(a) Total normal force, $F_{bn}(t)$.

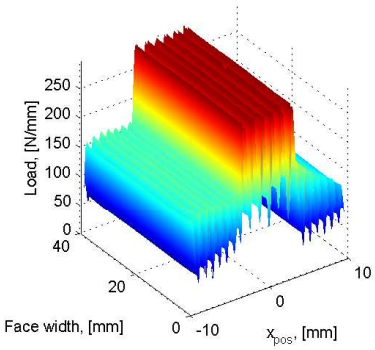

(b) Load per unit of line length, $f_N(x, y)$.

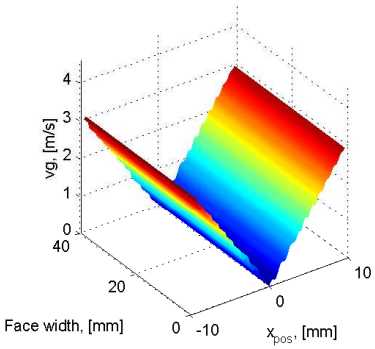

(c) Sliding velocity, $V_g(x, y)$.

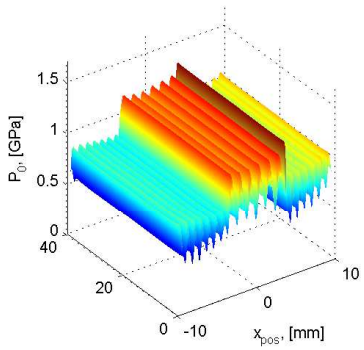

(d) Hertzian pressure, $P_0(x, y)$.

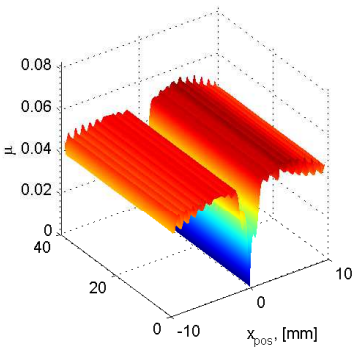

(e) CoF, $\mu^{Xu}(x, y)$.

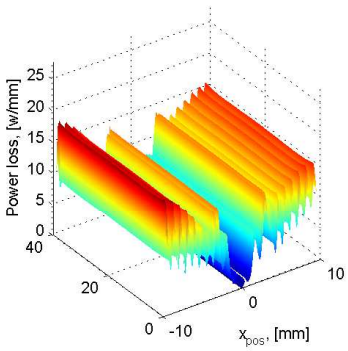

(f) Power loss per unit of line length, $p_{VZP}(x, y)$.

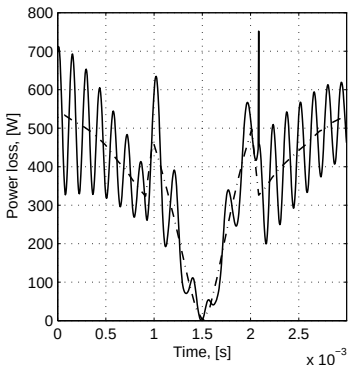

(g) $P_{VZP}^{single}(t)$.

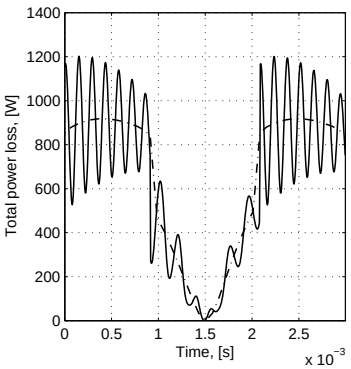

(h) $P_{VZP}^{total}(t)$.

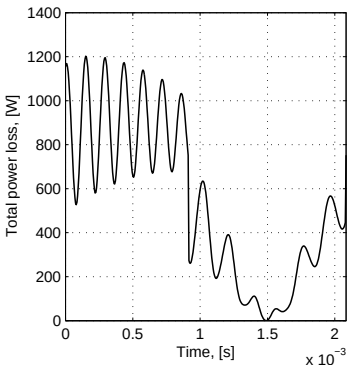

(i) $P_{VZP}^{total}(0 : t : T^{mesh})$.

Figure 3.9.: Local quantities and power loss at stabilized dynamic conditions ($\omega_n^1 =$ 1200 rpm) - C40.

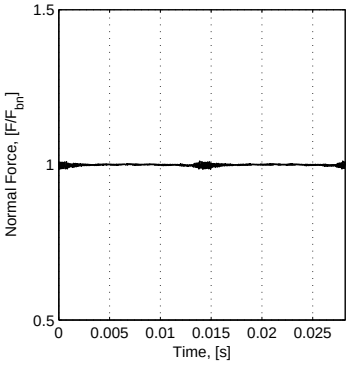

(a) Total normal force, $F_{bn}(t)$.

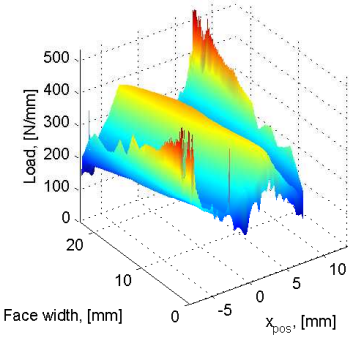

(b) Load per unit of line length, $f_N(x, y)$.

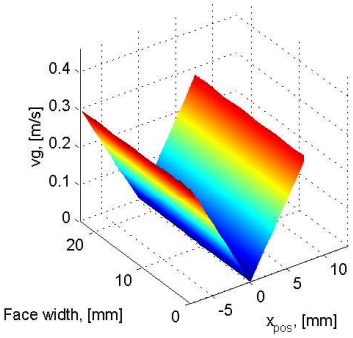

(c) Sliding velocity, $V_g(x, y)$.

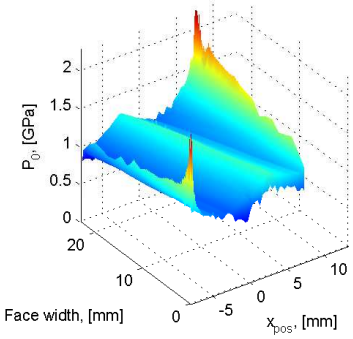

(d) Hertzian pressure, $P_0(x, y)$.

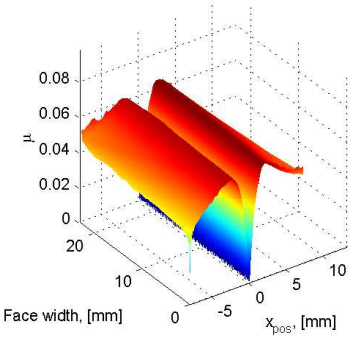

(e) CoF, $\mu^{Xu}(x, y)$.

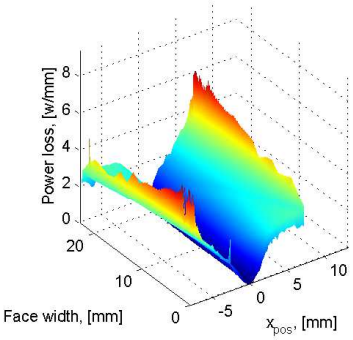

(f) Power loss per unit of line length, $p_{VZP}(x, y)$.

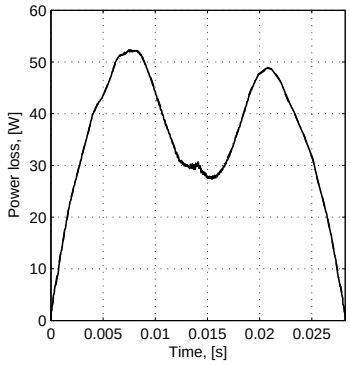

(g) $P_{VZP}^{single}(t)$.

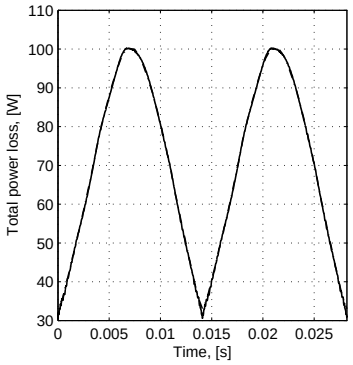

(h) $P_{VZP}^{total}(t)$.

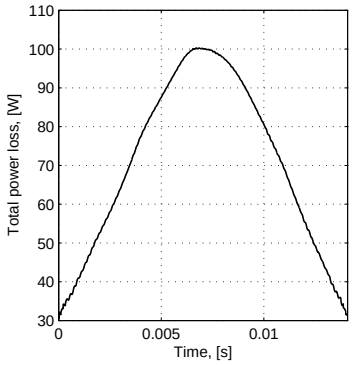

(i) $P_{VZP}^{total}(0 : t : T^{mesh})$.

Figure 3.10.: Local quantities and power loss at stabilized dynamic conditions ($\omega_{self}^{1} = 142.0$ rpm) - H501.

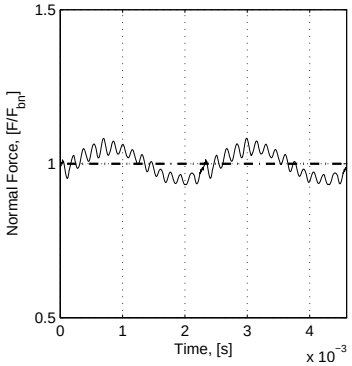

(a) Total normal force, $F_{bn}(t)$.

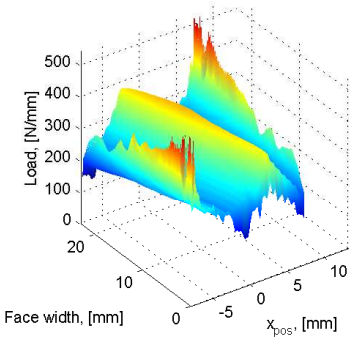

(b) Load per unit of line length, $f_N(x, y)$.

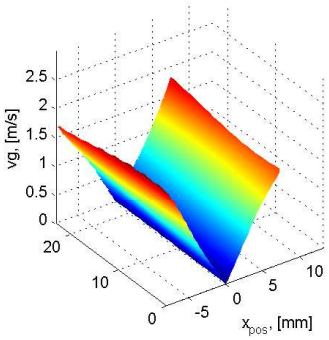

(c) Sliding velocity, $V_g(x, y)$.

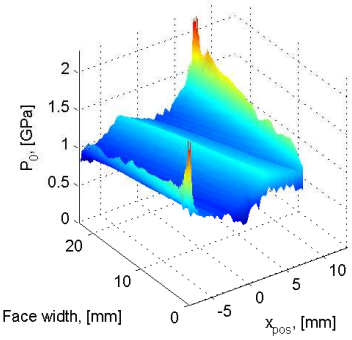

(d) Hertzian pressure, $P_0(x, y)$.

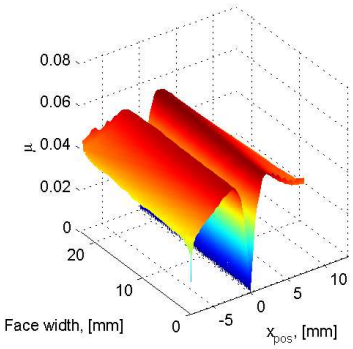

(e) CoF, $\mu^{Xu}(x, y)$.

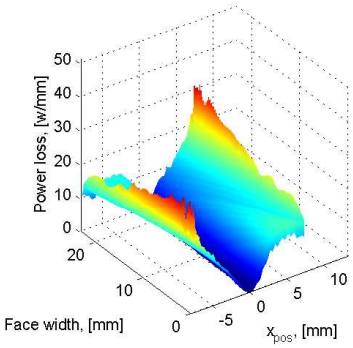

(f) Power loss per unit of line length, $p_{VZP}(x, y)$.

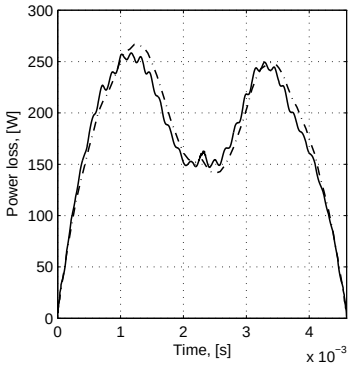

(g) $P_{VZP}^{single}(t)$.

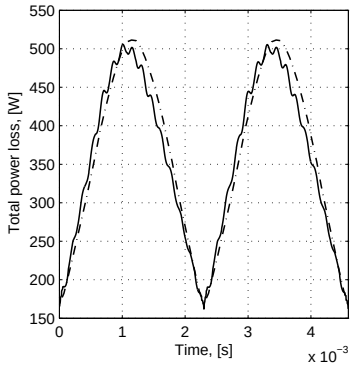

(h) $P_{VZP}^{total}(t)$.

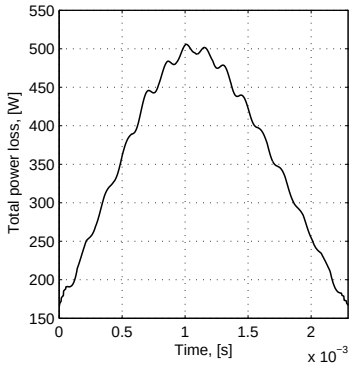

(i) $P_{VZP}^{total}(0 : t : T^{mesh})$.

Figure 3.11.: Local quantities and power loss at stabilized dynamic conditions ($\omega_{self}^2 = 871.4$ rpm) - H501.

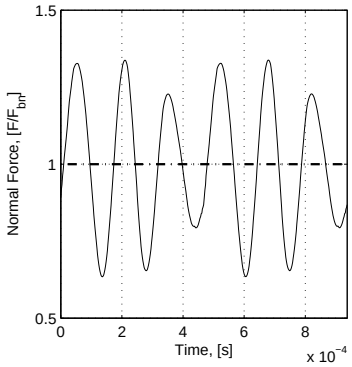

(a) Total normal force, $F_{bn}(t)$.

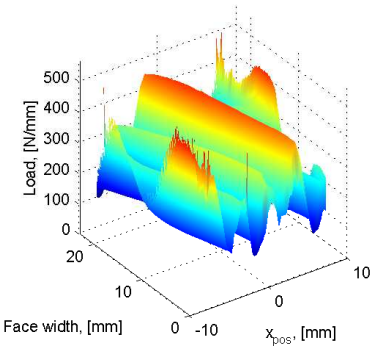

(b) Load per unit of line length, $f_N(x, y)$.

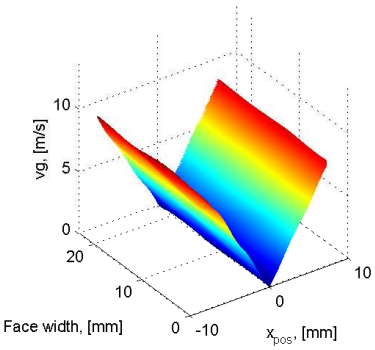

(c) Sliding velocity, $V_g(x, y)$.

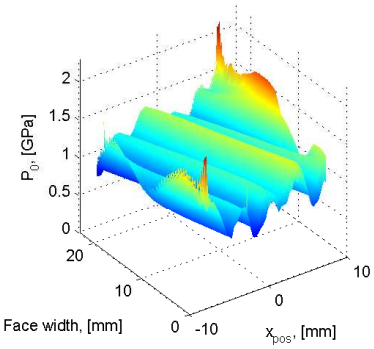

(d) Hertzian pressure, $P_0(x, y)$.

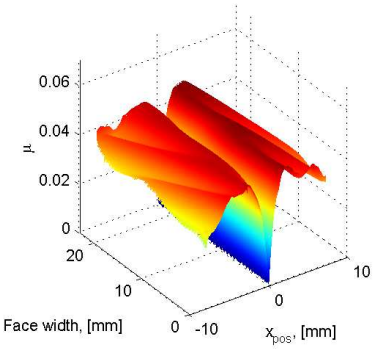

(e) CoF, $\mu^{Xu}(x, y)$.

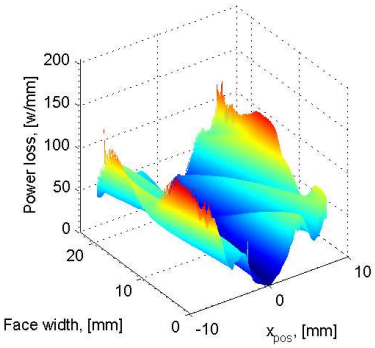

(f) Power loss per unit of line length, $p_{VZP}(x, y)$.

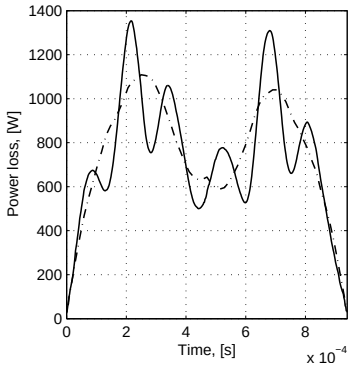

(g) $P_{VZP}^{single}(t)$.

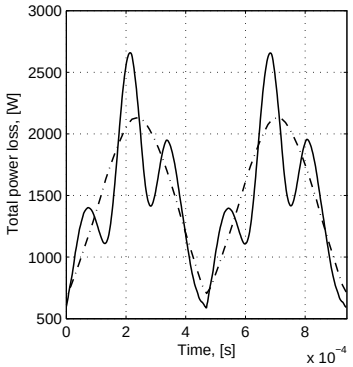

(h) $P_{VZP}^{total}(t)$.

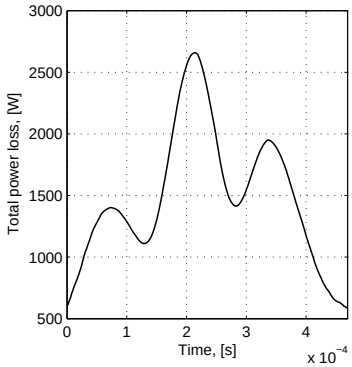

(i) $P_{VZP}^{total}(0 : t : T^{mesh})$.

Figure 3.12.: Local quantities and power loss at stabilized dynamic conditions ($\omega_n^1 =$ 4260.4 rpm) - H501.

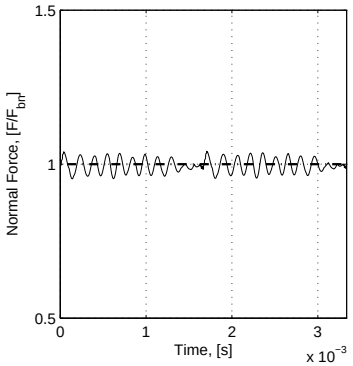

(a) Total normal force, $F_{bn}(t)$.

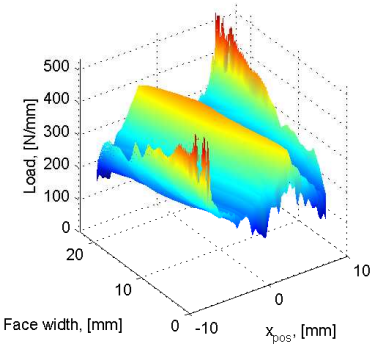

(b) Load per unit of line length, $f_N(x, y)$.

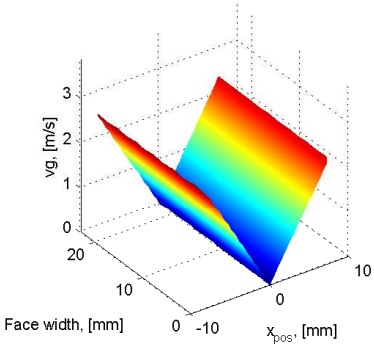

(c) Sliding velocity, $V_g(x, y)$.

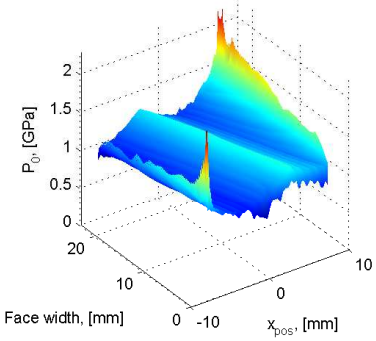

(d) Hertzian pressure, $P_0(x, y)$.

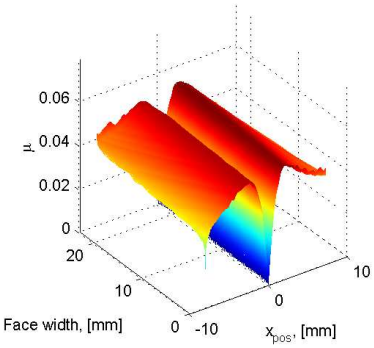

(e) CoF, $\mu^{Xu}(x, y)$.

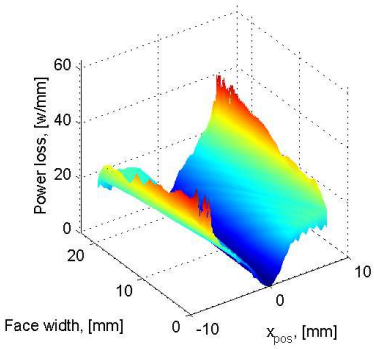

(f) Power loss per unit of line length, $p_{VZP}(x, y)$.

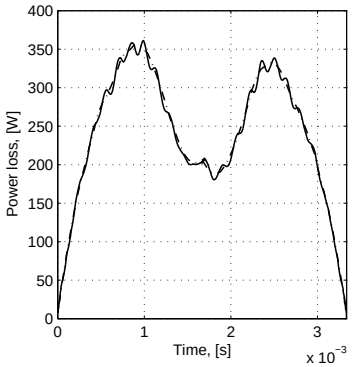

(g) $P_{VZP}^{single}(t)$.

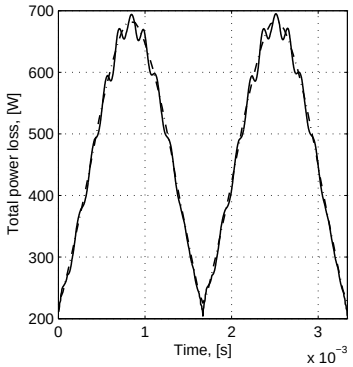

(h) $P_{VZP}^{total}(t)$.

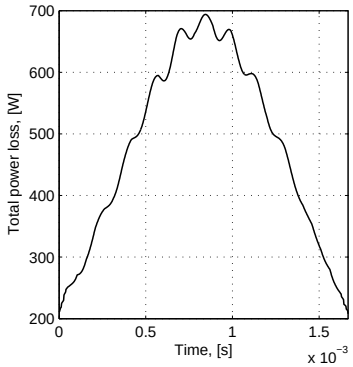

(i) $P_{VZP}^{total}(0 : t : T^{mesh})$.

Figure 3.13.: Local quantities and power loss at stabilized dynamic conditions ($\omega_n^1 =$ 1200 rpm) - H501.

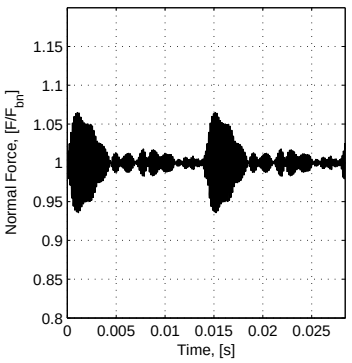

(a) Total normal force, $F_{bn}(t)$.

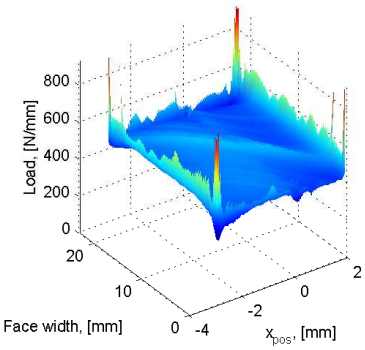

(b) Load per unit of line length, $f_N(x, y)$.

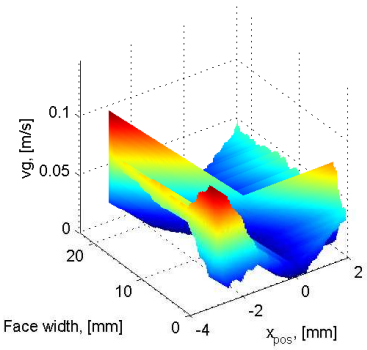

(c) Sliding velocity, $V_g(x, y)$.

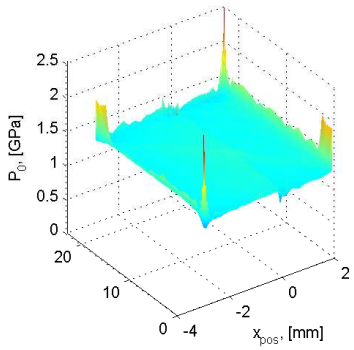

(d) Hertzian pressure, $P_0(x, y)$.

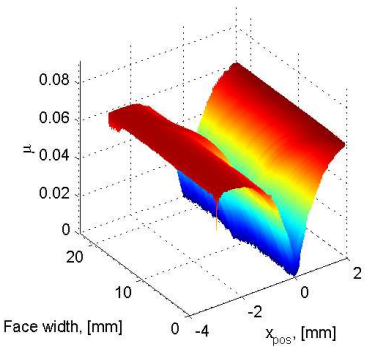

(e) CoF, $\mu^{Xu}(x, y)$.

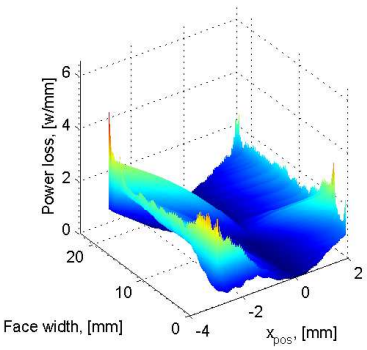

(f) Power loss per unit of line length, $p_{VZP}(x, y)$.

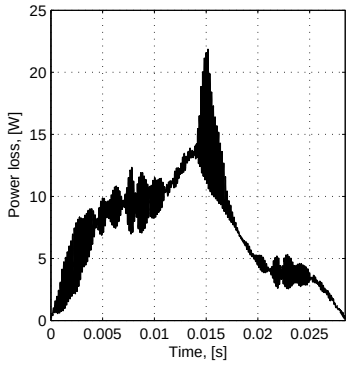

(g) $P_{VZP}^{single}(t)$.

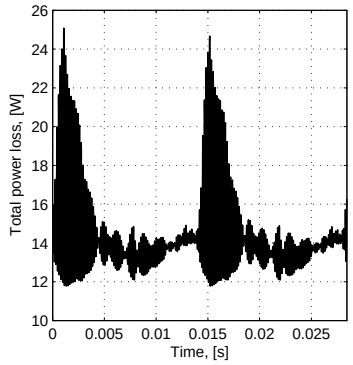

(h) $P_{VZP}^{total}(t)$.

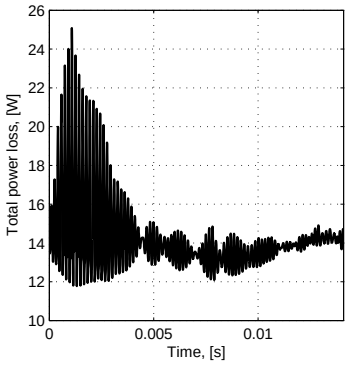

(i) $P_{VZP}^{total}(0 : t : T^{mesh})$.

Figure 3.14.: Local quantities and power loss at stabilized dynamic conditions ($\omega_{self}^{1} = 74.7$ rpm) - H951.

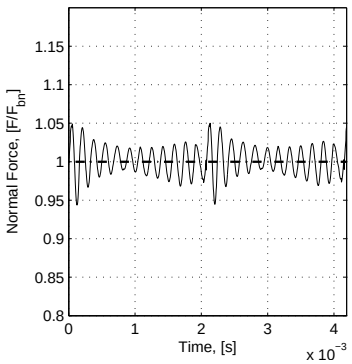

(a) Total normal force, $F_{bn}(t)$.

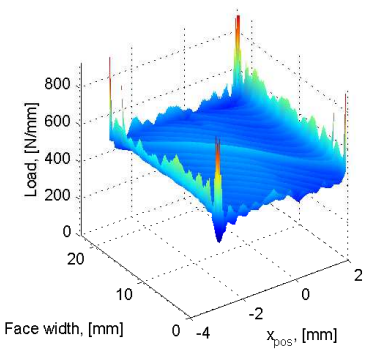

(b) Load per unit of line length, $f_N(x, y)$.

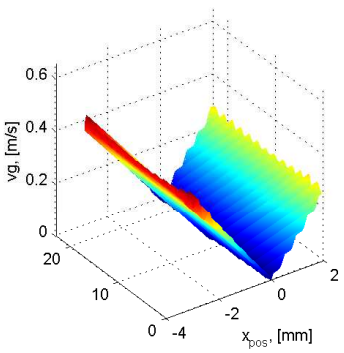

(c) Sliding velocity, $V_g(x, y)$.

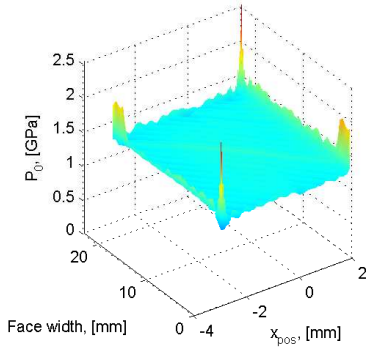

(d) Hertzian pressure, $P_0(x, y)$.

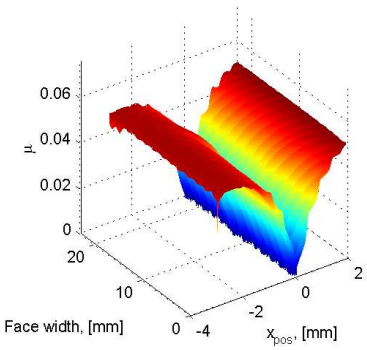

(e) CoF, $\mu^{Xu}(x, y)$.

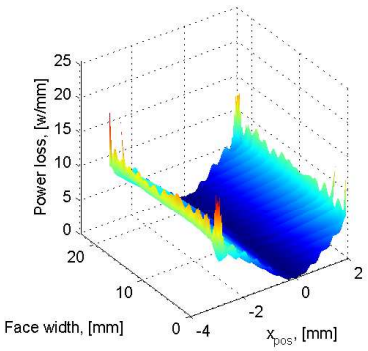

(f) Power loss per unit of line length, $p_{VZP}(x, y)$.

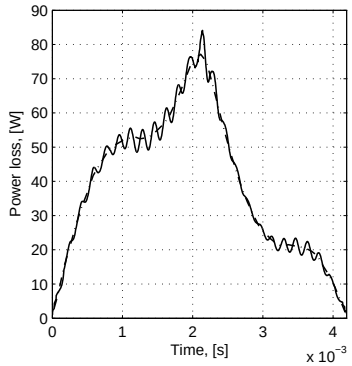

(g) $P_{VZP}^{single}(t)$.

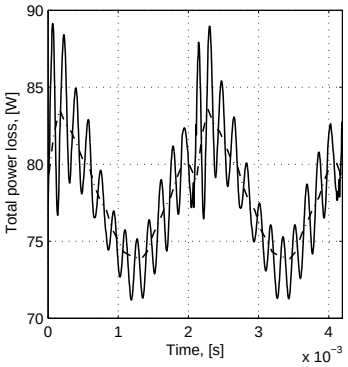

(h) $P_{VZP}^{total}(t)$.

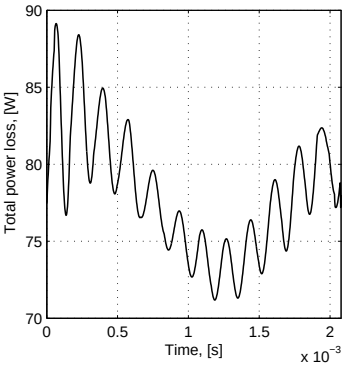

(i) $P_{VZP}^{total}(0 : t : T^{mesh})$.

Figure 3.15.: Local quantities and power loss at stabilized dynamic conditions ($\omega_{self}^2 = 506.6$ rpm) - H951.

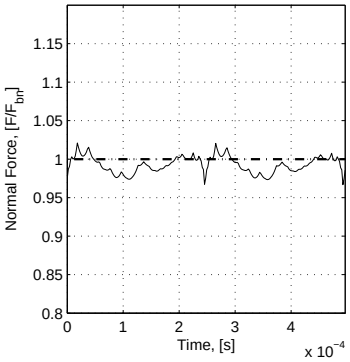

(a) Total normal force, $F_{bn}(t)$.

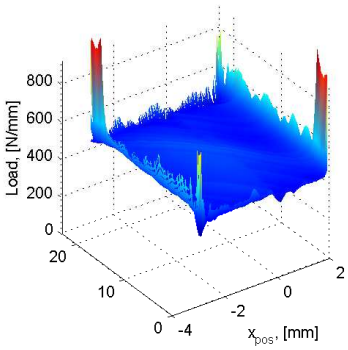

(b) Load per unit of line length, $f_N(x, y)$.

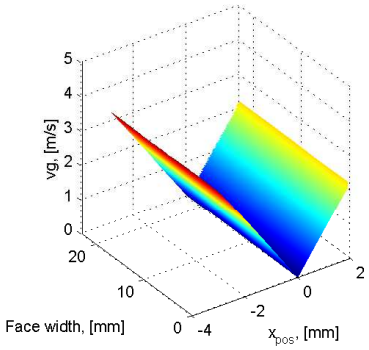

(c) Sliding velocity, $V_g(x, y)$.

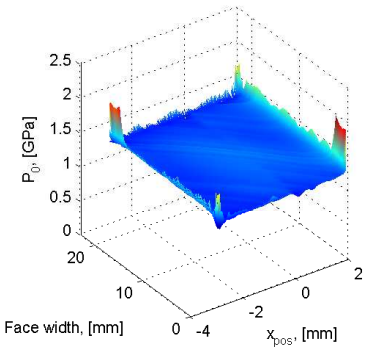

(d) Hertzian pressure, $P_0(x, y)$.

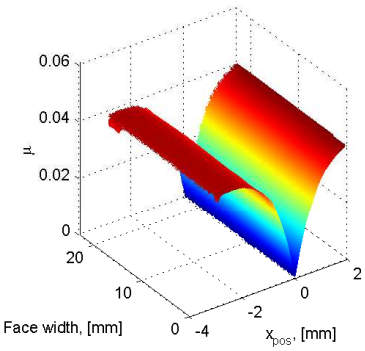

(e) CoF, $\mu^{Xu}(x, y)$.

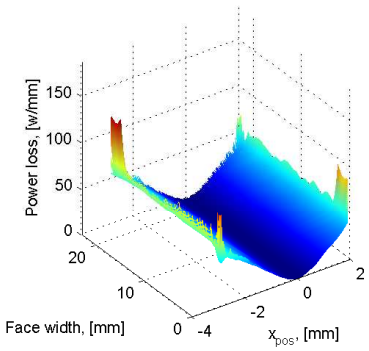

(f) Power loss per unit of line length, $p_{VZP}(x, y)$.

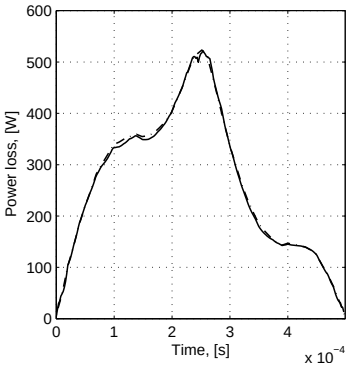

(g) $P_{VZP}^{single}(t)$.

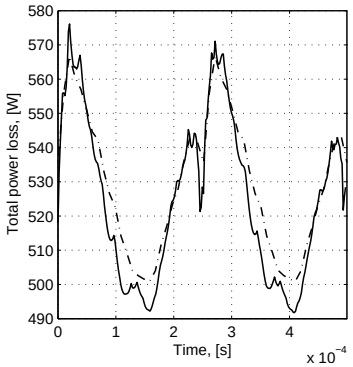

(h) $P_{VZP}^{total}(t)$.

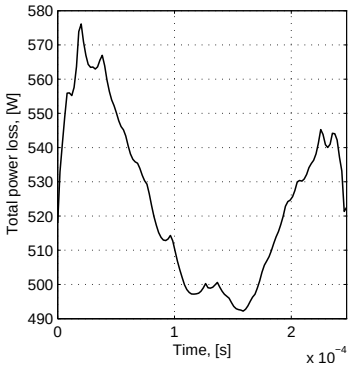

(i) $P_{VZP}^{total}(0 : t : T^{mesh})$.

Figure 3.16.: Local quantities and power loss at stabilized dynamic conditions ($\omega_n^1 =$ 4256.5 rpm) - H951.

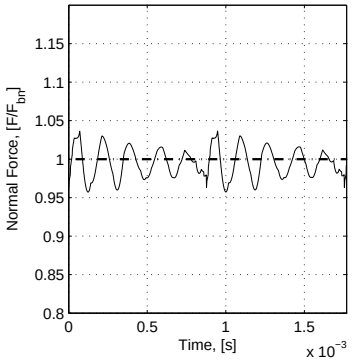

(a) Total normal force, $F_{bn}(t)$.

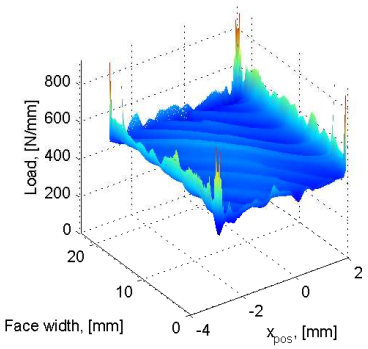

(b) Load per unit of line length, $f_N(x, y)$.

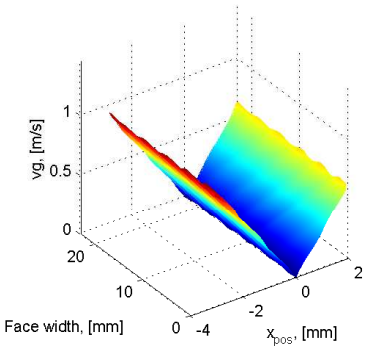

(c) Sliding velocity, $V_g(x, y)$.

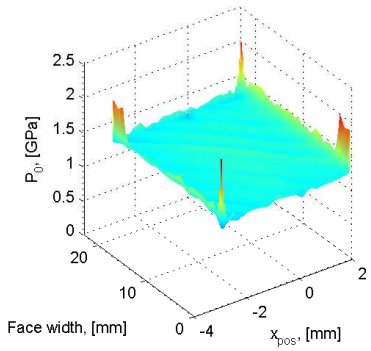

(d) Hertzian pressure, $P_0(x, y)$.

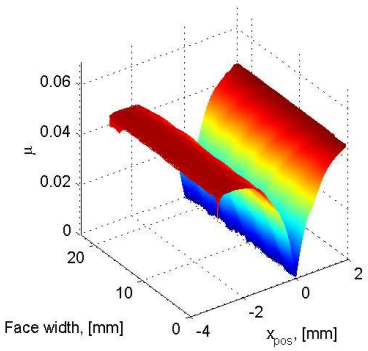

(e) CoF, $\mu^{Xu}(x, y)$.

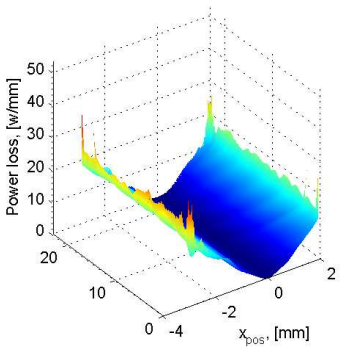

(f) Power loss per unit of line length, $p_{VZP}(x, y)$.

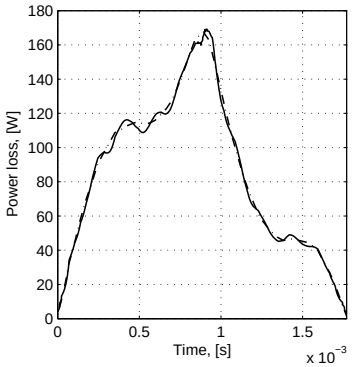

(g) $P_{VZP}^{single}(t)$.

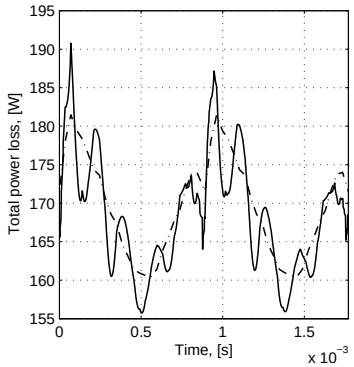

(h) $P_{VZP}^{total}(t)$.

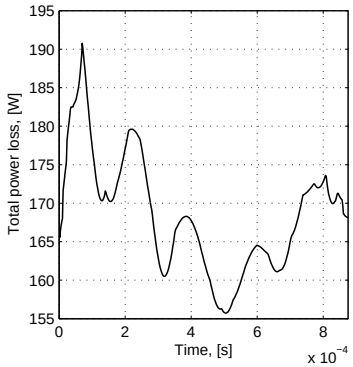

(i) $P_{VZP}^{total}(0 : t : T^{mesh})$.

Figure 3.17.: Local quantities and power loss at stabilized dynamic conditions ($\omega =$ 1200 rpm) - H951.

3.5. Closure

In this chapter a four degree of freedom torsional lumped mass gear dynamic model was deduced from the Principle of Least Action. The model considered the frictional effects in the vibrational behaviour. The effects of gear dynamics and gear geometry in the average power loss were then evaluated.

Gear geometry plays a very important role in gear dynamics. The spur gear showed higher dynamic overloads mainly due to the step like mesh stiffness variations at the transitions from gear mesh of multiple to single tooth pairs and vice versa. Friction has not shown a significant, yet visible, effect in the torsional dynamic behaviour of either spur and helical gears.

It was verified that there can be some differences (up to 3.6 % for the present simulations in the case of spur gears) between the quasi-static and dynamic average power loss (in this case at ω_n^1). This raises some concern because spur gears, namely C40 gears, are often used to perform efficiency tests and calibrate power loss models [2], namely the lubricant factor X_L in the case of Schlenk's CoF formulation [48] which has recently been adopted as a standard.

In subsection 2.5.4 it was demonstrated that the quasi static gear loss factor (constant CoF) can be affected by elastic and frictional effects for spur and helical geometries, table 2.4. Here it is demonstrated that gear power loss can be affected by dynamic effects, therefore there is more potential for the lubricant parameter X_L to be adulterated by non-lubricant dependent effects.

It was shown that gears with slow varying mesh stiffness are prone to be less affected by dynamic self-excitations. It was also shown that dynamic excitations can have an influence in the average power loss and potentially in the lubricant parameter (X_L), therefore a gear that is pre-disposed to promote a smoother operation should be better to perform power loss studies in which the aim is not to study the gear, but the lubricant. Such gear would ideally have a constant mesh stiffness (potentially less dynamic effects) and a gear loss factor similar to that of the C40 gear (≈ 0.2) in order to have an experimental torque loss less affected by measurement. Such gear would have to be an helical gear.

The model that was developed does not take into account the changes in the length of the path of contact due to elastic effects, manufacturing errors and transverse shaft stiffness. The effects that were neglected and the respective changes in the length of the path contact would most likely result in further modifications on the predicted power loss.

Despite power loss being the main focus of this work, gear dynamics still play a important role in gear design. Tooth root safety, transmission error and tooth surface distress related failures are still a concern. Previous studies [104, 105] showed that the load history plays a very important role in surface distress phenomena like wear and micropitting, therefore the scope of application of the proposed model (dynamic power loss model) can be extended and not limited to just efficiency studies.

4. Power Loss in a Multiplier Planetary Gearbox Lubricated with Wind Turbine Gear Oils

This chapter is dedicated to an experimental and numerical study in a multiplier planetary gearbox lubricated with wind turbine gear oils. The influence of operating conditions and gear oil formulation in the power loss and its components is studied. The lubricants that were selected are presented. The gearbox test rigs and all of the experimental procedures are explained. The numerical power loss model for the full planetary gearbox is also introduced and its estimations compared with the experimental results.

4.1. Planetary gearbox

The selected gearbox is an industrial planetary speed reducer with a transmission ratio of 4 with a nominal input speed of 1000 rpm and a nominal output torque of 2500 Nm.

Planetary transmissions have some advantages over parallel axis gearboxes. In a planetary gearbox, the axis of the input shaft is collinear with the axis of the output shaft, and due to this particularity it is possible to obtain compact designs with high power density (nominal power that the gearbox is capable of transmitting over the volume of the planetary transmission), which makes planetary gearboxes perfect candidates for a wide range of applications. The efficiency of this kind of gearboxes is already quite high, mainly due to the way the load is distributed between the gear meshes and the very low sliding velocities of the planet/ring gear mesh.

The tested planetary gearbox was fully disassembled (details shown in figures 4.1 and 4.2) and therefore the components of the gearbox could be measured and listed. The geometrical characteristics of the gears are listed in table 4.1 and the gearbox rolling bearings are listed in table 4.2. While disassembled it was possible to verify that the deep grove ball bearing is shielded and contains its own lubricant (grease). The tapered roller bearings are oils sump lubricated (gear oil). The planets connect to the planet carrier through a pin and roll over full-complement (cageless) needle roller bearings. Figure 4.3 is a manufacturer's scheme of the assembly of the planetary gearbox.

Figure 4.1.: Disassembled planetary gearbox.

Figure 4.2.: Detail of the full-complement (cageless) needle roller bearing.

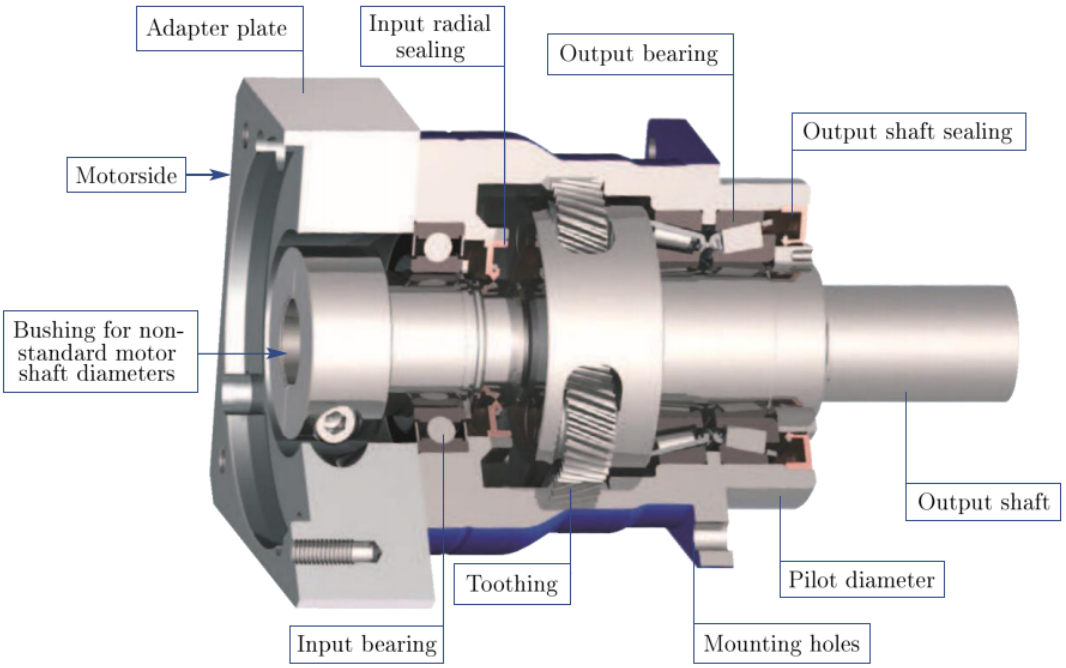

Figure 4.3.: Scheme of the planetary gearbox.

Table 4.1.: Geometrical characteristics of gears in the planetary gearbox.

	Sun	**Planet**	**Ring**
number	1	3	1
$\boldsymbol{m}$ [mm]		2	
$\boldsymbol{\alpha}$ [°]		20	
$\boldsymbol{\beta}$ [°]		11	
$\boldsymbol{z_i}$ [/]	36	36	-108
$\boldsymbol{b}$ [mm]	42	40	42
$\boldsymbol{x}$ [mm]	-0.0536	-0.0536	0.1609
$\boldsymbol{k \cdot m}$ [mm]	−0.0665	−0.0665	0
$\boldsymbol{Ra}$ [μm]		0.08	
$\boldsymbol{d}$ [mm]	73.348	73.348	-220.043
$\boldsymbol{d_b}$ [mm]	68.772	68.772	-206.318
$\boldsymbol{d_a}$ [mm]	77.000	77.000	-215.399
$\boldsymbol{d_w}$ [mm]	73.131	73.131	-219.392
$\boldsymbol{\alpha_{tw}}$ [°]		19.880	
$\boldsymbol{a_w}$ [mm]		73.131	

Table 4.2.: Rolling bearings and seals in the planetary gearbox.

Component	**Qty.**	**Ref.**	**Lubrication**
Tapered RB (TRB)	2	32022 X/Q	gear oil
Deep groove BB (DGB)	1	6217-2Z	LiM grease: ($\nu_{40} = 100$, $\nu_{100} = 10$ cSt)
Input seal (lip seal)	1	140×170×13	gear oil
Output seal (lip seal)	1	72×100×10	gear oil
Full-complement needle RB (FCNRB)	3 sets of 23 needle rollers	6×23	gear oil

4.2. Wind Turbine Gear Oils

The most important role of a lubricant is the reduction of friction and wear with the aim of providing smooth operation and a satisfactory life for machine components.

The lubricants that are usually found in a gearbox are the liquid lubricants (oils) and lubricating greases. Despite the main focus in this thesis being in the wind turbine gear oils, it should be noted that lubricant greases mainly the ones with polymer based thickeners have been the focus of many studies [106–111] (power loss in rolling bearings).

Wind turbine lubricants need to last as long as possible, offering excellent oxidation and shear stability, whilst protecting key turbine components such as main bearings from failure, and gears from micropitting [112].

Four fully formulated ISO VG 320 wind turbine gear oils were selected, two of them being mineral based oils (MINR and MINE) and the other two being synthetic based oils: a poly$-\alpha-$olefin (PAOR) and a polyalkyleneglycol (PAGD).

4.2.1. Techniques and devices

The chemical composition and the physical properties of the selected oils were listed in the manufacturer's data sheets. Nevertheless, a few measurements regarding the physical properties were carried out in order to confirm the data given by the manufacturers and to have a higher accuracy in the lubricant properties and behaviour.

Viscometry

To measure the viscosity of the selected lubricants an Engler viscometer was used, which consists of two containers, one inside another, supported by a three legged adjustable support [113].

The desired fluid is placed in the inner container which has a hole on the bottom. A wood pointer is used to close or open the hole, in order to stop or allow the fluid flow. The space between the inner and outer container is filled with thermal fluid. The containers are heated by an electrical element and the temperature of each fluid is controlled with a thermometer [114].

The measurement procedure followed the IP 212/92 standard [113]. Figure 4.4a shows the Engler viscometer used to measure the viscosity of the tested oils.

Densitimetry

In order to measure the variation of density of the tested oils at atmospheric temperature a density meter was used.

The density meter used, figure 4.4b, collects a 2ml sample and measures the density of a fluid in a range of temperatures between 0 and 40°C. The density of each oil sample was measured at three different temperatures so that the thermal expansion coefficient was determined [115], allowing the calculation of each oil's density at a given temperature.

(a) Engler viscometer. (b) Anton Paar DMA 35N density meter.

Figure 4.4.: Devices used.

Film Thickness and traction curves

Film thickness and stribeck curve measurements were performed on an EHD2 ball-on-disc test apparatus from PCS Instruments equipped with optical interferometry as presented in Figure 4.5 [116]. The machine measures the lubricant film thickness properties in the contact formed between a 3/4″ diameter steel ball and a rotating glass disk by optical interferometry. The lubricant film thickness at any point in the image can be accurately calculated by measuring the wavelength of light at that point. Normally the system measures the wavelength of the light returned from the central plateau of the contact and hence calculates the central film thickness.

For the traction measurements the ball runs against a steel disc and the load is applied by moving the ball upwards towards disc, generating contact pressures up to 1.11 GPa.

The EHD2 ball-on-disc test rig was already used in a previous work. For further details on the machine's working principle and test methodology please refer to ref. [116]. There are no film thickness and stribeck curve measurements for the PAGD gear oil. The reason being that PAGD's base oil might be incompatible with the seals used in the EHD2 machine.

Figure 4.5.: EHD2 ball-on-disc test apparatus from PCS Instruments.

4.2.2. Lubricant properties

The kinematic viscosity variation with temperature calculation followed the standard ASTM D341 [114]. For the four tested gear oils, the viscosity variation with temperature is shown in figure 4.6a.

It is possible to observe that at 40°C the gear oils have similar kinematic viscosity except for PAGD, which is lower. With temperature increase, the viscosity decreases, being the MINR the oil with the highest variation and PAGD being the lowest. MINE and PAOR show a very similar behavior for the considered range of temperatures. This behaviors are easily related to the viscosity index. In Table 4.3 is possible to observe that MINR has the lowest viscosity index while PAGD has the highest. MINE and PAOR have similar viscosity index and the same viscosity at 40°C thus showing a very similar behavior.

The density variation with temperature is shown in figure 4.6b. It is to be noticed that PAGD has a range of density considerably higher than all the other oils, having a higher density than water for temperatures below 90°C. The chemical composition and the physical properties are summarized in Table 4.3.

In terms of chemical composition, the largest differences are in the phosphorous, boron and sulphur values of PAGD when compared to the other oils. PAGD has more than twice the amount of phosphorus, while having values dozen of times lower of sulphur and boron. Phosphorus, boron and sulphur are known to be used in the chemical composition of the gear oils as extreme pressure additives.

Table 4.4 shows the pressure-viscosity coefficients given by Gold's equation [117], α_{Gold}, as well as, some values calculated after the experimental film thickness measurements [116]. The α_{FTM} values were calculated using a bounded non-linear least squares optimization algorithm. The objective function was the relative difference between the experimental and numerical data (film thickness). For further detail on the film thickness model that was used and optimization procedure please refer to ref. [116].

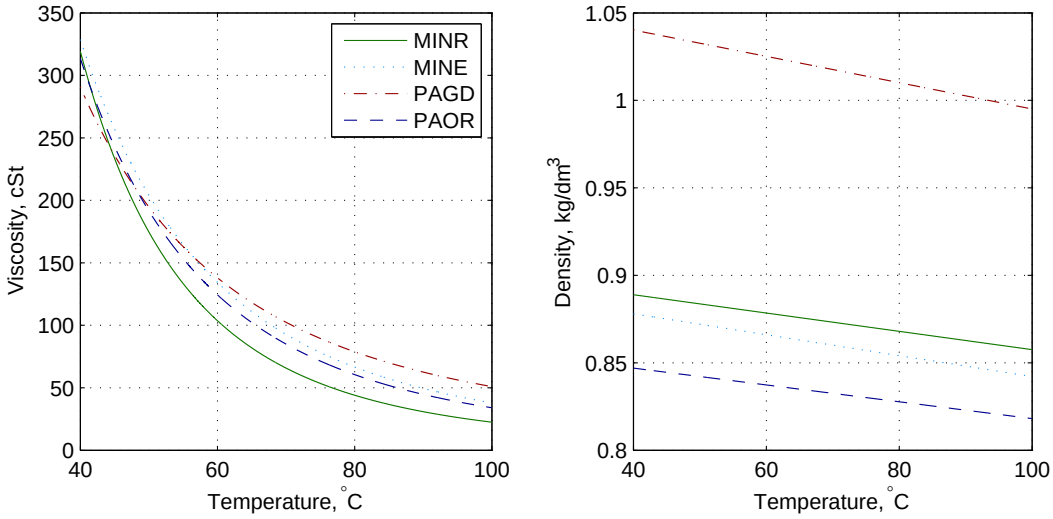

(a) Viscosity vs temperature.

(b) Density vs temperature.

Figure 4.6.: Tested oils' viscosity and density variations with temperature.

The values given by Gold's equation are clearly dependent on the lubricant type (base oil) and on the temperature. The α_{FTM} values are, in general, lower than the corresponding α_{Gold} values. Such difference is very large in the case of the MINE gear oil (42 % lower), which is known to have shear thinning properties due to the viscosity improving additive PAMA [116]. In fact Greenwood *et al.* [118] studied a Mineral+PAMA blend with 4% of PAMA that exhibited shear thinning properties. The influence of the temperature also doesn't seem consistent, e.g. α_{FTM} @ 40 °C≈α_{FTM}@ 80 °C for MINR.

This indirect prediction of the pressure-viscosity coefficient using film thickness measurements, although useful, needs further research since there is not a clear consensus in the literature [116, 119, 120].

The Stribeck curves were also measured at 80 and 120 °C and the results are presented in Figure 4.7. The coefficients of friction are presented using the modified Hersey number suggested by Brandão [40] and given by equation (4.2.1). The original Hersey number (S) is given by equation (4.2.2).

$$S_p = \frac{\eta_0 \cdot (U_1 + U_2) \cdot \alpha^{1/2}}{F_N^{1/2}} \tag{4.2.1}$$

$$S = \frac{\eta_0 \cdot (U_1 + U_2)}{F_N} \tag{4.2.2}$$

Brandão proposed that for a modified Hersey number $S_p < 10^{-9}$, the contact is under boundary film lubrication, while for $S_p > 10^{-7}$ it is under full film lubrication.

Table 4.3.: Chemical composition and physical properties of the tested lubricants.

	MINR	**PAOR**	**MINE**	**PAGD**
Base oil:	Mineral	Poly−α−olefin	Mineral +40% PAMA	Polyalkalene Glycol
		Chemical composition		
Zinc (Zn) [ppm]	0.9	<1	3.5	1.0
Magnesium (Mg) [ppm]	0.9	<1	0.5	1.4
Phosphorus (P) [ppm]	354.3	460	415.9	1100
Calcium (Ca) [ppm]	2.5	2	0.5	0.8
Boron (B) [ppm]	22.3	36	38.4	1.0
Sulfur (S) [ppm]	11200	6750	5020	362
		Physical properties		
Density @ 15$^{\circ}C$ [g/cm^3]	0.902	0.859	0.893	1.059
Thermal expansion coefficient x 10^{-4} [K^{-1}]	-5.8	-5.6	-6.7	-7.1
Viscosity @ 40$^{\circ}C$ [cSt]	319.22	313.52	328.30	290.26
Viscosity @ 70$^{\circ}C$ [cSt]	65.81	84.99	93.19	102.33
Viscosity @ 100$^{\circ}C$ [cSt]	22.33	33.33	37.13	51.06
Viscosity Index	85	150	163	241

The results presented in Figure 4.7 show the expected behaviour for $S_p > 10^{-7}$. Under these conditions the coefficient of friction of the synthetic formulations is quite similar for the same temperature and significantly lower than MINR. The influence of the temperature is clear for all the wind turbine gear oils: the coefficient of friction decreases when the temperature increases (see Figures 4.7a and 4.7b).

At 80 °C, the modified Hersey number never reaches 10^{-9} and so the oils remain under mixed film lubrication for values $S_p < 10^{-7}$. At 120 °C the oils come closer to the expected boundary lubrication condition, and for these conditions very similar coefficients of friction values are observed, see Figure 4.7b, whatever the base oil and additive package considered.

The specific film thickness and Stribeck curves results indicate that the base oil is

Table 4.4.: Pressure-viscosity coefficients determined based on film thickness measurements (α_{FTM}) and Gold equation (α_{Gold}).

θ_{oil}	**Pressure-viscosity**	**MINR**	**PAOR**	**MINE**	**PAGD***
50 °C	α_{FTM}	1.443	1.143	0.651	–
	α_{Gold}	1.995	1.469	1.346	1.208
80 °C	α_{FTM}	1.403	1.053	0.653	–
	α_{Gold}	1.667	1.262	1.112	1.057
100 °C	α_{FTM}	1.308	0.942	0.644	–
	α_{Gold}	1.526	1.181	1.011	0.9843

* - PAGD was not tested due to incompatibility with the PCS EHD2 test rig seals.

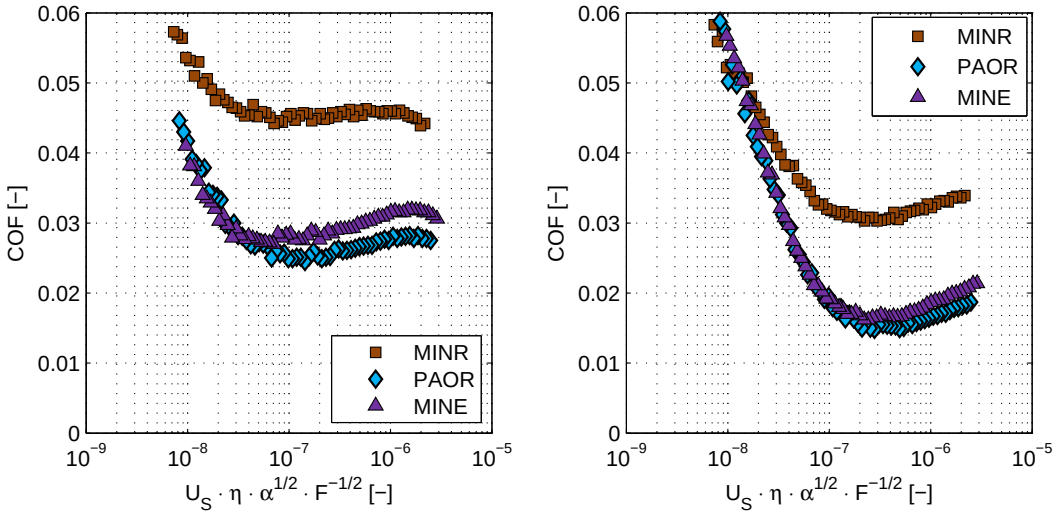

(a) 80 °C. (b) 120 °C.

Figure 4.7.: Stribeck curve measurements [116].

a deciding factor regarding traction under full film conditions. However, in boundary conditions the traction coefficient is quite similar between the different oil formulations [9, 116].

4.3. Gearbox Efficiency Measurement

As previously discussed in chapter 1 power loss models often need to be experimentally validated or calibrated in order to be confidently used. This section is dedicated to the presentation of the experimental methodology that was followed to study the power loss in a planetary gearbox. The planetary gearbox in study is presented as well as the gearbox test rigs. The experimental procedure that was followed for the total and no-load losses was also presented. The reasoning behind the experimental plan that was devised is also demonstrated.

4.3.1. Gearbox test rigs

Two different test rigs were used to study the power loss in the planetary gearbox. One of the rigs was used to evaluate the total losses and the other one the no-load losses.

Total power losses

The gearbox test rig works on a back-to-back configuration with recirculating power. Two sets of helical gears, represented by number 2 and 7 on figure 4.8, are used in order to recirculate the power. Both sets are lubricated by oil injection.

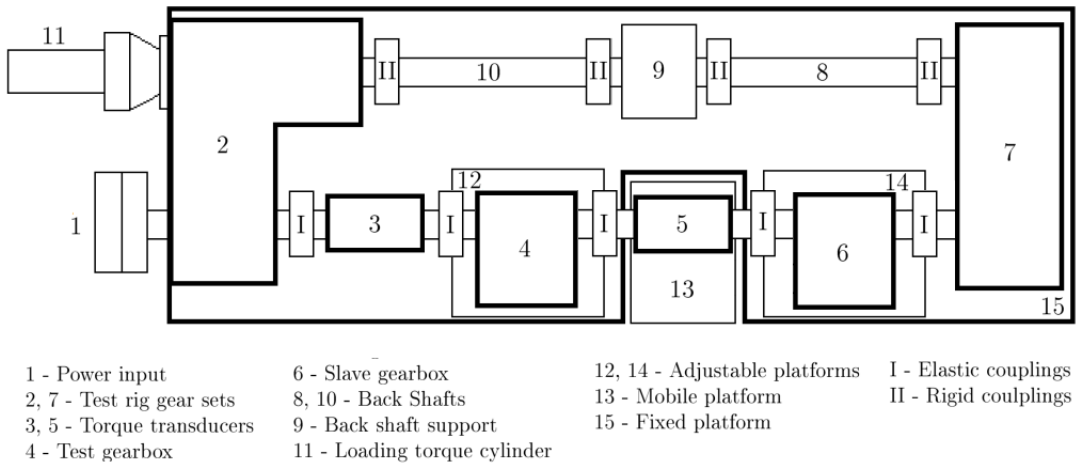

Figure 4.8.: Top view diagram of the gearbox test rig.

The test and slave gearboxes, numbers 4 and 6, work on a back-to-back configurations, matching the input speed of one gearbox with the output speed of the other. Thus, only reversible gearboxes can be tested. The test rig and the back-to-back configuration of the gearboxes is presented in figure 4.9.

The test rig is able to test gearboxes with asymmetrical geometries, due to the adjustable platforms (12 and 14). The torque transducer (5) placed between the test and slave gearboxes can have its height and depth adjusted by the mobile platform (13).

The torque loading mechanism consists of a hydraulic cylinder that introduces an axial displacement on one of the helical gears of the gear set 2. The axial displacement forces the wheel to slightly rotate, creating a torsional displacement in the test rig components and so loading it with a static torque.

The rotational speed of the electric motor and the torque on the torque transducer (5) are set on the central control board, show in figure 4.10.

On its current configuration, the test rig has the highest torque in between the gearboxes promoting a smoother operation. The test rig allows operating conditions in the following range:

- Rotational speed: $100 - 1900$ rpm;
- Torque: $100 - 1300$ Nm.

The torque control is done in the torque transducer (5) which is located between both gearboxes. The gearboxes setup is so that the highest torque only occurs in between gearboxes, allowing to test higher loads without submitting the rest of the test rig to those loads, therefore, the rest of the test rig operates at lower loads and higher speeds, which benefits speed control of the driving motor.

In order to assess the working temperatures, the test rig is equipped with several thermal sensors, some of which were installed in the test gearbox. The sensors are measuring:

- The oil temperature in two different zones (industrial grade PT100 RTD's);
- The wall temperature (industrial grade PT100 RTD's);
- The room temperature.

A picture of the gearbox instrumented with the three temperature sensors is shown in figure 4.11.

The input and output torque as well as rotating speeds were also constantly measured and recorded over time.

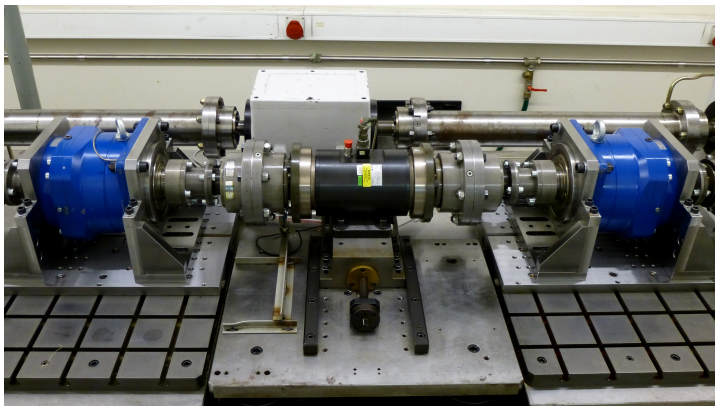

Figure 4.9.: Photograph of the test rig (back-to-back configuration).

Figure 4.10.: Central control board.

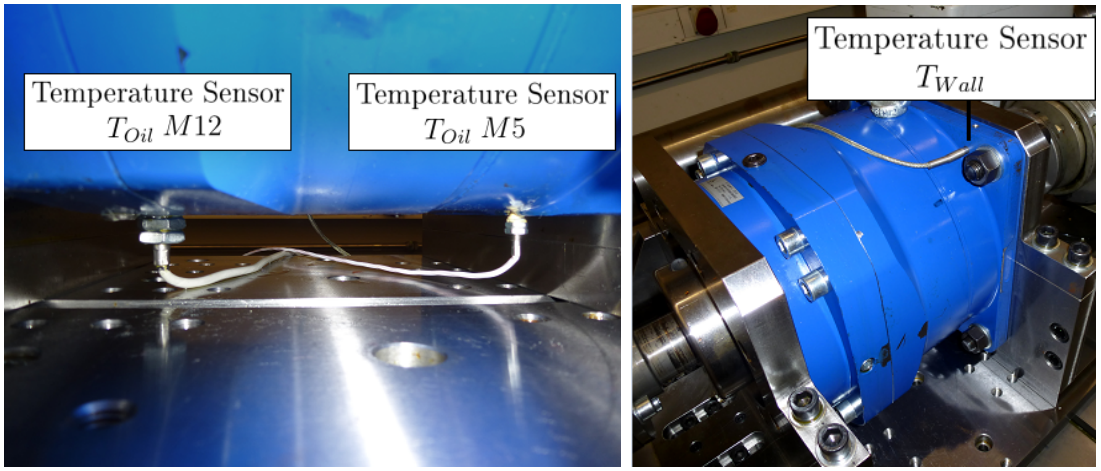

(a) Oil temperature sensors. (b) Wall temperature sensor.

Figure 4.11.: Temperature sensors' positioning in the test gearbox.

No-load power losses

A no-load power loss test rig was developed from the ground up in order to more precisely evaluate the no-load power loss in the planetary gearbox. Figure 4.12 shows the no-load gearbox test rig and its central control board.

The test rig allows the study of no-load losses in several gearbox configurations as long as they are guaranteed to fit within the dimensional restrictions of the test rig and the no-load loss is not higher than the torque that the torque cell is capable of measuring. The electric motor of the test rig has a nominal power of 7.5 kW and a nominal rotational speed of 2920 rpm at 400 V / 50 Hz. In its current configuration the gearbox test rig allows input speeds from ≈30 up to ≈1000 rpm. It should also be noted that different operating ranges are available by changing the driving pulleys.

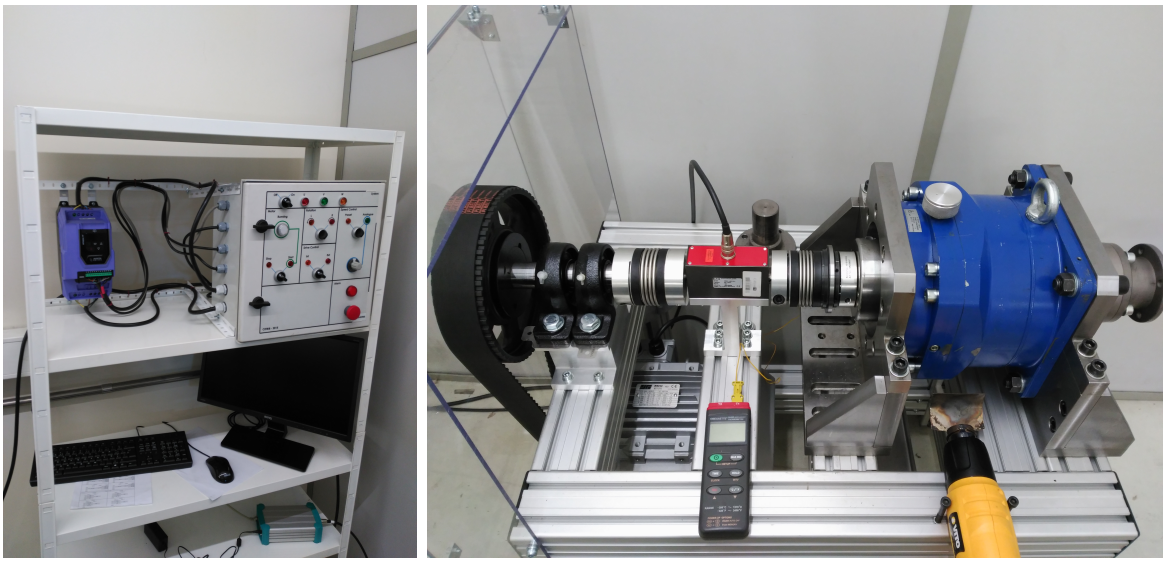

(a) Central control. (b) No-load gearbox test rig.

Figure 4.12.: No-load gearbox test rig and central control.

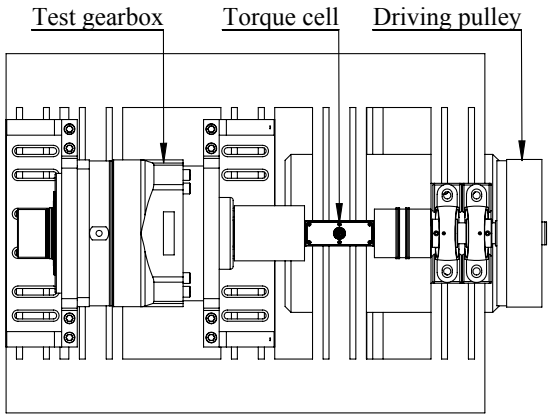

Figure 4.13.: Scheme of the no-load power loss gear box test rig

The torque measuring device is an ETH Messtechnik DRDL II torque transducer assembled at the input of the test gearbox, as shown in figure 4.13. The technical characteristics of the sensor are displayed in Table 4.5. The system uses a sensor interface (Valuemaster$_{Base}$) to communicate with a PC or Notebook with an Ethernet connection. The integration of the torque cell with the software allows to record the torque values with an adjustable sampling rate (from 1 to 1000 Hz).

Table 4.5.: Technical specifications of the ETH DRDL II torque cell.

Torque Transducer Type DRDL II	
Nominal torque [Nm]	50
Measurement range [Nm]	5/10/20/50
Non-linearity [%]	< 0.1
Hysteresis [%]	< 0.1
Accuracy [%]	0.01
Temperature sensitivity [$\%/K$]	0.01
Torque Measuring Module Type $ValueMaster_{Base}$	
Accuracy [%]	0.02
Non-linearity [%]	0.1
AD converter resolution	11 bit + 1 bit for leading sign

The gearbox oil sump temperature was measured using a Type-k thermocouple installed in a Data Logger OMEGAETTE HH306 THERMOMETER. Figure 4.14 shows the Type-k thermocouple installed in the planetary gearbox as well as the temperature data logger.

4.3.2. Experimental campaign

Load tests

In order to fully understand the influence of the operating conditions on the torque loss behaviour of the gearbox, a grid of 16 tests was planned, comprising 4 different loads (1600/2000/2400/2800 Nm) and 4 different speeds (100/150/200/250 rpm). The operating conditions of the 16 tests grid were selected according to the working conditions allowed by the test rig and according to the planetary gearbox specifications. From that grid, 5 tests were selected aiming to match the working conditions of one of the stages of a gearbox used in wind turbines, in terms of Hertz pressure and tangential speed.

For the same geometry the Hertzian pressure is essentially function of the load while the tangential speed is function of the rotational speed. The contact pressures and the tangential speeds resulting from the imposed working conditions on the test gearbox are presented in Table 4.6, and the contact pressures and tangential speeds of a gearbox used in a 2.5 MW wind turbine [121] are presented in Table 4.7. The full planning of the 5 grid tests is shown in Table 4.8. The speeds and torques mentioned are the ones measured between the gearboxes (Figure 4.8).

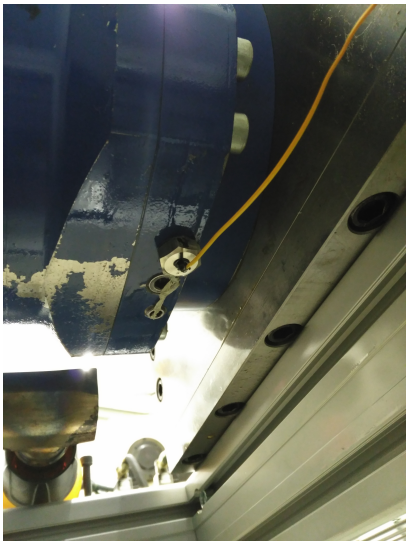

(a) Type-k thermocouple.

(b) Data Logger OMEGAETTE HH306 THERMOMETER.

Figure 4.14.: Type-k thermocouple and temperature data logger in the no-load gearbox test rig.

Table 4.6.: Tangential speed at the pitch line and average Hertz Pressure in the test gearbox.

Imposed rotational speed [rpm]	**Tangential speed** [m/s]	**Imposed torque** [Nm]	**Hertz pressure** [N/mm^2]
100	1.15	1600	598.6 (SP)
			323.1 (PR)
150	1.72	2000	665.3 (SP)
			357.8 (PR)
200	2.30	2400	724.9 (SP)
			388.8 (PR)
250	2.87	2800	779.3 (SP)
			416.8 (PR)

SP – Sun-Planet contact
PR – Planet-Ring contact

Table 4.7.: Tangential speed at the pitch line and average Hertz Pressure in gearboxes used in wind turbines.

Gear Stage	**Tangential Speed** [m/s]	**Hertz pressure** [N/mm^2]
1^{st} Stage	1.63	726.3 (SP)
		383.3 (PR)
2^{nd} Stage	5.49	739.2 (SP)
		562.7 (PR)

SP – Sun-Planet contact
PR – Planet-Ring contact

Table 4.8.: Experimental test plan.

Oil	Speed [rpm]	Torque [Nm]	Power [kW]	Test time [min]
PAOR/MINR/MINE/PAGD	100	2800	29	240
	150	2000	31	240
		2400	38	240
		2800	44	240
	200	2800	59	240

The duration of each load test was four hours so that stabilized operating conditions (load, speed and temperatures) could be achieved.

The ventilation of the room where the test rig operates could not guarantee a stabilized room temperature. Nevertheless, the power loss is function of a temperature difference ($\Delta T = T_{oil} - T_{room}$) which achieved reasonably stable values (variation < 0.8 °C/h).

The values read by the sensors were automatically recorded by the central control with a frequency of 0.5 Hz. The calibration values of the torque transducers were checked periodically in order to assure proper function.

The gearboxes' (test and slave) lubricating oil was always changed at the same time. The oil was drained through a plug in the bottom and then the gearboxes were flushed with petroleum ether, except for PAGD which was first flushed with an ISO VG320 ester oil and a special solvent afterwards (isopropanol). The solvent was removed the same way as the oil, and then the gearboxes were left to dry out any solvent remains for 12 h and then were filled with 1 L of fresh lubricant.

No-load tests

The no-load loss tests were done in the in-house developed no-load gearbox test rig (subsection 4.3.1).

The tests were done taking into account and imposing the oil sump temperature that was measured in the free oil sump temperature load tests. Table 4.14 shows the oil sump temperatures at stabilized conditions, as measured at temperature probe $T_{Oil}\ M12$ (Figure 4.11a).

The test gearbox was mounted on the gearbox no-load loss test rig as shown in Figure 4.12b. The nominal speed of a certain test was imposed using the test rig central control board (Figure 4.12a) and the gearbox was heat up using an heat chamber up to the desired test temperature. For each single test the torque measurement starts at $T_{Oil}\ M12\ -1$°C and finishes at $T_{Oil}\ M12\ +1$°C. The no-load torque loss is then taken as the average of the torque values measured between $T_{Oil}\ M12\ \pm 1$°C

In order to test different lubricants the gearbox was flushed following the already described process in subsection 4.3.2.

4.4. Planetary Gearbox Power Loss (classical model)

The classical power loss model that was presented in chapter 1 can be applied to estimate the power loss in the planetary gearbox presented in chapter 4.3, but some particular aspects must be taken into consideration. In this chapter the speeds, loads and particular model implementation details are discussed.

4.4.1. Kinematics and loads

According to Anderson *et al.* [122] the angular speed of tooth engagement is the gear speed that would be obtained as if the planet carrier was stationary. In this configuration the sun/planet speed is the sun gear absolute speed minus the carrier speed. The planet/ring mesh speed is found by setting the ring speed equal to the negative of the carrier speed [122]. In this way the torque balance is not modified, therefore the loads are still identical for a fixed or rotating carrier [122]. Figure 4.15 is a two view schematic of a fixed ring planetary gearbox with three planets. Figure 4.16 shows the graphical determination of the peripheral and rotational speeds of a planetary gearbox [123].

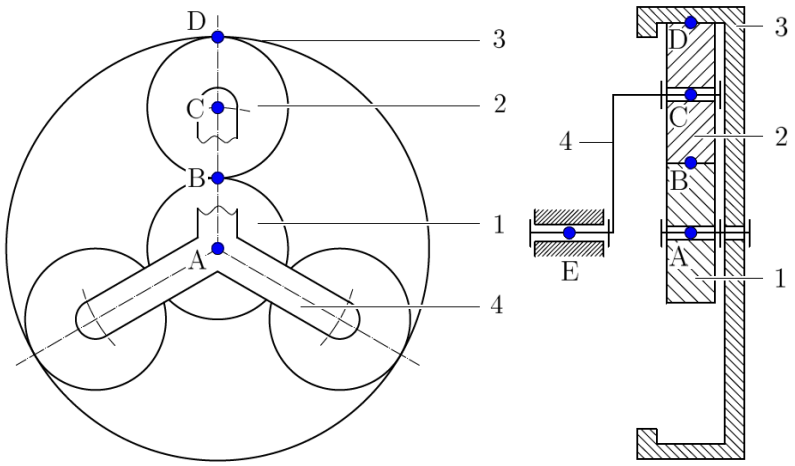

(a) Front view. (b) Side view.

1 - Sun; 2 - Planet; 3 - Ring; 4 - Planet carrier.

Figure 4.15.: Schematic representation of a planetary gear.

With the aid of figures 4.15, 4.16 and the concept of the stationary planet carrier already introduced, the relevant speeds of the sun, planet, ring and planet carrier were calculated (equations (4.4.1) to (4.4.5)).

The gear ratio in a planetary gear is given by equation (4.4.1).

$$u^{plnt} = 2 + \frac{2 \cdot z_p}{z_s} \tag{4.4.1}$$

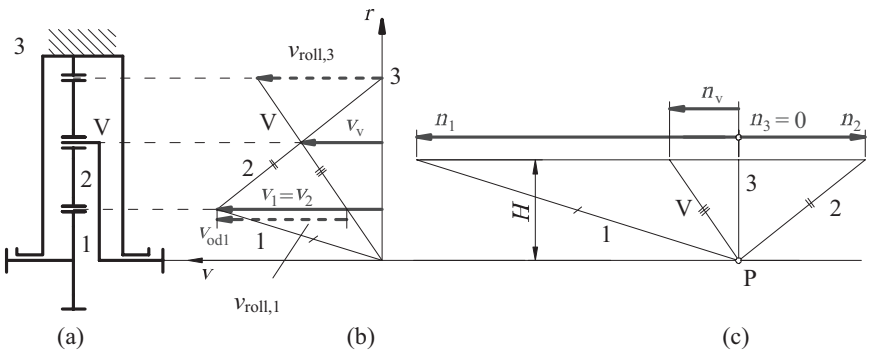

Figure 4.16.: Graphical dethermination of the peripheral and rotational speeds: a) schematic of the planetary train, b) peripheral speed diagram, c) rotational speed diagram [123].

Following the gear ratio, the planet carrier speed is calculated according to equation (4.4.2).

$$\omega_c = \frac{\omega_s}{u^{plnt}} \tag{4.4.2}$$

To find the relative speed (frame of reference attached to the planet carrier) of the sun gear the speed of the speed of the planet carrier (4.4.2) must be subtracted to the the speed of the sun gear (in a fixed frame of reference) which yields equation (4.4.3).

$$\omega_s^r = \omega_s - \omega_c \tag{4.4.3}$$

Since a reference frame rotating attached to the planet carrier is considered the centres of the planets remain stationary in this referential, therefore the relevant relative speed is given by equation (4.4.4).

$$\omega_p^r = \omega_s^r \cdot \frac{z_s}{z_p} \tag{4.4.4}$$

The relative speed of ring is simply equal (in absolute value) to the speed to the planet carrier (equation (4.4.5)).

$$\omega_r^r = \omega_c \tag{4.4.5}$$

Table 4.9.: Calculated gear loss factor, H_V.

Contact	H_V^G
Sun-Planet	0.1497
Planet-Ring	0.0446

The normal and tangential loads in the sun, planets and ring gears in a planetary gearbox can be calculated according to the expressions suggested in the MAAG gear book [91]. Equations (4.4.6) to (4.4.8) express the loads for each gear contact in the planetary gearbox (sun-planet and planet-ring contacts).

$$F_{bt} = \frac{Tc}{u \cdot N_p \cdot r_{bs}} \tag{4.4.6}$$

$$F_{bn} = \frac{F_{bt}}{\cos(\beta_b)} \tag{4.4.7}$$

$$F_{axi} = F_{bt} \cdot \tan(\beta_b) \tag{4.4.8}$$

4.4.2. Gears load losses

The gears load dependent losses were calculated according to the classical model, equation (1.1.1).

The gear loss factor H_V was calculated using the average power loss method suggested in equation (2.5.6) in subsection 2.5.1. The load distribution was calculated applying the quasi-static local elastic model previously introduced in section 2.3. Table 4.9 displays the gear loss factors that were calculated (planetary gear geometry from table 4.1).

Following the methodology introduced in previous works [2,9] Schlenk's CoF formulation, equation (1.1.14) was selected to estimate the average CoF in the gear contact. The lubricant parameters, X_L for the lubricants presented in section 4.2 are already available [2] (Table 4.10). According to what it is known from traction curve experiments and also experimentally observed in this work (figures 4.7), the coefficient of friction reaches a minimum under mixed film steadly increasing in different conditions. The formulation proposed by Schlenk [48] cannot replicate this increase with Λ, therefore its domain of application is limited from boundary up to mixed lubrication. In fact according to the findings in previous works [2] Schlenk's equation only holds up to specific film thicknesses of $\Lambda = 2.5$. In order to mitigate this issue for operating points where $\Lambda \geq 2.5$ the average CoF μ_{mz} was calculated with the

sum velocity at pitch point $U_1 + U_2$ that would give $\Lambda = 2.5$ (the lowest acceptable μ_{mz}).

Table 4.10.: Lubricant parameter X_L for the selected oils [2].

Oil	X_L
PAOR	0.666
MINR	0.846
MINE	0.751
PAGD	0.585

In order to calculate the gear mesh input power P_{IN} (1.1.1) ($P_{IN} = F_{bti} \cdot \omega_i \cdot r_{bi}$) as well as the sum velocity at pitch point ($U_1 + U_2$) in the Schlenk's CoF (1.1.14) the rotational speeds of the gears that must be considered are the ones that are in a reference frame that runs attached to the planet carrier, i.e., the speeds of the gears as if the planet carrier was stationary. The angular speeds to find these quantities were described in subsection 4.4.1.

4.4.3. Rolling bearings losses

According to table 4.2 the planetary gearbox presented in subsection 4.1 has 3 full-complement needle roller bearings, a deep groove ball bearing and two pre-loaded tapered roller bearings.

Full-complement needle roller bearings

The power loss of the full-complement needle roller bearings presented in table 4.2 was estimated considering the "Old SKF Model" presented in subsection 1.3.2.

For full-complement needle roller bearings Harris [124,125] suggests that the power loss is that of a needle roller bearing with rolling elements of the same size multiplied by a factor of 1.5 to 2, a factor of 1.75 was selected. The selection of this particular value (1.75) lies on the idea that a precise value could not be assessed without direct torque loss measurement, therefore the middle/average value was selected.

The f_1 factor (table 4.11) is the CoF due to radial load for needle roller bearings. SKF suggests the same constant value for every lubricant which is not optimal. According to table 4.10, MINR is the oil with the worst relative performance, then f_1 was kept at $f_1 = 0.002$, as suggested by SKF, for MINR. The relative reduction expressed in X_L, promoted by the other lubricants was applied to the base f_1, as represented by equation (4.4.9).

$$f_1^{oil} = f_1 \cdot \frac{X_L^{oil}}{X_L^{MINR}} \tag{4.4.9}$$

Table 4.11.: Selected factors of influence for the full complement needle roller bearings.

Factor	Value
f_0	6
f_1	0.002
f_2	0.006

The speed that should be considered to calculate the full-complement needle rolling bearings losses (model presented in subsection 1.3.2) is the relative speed of the planets ω_p^r (equation (4.4.4)).

The radial load in each full-complement needle roller bearing is given by equation (4.4.10). Due to the nature of the helical planetary gears the resulting axial load in the planets is theoretically equal to zero.

$$F_R = \frac{T_C}{Np \cdot a} \tag{4.4.10}$$

It should be noted that in no-load conditions the full-complement needle roller bearing no-load power loss is estimated considering $M_{1,2}^{rol} = 0$ in equation (1.3.3). The aforementioned 1.75 correction factor still applies to the no-load component M_0^{rol}, equation (1.3.3).

Tapered roller bearings

The model that was presented in subsection 1.3.3 was considered to calculate the tapered roller bearing power loss.

The taper roller bearings (table 4.2) in the planetary gearbox are in a back-to-back configuration and subjected to an axial pre-load. This axial pre-load was estimated to be equal to the minimum axial load for proper function, which is $F_{axi}^0 = 4.66$ kN. The total load in the tapered rolling bearings is then given by the combination of the axial pre-load and the axial force introduced by the three gear contacts, $3 \cdot F_{axi}$, (equation (4.4.8)), i.e. $F_{axi}^0 \pm 3 \cdot F_{axi}$ (in no-load operating conditions $F_{axi} = 0$ and $F_{axi}^0 =$ pre-load).

In its standard configuration the SKF rolling bearing torque loss model, presented in subsection 1.3.3, suggests for the sliding CoF μ_{sl}^{SKF} the reference values of $\mu_{bl}^{SKF} = 0.15$ and $\mu_{EHD}^{SKF} = 0.002$.

In previous works [1] the influence of the lubricants presented in table 4.3 in the μ_{sl}^{SKF} was studied for thrust ball and roller bearings. It was observed that the reference μ_{bl}^{SKF} and μ_{EHD}^{SKF} are not the same for each lubricant, in fact the values given by SKF are the worst case scenario, which makes sense from a safe design perspective. The reference μ_{bl}^{SKF} and μ_{EHD}^{SKF} for either thrust roller and ball bearings are quite different from the ones suggested for tapered roller bearings. The custom

μ_{bl}^{exp} and μ_{EHD}^{exp} that were derived from experimental results in thrust roller bearings [1] (the rolling elements are more similar to the ones found in a tapered roller bearing) were compared with the reference ones given by SKF and a reduction ratio was calculated according to equation (4.4.11). Table 4.13 shows the calculated $\mu_{bl,EHD}^{ratio}$ ratios. This same ratio was then applied to the reference μ_{bl}^{SKF} and μ_{EHD}^{SKF} for tapered roller bearings. Table 4.12 shows the reference μ_{bl}^{SKF} and μ_{EHD}^{SKF} for thrust roller and tapered roller bearings.

Table 4.12.: μ_{bl}^{SKF} and μ_{EHD}^{SKF} .

Oil	μ_{bl}^{SKF}	μ_{EHD}^{SKF}
Tapered RB	0.15	0.002
Thrust RB	0.15	0.05(mineral)/0.04(synthetic)

$$\mu_{bl,EHD}^{ratio} = \frac{\mu_{bl,EHD}^{exp}}{\mu_{bl,EHD}^{SKF}} \tag{4.4.11}$$

Table 4.13.: Ratio for the calculation of μ_{bl}^{SKF} and μ_{EHD}^{SKF} in tapered roller bearings for each lubricant.

Oil	μ_{bl}^{ratio}	μ_{EHD}^{ratio}
PAOR	0.26	0.25
MINR	0.23	0.36
MINE	0.29	0.20
PAGD	0.17	0.25

Deep groove ball bearings

The "New SKF model" that was presented in subsection 1.3.3 was considered to calculate the deep groove ball bearing power loss.

A lubricating grease with viscosity $\nu_{40} = 100$ cSt and $\nu_{100} = 10$ cSt was considered for the deep groove ball bearing. The load acting in this rolling bearing is simply the resultant of the axial forces, i.e $3 \cdot F_{axi}$. It should be noted that as per SKF's recomendation [66] the churning losses due to grease lubrication should disregarded. In no-load conditions $F_{axi} \approx 0$ therefore the DGBB power loss in no-load conditions is estimated to be zero.

4.4.4. Seals power Loss

Following the results of previous works [2, 9] the Simrit equation (1.4.2) was selected. The model that was selected only considers the rotational speed of the shaft, in this case, the input and output speeds which are related by the gearbox ratio as shown in equation (4.4.1). The seal dimensions were presented in table 4.2.

4.4.5. Power losses due to fluid-body interactions

As it was previously referred in section 1.2 the no-load power losses in gears have been object of study by several different authors and a considerable amount of experimental and analytical studies are available. Some of the most relevant are the ones presented by Terekhov [64], Boness [59], Höhn *et al.* [28], Seetharaman [60] and Changenet *et al.* [55,62]. Recently Concli *et al.* [11,12,63] proposed a solution for the problem of the churning power loss in a planetary speed reducer which was based on a CFD approach.

In the present work, due to the complexity of the problem the churning losses ($P_{VZ0} + P_{VX}$) were not directly estimated with models, but were rather estimated from no-load loss measurements that were performed in the newly developed no-load loss gearbox test rig that was described in subsection 4.3.1. As described in the experimental procedure (subsection 4.3.2) the no-load loss tests were performed after the load tests so that the oil sump operating temperatures could be known and therefore imposed during the no-load loss test. In this way the planetary gearbox no-load loss could be measured with an oil sump temperature that matched the temperatures of the corresponding load test.

Estimating the no-load gear and planet carrier losses, $P_{VZ0} + P_{VX}$

In no-load conditions different sources contribute to the no-load loss of the planetary gearbox that was tested, namely: the input and output seals, the tapered roller bearings due to pre-load and churning, the full-complement needle roller bearings due to churning, the gears no-load losses due to churning and pocketing and the auxiliary churning loss due to the action of the planet carrier. From all of the mentioned no-load loss sources only the gears no-load losses due to churning and pocketing and the auxiliary churning loss due to the action of the planet carrier can't be properly estimated ($P_{VZ0} + P_{VX}$) due to the lack of reliable models.

Considering the information presented above, from the no-load power loss measurements, here referred to as P_{V0}^{exp}, it is possible to estimate the sum of the gear churning and auxiliary losses ($P_{VX} + P_{VZ0}$).

As shown in chapter 1 the total power loss can be estimated by summing all of the power loss sources, equation (4.4.12).

$$P_V = P_{VZ0} + P_{VZP} + P_{VL} + P_{VD} + P_{VX} \tag{4.4.12}$$

In no-load conditions equation (4.4.12) becomes equation (4.4.13)

$$P_{V0}^{exp} = P_{VZ0} + P_{VL} + P_{VD} + P_{VX} \tag{4.4.13}$$

In equation (4.4.14) the P_{VL} includes the full complement needle roller bearing no-load and the tapered rolling bearings losses including the pre-load. The details of calculation of the rolling bearings no-load power loss in no-load conditions were highlighted in subsection 4.4.3. P_{VD} are the seals losses which can be calculated directly as described in subsection 4.4.4.

From the no-load loss measurement $P_{V0}^{exp.}$ it is now possible to estimate a value for the gears no-load losses due to churning and pocketing and the auxiliary churning loss due to the action of the planet carrier ($P_{VX} + P_{VZ0}$), according to equation (4.4.14). It should be noted that the quality of the $P_{VX} + P_{VZ0}$ estimation is dependent on the quality of the estimation of the other no-load loss components.

$$P_{VX} + P_{VZ0} = P_{V0}^{exp.} - (P_{VL} + P_{VD}) \tag{4.4.14}$$

4.5. Power Loss: Correlation Between Experimental and Model Results

In order to test the accuracy and validity of the gearbox power loss model, load and no-load dependent tests were performed in the planetary gearbox using the conditions previously stated. In this chapter the experimental (load and no-load loss results) will be presented and compared with the model estimations. The power loss will also be broken down to its elementary components aiming to understand the main power loss sources.

4.5.1. Experimental results

The oil sump and stabilized operating ($\Delta T = T^{oil}_{M5} - T^{room}$) temperatures for the tested oils are shown in Figure 4.17.

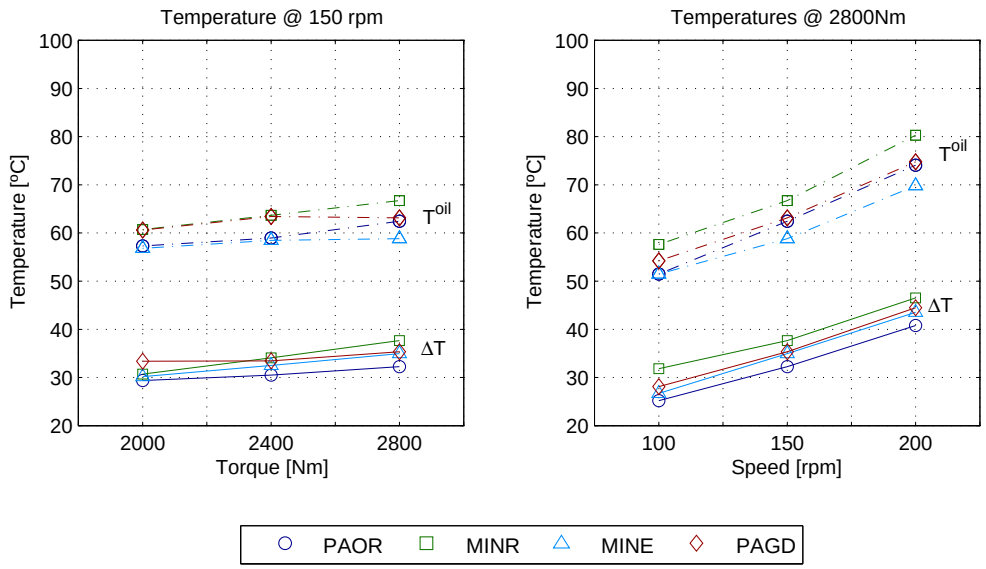

Figure 4.17.: Stablization (ΔT) and operating temperatures (T^{oil}_{M5}) of the planetary gearbox.

For all the operating conditions, PAOR showed the lowest stabilization temperature (ΔT). According to section 1.5 this indicates that PAOR is the oil that promotes the most efficient operation.

For the lowest input torque (2000 Nm), PAGD showed the highest stabilization temperature. For all the other tests, the highest stabilization temperature was reached by MINR. To be noticed is the fact that for constant speed, MINR showed a significant increase of the stabilization temperature with increasing torque, while PAGD started with the highest value, but kept the stabilization temperature almost constant.

At constant torque, all the oils showed a significant increase of the stabilization temperature with increasing speed (increasing input power).

The stabilization temperature is an indication of the ranking of the gear oils regarding their efficiency. The gearbox no-load losses as well as the film thickness are affected by the oil sump temperature (density and viscosity depend of the oil sump temperature). The oil operating temperatures (T^{oil}), which are affected by ambient temperature, are also presented in Figure 4.17.

In Figures 4.18 the experimental total power loss results are presented. The power loss results (figures 4.18) follow the same trends (ΔT) that were observed in figures 4.17. PAOR showed the best power loss performance while MINR usually had the worst, exception being the PAGD at 150 rpm/2000 Nm. As for the other tests PAGD and MINE showed similar power loss.

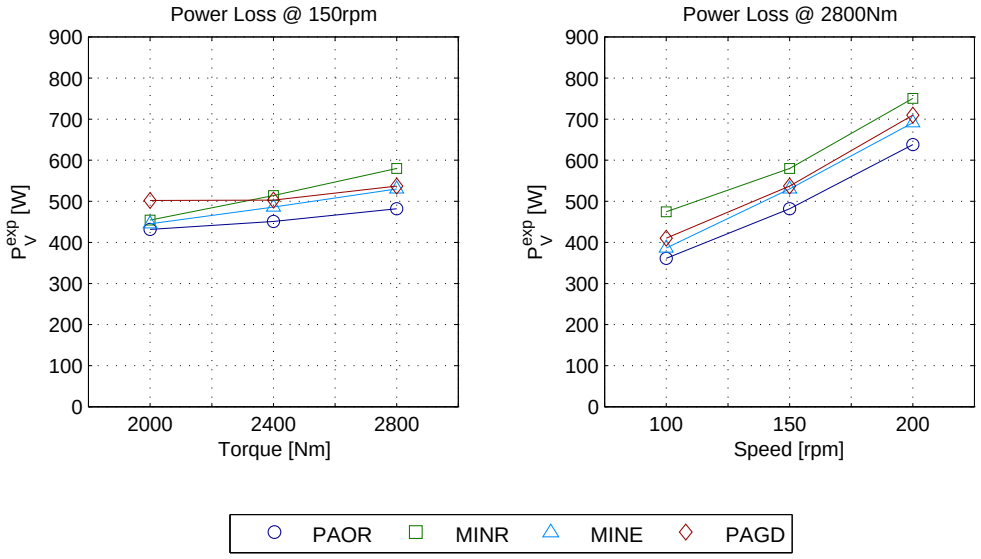

Figure 4.18.: Power loss in the planetary gearbox at stabilized conditions.

The no-load losses that were measured include not only the gear and auxiliary churning losses, but also the rolling bearings and seals no-load losses. As it was previously mentioned the tapered roller bearings are pre-loaded which means that in the measured no-load gearbox power loss there is a tapered rolling bearing load loss component.

After the gearbox load tests were concluded the no-load losses were performed at the corresponding speeds and oil sump temperatures (table 4.14). Figures 4.19 show the measured no-load power loss results.

Regarding the no-load losses PAOR, MINR and MINE performed almost identically exception being the operating condition 200 rpm/2800 Nm where there is a little bit of separation in the results. PAGD has promoted much higher no-load losses than the others. PAGD is by far the oil with the highest density, so to keep accelerating a larger mass of fluid, more energy must be dispensed in the process, therefore it is believed that these differences should be mostly related to gear churning and auxiliary

Table 4.14.: Experimental test plan (no-load temperatures, T^{oil}_{M12}).

Speed [rpm]	**Torque** [Nm]	**Temperature [°C]**			
		PAOR	**MINR**	**MINE**	**PAGD**
100	**2800**	55.32	60.26	55.13	57.05
	2000	62.86	68.5	62.85	65.54
150	**2400**	65.08	70.66	64.72	68.19
	2800	68.84	73.36	66.34	70.01
200	**2800**	78.03	84.5	73.72	80.33

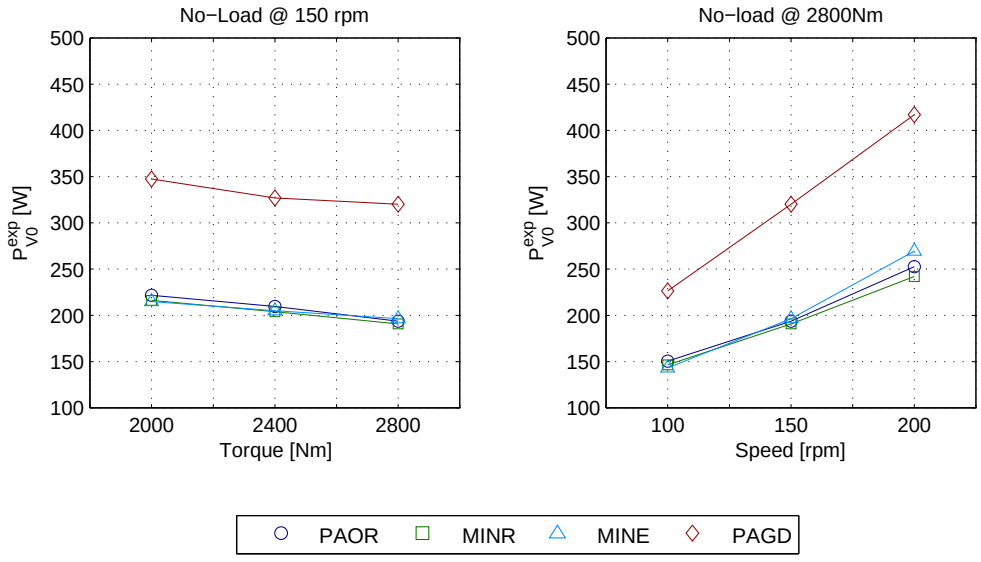

Figure 4.19.: Measured no-load power loss in the planetary gearbox at the temperatures presented in table 4.14.

losses (spin losses). It should be noted that the no-load loss variation with load in Figure 4.19a is due to the fact that at higher loads the operating temperature (T) was higher (Figure 4.17) leading to lower operating oil viscosity and density potentially lowering the spin loss and therefore the total no-load loss.

Specific film thickness

The specific film thickness was calculated with the Dowson *et al.* [126] equations considering the lubricant properties at stabilized temperatures. Figure 4.20 shows the specific film thickness Λ as a function of the operating conditions.

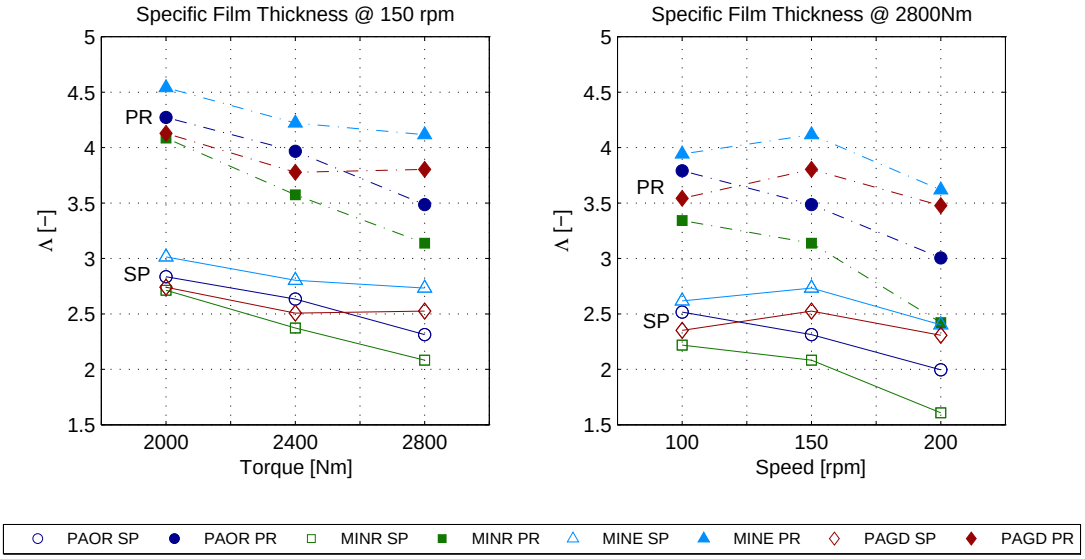

Figure 4.20.: Specific film thickness in the sun-planet (SP) and planet-ring (PR) contacts as a function of the operating conditions and pitch line velocity, v_t.

Generally MINE showed the highest specific film thickness for the tested working conditions, while MINR showed the lowest. According to Fernandes *et al.* [116] Mineral+PAMA mixtures are known to be affected by shear thinning effects, so it is possible that Λ may be overestimated for MINE.

Due to very low average roughness the specific film thickness of the gears is quite high specially for the planet-ring contact. As pointed out in chapter 4.4 this requires special attention in the application of the Schlenk's equation which according to previous works [2] is only valid for $\Lambda \leq 2.5$.

4.5.2. Power loss estimations

The classical gearbox power loss model that was presented in chapter 1 was implemented according to what was suggested in chapter 4.4. The power loss estimations were then compared with the measurements.

The implementation suggested in chapter 4.4 was applied to the no-load loss results (figures 4.19). The no-load loss breakdown (figures 4.21) is quite similar for each lubricant, with the exception of PAGD which shows distinctively higher churning losses. The churning losses ($P_{VZ0} + P_{VX}$) were then calculated from the no-load loss measurements according to equation (4.4.14). Figures 4.21 show the no-load loss broken down in its different components. At constant speed the no-load loss in the TRBs decreases mainly due to decreasing operating viscosity. At constant load there is a sudden increase in the TRBs loss from 100 to 150 rpm.

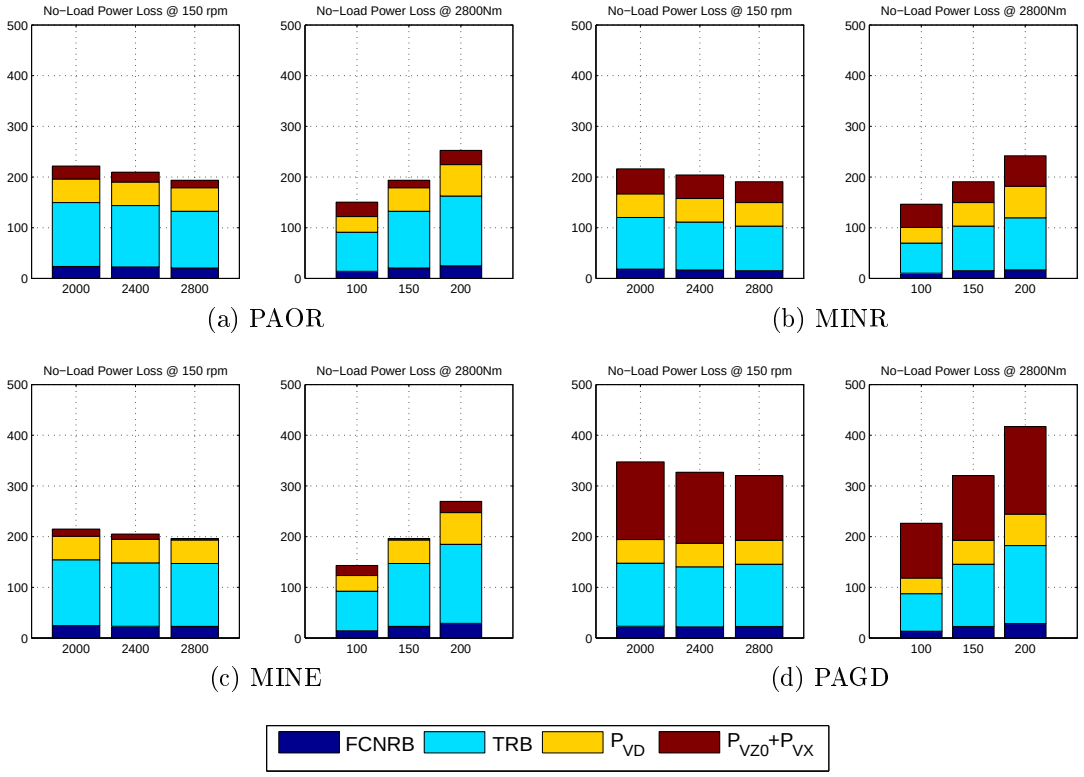

Figure 4.21.: No-load power loss ($P_{V0}^{exp}[W]$) breakdown in its different components.

In figure 4.22 the churning losses ($P_{VZ0} + P_{VX}$) were separated from the total no-load losses. These are the results from the application of equation (4.4.14) that was introduced in subsection 4.4.5.

The churning loss at constant speed (figure 4.22a) decreases with load. This behaviour is connected to the fact that the oil sump temperature was set free, so with increasing load the overall oil sump temperature (T^{oil}) increases due to increasing power loss in the power transmitting contacts, as shown in figures 4.17a and 4.18a. At constant load (figure 4.22b) the spin loss seems to have a minimum at 150 rpm. This minimum is due to the sudden increase in the tapered rolling bearings loss from 100 to 150 rpm that is observed in figures 4.21.

After breaking down and extracting the churning losses from the no-load loss measurements the planetary gearbox power loss at the operating conditions presented in table 4.8 could be estimated. Figures 4.23 show a comparison between the model predictions and the experimental power loss.

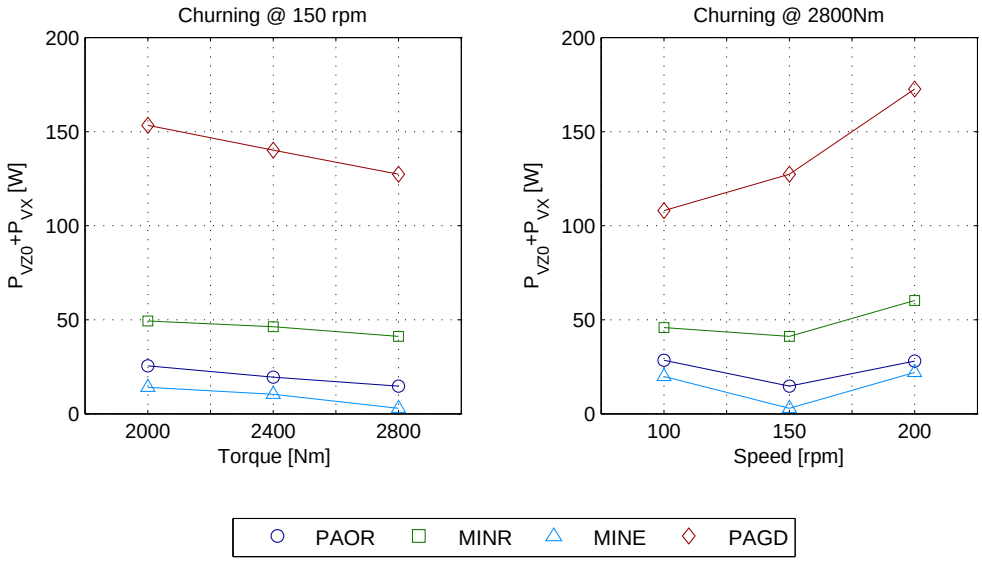

Figure 4.22.: Calculated churning losses at the stabilized temperatures (T^{oil}, table 4.14) from the load tests.

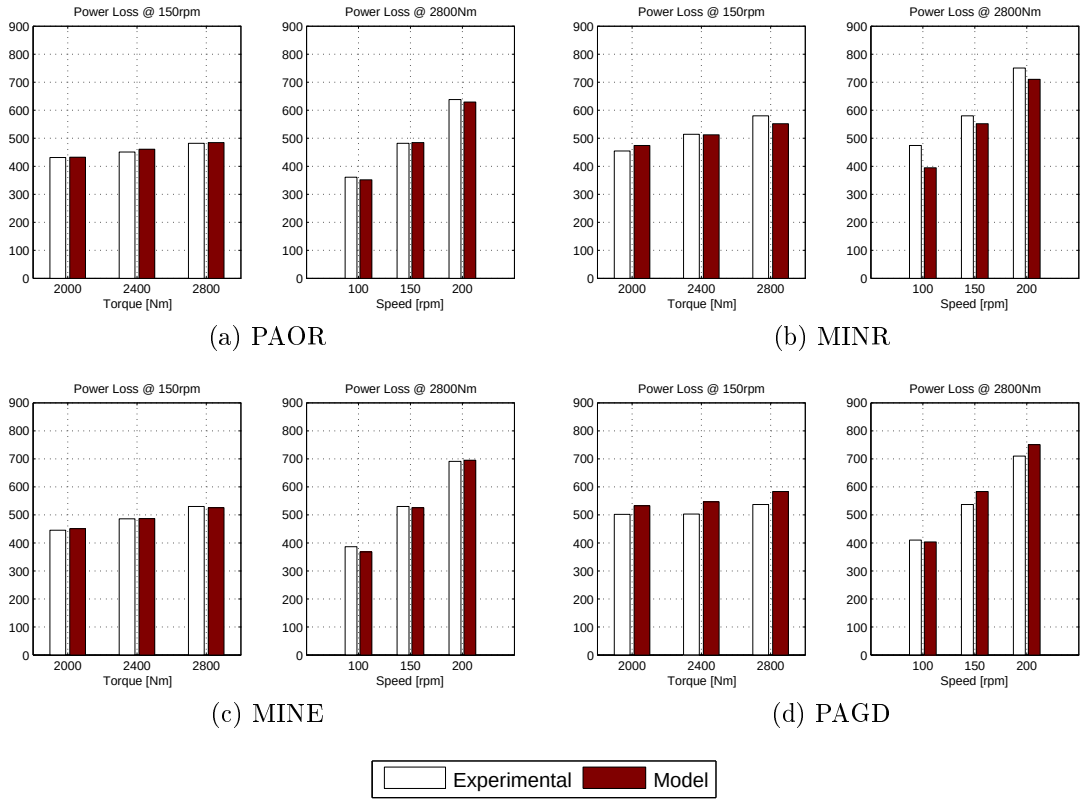

(a) PAOR (b) MINR

(c) MINE (d) PAGD

Figure 4.23.: Experimental vs Estimated power loss, (P_V vs P_V^{exp} [W]), in the planetary gearbox.

These results show that the model and methodology that were employed are suitable to predict gearbox power loss. In table 4.15 the relative error between the measurements and power loss predictions is presented. In most of the cases the error is below 5% with a few exceptions for PAGD and MINR. The highest relative error and only point above 9% was the prediction for MINR @ 100 rpm /2800 Nm.

Table 4.15.: Relative error of the power loss model estimations.

Speed [rpm]	**Torque** [Nm]	**Δ** [%]			
		PAOR	**MINR**	**MINE**	**PAGD**
100	**2800**	-2.5	-16.7	-4.7	-1.7
	2000	0.5	4.4	1.3	6.2
150	**2400**	2.2	-0.4	0.2	8.7
	2800	0.63	-4.8	-0.8	7.9
200	**2800**	-1.4	-5.3	0.6	5.8

One of the advantages of having a proper power loss model is that the power loss can be broken down in its different components. Figures 4.24 and 4.25 show the numerical power loss breakdown for each one of the tested lubricants at every operating condition.

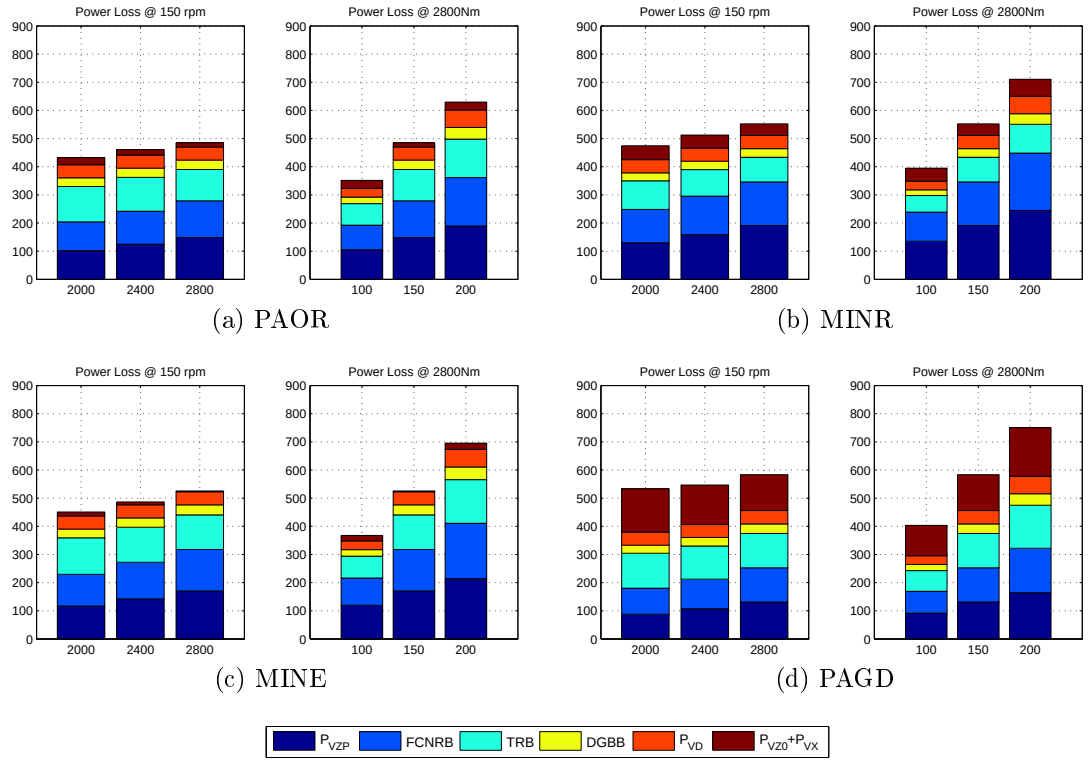

(a) PAOR (b) MINR

(c) MINE (d) PAGD

Figure 4.24.: Power loss (P_V [W]) breakdown in its different components in the planetary gearbox.

At the selected operating conditions, near nominal output torque, the gears load losses are the most influential component. The pre-loaded back-to-back TRBs and the FCNRBs are both competing for the spot of second most important power loss

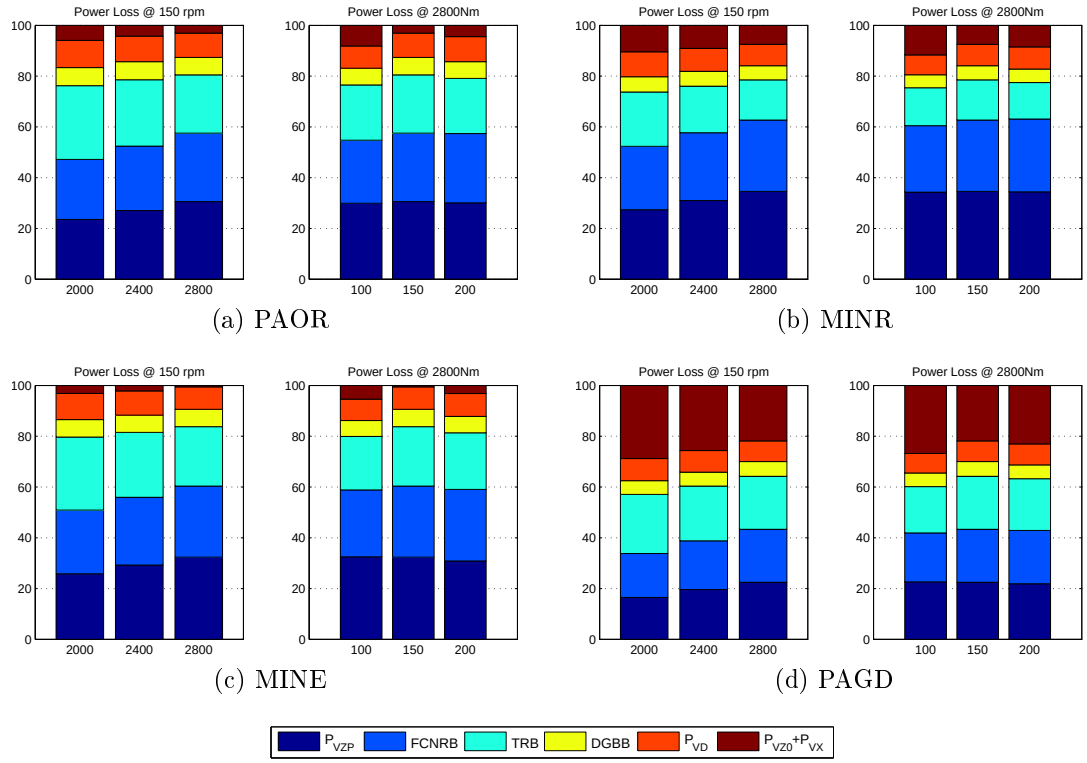

Figure 4.25.: Power loss breakdown in its different components in the planetary gearbox (normalized to 100%).

component. However when combined the power losses of the TRBs, FCNRBs and the DGBB are higher than the load power loss of the gears.

The axial loads introduced by the helical gears are not enough to significantly change the total load in the TRB's and that is why for a constant speed the power loss does not change that much for these elements. Mainly due to their diameter, the seals are an important source of power loss.

As it was previously discussed for the case of the PAGD the churning losses assume a very important role.

The average coefficient of friction between both Sun-Planet and Planet-Ring gear teeth is presented in Figure 4.26 as a function of Λ.

The coefficient of friction comparison between oils is very clear: PAGD leads to the lowest coefficient of friction, followed by PAOR and MINE, respectively, while MINR lead to the highest value. In the other hand, it is possible to conclude that when using PAGD, the reduction in gear losses due to the lower friction coefficient is not enough to compensate the higher churning losses, as the PAGD stabilization temperature and power loss are higher than those of PAOR and MINE.

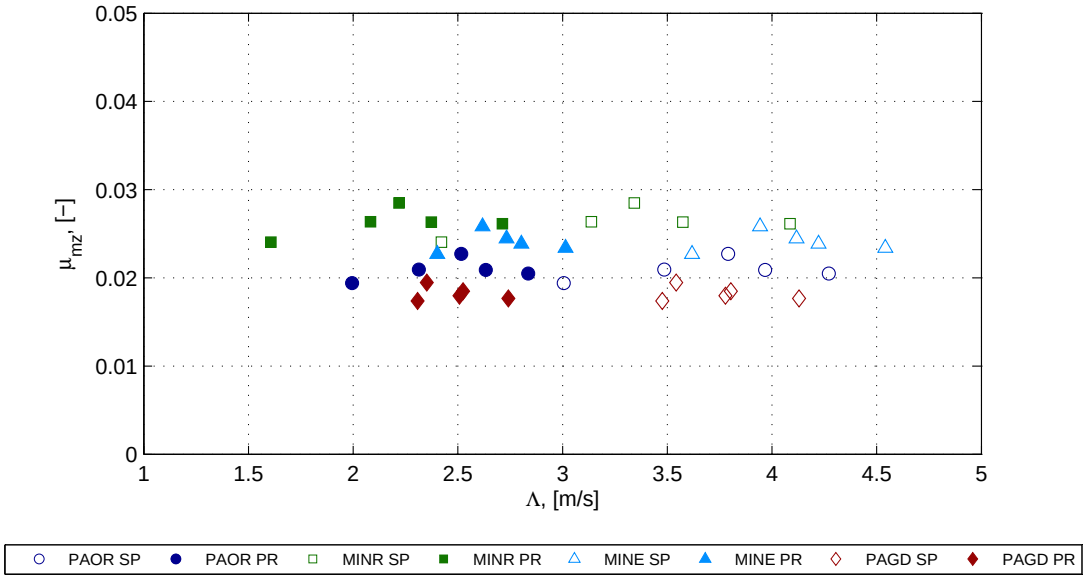

Figure 4.26.: Oil comparison: Coefficient of friction between the planet-ring and sun-planet gear teeth.

4.6. Closure

Lubricant properties stand as one of the most important input variables in a power loss model and as such the oils that were to take part in the experimental tests were sampled and the main properties were measured. The experimental efficiency tests were done at free temperature so the evolution of properties like kinematic viscosity and density with temperature were studied using an Engler viscometer and a commercial density meter. The film thickness and traction curves for three of the four wind turbine gear oils that were selected were also obtained using a PCS EHD2 ball-on-disc device. The traction curves allowed to understand the relative position of the lubricants in terms of traction coefficient. The film thickness measurements were also quite useful because they allowed to understand to some extent validity of the piezoviscosity formulas and film thickness equations.

The gearbox test rigs as well as the planetary gearbox that was tested were presented. The experimental procedures as well as the characteristics of the measuring devices, torque cells thermocouples and RTD's were also presented. The reasoning behind the selection of the operating conditions for the experimental plan was also shown.

The classical gearbox power loss model presented in chapter 1 was implemented and applied to a planetary gearbox. Certain aspects of the implementation of the power loss model to the planetary gearbox in study were evaluated.

The experimental power loss study in a planetary gearbox was presented and compared with the numerical estimations using some of the methods presented in previous chapters.

PAOR lead to the lowest values of stabilization temperature. MINR lead to the highest stabilization temperatures, except for the test at 100 rpm, where the highest temperature was achieved with PAGD. The differences between oils never exceeded 7°C.

PAOR also showed to be more sensitive to both speed and torque increases than PAGD, both standing between the two mineral based oils. The differences found were maximum at the most severe conditions, and were about $10°C$.

The numerical model showed that at the ranged working conditions, the gears are the most significant power loss source. However, it should be noted that in all cases the power loss in the rolling bearings (TRBs+FCNRBs+DGBB) accounts for the majority of the power loss in the planetary gearbox.

For the same operating conditions, the numerical results indicate that PAGD had the lowest load dependent power loss that is due to its lowest gear load losses which are justified by the lower gear coefficient of friction of PAGD. The rest of the components have nearly the same losses for the tested oils. The gears losses vary accordingly to the coefficient of friction calculated for each oil.

PAGD achieved the lowest values for the coefficient of friction while MINR had the highest. PAOR and MINE stood in between, although PAOR had lower values than MINE.

The churning losses are quite relevant, specially for PAGD which despite showing the lowest coefficient of friction in the gears (most important source of power loss) it did not present the best power loss performance. The reduction of the friction in the gears was not high enough to overcome the increase in the churning losses relatively to the other lubricants.

The methodology and mechanical power loss model presented in this work seems to perform quite well in what regards gearbox power loss prediction namely the load losses, given the proper operating temperatures.

5. Planetary Gears: Load Sharing and Local Power loss (quasi-static vs dynamic)

The concepts introduced in chapters 2 and 3 for a single gear pair (load distribution models and gear dynamics approach) were applied to the planetary gearbox in study. The quasi-static average power loss solution is compared with the power loss including dynamic effects. The planetary gear dynamics model will be presented as well as the simulation results for the operating conditions that are presented in Table 4.8 with the addition of two self-excitation speeds.

5.1. Quasi-static Load distribution and gears power loss

The quasi-static rigid, elastic and local elastic load distribution models that were previously presented in sections 2.1, 2.2 and 2.3 were applied to the planetary gearbox. These models can be readily applied to the sun-planet (external gear) and planet-ring (internal gear) gear meshes.

Figures 5.1 show the load distribution and mesh stiffness that were obtained. The load distribution obtained with each of the three models that were developed shows some differences, namely at the maximum in the top of the load distribution curves. These differences are intimately related to the mesh stiffness of the meshing tooth which is shown in figures 5.1b and 5.1d. The main shape of the stiffness function is quite similar, however the elastic model lacks some of the details of the local elastic model which shows smoother transitions as well as an overall lower average stiffness value. In section 2.4 it was shown that the results obtained with the elastic and local elastic models were quite similar, however here there are some significant deviations which should be attributed to the reference value $K_{max} = K_{max}^{ISO}$ which is in this case an overestimation of the maximum single stiffness.

The results of the quasi-static local elastic model were used to estimate the power loss evolution along the path of contact for both of the gear meshes. The PAOR lubricant (@ 78.03 $^{\circ}C$) was selected, the speed on the planet carrier was set to 200 rpm and the output torque on the sun gear was imposed to 700 Nm (2800 Nm at the planet carrier). Figures 5.2 and 5.3 show the load distribution, sliding velocity, Hertzian pressure, local CoF and power loss at stabilized dynamic conditions for both

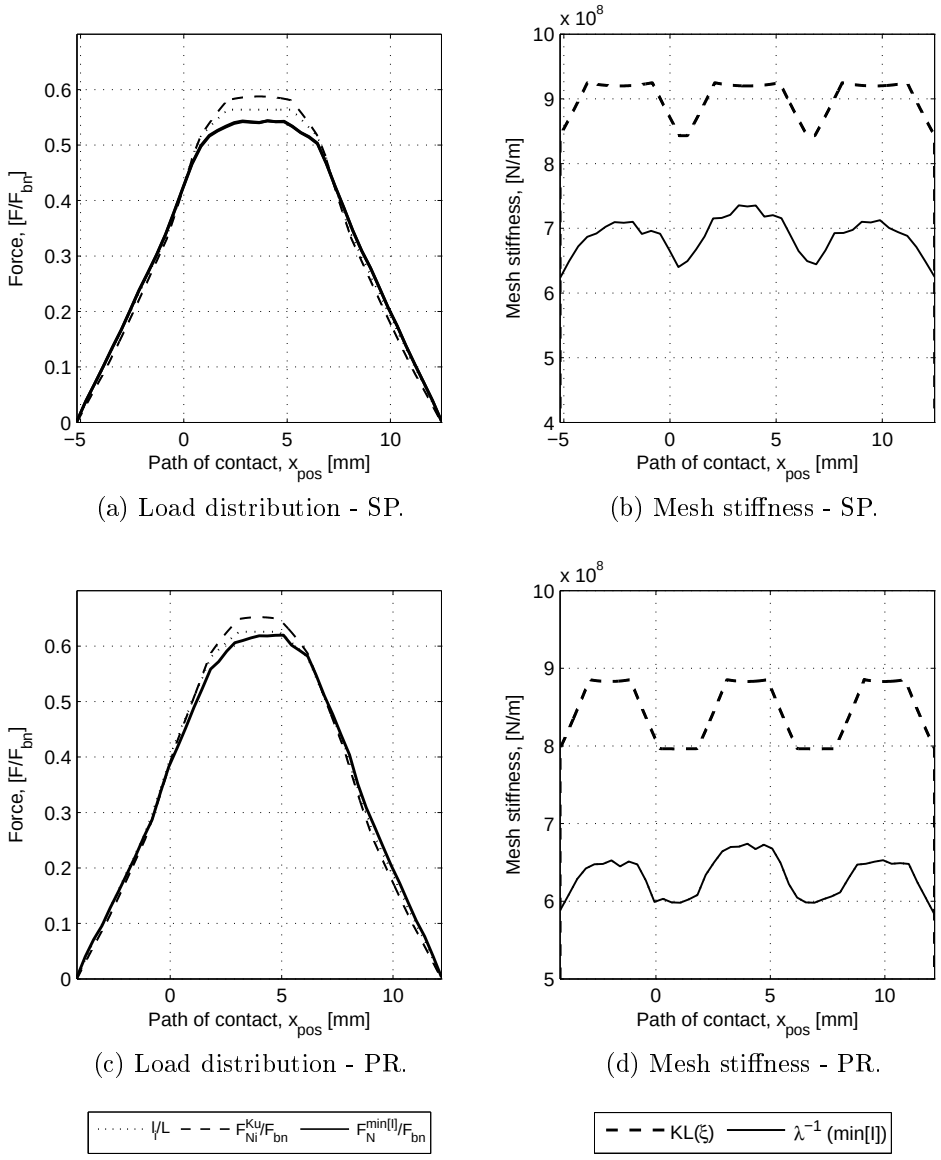

(a) Load distribution - SP. (b) Mesh stiffness - SP.

(c) Load distribution - PR. (d) Mesh stiffness - PR.

$\boldsymbol{l/L}$ - Quasi-static rigid model; $\boldsymbol{F_{Ni}^{Ku}/F_{bn}}$, $\boldsymbol{KL(\xi)}$ - Quasi-static elastic model; $\boldsymbol{F_{Ni}^{min[I]}/F_{bn}}$, $\boldsymbol{\lambda^{-1}(min[I])}$ - Quasi-static local elastic model.

Figure 5.1.: Load sharing and mesh stiffness according to the different models applied to the sun-planet and planet-ring gear meshes, ($i = 0$, $\mu = 0$, $\alpha_k = 4/5$, $K_{max} = K_{max}^{ISO}$).

of the gear contacts (SP and PR). It should be noted that the power loss per unit of line length and total power loss of the planet-ring contact are much lower than the same quantities in the sun-planet contact. This difference comes down to the fact that the internal gearing of the PR contact has lower contact pressure and much lower sliding velocity which results in a lower CoF and power loss.

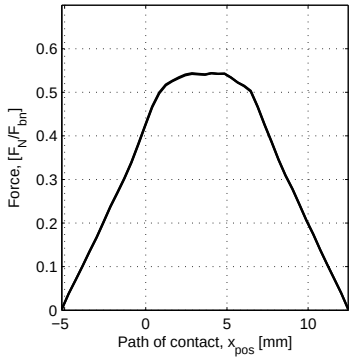

(a) Total normal force, $F_{bn}(t)$.

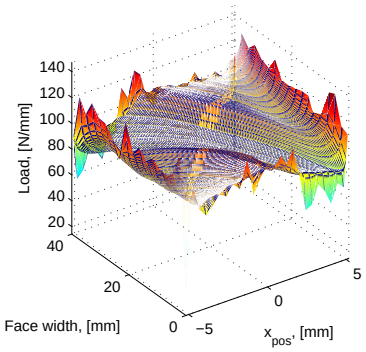

(b) Load per unit of line length, $f_N(x, y)$.

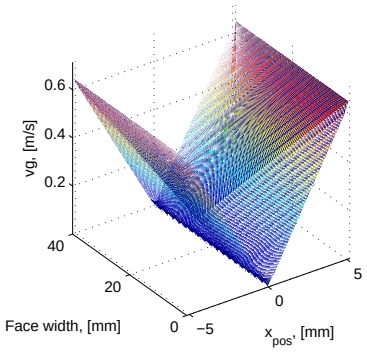

(c) Sliding velocity, $V_g(x, y)$.

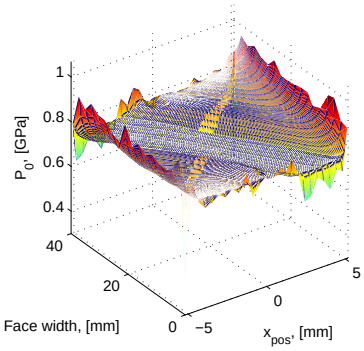

(d) Hertzian pressure, $P_0(x, y)$.

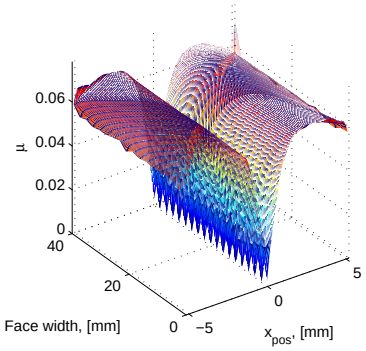

(e) Coefficient of friction, $\mu^{Xu}(x, y)$.

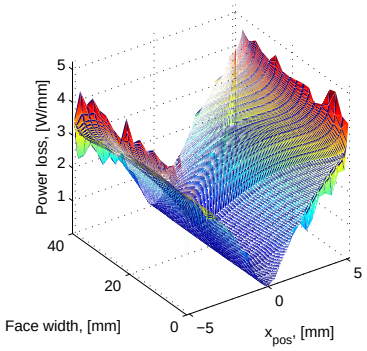

(f) Power loss per unit of line length, $p_{VZP}(x, y)$.

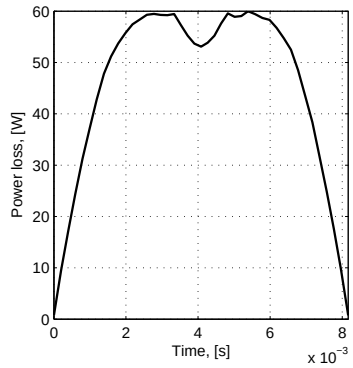

(g) $P_{VZP}^{single}(t)$.

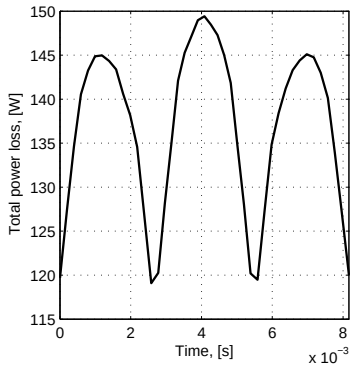

(h) $P_{VZP}^{total}(t)$.

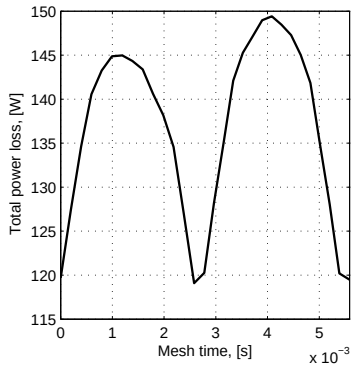

(i) $P_{VZP}^{total}(0 : t : T^{mesh})$.

Figure 5.2.: Local quantities and power loss under quasi-static conditions (PAOR @ 200 rpm, 2800 Nm) - Sun-Planet (SP).

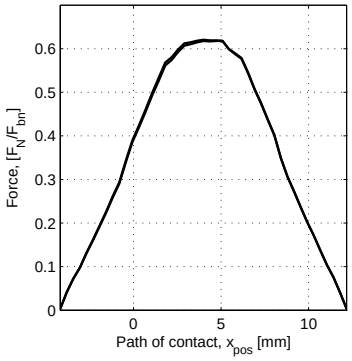

(a) Normal force, $F_N/F_{bn}(t)$.

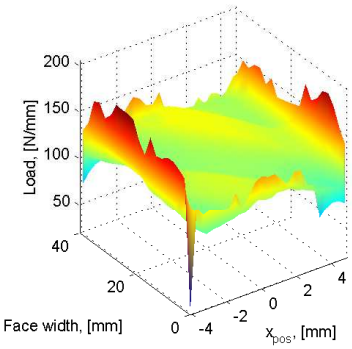

(b) Load per unit of line length, $f_N(x, y)$.

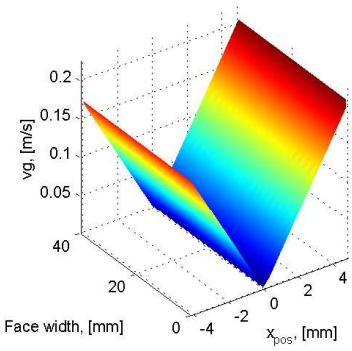

(c) Sliding velocity, $V_g(x, y)$.

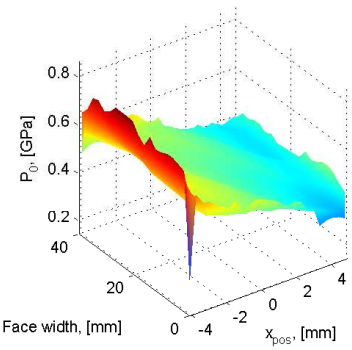

(d) Hertzian pressure, $P_0(x, y)$.

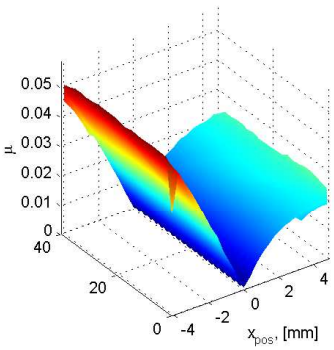

(e) Coefficient of friction, $\mu^{Xu}(x, y)$.

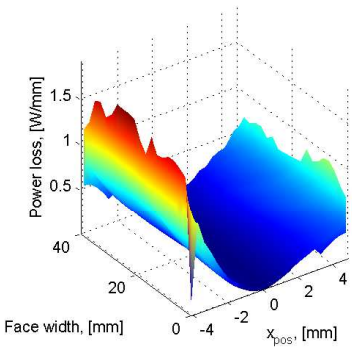

(f) Power loss per unit of line length, $p_{VZP}(x, y)$.

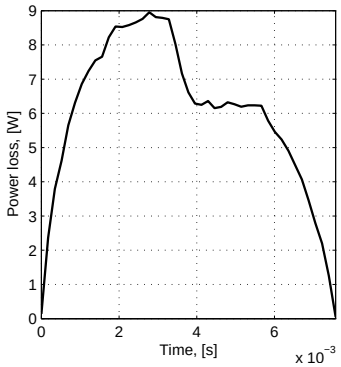

(g) $P_{VZP}^{single}(t)$.

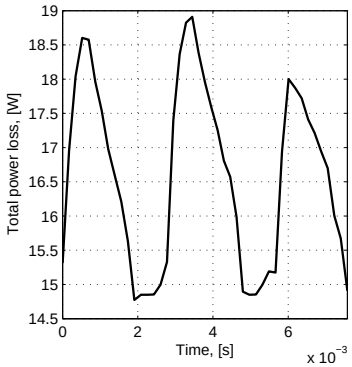

(h) $P_{VZP}^{total}(t)$.

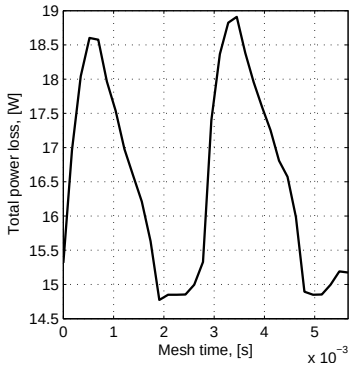

(i) $P_{VZP}^{total}(0 : t : T^{mesh})$.

Figure 5.3.: Local quantities and power loss under quasi-static conditions (PAOR @ 200 rpm, 2800 Nm) - Planet-Ring (PR)

5.2. Planetary gear dynamics

In chapter 3 a model for a simple gear mesh pair was presented and the influence of gear dynamics in power loss demonstrated. In this section the same concepts and basic assumptions were taken into account a lumped mass planetary gearbox dynamics model was developed.

Consider a planetary gearbox with elastic shafts attached to the planet carrier and the sun gear. The planetary gearbox is considered to have n planets of mass m_p. The ring gear is fixed. Figure 5.4 shows the simplified planetary gearbox model.

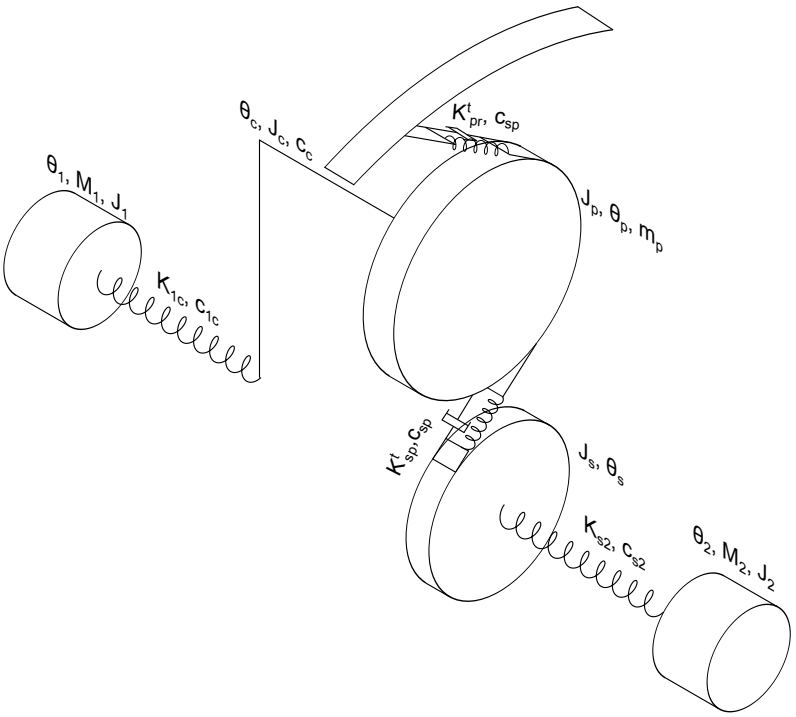

Figure 5.4.: Dynamic planetary gear model.

The equations that describe the dynamics of the planetary gearbox were derived following the procedure that was already employed to obtain the equations for the dynamic behaviour of a simple gear pair (PLA).

The variables that describe the motion θ_i are represented in a frame of reference at the center of each rotating element.

The kinetic energy of the system can be written according to equation (5.2.1). It should be noted that the term $\sum_{i=1}^{n}\left[J_p \cdot \dot{\theta}_p^{i\,2} + m_p \cdot \left(\dot{\theta}_c \cdot a\right)^2\right]$ accounts for both the rotational kinetic energy of the planets around their own center and the kinetic energy that results from the movement with the planet carrier.

$$T = \frac{1}{2}\Bigg[J_1 \cdot \dot{\theta_1}^2 + J_2 \cdot \dot{\theta_2}^2 + J_s \cdot \dot{\theta_s}^2 + J_c \cdot \dot{\theta_c}^2 + \sum_{i=1}^{n}\Bigg[J_p \cdot \dot{\theta_p^i}^2 + m_p \cdot \left(\dot{\theta_c} \cdot a\right)^2\Bigg]\Bigg] \tag{5.2.1}$$

The potential energy of the system can be written according to equation (5.2.2).

$$V = \frac{1}{2}\Bigg[K_{1c} \cdot (\theta_c - \theta_1)^2 + K_{s2} \cdot (\theta_2 - \theta_s)^2 + \sum_{i=1}^{n}\Bigg[K_{sp} \cdot \left(r_{bp} \cdot \left(\theta_p^i + \theta_c\right) - r_{bs} \cdot (\theta_s - \theta_c)\right)^2 + K_{pr} \cdot \left(r_{br} \cdot \theta_c - r_{bp} \cdot \left(\theta_p^i + \theta_c\right)\right)^2\Bigg]\Bigg] \tag{5.2.2}$$

Quantity δW_{nc}, equation (5.2.3), accounts for the variation of work of external forces.

$$\delta W_{nc} = M_1 \cdot \delta\theta_1 - M_2 \cdot \delta\theta_2 \tag{5.2.3}$$

R, equation (5.2.4), accounts for the damping effects.

$$R = \frac{1}{2}\Bigg[c_1 \cdot (\dot{\theta_c} - \dot{\theta_1})^2 + c_2 \cdot (\dot{\theta_2} - \dot{\theta_s})^2 + c_c \cdot \dot{\theta_c}^2 + \sum_{i=1}^{n}\Bigg[c_{sp} \cdot \left(r_{bp} \cdot \left(\dot{\theta_p^i} + \dot{\theta_c}\right) - r_{bs} \cdot \left(\dot{\theta_s} - \dot{\theta_c}\right)\right)^2 + c_{pr} \cdot \left(r_{br} \cdot \dot{\theta_c} - r_{bp} \cdot \left(\dot{\theta_p^i} + \dot{\theta_c}\right)\right)^2\Bigg]\Bigg] \tag{5.2.4}$$

Considering equation (3.1.7) and equations (5.2.1) to (5.2.4) and applying the Euler-Lagrange equations considering damping effects a system of four diferential equations that describes the motion of the system is obtained, equation (5.2.5) to (5.2.9).

$$J_1 \cdot \ddot{\theta}_1 - \Big[K_1 \cdot (\theta_c - \theta_1) + M_1\Big] - c_1 \cdot (\dot{\theta}_c - \dot{\theta}_1) = 0 \tag{5.2.5}$$

$$\begin{aligned} J_c \cdot \ddot{\theta}_c + \sum_{i=1}^{n}\Big[m_p \cdot a^2 \ddot{\theta}_c\Big] - \\ \Bigg[-K_1 \cdot (\theta_c - \theta_1) - \sum_{i=1}^{n}\Bigg[(r_{bp} + r_{bs}) \cdot K_{sp}^i \cdot \Big(r_{bp}\left(\theta_p^i + \theta_c\right) - r_{bs} \cdot (\theta_s - \theta_c)\Big) \\ + (r_{br} - r_{bp}) \cdot K_{pr}^i \cdot \Big(r_{br} \cdot \theta_c - r_{bp} \cdot \left(\theta_p^i + \theta_c\right)\Big)\Bigg]\Bigg] + \\ \sum_{i=1}^{n}\Bigg[(r_{bp} + r_{bs}) \cdot c_{sp} \cdot \Big(r_{bp} \cdot \left(\dot{\theta}_p^i + \dot{\theta}_c\right) - r_{bs} \cdot \left(\dot{\theta}_s - \dot{\theta}_c\right)\Big) \\ + (r_{br} - r_{bp}) \cdot c_{pr} \cdot \Big(r_{br} \cdot \dot{\theta}_c - r_{bp} \cdot \left(\dot{\theta}_p^i + \dot{\theta}_c\right)\Big)\Bigg] + c_c \cdot \dot{\theta}_c + c_1 \cdot (\dot{\theta}_c - \dot{\theta}_1) = 0 \end{aligned} \tag{5.2.6}$$

$$\begin{aligned} J_s \cdot \ddot{\theta}_s - \Bigg[K_2 \cdot (\theta_2 - \theta_s) + \\ \sum_{i=1}^{n}\Big[r_{bs} \cdot K_{sp}^i \cdot \Big(r_{bp} \cdot \left(\theta_p^i + \theta_c\right) - r_{bs} \cdot (\theta_s - \theta_c)\Big)\Big]\Bigg] + \\ \sum_{i=1}^{n}\Big[-r_{bs} \cdot c_{sp} \cdot \Big(r_{bp} \cdot \left(\dot{\theta}_p^i + \dot{\theta}_c\right) - r_{bs} \cdot \left(\dot{\theta}_s - \dot{\theta}_c\right)\Big)\Big] - c_2 \cdot (\dot{\theta}_2 - \dot{\theta}_s) = 0 \end{aligned} \tag{5.2.7}$$

$$\begin{aligned} \sum_{i=1}^{n}\Big[J_p \cdot \ddot{\theta}_p^i\Big] - \Bigg[-\sum_{i=1}^{n}\Bigg[r_{bp} \cdot K_{sp}^i \cdot \Big(r_{bp} \cdot \left(\theta_p^i + \theta_c\right) - r_{bs} \cdot (\theta_s - \theta_c)\Big) \\ - r_{bp} \cdot K_{pr}^i \cdot \Big(r_{br} \cdot \theta_c - r_{bp} \cdot \left(\theta_p^i + \theta_c\right)\Big)\Bigg]\Bigg] + \\ \sum_{i=1}^{n}\Bigg[r_{bp} \cdot c_{sp} \cdot \Big(r_{bp} \cdot \left(\dot{\theta}_p^i + \dot{\theta}_c\right) - r_{bs} \cdot \left(\dot{\theta}_s - \dot{\theta}_c\right)\Big) - \\ r_{bp} \cdot c_{pr} \cdot \Big(r_{br} \cdot \dot{\theta}_c - r_{bp} \cdot \left(\dot{\theta}_p^i + \dot{\theta}_c\right)\Big)\Bigg] = 0 \end{aligned} \tag{5.2.8}$$

$$J_2 \cdot \ddot{\theta_2} - \Big[-K_2 \cdot (\theta_2 - \theta_s) - M_2\Big] + c_2 \cdot (\dot{\theta_2} - \dot{\theta_s}) = 0 \tag{5.2.9}$$

This problem can then be rewritten in matrix form according to equation (5.2.10).

$$[M]\{\ddot{\theta}\} + [C]\{\dot{\theta}\} + [K]\{\theta\} - \{F\} = \{0\} \tag{5.2.10}$$

Equations (5.2.11) to (5.2.15) are the matrices that compose equations (5.2.10).

$$\{\theta\} = \begin{bmatrix} \theta_1 \\ \theta_c \\ \theta_s \\ \theta_p^1 \\ \vdots \\ \theta_p^i \\ \vdots \\ \theta_p^n \\ \theta_2 \end{bmatrix} \tag{5.2.11}$$

$$[M] = \begin{bmatrix} J_1 & 0 & 0 & 0 & \cdots & 0 & \cdots & 0 & 0 \\ 0 & J_c + \sum_{i=1}^{n}\Big[m_p \cdot a^2\Big] & 0 & 0 & \cdots & 0 & \cdots & 0 & 0 \\ 0 & 0 & J_s & 0 & \cdots & 0 & \cdots & 0 & 0 \\ 0 & 0 & 0 & J_p^1 & \cdots & 0 & \cdots & 0 & 0 \\ 0 & 0 & 0 & 0 & \vdots & 0 & \vdots & 0 & 0 \\ 0 & 0 & 0 & 0 & \cdots & J_p^i & \cdots & 0 & 0 \\ 0 & 0 & 0 & 0 & \vdots & 0 & \vdots & 0 & 0 \\ 0 & 0 & 0 & 0 & 0 & 0 & 0 & J_p^n & 0 \\ 0 & 0 & 0 & 0 & 0 & 0 & 0 & 0 & J_2 \\ \end{bmatrix} \tag{5.2.12}$$

$$
[K] = \begin{bmatrix}
K_1 & -K_1 & 0 \\
-K_1 & K_1 + \sum_{i=1}^{n}\left[(r_{bp}+r_{bs})^2 \cdot K_{sp}^i + (r_{br}-r_{bp})^2 \cdot K_{pr}^i\right] & -\sum_{i=1}^{n}\left[(r_{bs}+r_{bp}) \cdot r_{bs} \cdot K_{sp}^i\right] \\
0 & -\sum_{i=1}^{n}\left[(r_{bs}+r_{bp}) \cdot r_{bs} \cdot K_{sp}^i\right] & K_2 + \sum_{i=1}^{n}\left[r_{bs}^2 \cdot K_{sp}^i\right] \\
0 & r_{bp} \cdot \left((r_{bp}+r_{bs}) \cdot K_{sp}^1 - (r_{br}-r_{bp}) \cdot K_{pr}^1\right) & -r_{bs} \cdot r_{bp} \cdot K_{sp}^1 \\
\vdots & \vdots & \vdots \\
0 & r_{bp} \cdot \left((r_{bp}+r_{bs}) \cdot K_{sp}^i - (r_{br}-r_{bp}) \cdot K_{pr}^i\right) & -r_{bs} \cdot r_{bp} \cdot K_{sp}^i \\
\vdots & \vdots & \vdots \\
0 & r_{bp} \cdot \left((r_{bp}+r_{bs}) \cdot K_{sp}^n - (r_{br}-r_{bp}) \cdot K_{pr}^n\right) & 0 \\
0 & 0 & -K_2
\end{bmatrix}
$$

$$
\begin{bmatrix}
0 & \cdots & 0 \\
r_{bp} \cdot \left((r_{bp}+r_{bs}) \cdot K_{sp}^1 - (r_{br}-r_{bp}) \cdot K_{pr}^1\right) & \cdots & r_{bp} \cdot \left((r_{bp}+r_{bs}) \cdot K_{sp}^i - (r_{br}-r_{bp}) \cdot K_{pr}^i\right) \\
-r_{bs} \cdot r_{bp} \cdot K_{sp}^1 & \cdots & -r_{bs} \cdot r_{bp} \cdot K_{sp}^i \\
r_{bp}^2 \cdot \left(K_{sp}^1 + K_{pr}^1\right) & 0 & 0 \\
\vdots & \vdots & \vdots \\
0 & 0 & r_{bp}^2 \cdot \left(K_{sp}^i + K_{pr}^i\right) \\
\vdots & \vdots & \vdots \\
0 & 0 & 0 \\
0 & 0 & 0
\end{bmatrix}
$$

$$
\begin{bmatrix}
\cdots & 0 & 0 \\
\cdots & r_{bp} \cdot \left((r_{bp}+r_{bs}) \cdot K_{sp}^n - (r_{br}-r_{bp}) \cdot K_{pr}^n\right) & 0 \\
\cdots & -r_{bs} \cdot r_{bp} \cdot K_{sp}^n & -K_2 \\
0 & 0 & 0 \\
\vdots & \vdots & \vdots \\
0 & 0 & 0 \\
\vdots & \vdots & \vdots \\
0 & r_{bp}^2 \cdot \left(K_{sp}^n + K_{pr}^n\right) & 0 \\
0 & 0 & K_2
\end{bmatrix}
\tag{5.2.13}
$$

$$
[C] = \begin{bmatrix}
c_1 & -c_1 & 0 \\
-c_1 & c_c + c_1 + \sum_{i=1}^{n}\Big[(r_{bp}+r_{bs})^2 \cdot c_{sp} + (r_{br}-r_{bp})^2 \cdot c_{pr}\Big] & -\sum_{i=1}^{n}\Big[(r_{bs}+r_{bp}) \cdot r_{bs} \cdot c_{sp}\Big] \\
0 & -\sum_{i=1}^{n}\Big[(r_{bs}+r_{bp}) \cdot r_{bs} \cdot c_{sp}\Big] & c_2 + \sum_{i=1}^{n}\Big[r_{bs}^2 \cdot c_{sp}\Big] \\
0 & r_{bp} \cdot \Big((r_{bp}+r_{bs}) \cdot c_{sp} - (r_{br}-r_{bp}) \cdot c_{pr}\Big) & -r_{bs} \cdot r_{bp} \cdot c_{sp} \\
\vdots & \vdots & \vdots \\
0 & r_{bp} \cdot \Big((r_{bp}+r_{bs}) \cdot c_{sp} - (r_{br}-r_{bp}) \cdot c_{pr}\Big) & -r_{bs} \cdot r_{bp} \cdot c_{sp} \\
\vdots & \vdots & \vdots \\
0 & r_{bp} \cdot \Big((r_{bp}+r_{bs}) \cdot c_{sp} - (r_{br}-r_{bp}) \cdot c_{pr}\Big) & -r_{bs} \cdot r_{bp} \cdot c_{sp} \\
0 & 0 & -c_2
\end{bmatrix}
$$

$$
\begin{bmatrix}
0 & \cdots & 0 \\
r_{bp} \cdot \Big((r_{bp}+r_{bs}) \cdot c_{sp} - (r_{br}-r_{bp}) \cdot c_{pr}\Big) & \cdots & r_{bp} \cdot \Big((r_{bp}+r_{bs}) \cdot c_{sp} - (r_{br}-r_{bp}) \cdot c_{pr}\Big) \\
-r_{bs} \cdot r_{bp} \cdot c_{sp} & \cdots & -r_{bs} \cdot r_{bp} \cdot c_{sp} \\
r_{bp}^2 \cdot (c_{sp}+c_{pr}) & 0 & 0 \\
\vdots & \vdots & \vdots \\
0 & 0 & r_{bp}^2 \cdot (c_{sp}+c_{pr}) \\
\vdots & \vdots & \vdots \\
0 & 0 & 0 \\
0 & 0 & 0
\end{bmatrix}
$$

$$
\begin{bmatrix}
\cdots & 0 & 0 \\
\cdots & r_{bp} \cdot \Big((r_{bp}+r_{bs}) \cdot c_{sp} - (r_{br}-r_{bp}) \cdot c_{pr}\Big) \cdot c_{pr} & 0 \\
\cdots & -r_{bs} \cdot r_{bp} \cdot c_{sp} & -c_2 \\
0 & 0 & 0 \\
\vdots & \vdots & \vdots \\
0 & 0 & 0 \\
\vdots & \vdots & \vdots \\
0 & r_{bp}^2 \cdot (c_{sp}+c_{pr}) & 0 \\
0 & 0 & c_2
\end{bmatrix}
\tag{5.2.14}
$$

$$\{F\} = \begin{bmatrix} -M_1 \\ 0 \\ 0 \\ 0 \\ \vdots \\ 0 \\ \vdots \\ 0 \\ M_2 \end{bmatrix} \tag{5.2.15}$$

5.2.1. Natural modes and self-excitation

In a dynamic system the amplitude of vibration is highest for excitations near the modal frequencies. The characteristic problem was then studied for the system presented in figure 5.4 aiming to understand the range of operating speeds at which maximum amplitude of vibration occurs.

The natural modes of vibration (modal shapes and frequencies) were calculated for the gears that were presented considering the mass and stiffness properties presented in table 5.1. The damping parameters, c_{sp}, c_{pr}, c_{1c} and c_{s2}, (figure 5.4) were forced to 0 in order to solve de characteristic problem.

The mass properties of the gears, J_S and J_P, were calculated from the dimensions of the gears' pitch diameter and face width. The average mesh stiffness was obtained averaging the mesh stiffness obtained with the quasi-static local elastic model (section 2.3) for a single meshing period ($\mu = 0$).

Table 5.1 shows the mass and stiffness properties considered in the gear dynamics model.

Table 5.1.: Mass and stiffness properties (gear dynamics model, figure 5.4).

Property	Value	Units
$\boldsymbol{J_1}$	4.0×10^{-2}	kgm^2
$\boldsymbol{J_c}$	2.23×10^{-3}	kgm^2
$\boldsymbol{J_p}$	8.86×10^{-4}	kgm^2
$\boldsymbol{J_s}$	9.93×10^{-4}	kgm^2
$\boldsymbol{J_2}$	4.0×10^{-2}	kgm^2
$\boldsymbol{K_{1c}}$	3×10^5	Nm/rad
$\boldsymbol{K_{sp}^{avg}}$	6.84×10^3	Nm/rad
$\boldsymbol{K_{pr}^{avg}}$	6.28×10^3	Nm/rad
$\boldsymbol{K_{s2}}$	3×10^5	Nm/rad

Figures 5.5 show the modal shapes normalized to unitary modal masses for the three gear geometries. The natural frequencies are displayed in table 5.2. The system is semi-definite, so the first mode is a rigid body mode with a natural frequency of 0 rpm, the modal shape follows the gearbox ratios.

Table 5.2.: Modal frequencies considering the average mesh stiffness and $\mu = 0$, (Planetary gearbox).

ω_n^i [rpm]						
ω_n^0	ω_n^1	ω_n^2	ω_n^3	ω_n^4	ω_n^5	ω_n^6
0	25 963.0	97 221.6	323 768.4	398 755.1	398 755.1	607 833.4

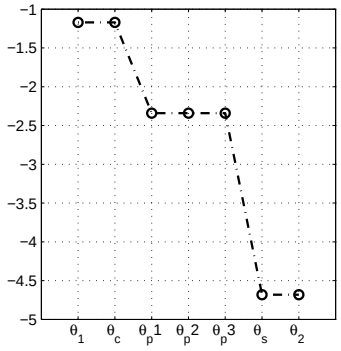

(a) Mode 0, 0 rpm

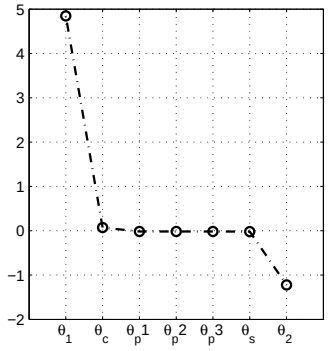

(b) Mode 1, 25 963.0 rpm

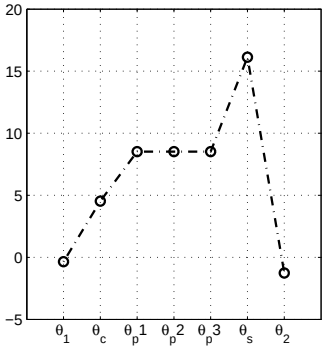

(c) Mode 2, 97 221.6 rpm

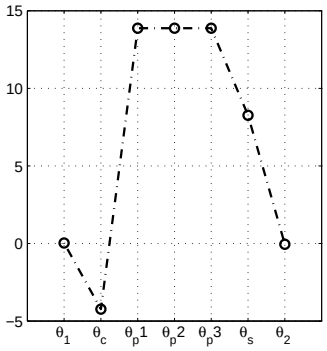

(d) Mode 3, 323 768.4 rpm

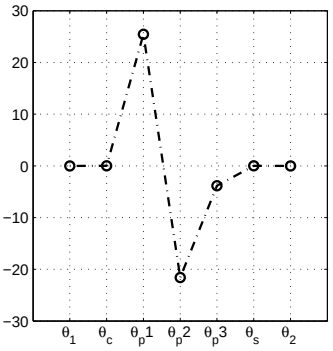

(e) Mode 4, 398 755.1 rpm

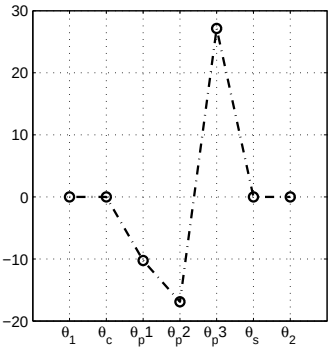

(f) Mode 5, 398 755.1 rpm

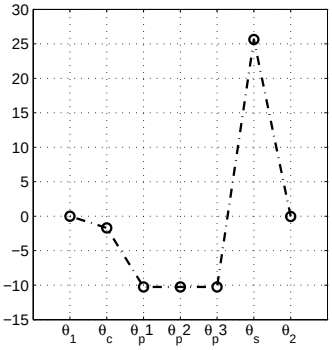

(g) Mode 6, 607 833.4 rpm

Figure 5.5.: Modal shapes normalized to unitary modal masses. (planetary gearbox).

Self-excitation

The characteristic problem was studied considering the average mesh stiffness. However the mesh stiffness varies periodically in time, being the period of this variation coincident with the meshing period T^{mesh}. The time varying mesh stiffness introduces a periodic excitation which has a frequency higher that the frequency of rotation of the shaft. This means that it is possible to excite the natural modes at rotational speeds that are much lower (self-excitation speeds) than the actual natural frequency corresponding to that particular mode.

In a planetary gearbox the mesh period (T^{mesh}_{plnt}) must be calculated in a referential attached to the planet carrier, i.e. the speed of the sun gear to consider is ω^r_s, equation (4.4.3).

The self-excitation speeds can be calculated equalling the mesh period to the natural period of a certain mode, as represented in equation (5.2.16).

$$T^{mesh}_{plnt} = \frac{2\pi}{(1 - \frac{1}{u^{plnt}}) \cdot \omega_s \cdot z_s} \tag{5.2.16}$$

Following equation (3.2.1) the self excitation speed in a planetary gearbox is given by equation (5.2.17).

$$\omega^s_{self} = \frac{\omega^i_n}{(1 - \frac{1}{u^{plnt}}) \cdot z_s} \tag{5.2.17}$$

The self excitation speeds for each mode were calculated and the results are presented in table 5.3. Figure 5.6 also shows the self-excitation speeds but in a graphical manner. Despite the second and third natural modes (first and second non rigid) appearing at very high speeds (table 5.2) they can be excited at more common operating speeds due to mesh stiffness excitations.

Table 5.3.: Self excitation speeds. (Planetary gearbox).

ω^i_n [rpm]					
$\omega^{s,1}_{self}$	$\omega^{s,2}_{self}$	$\omega^{s,3}_{self}$	$\omega^{s,4}_{self}$	$\omega^{s,5}_{self}$	$\omega^{s,6}_{self}$
961.2	3 600.8	11 991.4	14 768.7	14 768.7	22 512.3

5.2.2. Power loss simulations

Speeds near the ones presented in tables 5.2 and 5.3 are prone to induce high vibration amplitudes which may result in substantial dynamic overloads. These high amplitude modes near de critical speeds have the potential to result in dynamic normal tooth loads below zero, which means that the meshing teeth loose contact, therefore

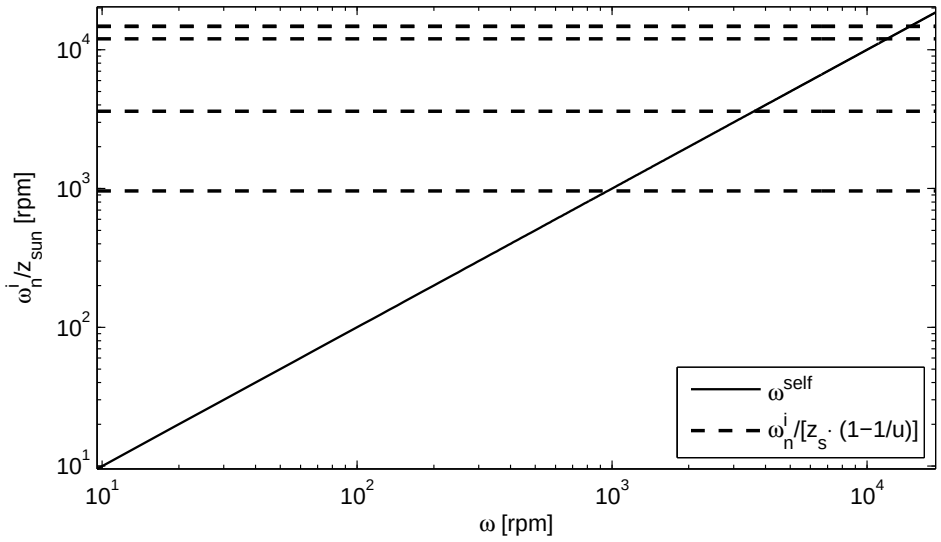

Figure 5.6.: Self excitation speeds due to the time varying mesh stiffness.

rendering the proposed gear dynamics model invalid in such situations. Simulation conditions that make the meshing teeth loose contact will be disregarded.

Previously, the natural modes were studied forcing the damping parameters c_{sp}, c_{pr}, c_{1c} and c_{s2}, (figure 5.4) to 0, however some reference values for the mesh damping c_{pw} can be found in the literature [25]. For the current simulations the values of $c_{sp} = c_{pr} = 700$ Ns/m and $c_{1c} = c_{s2} = 0.04$ Nm·s were selected according to Vedmar's *et al.* work [101], shown in table 5.4.

Table 5.4.: Damping coefficients (Planetary gearbox simulations).

Property	Value	Units
$\boldsymbol{c_{sp}}$	700	Ns/m
$\boldsymbol{c_{pr}}$	700	Ns/m
$\boldsymbol{c_{1c}}$	0.04	Nm·s
$\boldsymbol{c_{s2}}$	0.04	Nm·s

The time varying mesh stiffness's, K_{sp}^t and K_{pr}^t, were once again obtained according to the method suggested in section 2.3 where the load distribution was calculated minimizing the total potential energy of the system and the boundary conditions introduced using a Lagrange multiplier. The frictional effects in gear dynamics were taken into account in the time varying mesh stiffness. The local CoF formulation proposed by Xu [53] was once again considered (detailed in 1.1.2).

In order to perform the dynamic power loss simulations the PAOR gear oil was selected. The loads and speeds were selected according to table 4.8. The oil temperature was imposed according to table 4.14.

As it was previously mentioned the amplitude of vibration is highest in the vicinity of the natural modes. The two first (non-zero) self excitation speeds were selected. The load was set at 2800 Nm and the oil temperature was set at 80 °C.

A centred finite differences scheme was used to numerically solve equations (5.2.5) to (5.2.9). A proper integration time Δt was selected for each simulation. As for the boundary conditions, the input speed ($\dot{\theta}_1$) and output torque (M_2) were fixed.

5.2.3. Results

Table 5.5 shows a comparison between the dynamic (D) and quasi-static (S) average power loss for a single planet. For the simulations at the conditions presented in table 4.8 the differences ($\Delta\%$) between the quasi-static and dynamic average power losses were between 0.61 and 2.41 %, however the simulation at $\omega_{self}^{s,2}$ resulted in a difference of -5.3 % for the planet-ring contact. It should be noted that the largest differences are observed for the planet-ring contact. In fact the average deviation for the sun-planet is 1.4 % while for the planet-ring contact is 2.4 %. Figures 5.7 to 5.16 show the local quantities at stabilized dynamic conditions for the operating conditions specified in subsection 5.2.2. The figures for the 150 rpm simulations at 2000 Nm and 2400 Nm were omitted due to the similarities with the figures for the 150 rpm /2800 Nm simulation.

In these figures it becomes apparent that usually the load variations due to dynamic effects are more pronounced in the planet-ring contact, hence the highest deviations between the quasi-static and dynamic average power losses.

The results found in this section are in line with what was already found for the dynamic power loss study in for single gear pairs done in chapter 3. For selected operating conditions, specifically the ones that excite certain natural modes, the influence of dynamics in the average power loss can be relevant specially considering that at nominal load conditions the gears are usually the most important power loss source.

Table 5.5.: Quasi-static vs dynamic average power loss for PAOR (one planet).

Speed [rpm]	**Torque** [Nm]	**Power Loss [W]**					
		SP			**PR**		
		S	**D**	**Δ** [%]	**S**	**D**	**Δ** [%]
$\omega_{self}^{s,1}$ **= 961.2**	**2800**	161.95	159.83	1.3	19.53	19.08	2.36
$\omega_{self}^{s,2}$ **= 3600.8**	**2800**	531.03	519.86	2.14	64.04	67.61	-5.3
100	**2800**	110.88	109.34	-1.38	15.53	15.26	1.77
	2000	100.96	99.62	1.35	11.83	11.58	2.16
150	**2400**	114.42	112.85	1.39	14.15	13.84	2.24
	2800	123.00	121.28	1.42	15.74	15.37	2.41
200	**2800**	137.31	135.87	1.06	16.56	16.46	0.61

S - Quasi-static load; **D** - Dynamic load

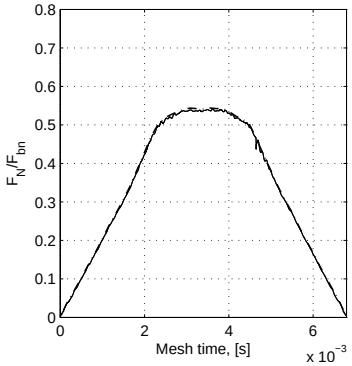

(a) Total normal force, $F_{bn}(t)$.

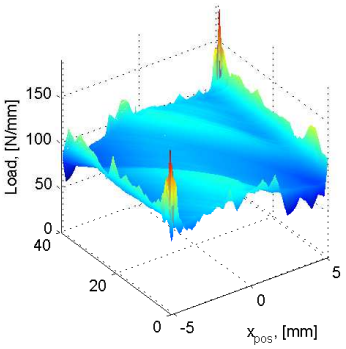

(b) Load per unit of line length, $f_N(x, y)$.

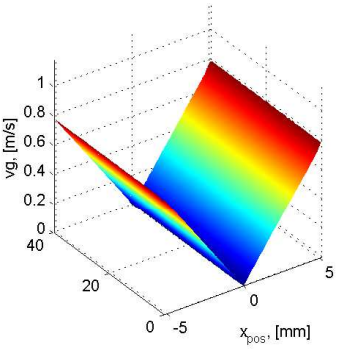

(c) Sliding velocity, $V_g(x, y)$.

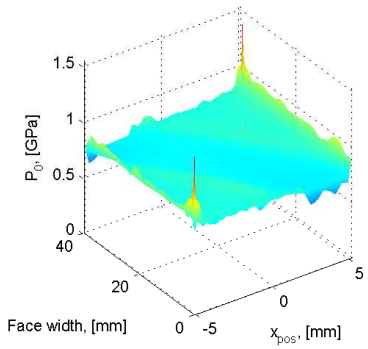

(d) Hertzian pressure, $P_0(x, y)$.

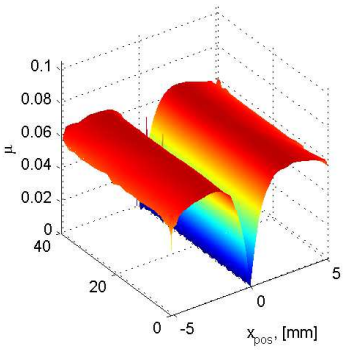

(e) CoF, $\mu^{Xu}(x, y)$.

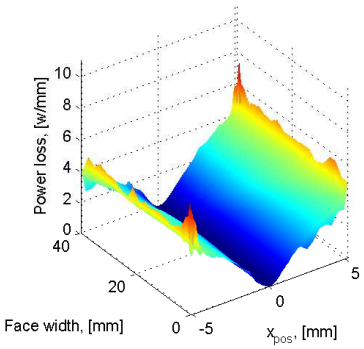

(f) Power loss per unit of line length, $p_{VZP}(x, y)$.

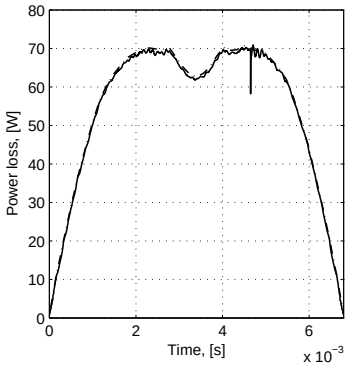

(g) $P_{VZP}^{single}(t)$.

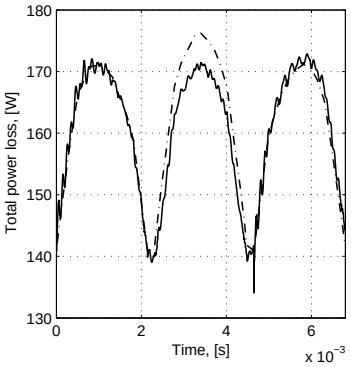

(h) $P_{VZP}^{total}(t)$.

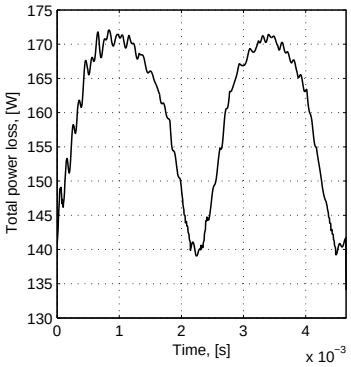

(i) $P_{VZP}^{total}(0 : t : T^{mesh})$.

Figure 5.7.: Local quantities and power loss at stabilized dynamic conditions (PAOR @ $\omega_{self}^{s,1} s$ rpm, 2800 Nm) - SP.

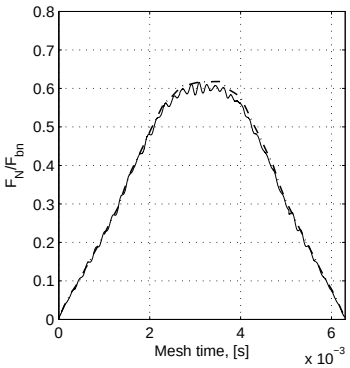

(a) Total normal force, $F_{bn}(t)$.

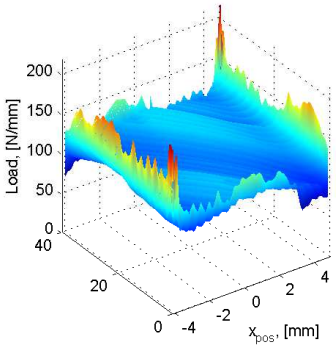

(b) Load per unit of line length, $f_N(x, y)$.

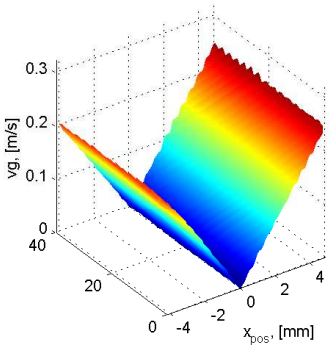

(c) Sliding velocity, $V_g(x, y)$.

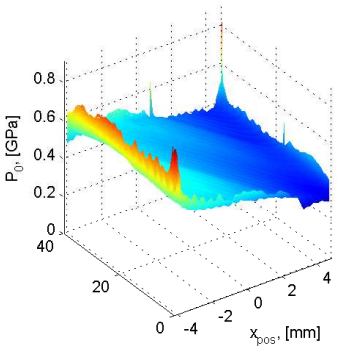

(d) Hertzian pressure, $P_0(x, y)$.

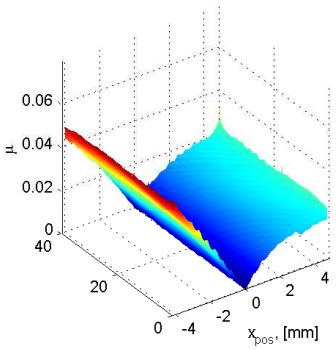

(e) CoF, $\mu^{Xu}(x, y)$.

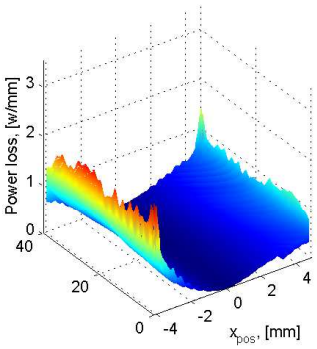

(f) Power loss per unit of line length, $p_{VZP}(x, y)$.

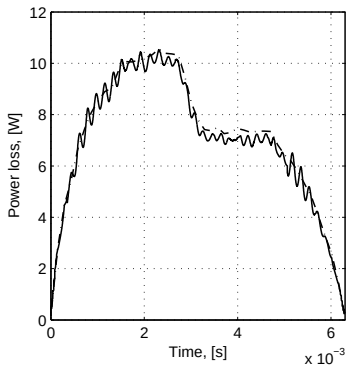

(g) $P_{VZP}^{single}(t)$.

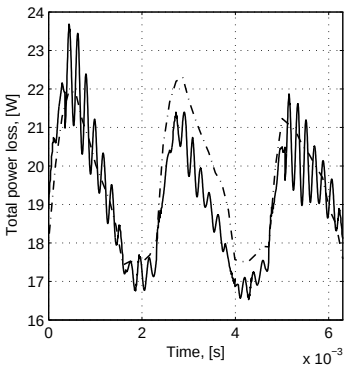

(h) $P_{VZP}^{total}(t)$.

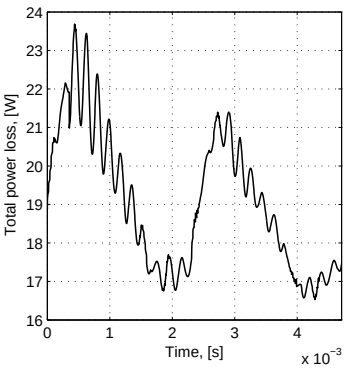

(i) $P_{VZP}^{total}(0 : t : T^{mesh})$.

Figure 5.8.: Local quantities and power loss at stabilized dynamic conditions (PAOR @ $\omega_{self}^{s,1}s$ rpm, 2800 Nm) - PR.

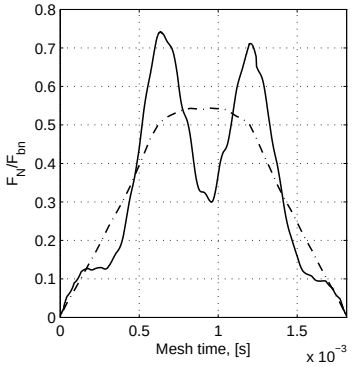

(a) Total normal force, $F_{bn}(t)$.

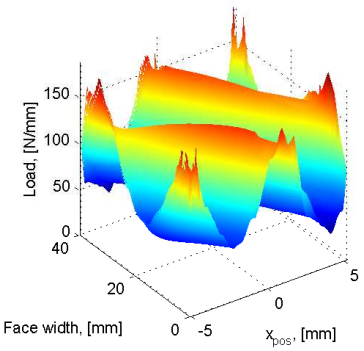

(b) Load per unit of line length, $f_N(x, y)$.

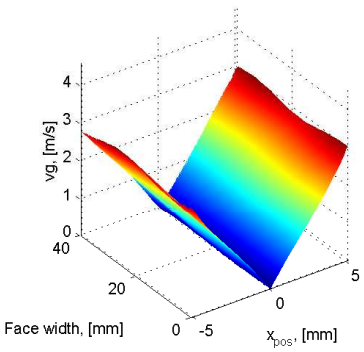

(c) Sliding velocity, $V_g(x, y)$.

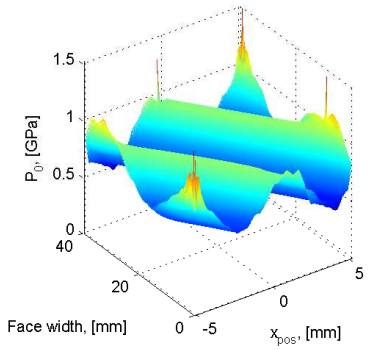

(d) Hertzian SPessure, $P_0(x, y)$.

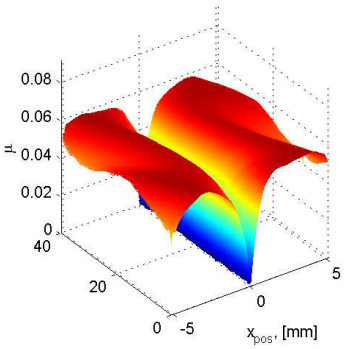

(e) CoF, $\mu^{Xu}(x, y)$.

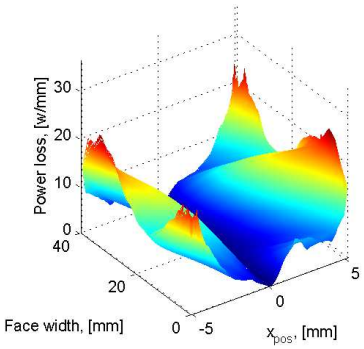

(f) Power loss per unit of line length, $p_{VZP}(x, y)$.

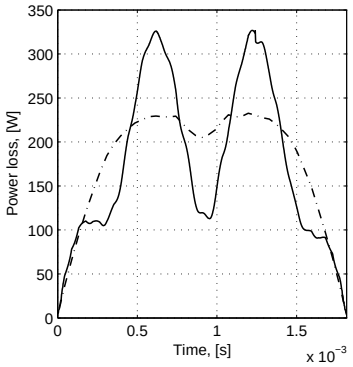

(g) $P_{VZP}^{single}(t)$.

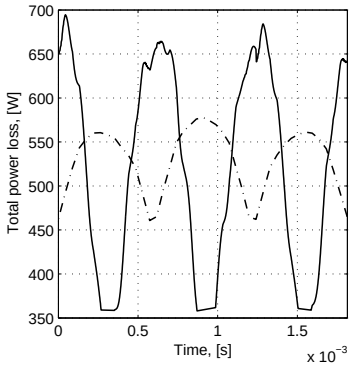

(h) $P_{VZP}^{total}(t)$.

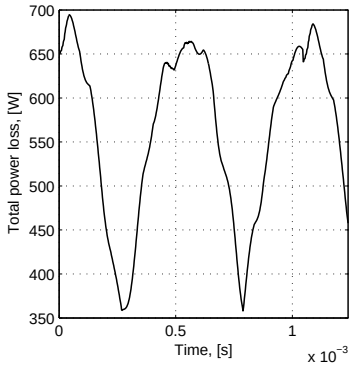

(i) $P_{VZP}^{total}(0 : t : T^{mesh})$.

Figure 5.9.: Local quantities and power loss at stabilized dynamic conditions (PAOR @ $\omega_{self}^{s,2}s$ rpm, 2800 Nm) - SP.

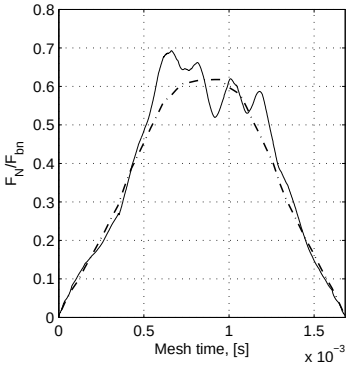

(a) Total normal force, $F_{bn}(t)$.

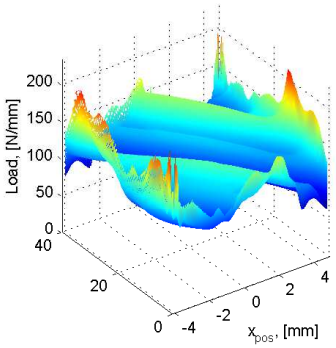

(b) Load per unit of line length, $f_N(x, y)$.

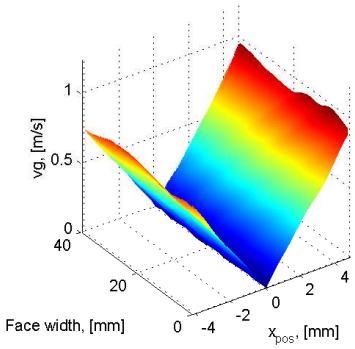

(c) Sliding velocity, $V_g(x, y)$.

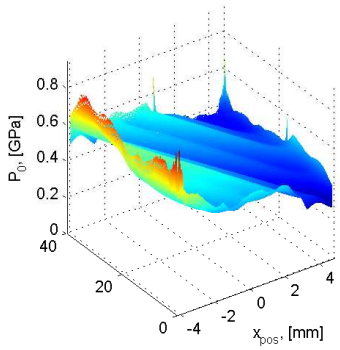

(d) Hertzian pressure, $P_0(x, y)$.

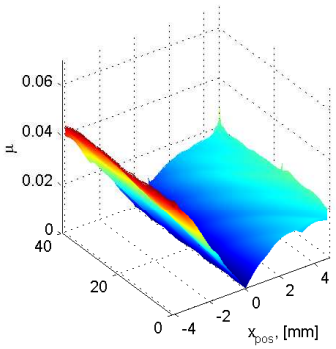

(e) CoF, $\mu^{Xu}(x, y)$.

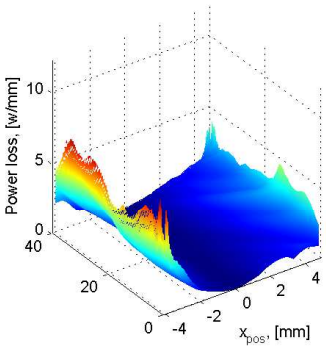

(f) Power loss per unit of line length, $p_{VZP}(x, y)$.

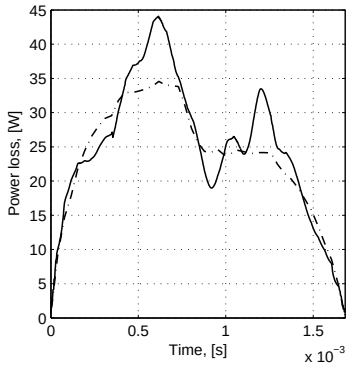

(g) $P_{VZP}^{single}(t)$.

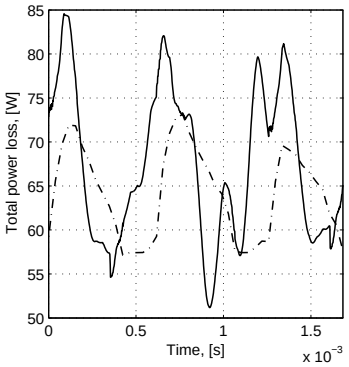

(h) $P_{VZP}^{total}(t)$.

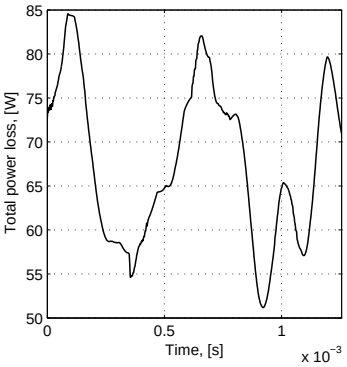

(i) $P_{VZP}^{total}(0 : t : T^{mesh})$.

Figure 5.10.: Local quantities and power loss at stabilized dynamic conditions (PAOR @ $\omega_{self}^{s,2}s$ rpm, 2800 Nm) - PR.

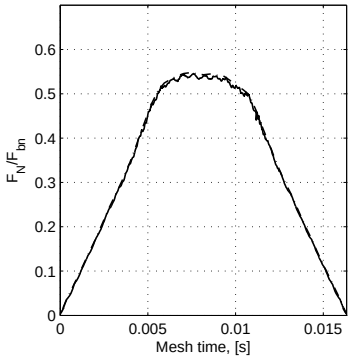

(a) Total normal force, $F_{bn}(t)$.

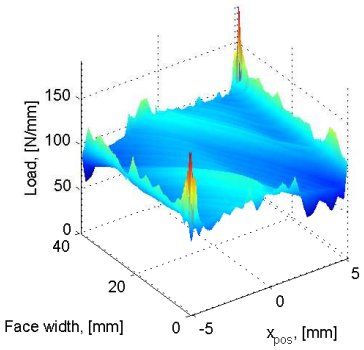

(b) Load per unit of line length, $f_N(x, y)$.

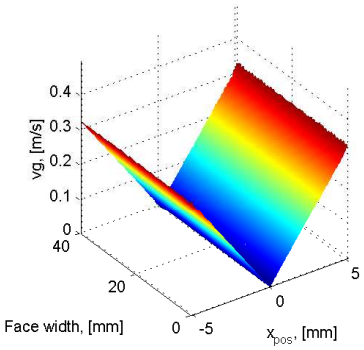

(c) Sliding velocity, $V_g(x, y)$.

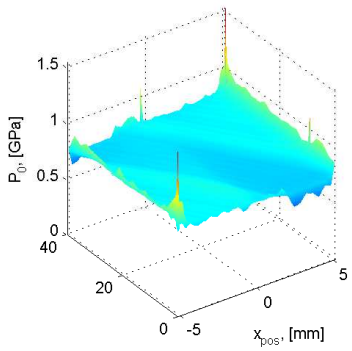

(d) Hertzian SPessure, $P_0(x, y)$.

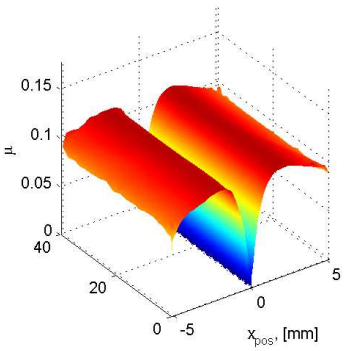

(e) CoF, $\mu^{Xu}(x, y)$.

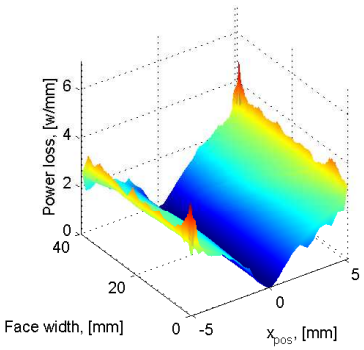

(f) Power loss per unit of line length, $p_{VZP}(x, y)$.

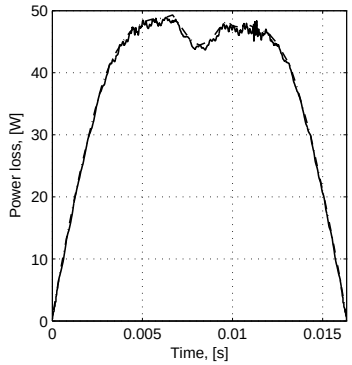

(g) $P_{VZP}^{single}(t)$.

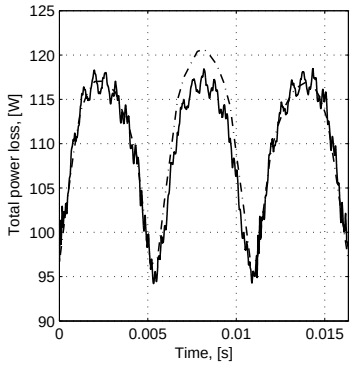

(h) $P_{VZP}^{total}(t)$.

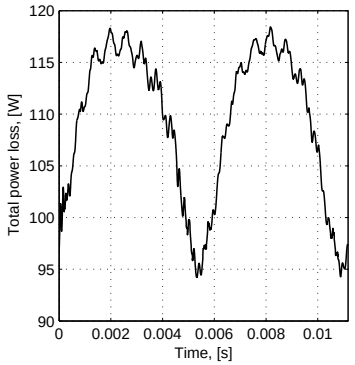

(i) $P_{VZP}^{total}(0 : t : T^{mesh})$.

Figure 5.11.: Local quantities and power loss at stabilized dynamic conditions (PAOR @ 100 rpm, 2800 Nm) - SP.

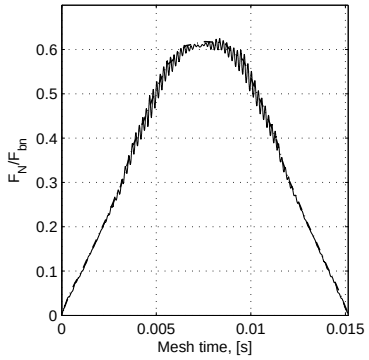

(a) Total normal force, $F_{bn}(t)$.

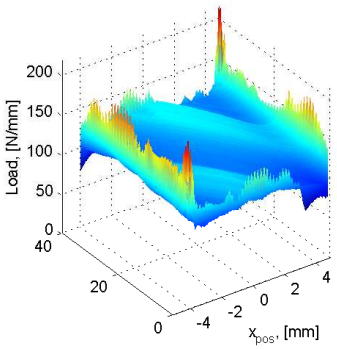

(b) Load per unit of line length, $f_N(x, y)$.

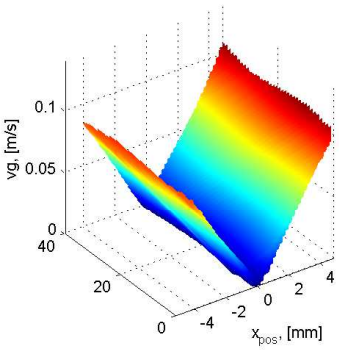

(c) Sliding velocity, $V_g(x, y)$.

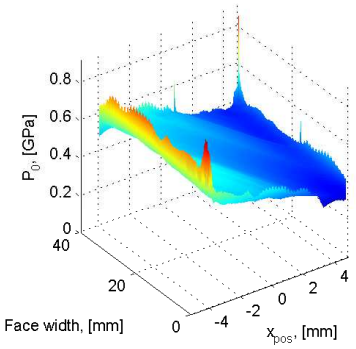

(d) Hertzian pressure, $P_0(x, y)$.

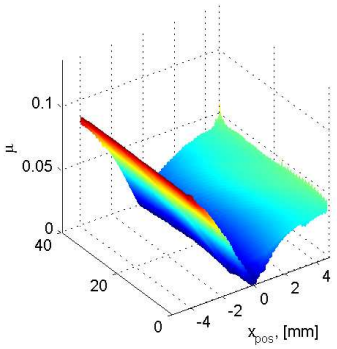

(e) CoF, $\mu^{Xu}(x, y)$.

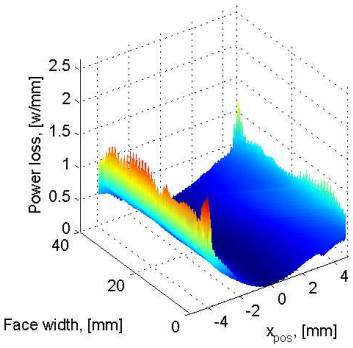

(f) Power loss per unit of line length, $p_{VZP}(x, y)$.

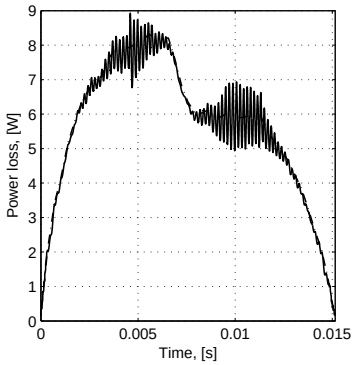

(g) $P_{VZP}^{single}(t)$.

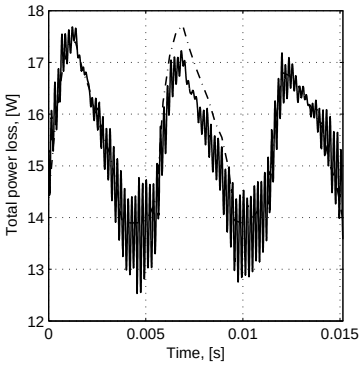

(h) $P_{VZP}^{total}(t)$.

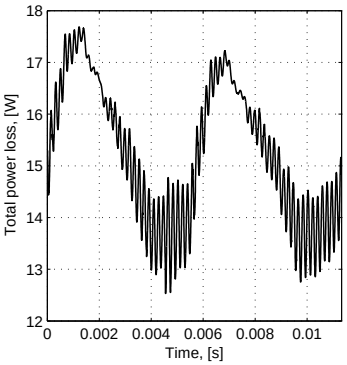

(i) $P_{VZP}^{total}(0 : t : T^{mesh})$.

Figure 5.12.: Local quantities and power loss at stabilized dynamic conditions (PAOR @ 100 rpm, 2800 Nm) - PR.

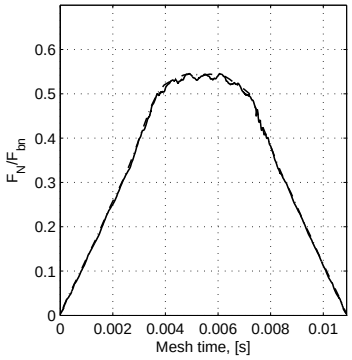

(a) Total normal force, $F_{bn}(t)$.

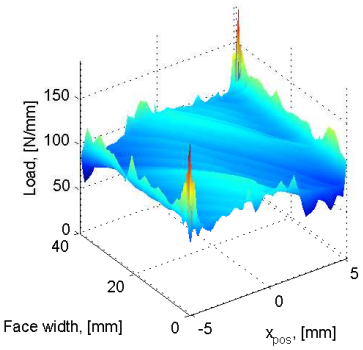

(b) Load per unit of line length, $f_N(x, y)$.

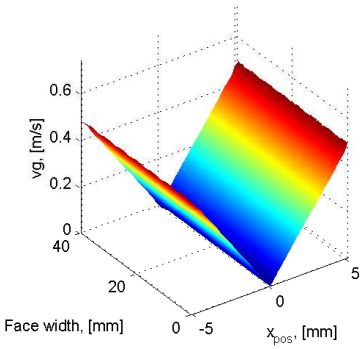

(c) Sliding velocity, $V_g(x, y)$.

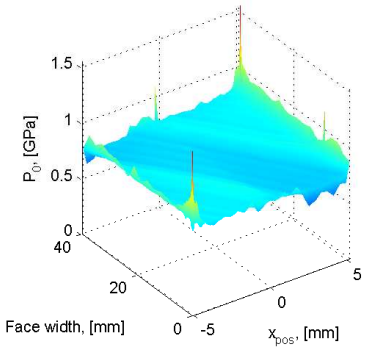

(d) Hertzian pressure, $P_0(x, y)$.

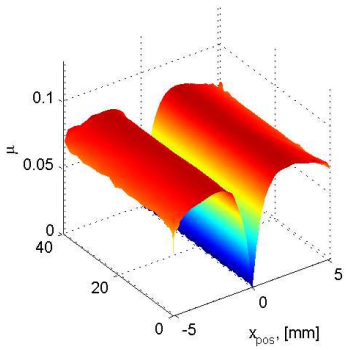

(e) CoF, $\mu^{Xu}(x, y)$.

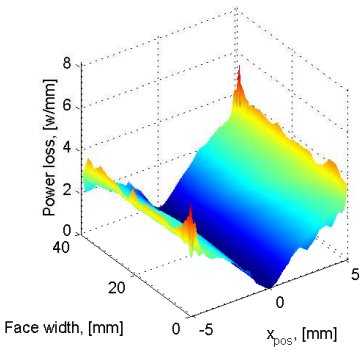

(f) Power loss per unit of line length, $p_{VZP}(x, y)$.

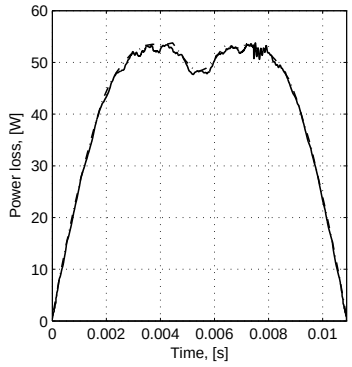

(g) $P_{VZP}^{single}(t)$.

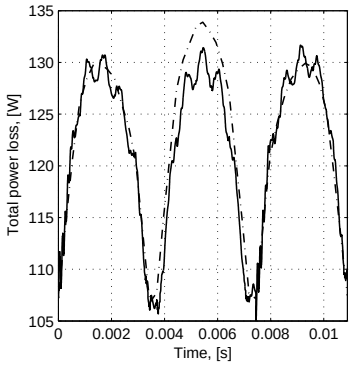

(h) $P_{VZP}^{total}(t)$.

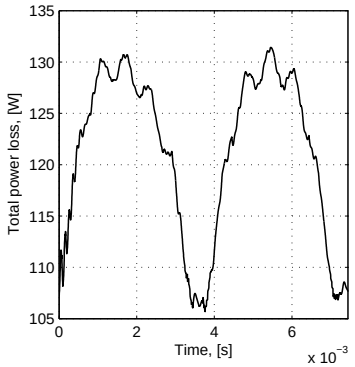

(i) $P_{VZP}^{total}(0 : t : T^{mesh})$.

Figure 5.13.: Local quantities and power loss at stabilized dynamic conditions (PAOR @ 150 rpm, 2800 Nm) - SP.

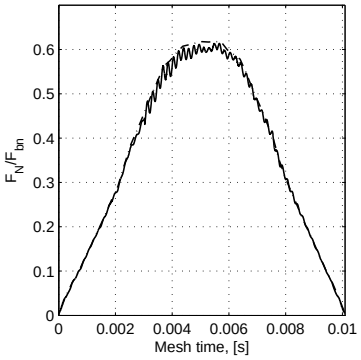

(a) Total normal force, $F_{bn}(t)$.

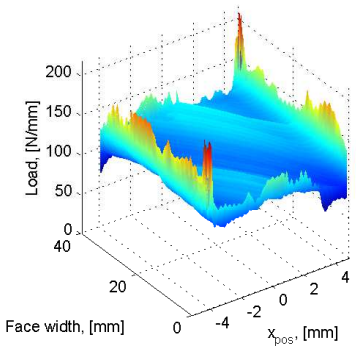

(b) Load per unit of line length, $f_N(x, y)$.

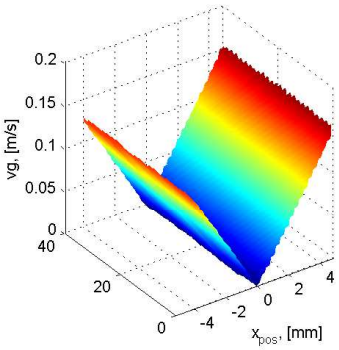

(c) Sliding velocity, $V_g(x, y)$.

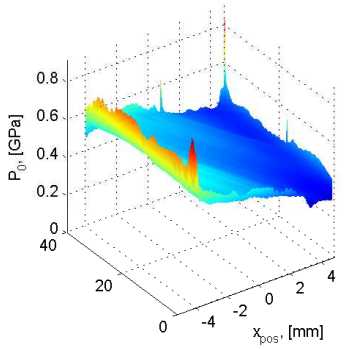

(d) Hertzian pressure, $P_0(x, y)$.

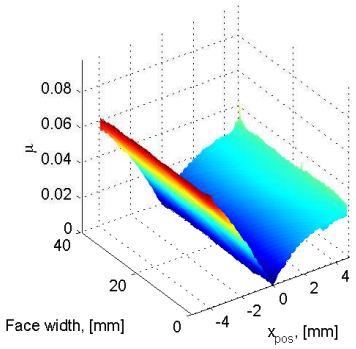

(e) CoF, $\mu^{Xu}(x, y)$.

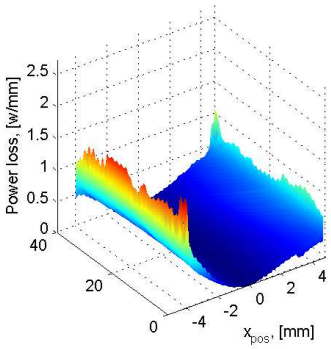

(f) Power loss per unit of line length, $p_{VZP}(x, y)$.

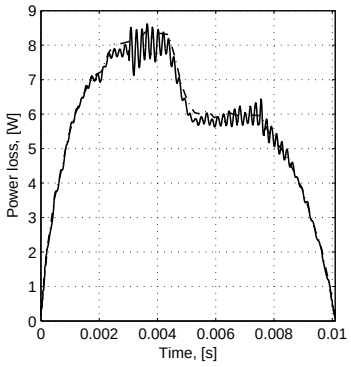

(g) $P_{VZP}^{single}(t)$.

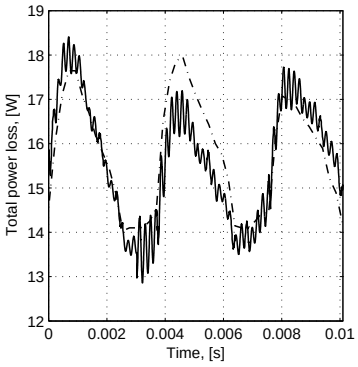

(h) $P_{VZP}^{total}(t)$.

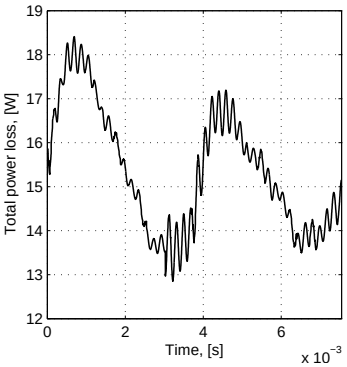

(i) $P_{VZP}^{total}(0 : t : T^{mesh})$.

Figure 5.14.: Local quantities and power loss at stabilized dynamic conditions (PAOR @ 150 rpm, 2800 Nm) - PR.

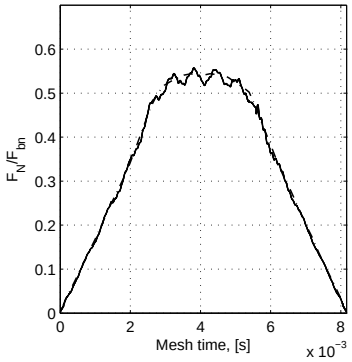

(a) Total normal force, $F_{bn}(t)$.

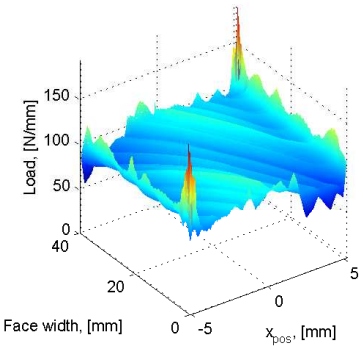

(b) Load per unit of line length, $f_N(x, y)$.

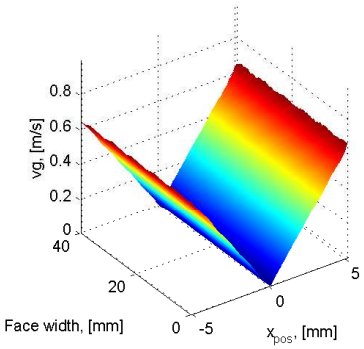

(c) Sliding velocity, $V_g(x, y)$.

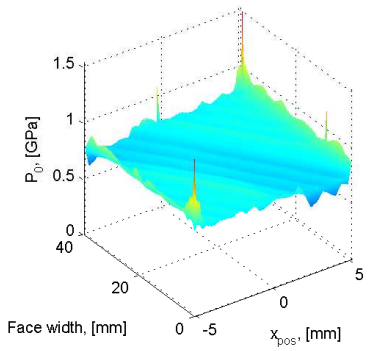

(d) Hertzian pressure, $P_0(x, y)$.

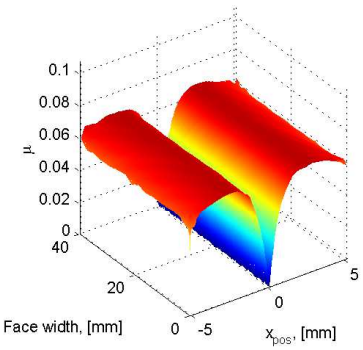

(e) CoF, $\mu^{Xu}(x, y)$.

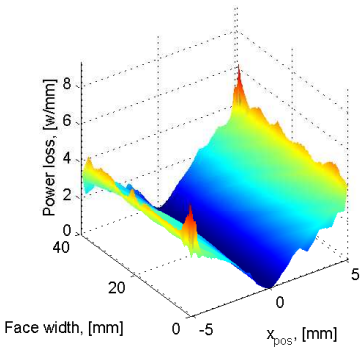

(f) Power loss per unit of line length, $p_{VZP}(x, y)$.

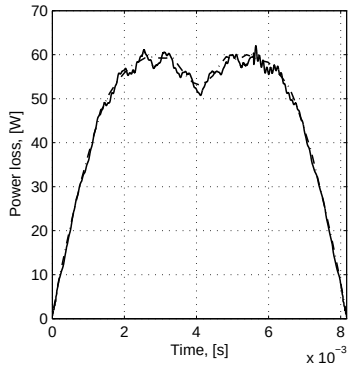

(g) $P_{VZP}^{single}(t)$.

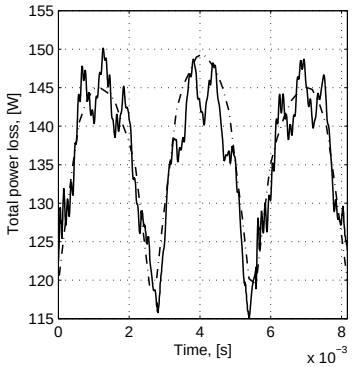

(h) $P_{VZP}^{total}(t)$.

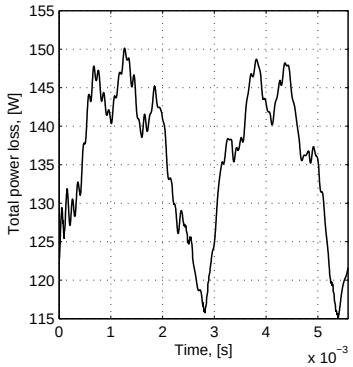

(i) $P_{VZP}^{total}(0 : t : T^{mesh})$.

Figure 5.15.: Local quantities and power loss at stabilized dynamic conditions (PAOR @ 200 rpm, 2800 Nm) - SP.

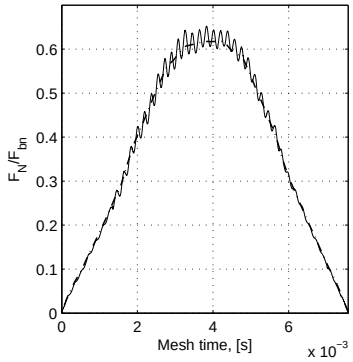

(a) Total normal force, $F_{bn}(t)$.

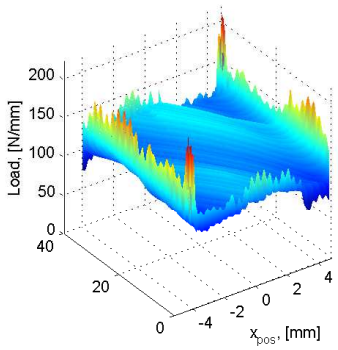

(b) Load per unit of line length, $f_N(x, y)$.

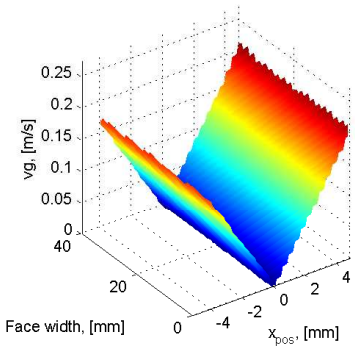

(c) Sliding velocity, $V_g(x, y)$.

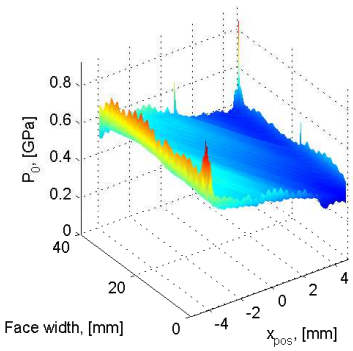

(d) Hertzian pressure, $P_0(x, y)$.

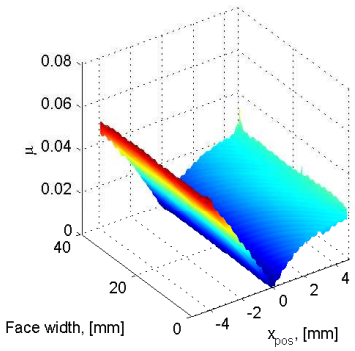

(e) CoF, $\mu^{Xu}(x, y)$.

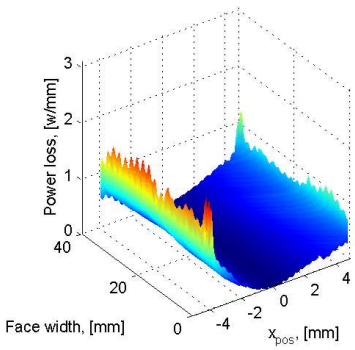

(f) Power loss per unit of line length, $p_{VZP}(x, y)$.

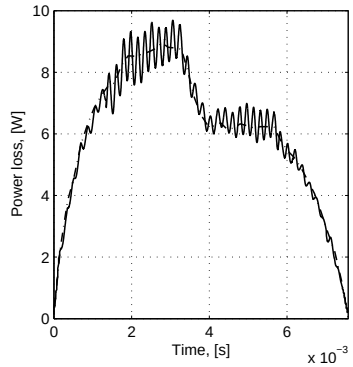

(g) $P_{VZP}^{single}(t)$.

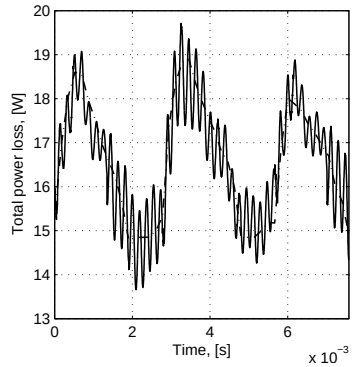

(h) $P_{VZP}^{total}(t)$.

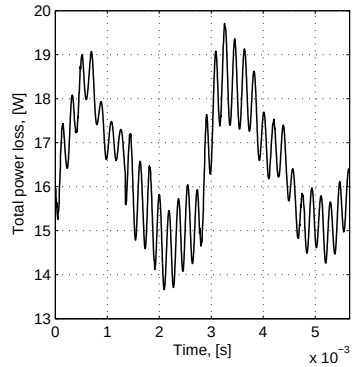

(i) $P_{VZP}^{total}(0 : t : T^{mesh})$.

Figure 5.16.: Local quantities and power loss at stabilized dynamic conditions (PAOR @ 200 rpm, 2800 Nm) - PR

5.3. Closure

In this chapter the concepts that were developed for a single gear pair in chapter 3 were applied to a planetary gearbox. The models that were developed could be readily applied without any specific modification. The three load distribution models yielded slightly different load distributions (F/F_{bn}). The reason for such differences could be observed in the differences in the mesh stiffness functions where some significant differences could be observed namely the average stiffness that was quite different between the quasi-static elastic and local elastic models. Regarding the power loss simulations the first thing that should be noted is that the internal gearing promotes lower loss than the external sun-planet gearing.

A planetary dynamics model was developed aiming to study the influence of gear dynamics in the average power loss in a planetary gearbox. A plan of simulations aiming to replicate the tangential speeds and average contact pressure of a real planetary gearbox in a real wind turbine was followed, two self excitation speeds were also included. The results showed that average differences in the average power loss of 1.4% for the sun-planet and 2.4% for the planet-ring contact can be observed. At the second self-excitation speed a difference of -5.3% was calculated for the planet ring-contact. The results once again indicate that in the right conditions there can be some significant deviations in the average power loss between the quasi-static and dynamic average power loss.

6. Conclusions and Future Work

6.1. Conclusions

This thesis was divided in six different chapters.

Chapter **1 - Classical Gearbox Powerloss Model** was dedicated to the introduction of the classical approach to gearbox power loss. The different power loss sources were categorised and different models to estimate each one of the sources were also presented and detailed. Through the course of chapter 1 it has become apparent that there are many solutions for the same power loss problems (gears, rolling bearings and seals).

It was also pointed out that one of the main deficiencies of any state of the art power loss models is in the prediction of the no-load losses, where different models applied to the same conditions yield very different results, differences of orders of magnitude between the models are sometimes calculated. The aim of chapter 1 was to introduce and show the multiple solutions regarding some of the multiple approaches to modelling different power loss sources.

Chapter **2 - Developments for a Gear Pair: Load Sharing and Power Loss in Meshing Gears** dealt with the load distribution problem including frictional effects in spur and helical gears, as well as a generalized approach to power loss estimation. A analytical approach to the gear contact line length based on Heaviside functions was developed. Three different, yet simple load distribution models, were proposed from the rigid tooth approach to the elastic solution including friction. A generalized power loss formulation was also presented.

The results obtained with the elastic models (load distribution and mesh stiffness) were in agreement with each other when the CoF was set to $\mu = 0$. The most advanced of the models considered the frictional effects in the load balance, so that modifications in the load distribution and mesh stiffness were observed due to friction. In the load distribution per unit of length the free edge effects were also observed. The frictional and elastic effects were clearly visible in results obtained for the spur gears, where a step could be observed at the pitch point in the case of constant CoF formulation. When the local CoF was considered the transition was done smoothly without sudden steps, but a slope was still observed. In the case of helical gears the frictional effects seem to play a lesser role in the load distribution even when the constant CoF is considered.

From the generalized gear power loss approach an average power loss and gear loss factors could be calculated. The differences that were observed in the gear loss factors

(rigid vs elastic+friciton) can be relevant depending on the accuracy and refinement of the desired power loss prediction. The calibration of the lubricant factor X_L that is used in Schlenk's *et al.* [48] average COF formulation can be done according to the methodology proposed by Fernandes *et al.* [2]. In this methodology an accurate gear loss factor is a fundamental piece in finding accurate X_L values and power loss estimations.

In Chapter **3 - Developments for a Gear Pair: Gear Dynamics and Power Loss** a four degree of freedom torsional lumped mass gear dynamic model was deduced from the Principle of Least Action. The model considered the frictional effects in the vibrational behaviour. The effects of gear dynamics and gear geometry in the average power loss were then evaluated.

Gear geometry plays a very important role in gear dynamics. The spur gear showed higher dynamic overloads mainly due to the step like mesh stiffness variations at the transitions from gear mesh of multiple to single tooth pairs and vice versa. Friction has not shown a significant, yet visible, effect in the torsional dynamic behaviour of either spur and helical gears.

It was verified that there can be some differences (up to 3.6 % for the present simulations in the case of spur gears) between the quasi-static and dynamic average power loss. This raises some concern because spur gears, namely C40 gears, are often used to perform efficiency tests and calibrate power loss models [2], namely the lubricant factor X_L in the case of Schlenk's CoF formulation [48] which has recently been adopted as a standard.

It was verified that gears with slow varying mesh stiffness are prone to be less affected by dynamic self-excitations. It was also shown that dynamic excitations can have an influence in the average power loss and potentially in the lubricant parameter (X_L), therefore a gear that is pre-disposed to promote a smoother operation should be better to perform power loss studies in which the aim is not to study the gear, but the lubricant itself. It was proposed that such gear would ideally have a constant mesh stiffness (potentially less dynamic effects) and a gear loss factor similar to that of the C40 gear (≈ 0.2) in order to have an experimental torque loss less affected by measurement. Such gear would have to be an helical gear.

Chapter **4 - Power Loss in a Multiplier Planetary Gearbox Lubricated with Wind Turbine Gear Oils** was dedicated to the experimental and numerical power loss study of a planetary gearbox in a multiplier configuration. Four fully formulated ISO VG 320 wind turbine gear oils were selected and characterized, two of them being mineral based oils (MINR and MINE) and the other two being synthetic based oils: a poly$-\alpha-$olefin (PAOR) and a polyalkyleneglycol (PAGD).

The global power loss of the selected gearbox was evaluated in a set of experimental tests aiming to promote similar pitch line speeds and contact pressures of a planetary gearbox of the first stage 2.5 MW wind turbine.

The power loss experiments showed that PAOR lead to the lowest values of stabilization temperature. MINR lead to the highest stabilization temperatures, except

for the test at 100 rpm, where the highest temperature was achieved with PAGD. The differences between oils never exceeded 7°C.

The numerical model showed that at the selected operating conditions, the gears are the most significant power loss source. However it should be noted that in all cases the power loss in the rolling bearings (TRBs+FCNRBs+DGBB) accounts for the majority of the power loss in the planetary gearbox. For the same operating conditions, the numerical results indicate that PAGD had the lowest load dependent power loss.

The churning losses are quite relevant, specially for PAGD which despite showing the lowest coefficient of friction in the gears it did not present the best power loss performance. The reduction of the friction in the gears was not high enough to overcome the increase in the churning losses relatively to the other lubricants.

In chapter **5 - Planetary Gears: Local Load Sharing and Power loss (quasi-static vs dynamic)** the load distribution and dynamics concepts and developments for a single gear pair were applied to the planetary gearbox in study. The quasi-static average power loss solution was compared with the power loss including dynamic effects. A planetary gear dynamics model was presented and some simulations/results were analysed.

The planetary dynamics model was also developed aiming to study the influence of gear dynamics in the average power loss in a planetary gearbox. A plan of simulations aiming to replicate the tangential speeds and average contact pressure of a real planetary gearbox in a real wind turbine was followed, two self excitation speeds were also included. The results showed that average differences in the average power loss of 1.4% for the sun-planet and 2.4% for the planet-ring contact can be observed. At the second self-excitation speed a difference of -5.3% was calculated for the planet ring-contact. The results once again indicate that in same conditions there can be some significant deviations in the average power loss between the quasi-static and dynamic average power loss.

6.2. Future work

The models that were developed had simplifying assumptions that could influence some of the results that were obtained, also some of the numerical implementations could be improved in different ways. Below some notes are left with topics and ideas/improvements for future works:

- Influence of the non-linear hertz stiffness (including surface roughness) in the load distribution and the gear mesh stiffness;
- "Out of" the plane of action gear contact due to elasticity;
- Full rotor dynamics model for gear dynamics (transverse vibrations as well as gyroscopic effects) including a time varying gear mesh damping;
- Influence of the dynamic loads on surface distress including surface roughness;

The effects that were neglected and their respective influence could result in further modifications on the predicted power loss.

Due to their potential benefits and advantages over regular gears the concept of constant mesh stiffness gears (CMSG's) should be studied and developed.

A. Scientific publications

Through the course of this PhD program the author has published some of his work in peer reviewed journals as well as scientific meetings and conferences.

Publications in peer reviewed Journals

1. Pedro M.T. Marques, Ramiro C. Martins, Jorge H.O. Seabra, Gear dynamics and power loss, Tribology International, Volume 97, May 2016, Pages 400-411.

2. Pedro M.T. Marques, Ramiro C. Martins, and Jorge H.O. Seabra. Power loss and load distribution models including frictional effects for spur and helical gears. Mechanism and Machine Theory, 96, Part 1:1 – 25, 2016.

3. Ramiro C. Martins, Pedro M.T. Marques, Diogo Pereira, and Jorge H.O. Seabra Torque loss in a planetary gearbox lubricated with wind turbine gear oils, Tribologie + Schmierungstechnik, 62, Jahrgang, 4/2015.

4. C. M. C. G. Fernandes, P. M. T. Marques, R. C. Martins, and J. H. O. Seabra. Influence of gear loss factor on the power loss prediction. Mechanical Sciences, 6(2):81–88, 2015.

5. Pedro M.T. Marques, Raquel Camacho, Ramiro C. Martins, and Jorge H.O. Seabra. Efficiency of a planetary multiplier gearbox: Influence of operating conditions and gear oil formulation. Tribology International, 92(0):272 – 280, 2015.

6. Carlos M.C.G. Fernandes, Pedro M.T. Marques, Ramiro C. Martins, and Jorge H.O. Seabra. Film thickness and traction curves of wind turbine gear oils. Tribology International, 86(0):1 – 9, 2015.

7. Carlos M.C.G. Fernandes, Pedro M.T. Marques, Ramiro C. Martins, and Jorge H.O. Seabra. Gearbox power loss. Part III: Application to a parallel axis and a planetary gearbox. Tribology International, 88(0):317 – 326, 2015.

8. Carlos M.C.G. Fernandes, Pedro M.T. Marques, Ramiro C. Martins, and Jorge H.O. Seabra. Gearbox power loss. Part II: Friction losses in gears. Tribology International, 88(0):298–308, 2015.

9. Carlos M.C.G. Fernandes, Pedro M.T. Marques, Ramiro C. Martins, and Jorge H.O. Seabra. Gearbox power loss. Part I: Losses in rolling bearings. Tribology International, 88(0):309–316, 2015.

10. Pedro M.T. Marques, Carlos M.C.G. Fernandes, Ramiro C. Martins, and Jorge H.O. Seabra. Efficiency of a gearbox lubricated with wind turbine gear oils. Tribology International, 71(0):7 – 16, 2014.

11. Pedro M.T. Marques, Carlos M.C.G. Fernandes, Ramiro C. Martins, and Jorge H.O. Seabra. Power losses at low speed in a gearbox lubricated with wind turbine gear oils with special focus on churning losses. Tribology International, 62(0):186 – 197, 2013.

Publications in conferences and scientific meetings

1. Pedro M.T. Marques, Carlos M. C. G. Fernandes,Ramiro C. Martins, Jorge H.O. Seabra, Influence of Dynamic Loads in Gear Power Loss. In Proceedings of the 5th International Conference on Integrity, Reliability and Failure, Porto/Portugal, 24-28th July 2016, ISBN 978-989-98832-4-6.

2. Carlos M. C. G. Fernandes, Pedro M.T. Marques, Ramiro C. Martins, Jorge H.O. Seabra, New Coefficient of Friction Equation for Gears Under Mixed Lubrication. In Proceedings of the 5th International Conference on Integrity, Reliability and Failure, Porto/Portugal, 24-28th July 2016, ISBN 978-989-98832-4-6.

3. Pedro M.T. Marques, Ramiro C. Martins, Jorge H.O. Seabra, Gear dynamics and power loss, TAE, January 2016, Esslingen.

4. Pedro M. T. Marques, Ramiro C. Martins, and Jorge H. O. Seabra. Load distribution in helical gears including elastic and friction effects. In Proceedings of the 6th International Conference on Mechanics and Materials in Design, pages 1949–1958, 2015.

5. Pedro M. T. Marques, Ramiro C. Martins, and Jorge H. O. Seabra. Efficiency of a gearbox lubricated with wind turbine gear oils. In Symposium on Mechanical Engineering, Session IV, 1st Doctoral Congress in Engineering, 11-12 June 2015, FEUP.

6. Pedro M. T. Marques, Ramiro C. Martins, and Jorge H. O. Seabra. Power loss in a gearbox lubricated with wind turbine gear oils. In Abstracts of the 3rd EJIL, LAETA Young Researchers Meeting, page 84. LAETA, 2015.

7. Ramiro Martins, Pedro Marques, Diogo Pereira, and Jorge Seabra. Torque loss in a planetary gearbox lubricated with wind turbine gear oils. In 19th International Colloquium Tribology, Industrial and Automotive Lubrication, Solving Friction and Wear Problems, Technische Akademie Esslingen e.V., Stuttgart / Ostfildern, Germany, January 2014.

8. Carlos M. C. G. Fernandes, Pedro M. T. Marques, Ramiro C. Martins, and Jorge H. O. Seabra. Influence of gear loss factor on the power loss prediction. In New Trends in Mechanism and Machine Science, From Fundamentals to Applications, Mechanisms and Machine Science 24, pages 799–806. Springer, 2014.

9. Pedro M. T. Marques, Carlos Fernandes, Ramiro C. Martins, and Jorge H. O. Seabra. Power loss in a planetary gearbox. In In International Gear Conference 2014 Volume II, pages 636–645. Woodhead Publishing, 2014.

10. Pedro M. T. Marques, Ramiro C. Martins, and Jorge H. O. Seabra. Load distribution in spur gears including the effects of friction. In New Trends in Mechanism and Machine Science, From Fundamentals to Applications, Mechanisms and Machine Science 24, pages 789–797. Springer, 2014.

11. Ramiro Martins, Carlos M.C.G. Fernandes, Pedro Marques, and Jorge H. O. Seabra. Friction behaviour of iso vg 320 gear oils in gearbox and thrust bearing tests. In International Conference on Gears, VDIBerichete 2199.2, VDI Wissensforum GmbH · VDI-Platz 1 · D-40468 Düsseldorf · Postfach 10 11 39 · D-40002 Düsseldorf, October 2013.

12. Pedro Marques, Carlos Fernandes, Ramiro Martins, and Jorge Seabra. Preliminary results on power loss modelling of planetary gearboxes. In IBERTRIB 2013, FEUP, Universidade do Porto, Rua Dr. Roberto Frias s/n, 4200-465 Porto, Portugal, June 2013.

13. Pedro M. T. Marques, Carlos Fernandes, Ramiro Martins, and Jorge Seabra. Power loss in a multiplier gearbox lubricated with wind turbine gear oils. In IBERTRIB 2013, FEUP, Universidade do Porto, Rua Dr. Roberto Frias s/n, 4200-465 Porto, Portugal, June 2013.

Bibliography

[1] Carlos M.C.G. Fernandes, Pedro M.T. Marques, Ramiro C. Martins, and Jorge H.O. Seabra. Gearbox power loss. part i: Losses in rolling bearings. *Tribology International*, 88:298 – 308, 2015.

[2] Carlos M.C.G. Fernandes, Pedro M.T. Marques, Ramiro C. Martins, and Jorge H.O. Seabra. Gearbox power loss. part ii: Friction losses in gears. *Tribology International*, 88:309 – 316, 2015.

[3] Carlos M.C.G. Fernandes, Pedro M.T. Marques, Ramiro C. Martins, and Jorge H.O. Seabra. Gearbox power loss. part iii: Application to a parallel axis and a planetary gearbox. *Tribology International*, 88:317 – 326, 2015.

[4] Carlos M.C.G. Fernandes, Pedro M. P. Amaro, Ramiro C. Martins, and Jorge H.O. Seabra. Torque loss in cylindrical roller thrust bearings lubricated with wind turbine gear oils at constant temperature. *Tribology International*, (0):under review, 2013.

[5] Carlos M.C.G. Fernandes, Ramiro C. Martins, and Jorge H.O. Seabra. Friction torque of thrust ball bearings lubricated with wind turbine gear oils. *Tribology International*, 58(0):47 – 54, 2013.

[6] Carlos M.C.G. Fernandes, Pedro M.P. Amaro, Ramiro C. Martins, and Jorge H.O. Seabra. Torque loss in thrust ball bearings lubricated with wind turbine gear oils at constant temperature. *Tribology International*, 66(0):194 – 202, 2013.

[7] Pedro M.T. Marques, Carlos M.C.G. Fernandes, Ramiro C. Martins, and Jorge H.O. Seabra. Power losses at low speed in a gearbox lubricated with wind turbine gear oils with special focus on churning losses. *Tribology International*, 62(0):186 – 197, 2013.

[8] Pedro M.T. Marques, Carlos M.C.G. Fernandes, Ramiro C. Martins, and Jorge H.O. Seabra. Efficiency of a gearbox lubricated with wind turbine gear oils. *Tribology International*, 71(0):7 – 16, 2014.

[9] Pedro M.T. Marques, Raquel Camacho, Ramiro C. Martins, and Jorge H.O. Seabra. Efficiency of a planetary multiplier gearbox: Influence of operating conditions and gear oil formulation. *Tribology International*, 92(0):272 – 280, 2015.

[10] H. Xu, A. Kahraman, N. E. Anderson, and D. G. Maddock. Prediction of mechanical efficiency of parallel-axis gear pairs. *Journal of Mechanical Design*, 129(1):58 – 68, 2006/06/14.

[11] Carlo Gorla, Franco Concli, Karsten Stahl, Bernd-Robert Höhn, Klaus Michaelis, Hansjörg Schultheiß, and Johann-Paul Stemplinger. Hydraulic losses of a gearbox: CFD analysis and experiments. *Tribology International*, 66:337 – 344, 2013.

[12] Franco Concli, Edoardo Conrado, and Carlo Gorla. Analysis of power losses in an industrial planetary speed reducer: Measurements and computational fluid dynamics calculations. *Journal of Engineering Tribology*, 288(1):11 – 21, 2014.

[13] David Gonçalves, Samuel Pinho, Beatriz Graça, Armando V. Campos, and Jorge H.O. Seabra. Friction torque in thrust ball bearings lubricated with polymer greases of different thickener content. *Tribology International*, 96:87 – 96, 2016.

[14] World Energy Council. Energy efficiency indicators, 2011.

[15] Pedro M. T. Marques, Ramiro C. Martins, and Jorge H. O. Seabra. Load distribution in spur gears including the effects of friction. In *New Trends in Mechanism and Machine Science, From Fundamentals to Applications*, Mechanisms and Machine Science 24, pages 789–797. Springer, 2014.

[16] Pedro M.T. Marques, Ramiro C. Martins, and Jorge H.O. Seabra. Power loss and load distribution models including frictional effects for spur and helical gears. *Mechanism and Machine Theory*, 96, Part 1:1 – 25, 2016.

[17] M.B. Peterson, W.O. Winer, and American Society of Mechanical Engineers. Research Committee on Lubrication. *Wear Control Handbook*. ASME centennial research project. American Society of Mechanical Engineers, 1980.

[18] Luís Magalhães, Ramiro Martins, Cristiano Locateli, and Jorge Seabra. Influence of tooth profile and oil formulation on gear power loss. *Tribology International*, 43(10):1861–1871, 2010. 36th Leeds-Lyon Symposium Special Issue: Multi-facets of Tribology.

[19] R. Martins, J. Seabra, and L. Magalhães. Austempered ductile iron (adi) gears: Power loss, pitting and micropitting. *Wear*, 264(9-10):838–849, 2008.

[20] R. Martins, J. Seabra, and L. Magalhães. Austempered ductile iron (adi) gears part i - power loss and friction coefficient. In *NORDTRIB 2006*, Helsingør, Denmark, 2006.

[21] Carlos M.C.G. Fernandes, Ramiro C. Martins, and Jorge H.O. Seabra. Torque loss of type C40 FZG gears lubricated with wind turbine gear oils. *Tribology International*, (0):–, 2013.

[22] B.-R. Höhn, K. Michaelis, and M. Hinterstoißer. Optimization of gearbox efficiency. *goriva i maziva*, 48(4):462–480, 2009.

[23] T. T. Petry-Johnson, a. Kahraman, N. E. Anderson, and D. R. Chase. An Experimental Investigation of Spur Gear Efficiency. *Journal of Mechanical Design*, 130(6):062601, 2008.

[24] L. Chang, Yeau-Ren Jeng, and Pay-Yau Huang. Modeling and Analysis of the Meshing Losses of Involute Spur Gears in High-Speed and High-Load Conditions. *Journal of Tribology*, 135(1):011504, 2012.

[25] H Nevzat Özgüven and Donald Russell Houser. Mathematical models used in gear dynamics—a review. *Journal of sound and vibration*, 121(3):383–411, 1988.

[26] E. Buckingham. *Analytical mechanics of gears*. Dover Books for Engineers. McGraw-Hill Book Co., 1949.

[27] G. Henriot. *Engrenages.: Conception, fabrication, mise en oeuvre, 7ème édition*. Technique et ingénierie. Série Mécanique. Dunod, 1999.

[28] B.-R. Höhn, K. Michaelis, and T. Vollmer. Thermal rating of gear drives: Balance between power loss and heat dissipation. *AGMA Technical Paper*, 1996.

[29] Eschmann Hasbargen Weigand. *Ball and Roller Bearings - Theory, Design, and Application*. Wiley, 1985.

[30] H. Ohlendorf. *Verlustleistung und Erwärmung von Stirnrädern*. PhD thesis, Dissertation TU München, 1958.

[31] A. J. Wimmer. *Lastverluste von Stirnradverzahnungen Konstruktive Einflüsse, Wirkungsgradmaximierung, Tribologie*. PhD thesis, Fakultät für Maschinenwesen der Technischen Universität München, 1996.

[32] G. Niemann and H. Winter. *Maschinenelemente: Band 2: Getriebe allgemein, Zahnradgetriebe - Grundlagen, Stirnradgetriebe*. Maschinenelemente /Gustav Niemann. Springer, 1989.

[33] P. Velex and F. Ville. An analytical approach to tooth friction losses in spur and helical gears-influence of profile modifications. *Journal of Mechanical Design, Transactions of the ASME*, 131(10):1010081–10100810, 2009. cited By (since 1996)11.

[34] R. Stribeck. *Die wesentlichen Eigenschaften der Gleit- und Rollenlager*. Mitteilungen über Forschungsarbeiten auf dem Gebiete des Ingenieurwesens. Heft 7. Julius Springer, 1903.

[35] R. Stribeck. Die wesentlichen eigenschaften der gleit- und rollenlager, pt I. *Zeitschrift des Vereines deutscher Ingenieure*, 46(37):1341–1348, 1902.

[36] R. Stribeck. Die wesentlichen eigenschaften der gleit- und rollenlager, pt II. *Zeitschrift des Vereines deutscher Ingenieure*, 46(38):1432–1438, 1902.

[37] R. Stribeck. Die wesentlichen eigenschaften der gleit- und rollenlager, pt III. *Zeitschrift des Vereines deutscher Ingenieure*, 46(39):1463–1470, 1902.

[38] A. J. Brandão, M. Meheux, F. Ville, Castro. M. J., and J. Seabra. Experimental traction and stribeck curves of mineral, pao and ester based fully formulated gear oils. *In: Proceedings of the 3rd International Conference on Integrity, Reliability & Failure, Porto, Portugal*, 20 - 24 July 2009.

[39] José A. Brandão, Mathilde Meheux, Fabrice Ville, Jorge H.O. Seabra, and Jorge Castro. Comparative overview of five gear oils in mixed and boundary film lubrication. *Tribology International*, 47(0):50 – 61, 2012.

[40] A. J. Brandão, M. Meheux, F. Ville, Castro. M. J., and J. Seabra. Traction curves and rheological parameters of fully formulated gear oils. *Proceedings of the Institution of Mechanical Engineers, Part J: Journal of Engineering Tribology (in press)*, 225:577–593, 2011.

[41] Y. A. Misharin. Influence of the friction condition on the magnitude of the friction coefficient in the case of rollers with sliding. *Proceedings International Conference on Gearing, Institute Mechanical Engineers,*, 1958, 1958.

[42] H Eiselt. *Beitrag zur experimentellen und rechnerischen Bestimmung der Fresstragfähigkeit von Zahnradgetrieben unter Berücksichtigung der Zahnflankenreibung*. PhD thesis, TH Desden, 1966.

[43] J. P. O'Donoghue and A. Cameron. Friction and temperature in rolling sliding contacts. *A S L E Transactions*, 9(2):186–194, 1966.

[44] Y.N. Drozdov and Y.A. Gavrikov. Friction and scoring under the conditions of simultaneous rolling and sliding of bodies. *Wear*, 11(4):291 – 302, 1968.

[45] Chotaro NARUSE, Shoji HAIZUKA, Ryozo NEMOTO, and Kazushi KUROKAWA. Studies on frictional loss, temperature rise and limiting load for scoring of spur gear. *Bulletin of JSME*, 29(248):600–608, feb 1986.

[46] B. Kelley and A. Lemanski. Lubrication of involute gearing. *Conference on Lubrication and Wear,Proceedings of the Institution of Mechanical Engineers*, 182:173–184, 1967.

[47] K. Michaelis and B. R. Höhn. Influence of lubricants on power loss of cylindrical gears. *S T L E Tribology Transactions*, 37(1):161–167, 1994.

[48] L. Schlenk. *Unterscuchungen zur Fresstragfähigkeit von Grozahnrädern*. PhD thesis, Dissertation TU München, 1994.

[49] ISO 6336-4. Calculation of load capacity of spur and helical gears-Part 4. *ISO*.

[50] B.-R. Höhn, K. Michaelis, and A. Doleschel. Frictional behavior of synthetic gear lubricants. In G. Dalmaz, A. Lubrecht, D. Dowson, and M. Priest, editors, *Tribology research: From model experiment to Industrial Problem*. Elsevier, 2001.

[51] S. Matsumoto and K. Morikawa. The new estimation formula of coefficient of friction in rolling-sliding contact surface under mixed lubrication condition for the power loss reduction of power transmission gears. *International Gear Conference*, 2014.

[52] Carlos M.C.G. Fernandes, Ramiro C. Martins, and Jorge H.O. Seabra. Coefficient of friction equation for gears based on a modified hersey parameter. *Tribology International*, pages –, 2016.

[53] Xu Hai. *Development of a Generalized Mechanical Efficiency Prediction Methodology for Gear Pairs*. PhD thesis.

[54] S Matsumoto, S Asanabe, K Takano, and M Yamamoto. Evaluation method of power loss in high-speed gears. *Japan Society of Lubrication Engineers,*, pages 1165–1170, 1985.

[55] C. Changenet, G. Leprince, F. Ville, and P. Velex. A note on flow regimes and churning loss modeling. *Journal of Mechanical Design*, 133(12):121009, 2011.

[56] C. Changenet and P. Velex. A model for the prediction of churning losses in geared transmissions—preliminary results. *Journal of Mechanical Design*, 129(1):128–133, 2007.

[57] A. S. Terekhov. Hydraulic losses in gearboxes with oil immersion. *Vestn. Mashinostroeniya*, 55(5):13–17, 1975.

[58] E. Lauster and M. Boos. Zum wärmehaushal mechanischer schaltgetriebe für nutzfahrzeuge. *VDI-Ber.*, 488:45–55, 1983.

[59] R. J. Boness. Churning losses of discs and gears running partially submerged in oil. *Procedings of ASME International Power Transmission Gearing Conference*, 1:355–359, 1989.

[60] S. Seetharaman and A. Kahraman. Load-independent spin power losses of a spur gear pair: Model formulation. *Journal of Tribology*, 131(2):022201, 2009.

[61] Gauthier LePrince, Christophe Changenet, Fabrice Ville, Philippe Velex, Christophe Dufau, and Frédéric Jarnias. Influence of Aerated Lubricants on Gear Churning Losses - An Engineering model. *Tribology Transactions*, 54(6):929–938, 2011.

[62] C. Changenet and P. Velex. Housing Influence on Churning Losses in Geared Transmissions. *Journal of Mechanical Design*, 130(6):062603, 2008.

[63] F Concli and C Gorla. Computational and experimental analysis of the churning power losses in an industrial planetary speed reducer. In *9th International Conference on Advances in Fluid Mechanics-Advances in Fluid Mechanics IX, WIT Transactions on Engineering Sciences*, volume 74, pages 287–298, 2012.

[64] A. S. Terekhov. Hydraulic losses in gearboxes with oil immersion. *Vestn. Mashinostroeniya*, 55(5):13–17, 1975.

[65] Sheng-Wei Chen and Susumu Matsumoto. Influence of relative position of gears and casing wall shape of gear box on churning loss under splash lubrication condition—some new ideas. *Tribology Transactions*, 59(6):993–1004, 216.

[66] SKF. *SKF General Catalogue 6000 EN*. SKF, 2013.

[67] Carlos M.C.G. Fernandes, Pedro M.P. Amaro, Ramiro C. Martins, and Jorge H.O. Seabra. Torque loss in thrust ball bearings lubricated with wind turbine gear oils at constant temperature. *Tribology International*, 66(0):194 – 202, 2013.

[68] Carlos M.C.G. Fernandes, Ramiro C. Martins, and Jorge H.O. Seabra. Friction torque of cylindrical roller thrust bearings lubricated with wind turbine gear oils. *Tribology International*, (0):–, 2012.

[69] Carlos M.C.G. Fernandes, Ramiro C. Martins, and Jorge H.O. Seabra. Friction torque of thrust ball bearings lubricated with wind turbine gear oils. *Tribology International*, 58(0):47 – 54, 2013.

[70] Jan Croes and Shoaib Iqbal. D2.1 document 3: Literature survey: seal losses. Technical report, ESTOMAD, 2009.

[71] Freudenberg Simrit GmbH & Co. KG. *Technische Grundlagen, Simerringue und Rotationsdichtungen*. Freudenberg Simrit GmbH & Co. KG, Technisches Handbuch 2007.

[72] H. Linke. Stirnradverzahnung. *Hanser Verlag*, 1996.

[73] Clemens Schlegel, Andreas Hösl, and Segej Diel. Detailed loss modelling of vehicle gearboxes. In *Proceedings 7th Modelica Conference*, pages 434–443, Como, Italy, 2009. The Modelica Association.

[74] J. Kettler. *Ölsumpftemperatur von Planetengetrieben: Abschlußbericht ; Forschungsvorhaben Nr. 313: Planetengetriebe-Sumpftemperatur*. Forschungsheft: Forschungsvereinigung Antriebstechnik. FVA, 2002.

[75] Dr. Frank Bauer and Werner Hass, Prof. Dr.-Ing. habil. The tribology of elastomeric lip seals - reducing emissions, preventing leakage, saving the ecology. In *World Tribology Congress*, Torino, Italy, 8-13, 2013.

[76] R. Martins, J. Seabra, A. Brito, Ch Seyfert, and A. Luther, R.and Igartua. Friction coefficient in fzg gears lubricated with industrial gear oils:biodegradable ester vs. mineral oil. *Tribology International*, 39(6):512–521, 2006.

[77] R. Martins, P. Moura, and J. Seabra. Power loss in fzg gears: Mineral oil vs. biodegradable ester and carburizedsteel vs. austempered ductile iron vs. mos2-ti coated steel. *VDI Berichte*, 1904.2(1904 II):1467–1486, 2005.

[78] R. Martins, N. Cardoso, and J. Seabra. Gear power loss performance of biodegradable low-toxicity ester-based oils. *Proceedings of the Institution of Mechanical Engineers Part J-Journal of Engineering Tribology*, 222(J3):431–440, 2008.

[79] R. Martins, J. Seabra, Ch Seyfert, R. Luther, A. Igartua, and A. Brito. Power loss in fzg gears lubricated with industrial gear oils: Biodegradable ester vs. mineral oil. In M. Priest G. Dalmaz D. Dowson and A. A. Lubrecht, editors, *Tribology and Interface Engineering Series*, volume Volume 48, pages 421–430. Elsevier, 2005.

[80] R. Martins, J. Seabra, Ch. Seyfert, R. Luther, A. Igartua, and A. Brito. Power loss in FZG gears lubricated with industrial gear oils: biodegradable ester vs. mineral oil. In *Proceedings of the 31th "Leeds-Lyon Symposium" on Tribology*, Leeds, UK, 2004.

[81] Luís Magalhães, Ramiro Martins, Cristiano Locateli, and Jorge Seabra. Influence of tooth profile and oil formulation on gear power loss. *Tribology International*, 43(10):1861–1871, 2010. 36th Leeds-Lyon Symposium Special Issue: Multi-facets of Tribology.

[82] C. Changenet, X. Oviedo-Marlot, and P. Velex. Power Loss Predictions in Geared Transmissions Using Thermal Networks-Applications to a Six-Speed Manual Gearbox. *Journal of Mechanical Design*, 128(3):618, 2006.

[83] J. Durand De Gevigney, C. Changenet, F. Ville, and P. Velex. Thermal modelling of a back-to-back gearbox test machine: Application to the fzg test rig. *Proceedings of the Institution of Mechanical Engineers, Part J: Journal of Engineering Tribology*, 226(6):501–515, 2012. cited By (since 1996)3.

[84] C. M. C. G. Fernandes, P. M. T. Marques, R. C. Martins, and J. H. O. Seabra. Influence of gear loss factor on the power loss prediction. *Mechanical Sciences*, 6(2):81–88, 2015.

[85] Agma 925-a03, effect of lubrication on gear surface distress.

[86] A. Fernandez del Rincon, F. Viadero, M. Iglesias, P. García, A. de Juan, and R. Sancibrian. A model for the study of meshing stiffness in spur gear transmissions. *Mechanism and Machine Theory*, 61(0):30 – 58, 2013.

[87] G. Niemann, C. Weber, and K. Banaschek. *Formänderung und Profilrücknahme bei gerad- und schrägverzahnten Rädern*. Schriftenreihe Antriebstechnik. Vieweg, 1953.

[88] Kunikazu HAYASHI. Load distribution on the contact line of helical gear teeth : Part 1 fundamental concept. *Bulletin of JSME*, 6(22):336–343, may 1963.

[89] José I. Pedrero, Miguel Pleguezuelos, Mariano Artés, and Juan A. Antona. Load distribution model along the line of contact for involute external gears. *Mechanism and Machine Theory*, 45(5):780 – 794, 2010.

[90] M. Ajmi and P. Velex. A model for simulating the quasi-static and dynamic behaviour of solid wide-faced spur and helical gears. *Mechanism and Machine Theory*, 40(2):173 – 190, 2005.

[91] MAAG Gear Company Ltd. *Maag Gear Book: Calculation and Practice of Gears, Gear Drives Toothed Couplings and Synchronous Clutch Couplings*. Maag Gear Company Limited, 1990.

[92] M. Maatar and P. Velex. An Analytical Expression for the Time-Varying Contact Length in Perfect Cylindrical Gears: Some Possible Applications in Gear Dnamics. *Journal of Mechanical Design*, Vol. 118:586–589, DECEMBER 1996.

[93] P. Velex, J. Bruyère, and D. R. Houser. Some Analytical Results on Transmission Errors in Narrow-Faced Spur and Helical Gears: Influence of Profile Modifications. *Journal of Mechanical Design*, 133(3):031010, 2011.

[94] ISO 6336-4. Calculation of load capacity of spur and helical gears-Part 1. *ISO*.

[95] Elmer: Open Source Finite Element Software for Multiphysical Problems.

[96] TetGen: A Quality Tetrahedral Mesh Generator and a 3D Delaunay Triangulator.

[97] F.L. Litvin and A. Fuentes. *Gear Geometry and Applied Theory*. Cambridge University Press, 2004.

[98] Pedro M.T. Marques, Ramiro C. Martins, and Jorge H.O. Seabra. Gear dynamics and power loss. *Tribology International*, 97:400 – 411, 2016.

[99] R. D. Houser and D. Talbot. The gear dynamic factor, historical and modern perspectives. *AGMA*, (07ftm10):13, 2007.

[100] A. Andersson and L. Vedmar. A dynamic model to determine vibrations in involute helical gears. *Journal of Sound and Vibration*, 260(2):195 – 212, 2003.

[101] L. Vedmar and A. Andersson. A method to determine dynamic loads on spur gear teeth and on bearings. *Journal of Sound and Vibration*, 267(5):1065 – 1084, 2003.

[102] S. Theodossiades, M. De la Cruz, and H. Rahnejat. Prediction of airborne radiated noise from lightly loaded lubricated meshing gear teeth. *Applied Acoustics*, 100:79 – 86, 2015.

[103] L.D. Landau and E.M. Lifshitz. *Mechanics*. Butterworth Heinemann. Butterworth-Heinemann, 1976.

[104] José A Brandão, Jorge HO Seabra, and Jorge Castro. Surface initiated tooth flank damage: Part i: Numerical model. *Wear*, 268(1):1–12, 2010.

[105] José A Brandão, Jorge HO Seabra, and Jorge Castro. Surface initiated tooth flank damage. part ii: Prediction of micropitting initiation and mass loss. *Wear*, 268(1):13–22, 2010.

[106] Tiago Cousseau, Beatriz Graça, Armando Campos, and Jorge Seabra. Friction torque in grease lubricated thrust ball bearings. *Tribology International*, 44(5):523 – 531, 2011. Special Issue: {ECOTRIB} 2009.

[107] Tiago Cousseau, Beatriz M. Graça, Armando V. Campos, and Jorge H.O. Seabra. Influence of grease rheology on thrust ball bearings friction torque. *Tribology International*, 46(1):106 – 113, 2012. 37th Leeds-Lyon Symposium on Tribology Special issue: Tribology for Sustainability: Economic, Environmental, and Quality of Life.

[108] David Gonçalves, Beatriz Graça, Armando V. Campos, J. Seabra, Johan Leckner, and René Westbroek. Formulation, rheology and thermal ageing of polymer greases—part i: Influence of the thickener content. *Tribology International*, 87:160 – 170, 2015.

[109] David Gonçalves, Rui Marques, Beatriz Graça, Armando V. Campos, Jorge H.O. Seabra, Johan Leckner, and Renéx Westbroek. Formulation, rheology and thermal aging of polymer greases—part ii: Influence of the co-thickener content. *Tribology International*, 87:171 – 177, 2015.

[110] David Gonçalves, Beatriz Graça, Armando V. Campos, J. Seabra, Johan Leckner, and René Westbroek. On the film thickness behaviour of polymer greases at low and high speeds. *Tribology International*, 90:435 – 444, 2015.

[111] David Gonçalves, Beatriz Graça, Armando V. Campos, and J. Seabra. On the friction behaviour of polymer greases. *Tribology International*, pages –, 2015.

[112] Deirdra Barr. Modern wind turbines: A lubrication challenge. Septmeber 2002.

[113] Determination of viscosity of bitumen emulsions - engler method.

[114] Astm d341 - 09, standard practice for viscosity - temperature charts for liquid petroleum products.

[115] J. Denis, J. Briant, and J.-C. Hipeaux. *Physico-Chimie des Lubrifiants - Analyses et Essais*. Éditions Technip, 1997.

[116] Carlos M.C.G. Fernandes, Pedro M.T. Marques, Ramiro C. Martins, and Jorge H.O. Seabra. Film thickness and traction curves of wind turbine gear oils. *Tribology International*, 86(0):1 – 9, 2015.

[117] JP. W. Gold, A. Schmidt, H. Dicke, H. Loos, and C. Aßmann. Viscosity-pressure-temperature behaviour of mineral and synthetic oils. *Journal of Synthetic Lubrication*, 18(1), 2001.

[118] J. A. Greenwood and J. J. Kauzlarich. Elastohydrodynamic film thickness for shear-thinning lubricants. *Proceedings of the Institution of Mechanical Engineers, Part J: Journal of Engineering Tribology*, 212(3):179–191, 1998.

[119] Scott Bair and Peter Gordon. Rheological challenges and opportunities for ehl. In R.W. Snidle and H.P. Evans, editors, *IUTAM Symposium on Elastohydrodynamics and Micro-elastohydrodynamics*, volume 134 of *Solid Mechanics and Its Applications*, pages 23–43. Springer Netherlands, 2006.

[120] Ivan Krupka, Scott Bair, Punit Kumar, M.M. Khonsari, and Martin Hartl. An experimental validation of the recently discovered scale effect in generalized newtonian ehl. *Tribology Letters*, 33(2):127–135, 2009.

[121] H. Dinner. Wind turbine gearbox calculation. *KISSsoft*, 2006.

[122] Neil E. Anderson, Stuart H. Loewenthal, Joseph D. Black, and United States. *An analytical method to predict efficiency of aircraft gearboxes [microform] / Neil E. Anderson and Stuart H. Loewenthal and Joseph D. Black*. National Aeronautics and Space Administration [Washington, D.C.?, 1984.

[123] D.T. Jelaska. *Gears and Gear Drives*. Wiley, 2012.

[124] T.A. Harris and M.N. Kotzalas. *Essential Concepts of Bearing Technology, Fifth Edition*. Rolling Bearing Analysis, Fifth Edtion. CRC Press, 2006.

[125] T.A. Harris and M.N. Kotzalas. *Advanced Concepts of Bearing Technology,: Rolling Bearing Analysis, Fifth Edition*. Rolling Bearing Analysis, Fifth Edtion. CRC Press, 2006.

[126] D. Dowson and G. R. Higginson. *Elasto-hydrodynamic Lubrication*. Pergamon Press, SI edition edition, 1977.